

**TECHNISCHE UNIVERSITÄT
BERGAKADEMIE FREIBERG**



49. Geomechanik-Kolloquium Tagungsbeiträge



Veröffentlichungen
des Institutes für Geotechnik der TU Bergakademie Freiberg
Herausgeber: H. Konietzky

**Heft
2020-4**



Leider mussten wir uns wegen der Corona-Epidemie schweren Herzens dazu entscheiden, das für den 13. November geplante 49. Geomechanik-Kolloquium nicht durchzuführen.

Die Autoren der geplanten Vorträge haben uns aber dankenswerter Weise ihre Beiträge zugesandt, so dass wir in der Lage waren, wie gewohnt die Proceedings zu erstellen. Nochmals vielen Dank an die Autoren!

Wir sind zuversichtlich, dass wir das 50. Geomechanik-Kolloquium in bewährter Zusammenarbeit mit dem IfG Leipzig im November 2021 durchführen können und sie dann in großer Runde wieder persönlich zu den Vorträgen und anregenden Fachgesprächen, aber auch zur beliebten Abendveranstaltung begrüßen zu können.

Bleiben sie vorsichtig und gesund! Viel Freude beim Lesen der Proceedings.

Mit einem herzlichen Glückauf grüßt das Team der Felsmechanik aus Freiberg,
Freiberg, 13.11.2020

Table of content

From point-wise stress data to a continuous description of the undisturbed 3D stress field <i>M. Ziegler, O. Heidbach, S. Morawitz, (GFZ Potsdam); K. Reiter (Technische Universität Berlin)</i>	1
The STIMTEC experiment at the Reiche Zeche underground laboratory <i>C. Böse, M. Bonhof, G. Dresen, C. Jansen, G. Kwiatek (GFZ Potsdam); H. Konietzky, S. Rehde (TU Bergakademie Freiberg); M. Krause, T. Meier (geomecon GmbH); B. Adero, Y. Cheng, V. A. Jimenez Martinez, J. Renner (Ruhr-Universität Bochum)</i>	13
Storage of Production Brine in Rooms of Potash Mines Mining Field Behavior: Modelling and Monitoring <i>J-P. Schleinig, S. Deppe (K+S Aktiengesellschaft, Kassel); M. Nest (Institut für Gebirgsmechanik GmbH, Leipzig); M. Günther, (K+S Minerals and Agriculture GmbH, Philippsthal); H. Zienert (K+S Minerals and Agriculture GmbH, Unterbreizbach)</i>	27
Problems related to Geomechanics in hard coal mining in the Asturian Central Coal Basin <i>F. Schmidt (Sachverständiger Santander, Spain); J. Menendez (Hunaser Energy, Oviedo, Spain); J. L. Perez (University of Oviedo, Spain)</i>	43
Die Beurteilung der von Steinschlag ausgehenden Gefahr mithilfe von Prozessmodellen: Stolpersteine und Risiken <i>A. Preh, E. Fleris, M. Illeditsch (TU Wien, Austria)</i>	55
Cross-border geographic information system and monitoring of rock falls events in the Saxon-Bohemian Switzerland <i>J. Wichert (TU Bergakademie Freiberg)</i>	71
Numerical investigations of fracture interference during hydraulic fracturing <i>Y. Yu, W. Zhu, L. Li, C. Wei, B. Yan, C. Qin (Northeastern University, Shenyang, China)</i>	79
Experimental approaches into process understanding and characterization of georeservoirs - Preliminary results of the GREAT cell poliaxial facility <i>M. Sauter, M. Fazio (University of Göttingen), A. P. Fraser-Harris, C. I. McDermott, G. D. Couples, A. Lightbody (University of Edinburgh, UK); T. Frühwirt (TU Bergakademie Freiberg)</i>	93

Ground movement predictions above coal mines after flooding <i>G. Lüttschwager, J. Zhao, H. Konietzky (TU Bergakademie Freiberg)</i>	107
Short-Term Pore Pressure Evolution around Tunnels in Opalinus Clay: Lessons Learned from an Overcoring Experiment <i>K. Khaledi, P. Hamdi, L. Winhausen, M. Jalali, F. Amann (RWTH Aachen)</i>	131
Sinkholes over Deep Caverns <i>W. Minkley, C. Lüdeling (Institut für Gebirgsmechanik GmbH, Leipzig)</i>	145
Investigations of the thermal impact on Elbe sandstone: real fire experiments, laboratory tests and numerical simulations <i>N. Freudenberg, T. Frühwirt, F. Wang (TU Bergakademie Freiberg)</i>	165
Crude oil storage caverns in India and their design aspects <i>A. Kaltenböck (Geoconsult ZT GmbH, Austria); F. Krenn (Geoconsult India Private Ltd.); O. Sigl (Geoconsult Singapore PTe Ltd.)</i>	177
Distinct Element Modelling on the Effect of Wellbore Arrangement on Fracture Propagation during Multi-Stage Hydraulic Fracturing <i>P. L. P. Wasantha (Victoria University, Melbourne, Australia); H. Konietzky (TU Bergakademie Freiberg); T. Xu (Northeastern University, Shenyang, China)</i>	197
The influence of stylolite on mechanical behavior of limestone: digital-image based discrete element analysis <i>T. Xu, Z. Heng, B. Zhao, J. Lu, J. Lu (Northeastern University, Shenyang, China)</i>	207

From point-wise stress data to a continuous description of the undisturbed 3D stress field

Von punktweisen Spannungsdaten zur kontinuierlichen Beschreibung des ungestörten 3D Spannungsfeldes

Moritz Ziegler¹, Oliver Heidbach¹, Sophia Morawietz^{1,2} and Karsten Reiter³

¹Helmholtz Centre Potsdam, GFZ German Research Centre for Geosciences, Telegrafenberg, 14473 Potsdam, Germany

²Technische Universität Berlin, Straße des 17. Juni 135, 10623 Berlin, Germany

³Institute of Applied Geosciences, Technical University Darmstadt, Schnittspahnstraße 9, 64287 Darmstadt, Germany

Abstract

Subsurface engineering requires information on the in situ stress to ensure the stability of geotechnical installations. Information on the stress tensor orientation is provided in the World Stress Map (WSM) – a global open access database with more than 40,000 data records. However, stress orientations are not sufficient for a reliable assessment of the criticality or stability of a rock mass, but stress magnitude data are required as well. For Germany the World Stress Map now also includes stress magnitude data and a global extension with magnitude data is planned. Still, stress magnitude data records – if they are available at all – are only pointwise information on the stress state. A continuous description of the 3D in situ stress is the true challenge that requires geomechanical-numerical modelling. For the calibration of such a stress model stress magnitude data are essential. In addition, stress model results should also deliver uncertainties of the predicted in situ stress to provide a measure for its reliability.

Zusammenfassung

Jegliche Untergrundnutzung erfordert Informationen über den in situ Spannungszustand, um die Stabilität der geotechnischen Anlagen zu gewährleisten. Informationen über die Spannungsorientierung werden in der World Stress Map (WSM) – einer globalen Open-Access-Datenbank mit mehr als 40.000 Datensätzen – bereitgestellt. Die Orientierung des Spannungstensors ist jedoch nicht ausreichend für eine zuverlässige Beurteilung der Kritikalität oder Stabilität des Untergrunds. Hierzu werden auch Daten zu Spannungsmagnituden benötigt. Für Deutschland ist eine Erweiterung der WSM Datenbank um Magnitudendaten verfügbar und eine globale Erweiterung ist geplant. Allerdings sind auch Spannungsmagnitudendatensätze – wenn sie überhaupt verfügbar sind – nur punktweise Informationen und die 3D kontinuierliche Beschreibung des Spannungszustandes ist die Herausforderung. Für diese wird geomechanisch-numerische Modellierung verwendet, die zur Kalibrierung insbesondere Spannungsmagnituden-Daten erfordert. Darüber hinaus müssen die Unsicherheiten der Modelle quantifiziert werden, um ein Maß für deren Robustheit zu erhalten.

1 Introduction

A broad utilisation of the subsurface in the 21st century is required to secure energy resources and for the transition to a sustainable energy supply, for infrastructure optimisation, and for fluid and solid waste disposal. Any subsurface activity bears a potential risk of rock failure of economic concern or even social concern in terms of induced seismicity. One component required to mitigate this risk is a sustainable management of the geomechanics. This requires an assessment of the in-situ stress in relation to the failure criteria of the associated rock.

However, information on the in-situ stress is sparse and available only pointwise. The World Stress Map (WSM) project provides an open access global database on the orientation of the maximum horizontal stress S_{Hmax} (Heidbach et al., 2018). Each data record is assigned a quality in order to make data from different stress indicators comparable. As an addition to the stress orientation data, a compilation of stress magnitude data records has been started. Currently, an initial dataset for Germany and adjacent areas is available (Morawietz et al., 2020) and a global compilation is in preparation.

Still, the compilation of pointwise stress data alone, both orientation and magnitude, is usually not sufficient for a comprehensive characterization of the stress field at any arbitrary location. Therefore, 3D geomechanical-numerical modelling is applied to provide a continuous stress field description based on a geological model and rock properties describing the associated lithologies. The stress data records available within the model volume are essential for the model calibration.

In the following, we present the WSM project and the compilation of S_{Hmax} orientation data records with an associated quality ranking. Furthermore, we describe the extension of the WSM to include magnitude data records. Eventually, we indicate the necessary steps to estimate a continuous stress state with a 3D geomechanical-numerical model with quantified uncertainties.

2 The stress tensor

The stress state is described by the second order stress tensor σ_{ij} . Due to its symmetry it consists of six independent components (Fig. 1a), namely three normal ($\sigma_{ij}, i=j$) and three shear components ($\sigma_{ij}, i \neq j$). To simplify the description of the stress state a main axis transformation rotates the stress tensor in a way that all shear stresses dissipate and only three perpendicular principal stress axis remain. In addition to their magnitudes, their orientation is then required to describe the stress state (Fig. 1b). For the upper crust it is assumed that the vertical stress S_V is a principal stress axis (Zoback, 2010). The other two principal stresses are the minimum (S_{Hmin}) and the maximum horizontal stress (S_{Hmax}). This reduced stress tensor requires only four information, the three magnitudes and the S_{Hmax} orientation are sufficient to describe the stress state (Fig. 1c).

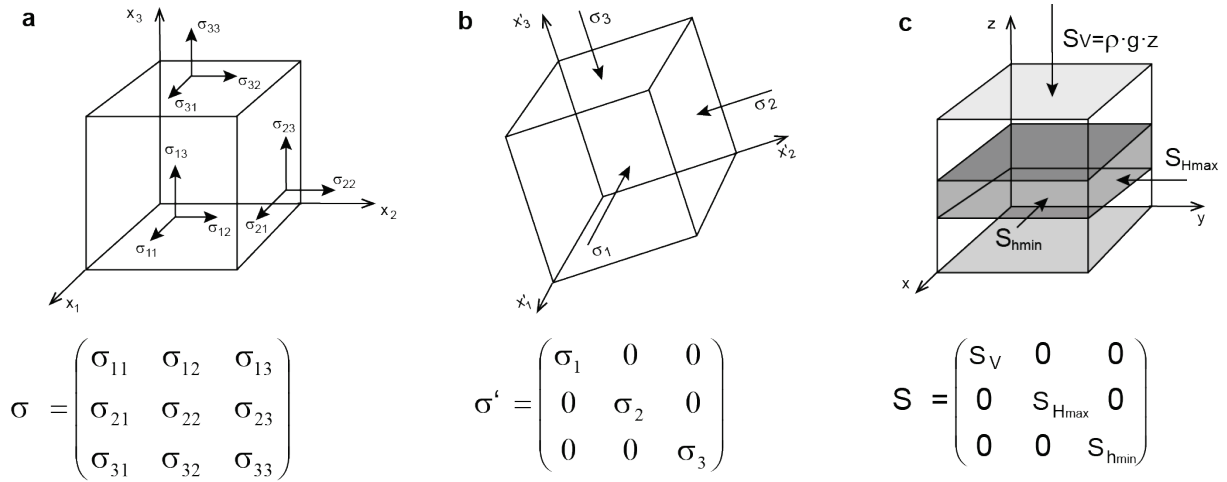


Fig. 1: (a) The stress tensor, (b) stress tensor in its principal axes system, (c) reduced stress tensor commonly applied to describe the stress state in the upper crust.

3 Pointwise stress data

Stress is a quantity that cannot be measured directly in-situ. Any estimation of the stress orientation and/or magnitudes is always an observation or measurement of a phenomenon that is influenced by the stress state. In synthesis with assumptions estimates on the stress state can be made. A wide variety of phenomena serve as indicators for the stress state and thus very different methods are applied to estimate the stress state. Any interpretation of the stress state based on data that originate from different indicators is challenged by the diversity of methods. Questions concerning the reliability of different estimations based on different indicators arise. In the following, we describe a stress orientation and a stress magnitude database that address this challenge.

3.1 Orientation of the maximum horizontal stress S_{Hmax}

The orientation of S_{Hmax} is globally compiled by the World Stress Map (WSM) project (Heidbach et al., 2018). It aims at quantification of the stress tensor components, to characterize the crustal stress pattern and to understand the stress sources. All stress information that result from the stress indicators is analysed and compiled in a standardized format and quality-ranked for reliability and comparability. The project is service oriented and provides besides the public database software tools that help to generate stress maps, investigate the stress pattern as well as to analyse and visualize the results from 3D geomechanical-numerical models (e. g. Stromeyer & Heidbach, 2017, Ziegler & Heidbach, 2019).

The first stress data compilations of the intra-plate crustal stress state were published in the early seventies. In 1986 the WSM as such was initialized as project of the International Lithosphere Program. The backbone of the WSM is the quality-ranking scheme (Zoback et al., 1989, Zoback & Zoback, 1991). This quality ranking ensures the global comparability of the different stress indicators that originate from geological and geophysical data as well as from engineering methods. Each data record is quality-ranked based on the WSM quality ranking system from A to E quality. A quality data indicate that the S_{Hmax} orientation is accurate to within $\pm 15^\circ$, B quality to within $\pm 20^\circ$, C quality to within $\pm 25^\circ$, D quality to within $\pm 40^\circ$. E quality is assigned to data records with incomplete, non-reliable information or when the standard deviation

is $> \pm 40^\circ$. Further information which is provided for subsets of the WSM database is the stress regime, i.e. the relative magnitudes of the three principal stresses. The current WSM database release 2016 has 42,870 data records 72 % of which are from foal mechanism solutions. 14 % of the data records are borehole breakouts, followed by stress inversions of several focal mechanisms and several other stress indicators (Fig. 2). 75 % of the data records are of a reliable A, B, or C quality and thus the indicated orientation of S_{Hmax} is expected to be $\pm 25^\circ$ accurate (Fig. 3). The full database as well as maps of several areas of interest can be downloaded for free from www.world-stress-map.org.

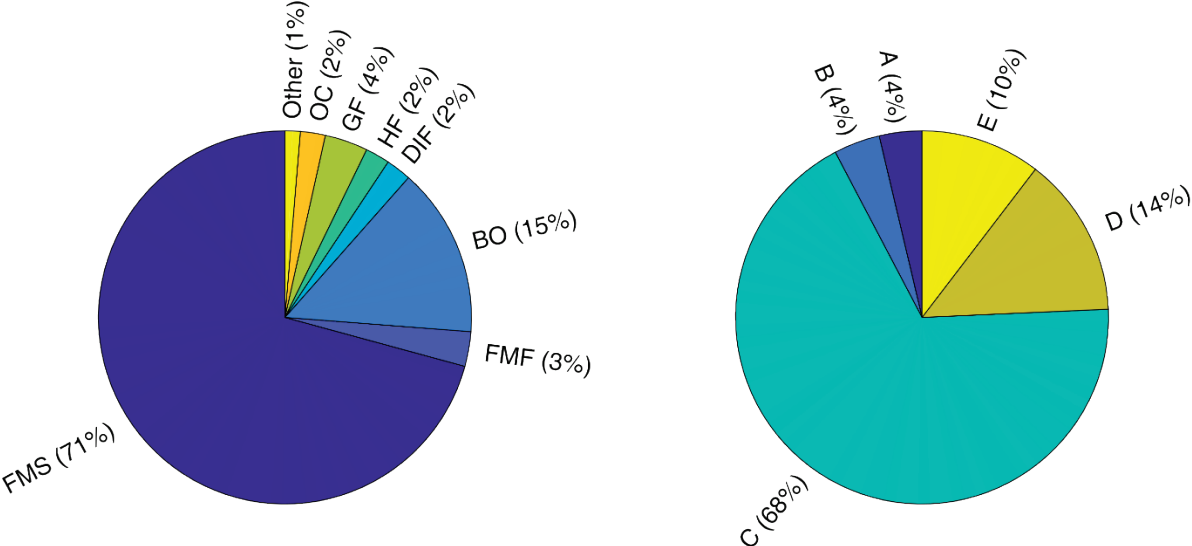


Fig. 2: Statistics of the WSM database. Left: The distribution of stress indicator types. FMS: Focal mechanism solution, FMF: Formal inversion of focal mechanism solutions, BO: Borehole breakout, DIF: Drilling induced tensile fracture, HF: hydraulic fracturing, GF: Geological indicators, OC: Overcoring measurement. Right: Distribution of the assigned qualities.

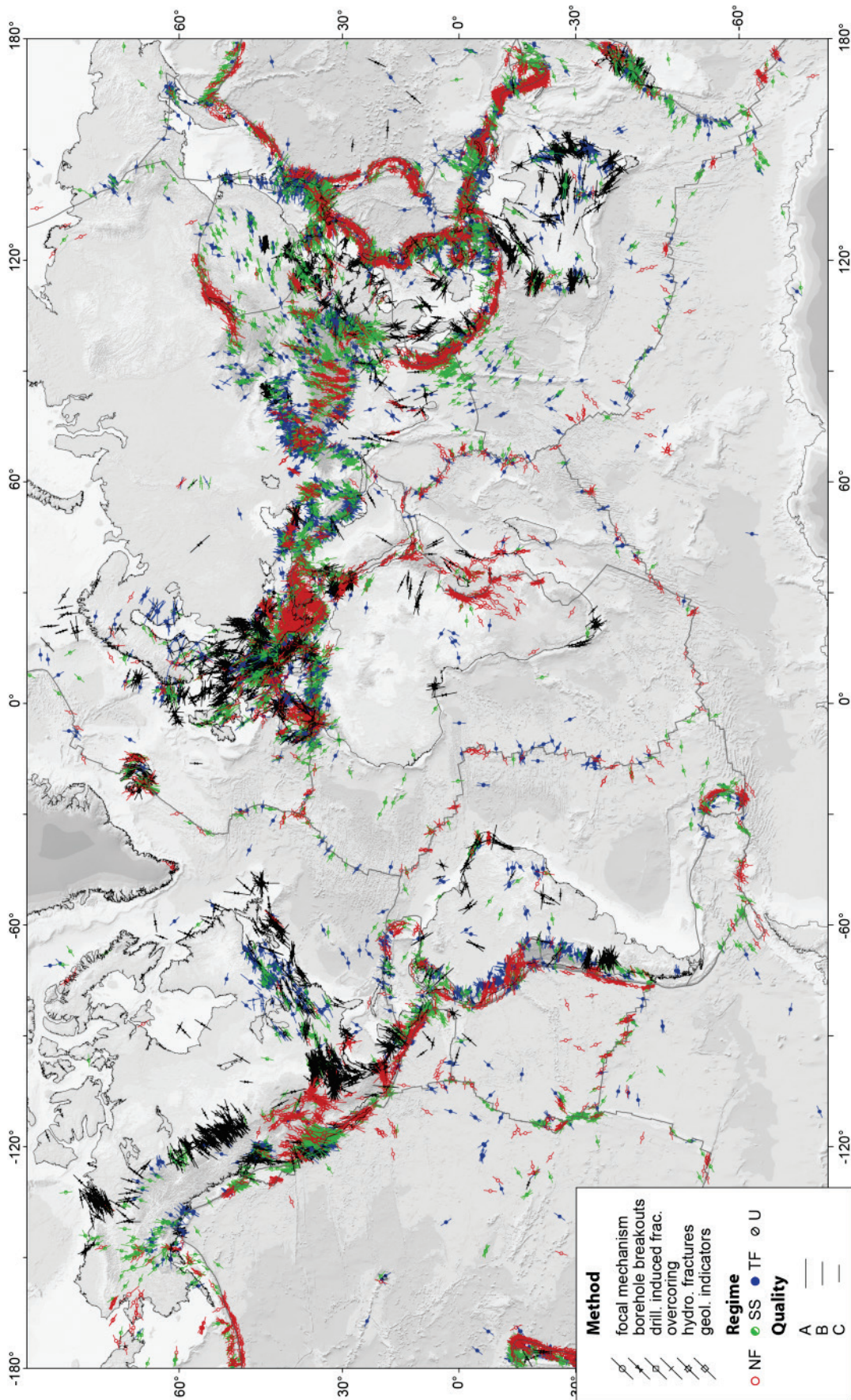


Fig. 3: The WSM 2016 displays the contemporary crustal stress in the upper 40 km based on the WSM database release 2016 (Heidbach et al., 2016, Heidbach et al., 2018).

Lines show the orientation of maximum horizontal stress (S_{Hmax}) from different stress indicators displayed by different symbols; line length is proportional to data quality. Displayed are the 20,757 data records with A-C quality according to the WSM quality ranking scheme except those that are labelled as possible plate boundary events (Heidbach et al., 2010). Colours of the symbols and lines indicate the tectonic stress regime with red for normal faulting (NF), green for strike-slip (SS), blue for thrust faulting (TF) and black for unknown (U) tectonic stress regime. Plate boundaries are taken from PB2002 (Bird, 2003), topography is based on the ETOPO1 data from the National Geophysical Data Center (NGDC) including bathymetry data from (Amante & Eakins, 2009). This map can be accessed and downloaded in high resolution at <http://doi.org/10.5880/WSM.2016.002>.

3.2 Stress magnitudes

Information on the orientation of the reduced stress tensor, however, is not sufficient for an integrated assessment of the rock stability. Information on the stress magnitudes are essential in addition to failure criteria of the respective rock. An extension of the WSM to integrate stress magnitude data is currently under construction. Analogously to the compilation of S_{Hmax} orientation data, a wide range of stress indicators are integrated into the database. To ensure comparability between the stress data records a quality ranking scheme is required. However, the wide range of available methods that indicate stress magnitudes as well as the few freely available data records and the associated high uncertainties pose a large challenge for a universally applicable quality ranking scheme.

As an initial step 568 stress magnitude data records from Germany and adjacent regions have been compiled and quality ranked according to a newly proposed scheme for stress magnitude data (Morawietz et al., 2020) and are available for download from <https://doi.org/10.5880/wsm.2020.004>. In its basics, the quality ranking scheme for stress magnitudes follows the well-established scheme for stress orientation data. A quality from A – E is assigned according to the expected reliability of the stress magnitude data record. Depending on the type of stress magnitude indicator different criteria have to be met in order to be assigned to a certain quality. Thus a direct comparison between the significance of different stress indicators is possible. If the information is incomplete in the reference an X-quality is assigned which indicates that the quality of the data record is unclear.

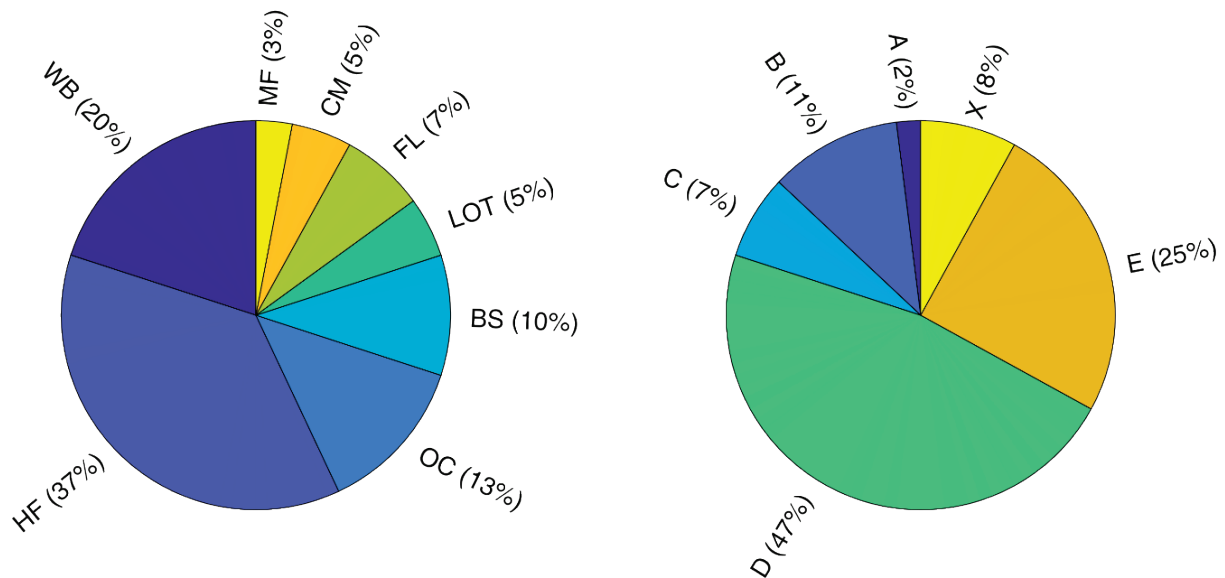


Fig. 4: Statistics of the magnitude database. Left: The distribution of stress indicator types. WB: Misc. wellbore fluid measurements, HF: Hydraulic fracturing, OC: Overcoring measurement, BS: Borehole slotting, LOT: Leak off tests and formation integrity tests, FL: Frictional limit considerations, CM: Core measurements, MF: Mini-frac. Right: Distribution of the assigned qualities.

From the 568 data records most (37 %) originate from hydrofrac measurements or the hydraulic testing on pre-existing fractures, followed by various borehole fluid measurements (20 %). 13 % originate from mostly shallow overcoring measurements and 10 % from borehole slotting (Fig. 4). Less important contributors are formation integrity tests (only as lower boundary of S_{hmin}), leak off tests, frictional limit considerations, core measurements, or mini-frac tests. The range of methods illustrates that the large majority of data records provide only a S_{hmin} magnitude. Less than 20 % of the data records are assigned A, B, or C quality, and the majority (47 %) is assigned a D quality (Fig. 4). This indicates the less than optimal reliability and quality of description of the average measurement.

4 Continuous description of the stress field

The analysis of the stress magnitude database indicates that at a single location, the vertical increase of the horizontal stress magnitudes is not necessarily following a gradient. This is partly a result of the variability of different rock properties of individual lithological units (Hergert et al., 2015). In particular, in tectonically complex settings with significant mechanical differences between lithologies a large effect of the lithology on the stress state can be observed. Thus, the stress state at a location of interest without stress magnitude information cannot be estimated by a simple extrapolation from the nearest available information.

However, 3D geomechanical-numerical modelling can be applied to estimate the continuous stress state in an area of interest (Reiter & Heidbach, 2014, Van Wees et al., 2003). Three pieces of information are required therefore: (1) Stress data records from within the model area are compared to the modelled stress state. The initial and boundary conditions are adapted until a good fit of the observed to the modelled stress state is achieved (Hergert et al., 2015, Rajabi et al., 2017). (2) A 3D geological model with all relevant lithologies and a degree of detail adapted to the appli-

cation is set up. The model boundaries are oriented orthogonally and parallel to the prevailing orientation of the S_{Hmax} component. The extent of the model is chosen in a way that it includes both, the area of interest in sufficient resolution and stress data records that can be used for calibration. (3) Information on the elastic rock properties of the represented lithological units are required. These are the Young's module, the Poisson ratio, and the density.

Once the stress data records are in agreement with the modelled stress state the assumption is made that the modelled stress state throughout the model volume is a good representation of the actual stress state. The stress state in the area of interest is then available for interpretation.

5 Discussion

The presented estimation of a continuous stress field using 3D geomechanical-numerical models is based on the availability of stress data records (Fig. 5). The WSM project provides both stress orientation data for the orientation of the model area and for initial assessment if exceptional stress patterns are observed. Stress magnitude data is currently provided for the initial region of Germany and will be provided globally in the future. The quality ranking scheme ensures that data records from various sources are comparable. Furthermore, different qualities can be used to weigh the orientation and magnitude data records accordingly.

A major challenge in this approach is the asymmetric distribution of stress data records available for calibration. While in some areas a lot of data is available in the majority of regions none or close to none is available. This may require large model Areas in order to include both, the area of interest and suitable data records for model calibration. This often leads to a trade-off between model size and resolution. To mitigate this, a multistage approach that uses a large and a small model is one possible solution (Ziegler et al., 2016).

Even though a 3D geomechanical-numerical model is a major step forward compared to an extrapolation of stress data records to the volume, significant uncertainties are associated with the model results. The uncertainties originate in the variability of the available stress data records (Ziegler & Heidbach, 2020), the uncertainties of the rock properties (Hergert et al., 2015), or the uncertainties in the geological model (Wellmann & Regenauer-Lieb, 2012). In contrast to the uncertainties associated with an extrapolation of stress data, a modelling approach allows the quantification (Ziegler & Heidbach, 2020) and even the reduction (Ziegler & Heidbach, *in review for JGR*) of uncertainties. Thus, the significance of the resulting stress state is increased in that an estimated range of possible stress states is available.

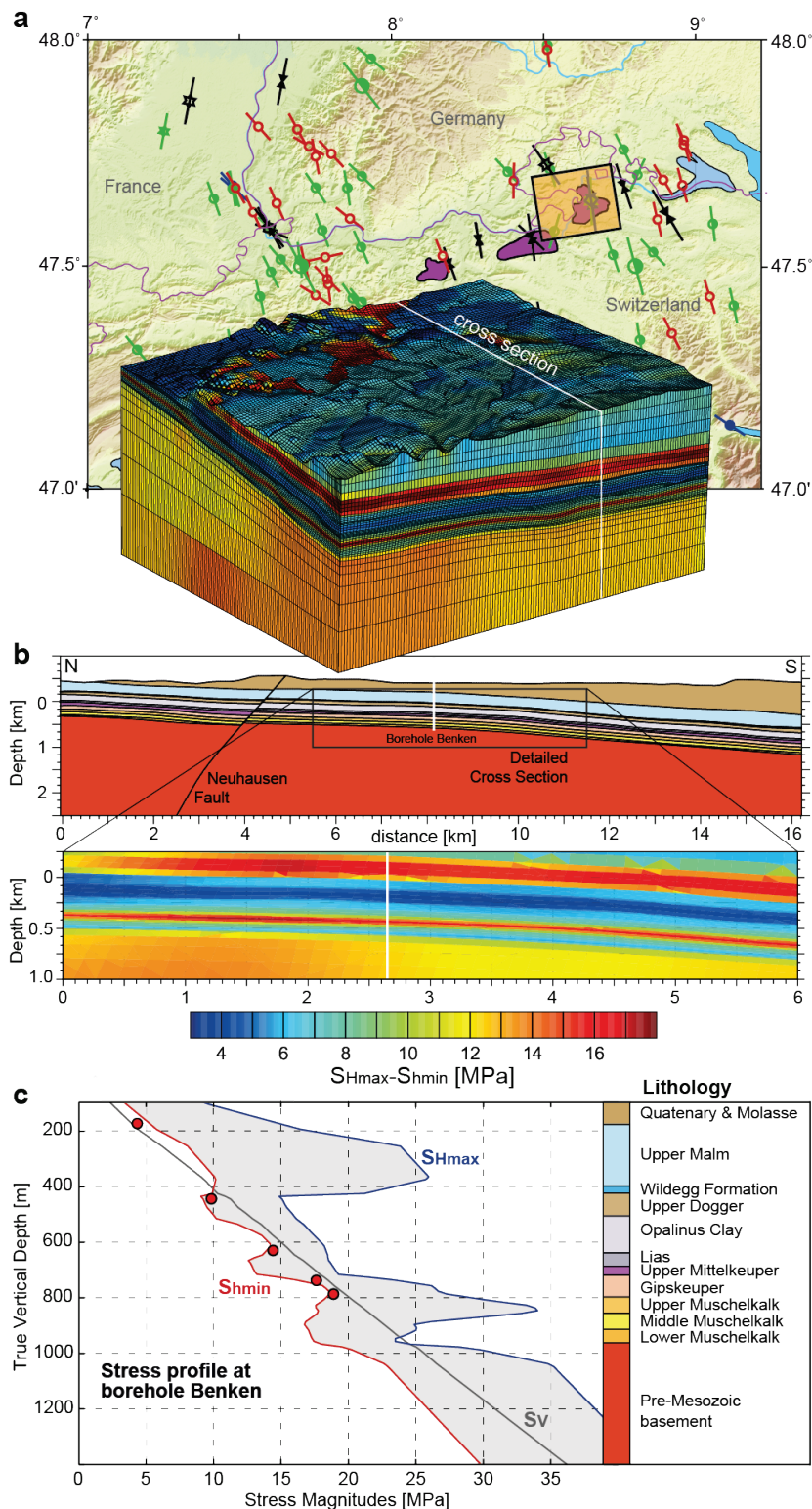


Fig. 5: From pointwise stress data to a continuous description of the stress field. (a) The WSM with orientations of the maximum horizontal stress component and the Benken area of interest for the deep geological nuclear waste repository in Switzerland. The discretization of the 3D geomechanical-numerical model is shown. (b) A representative cross-section showing the lithology (top) and the differential stress $S_{Hmax}-S_{Hmin}$ (bottom) which indicates the lithology dependence. (c) The stress 1D profile at Benken borehole derived from the model results (lines) together with data records on the S_{Hmin} magnitude (red dots).

6 Conclusion

Knowledge on the continuous in-situ stress state is gained from 3D geomechanical-numerical models that are calibrated on actual stress data records. Compared to extrapolation of stress data records this is beneficial in that associated uncertainties can be quantified which allows for a significant interpretation of the modelled stress state. The required stress data records for calibration are provided by the WSM project and made comparable by a quality ranking scheme. Thereby, stress data records from various sources can be compared and weighted before introduction to a model for calibration.

7 References

- Amante, C., & Eakins, B.W. 2009. ETOPO1 – 1 Arc-Minute Global Relief Model: Procedures, Data Sources and Analysis. *NOAA Technical Memorandum NESDIS NGDC-24. National Geophysical Data Center, NOAA.*
- Bird, Peter. 2003. An updated digital model of plate boundaries. *Geochemistry, Geophysics, Geosystems*, **4**(3), 1–52.
- Heidbach, Oliver, Tingay, Mark, Barth, Andreas, Reinecker, John, Kurfeß, Daniel, & Müller, Birgit. 2010. Global crustal stress pattern based on the World Stress Map database release 2008. *Tectonophysics*, **482**(1-4), 3–15.
- Heidbach, Oliver, Rajabi, Mojtaba, Reiter, Karsten, Ziegler, Moritz, & the WSM Team. 2016. *World Stress Map Database Release 2016*. GFZ Data Services. DOI: 10.5880/WSM.2016.001
- Heidbach, Oliver, Rajabi, Mojtaba, Cui, Xiaofeng, Fuchs, Karl, Müller, Birgit, Reinecker, John, Reiter, Karsten, Tingay, Mark, Wenzel, Friedemann, Xie, Furen, Ziegler, Moritz O., Zoback, Mary-Lou, & Zoback, Mark. 2018. The World Stress Map database release 2016: Crustal stress pattern across scales. *Tectonophysics*, **744**(oct), 484–498.
- Hergert, T., Heidbach, O., Reiter, K., Giger, S. B., & Marschall, P. 2015. Stress field sensitivity analysis in a sedimentary sequence of the Alpine foreland, northern Switzerland. *Solid Earth*, **6**(2), 533–552.
- Morawietz, S., Heidbach, O., Reiter, K., Ziegler, M., Rajabi, M., Zimmermann, G., Müller, B. & Tingay, M. An open-access stress magnitude database for Germany and adjacent regions. Accepted for publication in *Geothermal Energy*
- Rajabi, M, Heidbach, O, Tingay, Mark, & Reiter, K. 2017. Prediction of the present-day stress field in the Australian continental crust using 3D geomechanical-numerical models. *Australian Journal of Earth Sciences*, **64**(4), 435–454.
- Reiter, K., & Heidbach, O. 2014. 3-D geomechanical-numerical model of the contemporary crustal stress state in the Alberta Basin (Canada). *Solid Earth*, **5**(2), 1123–1149.
- Stromeyer, Dietrich, & Heidbach, Oliver. 2017. *Tecplot 360 Add-on GeoStress*. DOI: 10.2312/wsm.2017.001
- Van Wees, JD, Orlic, B, Van Eijs, R, Zijl, W, Jongerius, P, Schreppers, GJ, Hendriks, M, & Cornu, T. 2003. Integrated 3D geomechanical modelling for deep subsurface deformation: a case study of tectonic and human-induced deformation in the eastern Netherlands. *Geological Society, London, Special Publications*, **212**(1), 313–328.

- Wellmann, J Florian, & Regenauer-Lieb, Klaus. 2012. Uncertainties have a meaning: Information entropy as a quality measure for 3-D geological models. *Tectonophysics*, **526**, 207–216.
- Ziegler, Moritz, & Heidbach, Oliver. 2019. Manual of the Matlab Script Stress2Grid v1.1. *WSM Technical Report; 19-02*. DOI: 10.5880/wsm.2017.002
- Ziegler, Moritz O., & Heidbach, Oliver. 2020. The 3D stress state from geomechanical numerical modelling and its uncertainties: a case study in the Bavarian Molasse Basin. *Geothermal Energy*, **8**(1).
- Ziegler, Moritz O., Heidbach, Oliver, Reinecker, John, Przybycin, Anna M., & Scheck-Wenderoth, Magdalena. 2016. A multi-stage 3-D stress field modelling approach exemplified in the Bavarian Molasse Basin. *Solid Earth*, **7**(5), 1365–1382.
- Zoback, Mary Lou, Zoback, Mark D., Adams, J, Assumpção, M., Bell, S., Bergman, E. A., Blümling, P., Brereton, N. R., Denham, D., Ding, J., Fuchs, K., Gay, N., Gregersen, S., Gupta, H. K., Gvishiani, A., Jacob, K., Klein, R., Knoll, P., Magee, M., Mercier, J. L., Müller, B. C., Paquin, C., Rajendran, K., Stephansson, O., Suarez, G., Suter, M., Udias, A., Xu, Z. H., & Zhizhin, M. 1989. Global patterns of tectonic stress. *Nature*, **341**(6240), 291–298.
- Zoback, M.D. 2010. *Reservoir Geomechanics*. Cambridge: Cambridge University Press.
- Zoback, MD, & Zoback, ML. 1991. Tectonic stress field of North America and relative plate motions. *Pages 339–366 of: Slemmons, D.B., & Engdahl, E.R. (eds), Neotectonics of North America*. Boulder, Colorado: Geological Society of America.

The STIMTEC experiment at the Reiche Zeche underground laboratory

Das STIMTEC-Experiment im Forschungsbergwerk Reiche Zeche

Caroline Böse ¹, Marco Bonhof ¹, Georg Dresen ¹,
Christof Jansen ¹, Grzegorz Kwiatek ¹, Heinz Konietzky ², Sebastian Rehde ²,
Michael Krause ³, Thomas Meier ³, Bernard Adero ⁴, Yan Cheng ⁴,
Victoria A. Jimenez Martinez ⁴, Jörg Renner ⁴

¹ Helmholtz Centre Potsdam, GFZ German Research Centre for Geosciences

² TU Bergakademie Freiberg

³ geomecon GmbH

⁴ Ruhr-Universität Bochum

Abstract

Between early 2018 and late 2019, hydraulic stimulation experiments were performed ca. 130 m below surface at the Reiche Zeche research mine in Freiberg, Saxony/Germany. The STIMTEC project aimed at gaining insight into the creation and growth of fractures in anisotropic and heterogeneous crystalline rock units, to develop and optimise hydraulic stimulation techniques, important for the development of enhanced geothermal energy systems. We present the developed infrastructure and provide an overview of the obtained data, including 295 m of core material retrieved from 17 boreholes, 225 m of acoustic televiewer logs, > 50 TB of continuous passive seismic data from four testing campaigns, and ~ 300 active velocity measurements. We highlight some of the first results regarding the rock mass characterization in-situ and in the laboratory, the hydro-mechanical and seismic response to the stimulation, as well as 3-D numerical modelling of the stress state.

Zusammenfassung

Zwischen Anfang 2018 und Ende 2019 wurden in einer Tiefe von ca. 130 m hydraulische Stimulations-Experimente im Forschungsbergwerk Reiche Zeche (Freiberg, Sachsen) durchgeführt. Das STIMTEC Projekt hat zum Ziel, Erkenntnisse zu Erzeugung und Wachstum von Rissen in anisotropen und heterogenen kristallinen Gesteinseinheiten zu erlangen, um hydraulische Stimulationstechniken zu entwickeln und zu optimieren, die wichtig sind für die Entwicklung von EGS Systemen. Es wird die aufgebaute Infrastruktur vorgestellt und eine Übersicht über die erhaltenen Daten gegeben. Dies schließt 295 m an Kernmaterial, erhalten aus 17 Bohrungen, 225 m akustischer Bohrloch-Logs, mehr als 50 TB kontinuierlicher passiven seismischer Daten aus vier Testkampagnen und ca. 300 aktive seismische Geschwindigkeitsmessungen ein. Der Beitrag zeigt erste Resultate in Bezug auf die Gebirgscharakterisierung in-situ und im Labor, die hydro-mechanischen und seismischen Reaktionen auf die Stimulationen und die 3D Spannungsfeldsimulationen.

1 Introduction

The STIMTEC experiment was conducted at ca. 130 m below surface in the Reiche Zeche underground research laboratory (URL), Freiberg, Saxony/Germany. It comprised a pre-stimulation characterisation phase, a stimulation phase, and a post-stimulation validation and characterisation phase. The hydraulic stimulations were designed to investigate the hydro-mechanical processes controlling enhancement of hydraulic properties in anisotropic rock. Specifically, the main objective was the development of stimulation concepts with increased prognostic capacity by

- determination of seismic and hydraulic fingerprints of hydraulic stimulations,
- constraining the relevance of hydro-mechanical processes,
- validation of simulation results through drilling and sampling of the stimulated rock volume, and
- extension of models for stimulation processes with regard to the spatial patterns and time sequences of typical fracture and failure processes.

During the pre-stimulation phase, we hydraulically characterised sections of the 63 m-long, 16°-northward inclined injection borehole with a focus on pre-existing damage zones. During the stimulation phase, ten intervals of 0.7 m length in the injection borehole experienced the same treatment comprising pressurisation beyond breakdown during a frac sequence, followed by three refrac sequences, a step-rate test, and periodic pumping tests with periods between 60 and 800 s. The pressure response was continuously monitored above and below the deployed double-packer probe as well as in a second hydraulic monitoring borehole. Post-stimulation validation comprised drilling three new boreholes, two directed at stimulated rock volumes that exhibited seismic activity and one vertical for additional stress measurements and calibration of the seismic network's sensitivity. The changes in hydraulic properties were explored by extensive hydraulic interference testing between boreholes.

2 Results

The existing tunnel system at Wilhelm Stehender Süd in Reiche Zeche provided an ideal environment for STIMTEC. Two tunnels that run parallel at a distance of about 30 m but eventually merge allowed us to monitor the test volume comprehensively. Performing a project like STIMTEC in the confined space of a mine however also poses logistical challenges. The successful campaigns would not have been possible without the support of the miners at Reiche Zeche and the flexibility the involved companies exhibited. In the following, we report on the project progression and the results of the performed rock-mass characterisation, the hydro-mechanical and seismic responses to the stimulations, and the accompanying numerical modelling.

2.1 Project progression

The project reached all its technical milestones, i.e., the boreholes were successfully drilled (Figure 1) and proved to be stable such that the sensor network were installed and testing was conducted as planned. In the hydraulic experiments, almost 10 m³ of water were injected in total. Injection and monitoring boreholes were divided into sections of different lengths using single- and double-packer probes.

Seismic events were recorded during various pumping operations. The seismic activity of the 10 intervals originally investigated in the injection well varied considerably between a few 10,000 and no recorded events, which required analysing the detection threshold of the established network with high precision. This task was accomplished by a repeat injection and 5 more in the vertical validation well with modified instrumentation of the network as well as by extensive active sonic transmission of the test volume using all validation wells. Adapting the instrumentation to results was recognised as fundamentally important.

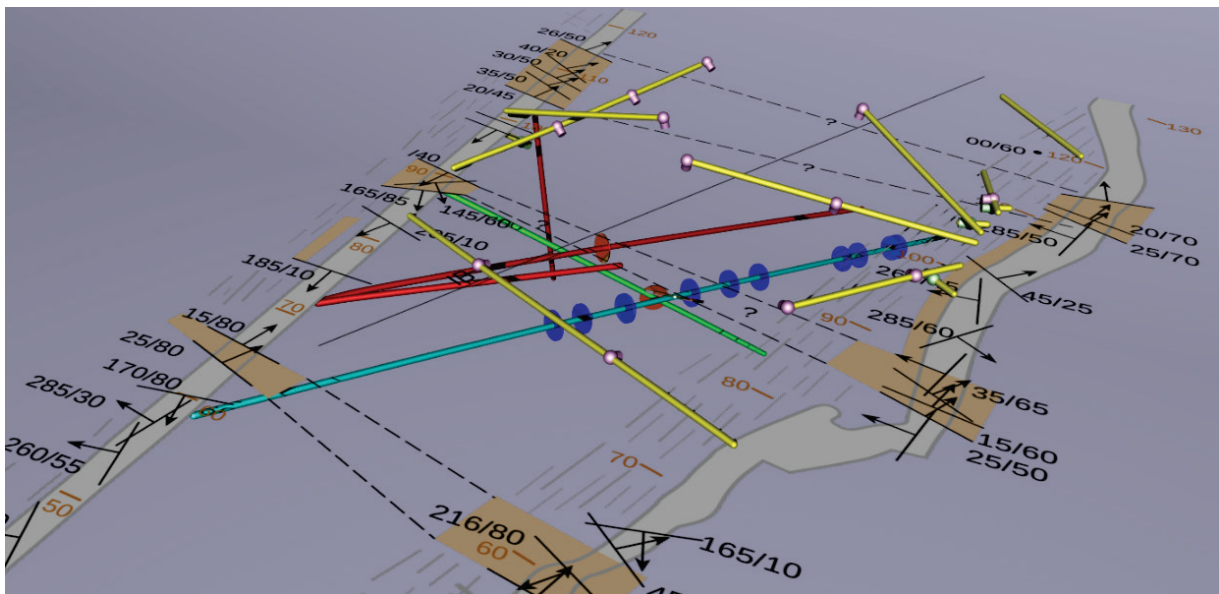


Figure 1: The system of exploratory drillings created in colliery of Reiche Zeche, Freiberg. The blue markings along the injection well BH10 (cyan) indicate the injection intervals.

2.2 Preliminary scientific results

2.2.1 Rock-mass characterization

The investigated rock volume of strongly foliated metamorphic gneiss is crosscut by multiple small-scale open and healed fractures and two major, steeply dipping, northwest-southeast trending deformation zones. Foliation is sub-horizontal causing elastic wave anisotropy approximately described by vertical transverse isotropy, as constrained by over 200 active ultrasonic measurements and laboratory tests on core material. The results of the transmission experiments on centimetre-sized samples in the laboratory and over ten-metre-long sections in the underground laboratory provide surprisingly well-correlated elastic wave propagation velocities (Figure 2).

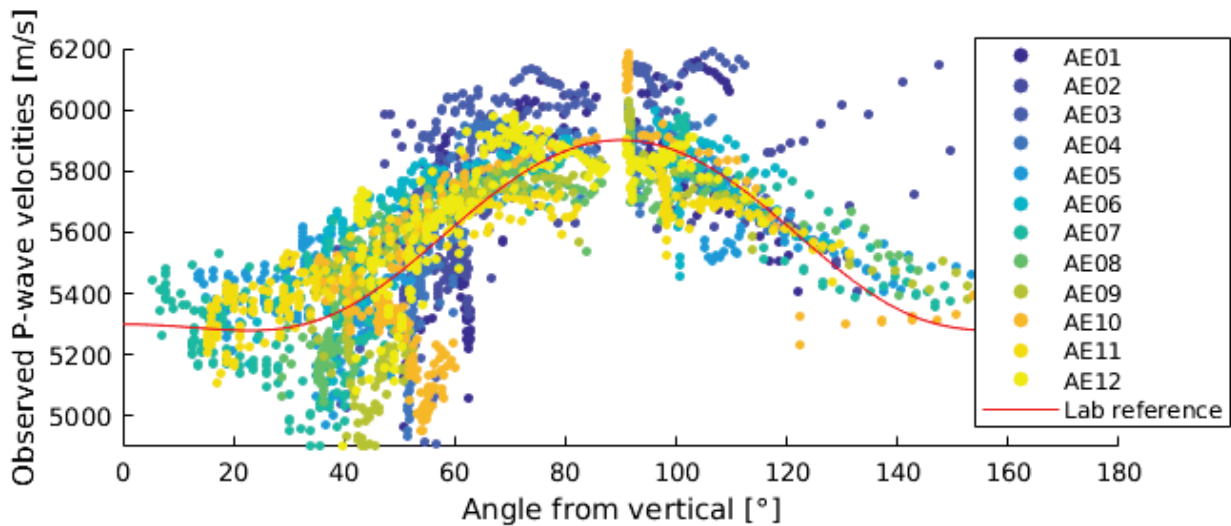


Figure 2: Comparison of the results of transmission experiments in Reiche Zeche (coloured dots with information on the receiver number) and in the laboratory (red line, representing the average of a total of approx. 100 individual measurements). The laboratory samples were prepared in five different orientations to the pronounced foliation of the gneiss. The approx. 20 samples of each direction exhibit a slightly lower variability in velocity than the field data. In addition to the agreement of the absolute values, the degree of anisotropy also matches between field and laboratory measurements.

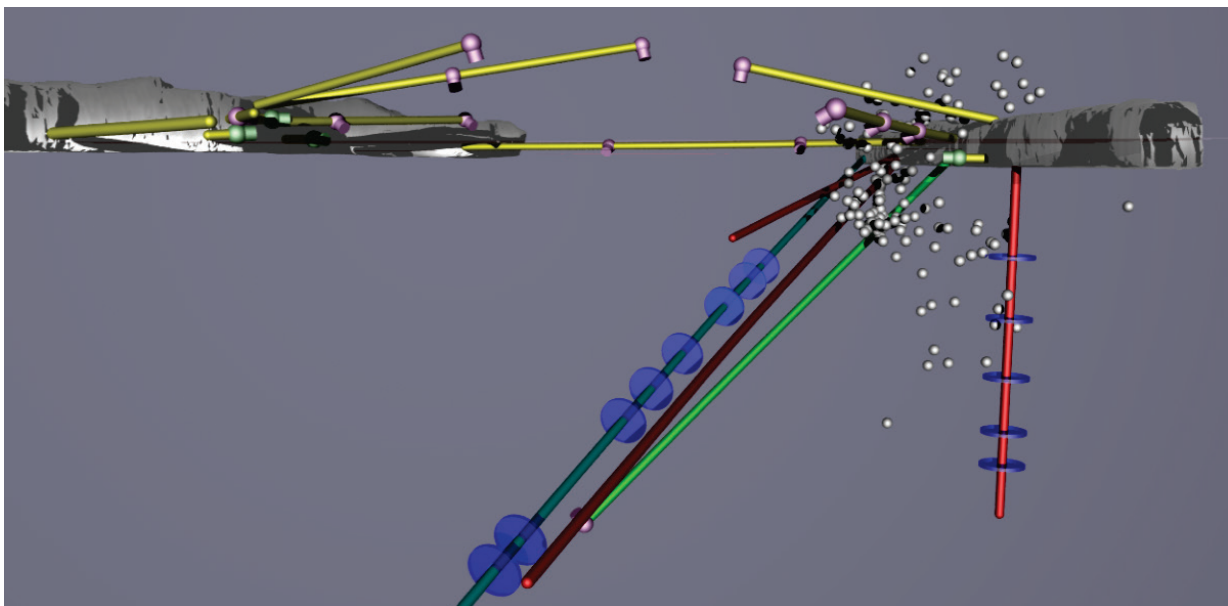


Figure 3: Spatial distribution of micro-seismic events (small coloured dots) for the stimulations of the top three injection intervals in BH10 and the mean injection interval in BH17.

2.2.2 Seismic activity

When seismicity was observed in the wake of fluid injection, the occurrence of micro-seismic events exhibited close correlation with pumping activity, in space (Figure 3) and time (Figure 4). It is particularly noticeable that slight periodic variations in injection pressure (flow rate) also lead to periodic seismic activity. It is therefore neces-

sary to consider the hypothesis that the form of the change in injection rate - and only to a lesser extent the strength of the change- is responsible for the seismicity. Such a role of injection-rate changes indicates that the direct hydro-mechanical coupling can be responsible for stress redistributions leading to seismicity to a similar extent as fluid-pressure diffusion.

A further indication of the relationship between hydro-mechanical coupling and micro-seismic activity is the size of the active rock volume, which in the case of the injections in validation well BH17 cannot be explained by localization uncertainties. The occurrence of events above the tunnel (Figure 3) is to be regarded as significant in the light of localization errors and cannot be explained by fluid-pressure diffusion because this area is not completely saturated.

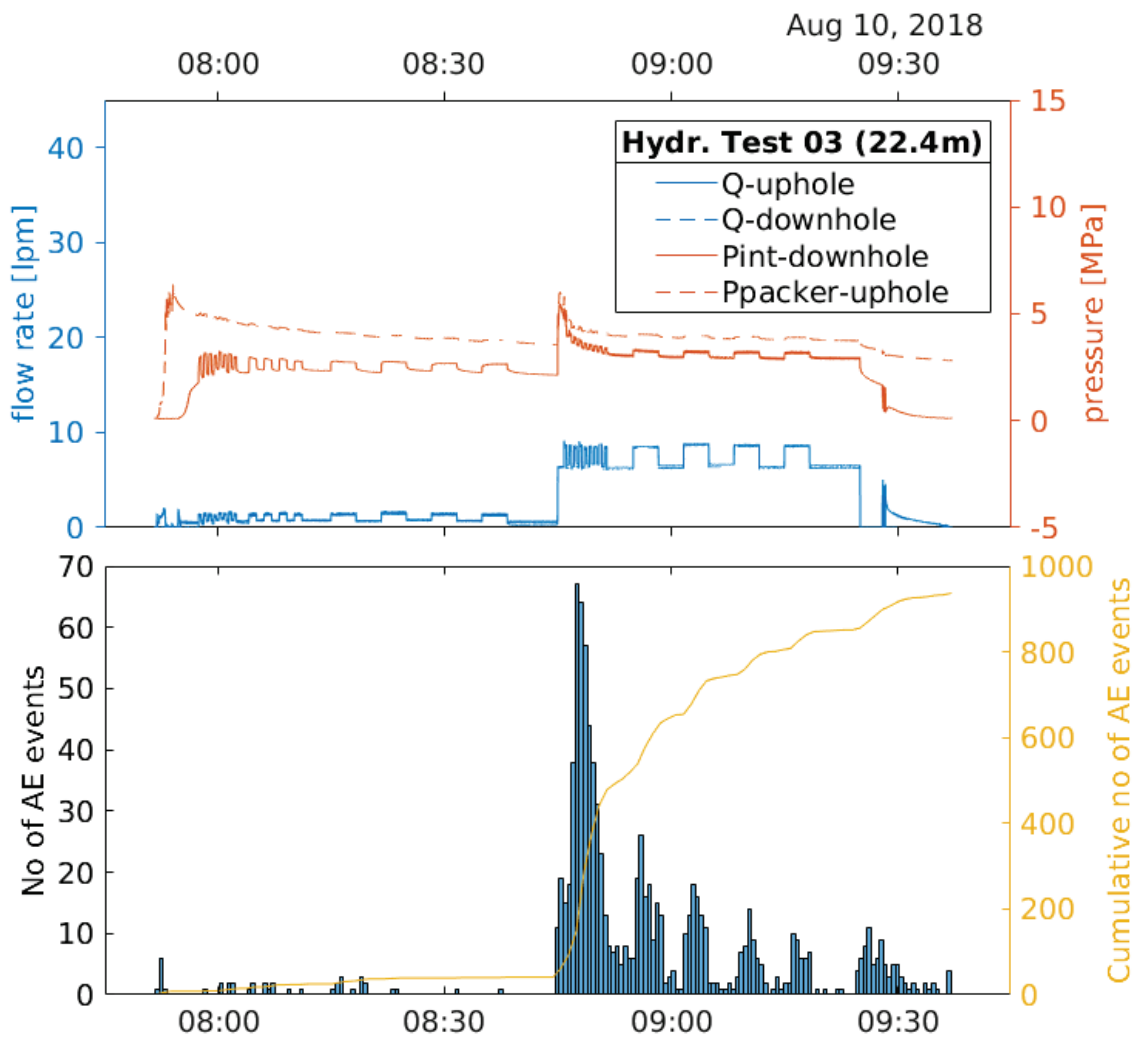


Figure 4: Time correlation of the pumping log and the seismic activity. Especially noteworthy is the periodic seismic activity (from about 08:50), which follows the low periodic perturbations of the injection pressure.

Derived fault-plane solutions exhibit small uncertainties of the orientations of the fault planes due to the density and the favourable spatial distribution of receivers (Figure 5). The variability of the nodal planes determined for individual events promises a high degree of certainty for future stress inversion.

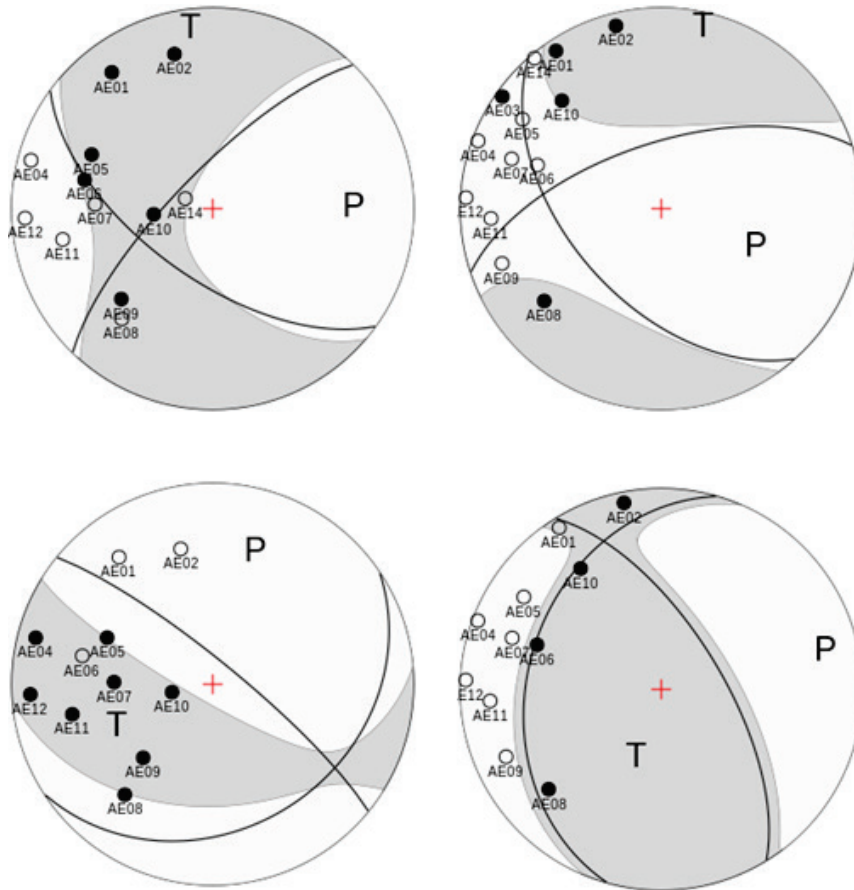


Figure 5: Examples of fault-plane solutions for micro-seismic events of the stimulation at depth interval 24.6 m in injection well BH10 (top row and bottom left) and the mini-frac measurements at 6.7 m depth in vertical validation well BH17 (bottom right). The continuous great-circle lines show the best fitting of the nodal planes assuming a pure-shear mechanism, the grey fields show the degree of shear and tensile fracture components.

2.2.3 Stimulation and hydraulic characterization

A considerable number of hydraulic experiments were carried out (Figure 8, top). In fact, the data basis for the development of hydro-mechanical models exceeds by far the hopes at the beginning of the project. Hydraulic characterisation showed transmissivity increases by up to two orders of magnitude for intervals with new fractures. However, these did not reach the transmissivity values observed in naturally fractured intervals close to or within the northern damage zone.

The use of periodic pumping tests made it possible to specifically investigate the hydraulic behaviour of the stimulated injection intervals as a function of the mean injection pressure and thus to gain more knowledge about the opening and closing of cracks. Pumping below and above jacking pressures of hydraulic conduits documented a dramatic increase in injectivity with pressure. How cracks, into which fluid is injected, interact with their environment depends largely on their stiffness, a parameter that has so far been inadequately investigated on the field scale.

The two close to horizontal validation boreholes, the mine-back aspect of STIMTEC, targeted seismically active and inactive zones. These confirmed hydraulic improve-

ment where AE events had occurred, and indicate the importance of pre-existing fluid pathways where no AEs were observed.

The pronounced foliation of the Freiberg gneiss and the fault zones in the reservoir volume influence the physical rock properties (e.g., anisotropy of seismic wave velocities, Figure 2). At face value, foliation did not affect fracture initiation, as evidenced by the orientations of fracture traces identified by impression-packer tests and televiewer logging (Figure 8, bottom). Laboratory experiments showed that the tensile strength of Freiberg gneiss is at least a factor of two lower for foliation planes than for random planes. The field observations appear to be a consequence of the orientation relation between foliation and in-situ stresses.

We observed small-scale heterogeneity in stress magnitudes and orientations, possibly related to the anisotropy and the heterogeneity due to foliation or rock variability. The vertical validation borehole confirmed the significant heterogeneity that if representative for crystalline rocks in general will have to be taken into account in reservoir engineering and modelling since stress heterogeneity will impact creation and orientation of induced fractures and therefore hydraulic properties of stimulated rock volumes. The spatial scale of the variations in stress is unexpected and raises fundamental questions for the characterization of reservoirs that are only accessible by a few boreholes and therefore direct stress measurements can only be carried out locally and to a limited extent.

2.2.4 Stress-state modelling

The knowledge about the in-situ stress field in the URL Reiche Zeche was very limited before the STIMTEC project. Only, a single in-situ stress field measurement was previously performed using the overcoring method (Mjakischew, 1987). Therefore, the experiments of the STIMTEC project are used to set-up a numerical stress field model based on the new field measurements, laboratory data, and a GIS-model. To perform the numerical simulations, first, 3D geological models were set up based on maps and digital data of the URL Reiche Zeche. The large-scale model M1 covers a volume of 2500 m x 2500 m x 500 m and includes topography, mine drifts, and 45 faults (Figure 6). The test area is centred in the model. The small-scale model M2 is centred in M1 and is 250 m x 250 m x 50 m. It includes the fault "Wilhelm Stehender", the mapped local joints and the two drifts (Figure 6). From M2, a slice model M3

(70 m x 5 m x 50 m) was extracted covering the area around borehole BH17 (Figure 6), for which M2 alone did not provide satisfying results. All 3D geological models were created using SKUA-GOCAD. The mesh for the numerical simulations with 3DEC was created using the Rhino plug-in GRIDDLE.

In general, we assumed isotropic or transverse-isotropic elastic behaviour for the rock mass and elasto-plastic behaviour for the faults in the simulations (Table 1). In addition, M3 considered excavation disturbed zones around the drifts by reduced stiffness (Table 2) and consists of 2474863 zones with zone edge lengths of 0.2 m and 0.3 m for the inner and outer EDZ, respectively, and 0.5 m in the rest of the model. The mesh for model M1 consists of 588,854 zones with edge lengths of 1 m to 250 m. The mesh size was gradually increased from the location of the measurements towards the boundaries. Gravity was acting. The model bottom was fixed. The lateral model boundaries were orientated parallel and perpendicular to the global tectonic stress regime acting in central Europe, which is also in close agreement with

the orientation of the maximum horizontal stress component determined by Mjakischew (1987). Stresses were applied to the outer boundaries, so that they fit the stress data from Mjakischew (1987).

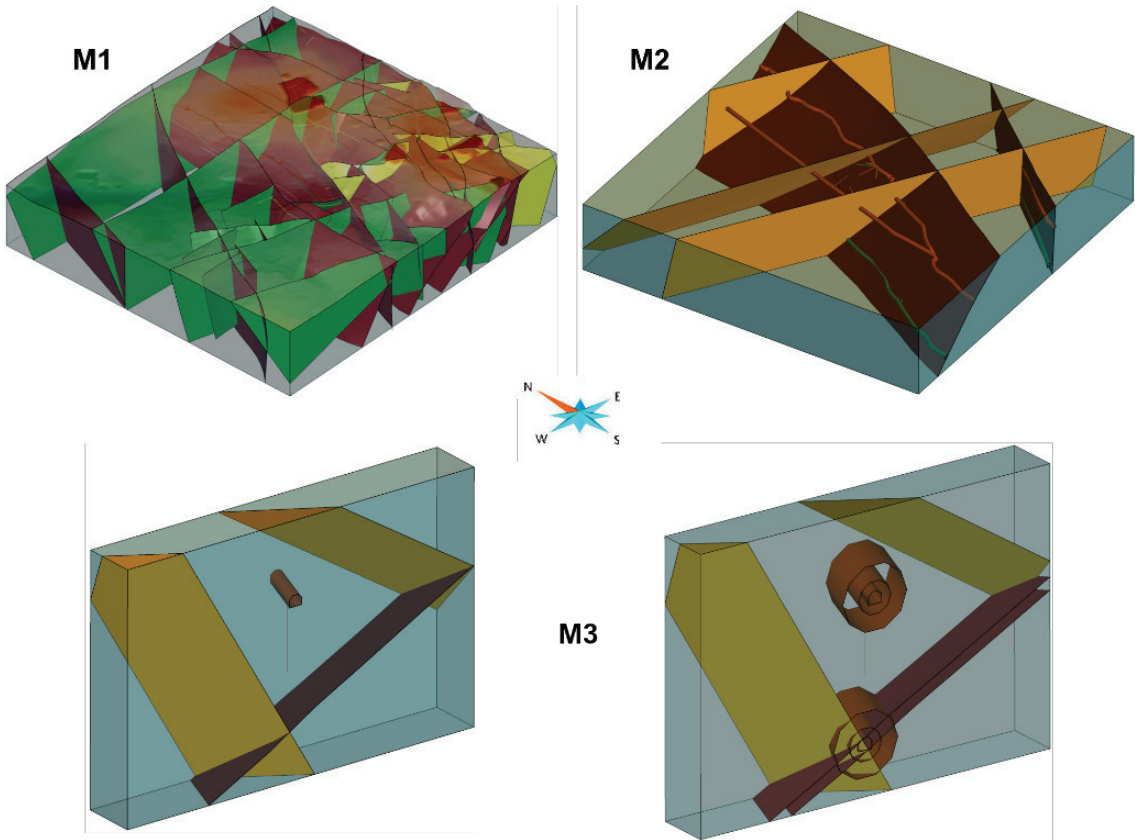


Figure 6: Large-scale, medium-scale, and small-scale GIS models (M1, M2, and M3) for numerical stress field modelling. Two versions of M3 are shown, with added features on the right.

Table 1: Elastic mechanical rock and rock mass parameters of Freiburger Graugneis.

	Density ρ (kg/m ³)	Young's modulus $E_{\text{host rock}}$ (GPa)	Poisson's ratio ν (-)	Young's modulus $E_{\text{GSI}=80}$ (GPa)	Poisson's ratio $\nu_{\text{GSI}=80}$ (-)
Foliation	2700	70.0	0.20	52.8	0.20
⊥ Foliation	2700	46.7	0.13	35.2	0.13

Table 2: Mechanical parameters of faults.

Normal stiffness k_n (MPa/m)	Shear stiffness k_s (MPa/m)	Friction angle θ (°)	Dilation angle ψ (°)	Cohesion c (MPa)	Tensile strength σ_t (MPa)
1885	1885	25	5	0	0

Stress data from Mjakischew (1987) and the hydrofrac stress measurements from BH10 are well reproduced by models M1 and M2. This stress field is also in agreement with regional stress field data. However, the strong stress field perturbations detected in BH17 could not be reproduced by the performed modelling. Future work is necessary to explain this local stress anomaly. Table 3 reports the overall stress field modelled for the first level at the URL Reiche Zeche that closely agrees with the in-situ stress field measurements. Local stress fluctuations due to faults, influence of topography, and excavations can be obtained by consulting the numerical stress field model, which provides the complete stress tensor for all locations inside the model (e.g., Figure 7).

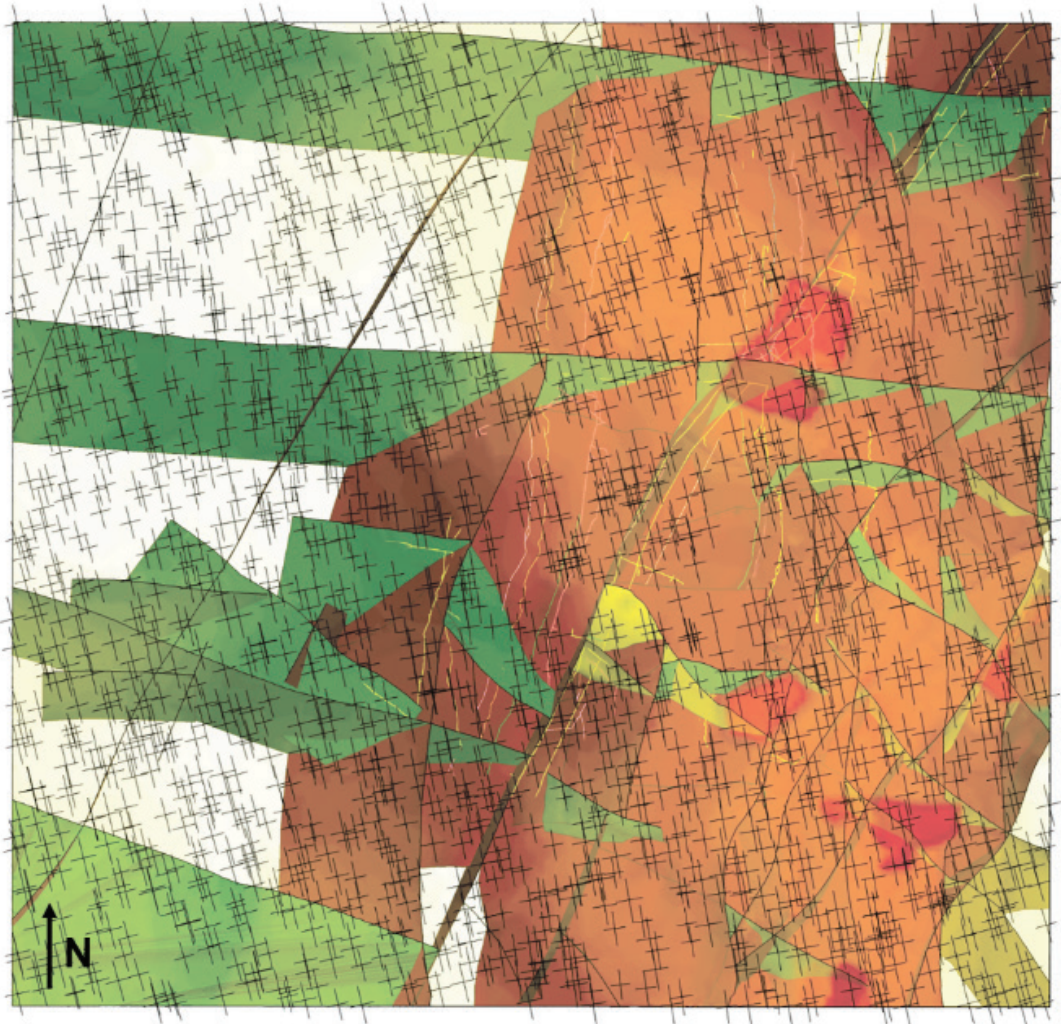


Figure 7: Stress field tensors projected on large-scale GIS-model of Reiche Zeche URL. Large tensor axis represents the larger horizontal stress S_H .

Table 3: Overall in-situ stress field modelled for URL Reiche Zeche at level 1. Stress ratio is 1.35 : S_v : 0.79.

Maximum horizontal stress S_H (MPa)	Minimum horizontal stress S_h (MPa)	Vertical stress S_v (MPa)	Dip direction α ($^\circ$)	Dip γ ($^\circ$)
4.56	2.68	3.38	347	0

3 Comparison to recent mine-scale experiments

The projects in the Grimsel and Bedretto Rock Laboratories and STIMTEC share the overarching goal to improve control on the creation of subsurface-heat exchangers by studying the hydro-mechanical processes that take place during hydraulic stimulation. The studies in Grimsel and Bedretto are at different stages of development. While for the "In-situ Stimulation and Circulation" project (ISC, Grimsel) the three experimental phases were completed, the "Bedretto Reservoir Project" (BRP) is in the initial phase, which includes the basic characterization of the selected rock volume. The Bedretto Reservoir Project comprises the two projects "Validation of Technologies for Reservoir Engineering (VALTER)" and "Demonstration of soft stimulation treatments of geothermal reservoirs (DESTRESS)", which deal with the optimization of stimulation protocols and therefore overlap with STIMTEC, and the project "Zonal Isolation, Drilling and Exploitation of EGS Projects (ZoDrEx)", which aims to develop drilling and completion techniques further.

The extent of the investigated rock volumes are comparable for STIMTEC and ISC, the BRP project represents an increase by about half an order of magnitude. Crystalline rocks are found at the two Swiss sites, Grimsel and Bedretto, as well as in the Reiche Zeche, Freiberg, but the former are far less anisotropic than Freiberg gneiss. In contrast to the ISC project, the STIMTEC project included validation by drilling into stimulated areas enabling us to adapt the hydraulic and seismic observation systems for characterization studies after the stimulations.

Intervals (m)	Pre-Stimulation Jul-18				Post-Stimulation								Validation Nov-19							
	Jul-18				Jul-18				Aug-18				Nov-19				Nov-19			
	BH10	BH10	BH12	PP	BH10	BH10	BH12	PP	BH10	BH10	BH12	PP	BH10	BH10	BH12	PP	PP above	PP below	PP above	PP
QP	VPP above	VPP below	PP	QP	VPP above	VPP below	PP	QP	VPP above	VPP below	PP	QP	VPP above	VPP below	PP	PP above	PP below	PP above	PP	
22.4	0	0	0	0	1	1	1	1	5	1	5	2	6	1	1	1	0	6	0	
24.6	0	0	0	0	1	1	1	1	0	0	0	0	0	0	0	0	0	0	0	
28.1	1	0	0	0	1	1	0	0	5	2	1	2	6	2	6	0	0	6	0	
33.9	6	0	0	0	1	1	1	0	5	3	1	3	6	6	0	4	0	0	0	
37.6	4	0	0	1	1	1	1	1	5	0	0	0	4	0	4	1	0	0	0	
40.6	3	0	0	0	0	0	0	0	6	2	2	4	6	3	0	0	0	0	0	
49.7	0	0	0	0	0	0	0	0	6	2	6	2	4	0	4	0	0	0	0	
51.6	3	0	1	0	0	0	0	0	0	0	0	0	0	0	0	0	0	0	0	
55.7	1	0	0	0	1	1	1	0	0	0	0	0	0	0	0	0	0	0	0	
56.5	0	0	0	0	6	4	3	1	0	0	0	0	5	4	5	1	0	0	0	

Test interval (m)	Pulse decay rate (s ⁻¹)	P _{breakdown} (MPa)	av. P _{refrac} (MPa)	av. P _{shut-in} (MPa)	jacking pressure (MPa)	Frac traces quality	
						Acoustic log	Impression foil
BH10							
22.4	0.077	13.31	5.2	3.9	3.4	2	1
24.6	0.072	13.34	3.5	3.8	3.2	1	1
28.1	0.090	11.12	3	3.6	3.3	2	1
33.9	0.057	6.45	3	1.9	3	3	3
37.6	0.139	15.56	6.3	5.6	5.7	2	1
40.6	2.551	9.24/8.46	3.3/5.49	3.6/3.8	3.6	2	2
49.7	0.954	9.42/-	5.2/3.94	3.4/3.2	3.8	1	1
51.6	4.098	7.73	4.4	4.5	4	3	3
55.7	2.874	5.82	2.7	3.5	2.8	2	1
56.5	4.717	8.18	4.8	4.1	3.8	1	1
BH17							
4.0	0.094	11.07	6.61	5.2	5.3	1	1
6.7	0.221	14.95	5.74	5.1	5	2	3
9.3	0.005	7.95	4.53	4.7	4.5	2	1
11.7	0.078	14.73	7.37	5	5.1	2	3
13.2		7.46	6.68	5	8.4	1	1

■ Low
■ High

■ Good
■ Bad

Figure 8: (top) Overview of the injections into BH10 performed during the three main phases of STIMTEC and the hydraulic interference observations made. (below) Overview of the characteristic pressures and fracture-trace recordings for the stimulations in BH10 and BH17

4 Outlook

As a very tangible result, the STIMTEC project has developed a well characterized and developed "underground laboratory" composed of an anisotropic and heterogeneous rock volume of almost 10^5 m^3 . The variety of micro-seismic responses of nominally homogeneous partial volumes of the reservoir to pumping processes represents a very important overall result, from which we already now derive the recommendation for real projects to provide substantial sensitivity studies for monitoring networks before the start of the project as well as during the course of the project. In our case, however, the dramatic differences in activity cannot be explained solely by the fact that seismic waves emitted by foci in the area of the deeper intervals are attenuated to such an extent that they can no longer be registered. However, the evaluations of the hydraulic recordings so far do not provide clear indications of different failure behaviour.

It is not yet clear why uniform stimulation procedures provide completely different seismic responses. This observation is not limited to the STIMTEC project, but could not be answered satisfactorily so far. Many central questions are concentrated on "silent" stimulations, i.e. about half of the 10 pumping measures carried out in the injection well. It is noticeable that the registered activity systematically decreases with depth. Even if a repeat stimulation and the measures in the vertical validation well could already make a considerable contribution to the sensitivity characterization of the micro-seismic observation network, the data from STIMTEC alone cannot conclusively answer the question of which of the two alternative alternatives, system sensitivity or material behaviour, is responsible for the differences in activity. Without an answer to this question, the prognostic potential for stimulation measures remains limited.

The motivation for our follow-up project STIMTEC-X lies in the unexpected results from STIMTEC on the variability of seismic activity with uniform pumping processes and on the heterogeneity of the prevailing stress field. These observations are of fundamental importance for the steering potential of hydraulic stimulation. Significant stress heterogeneity was also observed in the ISC experiment in the Grimsel underground laboratory. This observation is of fundamental importance, since a characterization of the stress field in a reservoir is of central importance for its development and production from it. So far, the causes of the local changes in Reiche Zeche and elsewhere are largely unknown.

The possibilities created within the framework of STIMTEC offer unique opportunities for the follow-up project STIMTEC-X for exploring the stress heterogeneity further, for the adaptation of observation networks as well as for the critical evaluation of stimulation procedures, and for the realization of a circulation experiment with manageable effort. The planned circulation includes fluid production, to assess the asymmetry of the conduit behaviour and the role of hydro-mechanical interactions.

5 Acknowledgements

Funding by BMBF (FKZ 03G0874A) is gratefully acknowledged. Special thanks go to Frank Reuter and his team of miners at Reiche Zeche for supporting our project in every imaginable way, to Felix Becker, Gerd Klee, and Florian Seebald of Solexperts

GmbH for conducting the injection experiments with us, to Thomas Fischer and Katrin Plenkers of GMuG GmbH for installing and operating the seismic network, to Katja Hesse, Thomas Grelle, Carlos Lehne, and Thomas Wonik of LIAG for performing the borehole logging.

6 Selected project publications

Adero, B. and Renner, J. (2019, April) Hydraulic stimulation of transversely isotropic rock. Geophysical Research Abstracts Vol. 21, EGU2019-10976, EGU General Assembly, Vienna

Adero, B. and Renner, J. (2019, September) Evolution of elastic wave velocities and amplitudes during triaxial deformation of anisotropic Freiberg gneiss. 13th Euro-Conference on Rock Physics and Geomechanics, Potsdam

Boese, C., Kwiatek, G., Starke, J., Plenkers, K. and Dresen, G. (2019, September) Stimulation and fracture network creation in anisotropic rock. EURO-Conference on Rock Physics & Geomechanics, Potsdam

Boese, C., Kwiatek, G., Dresen, G., Renner, J. and the STIMTEC Team (2020, April) Induced acoustic emission activity associated with the STIMTEC in-situ hydraulic-fracturing experiment. SSA conference, Albuquerque

Boese, C., Kwiatek, G., Dresen, G. and the STIMTEC Team (2020, May) Characterising induced acoustic emission activity observed during a mine-scale hydraulic-fracturing experiment in anisotropic crystalline rock. EGU General Assembly, Vienna

Boese, C., Blümle, F., Kwiatek, G., Starke, J., Plenkers, K. and Dresen, G. (2019, April) Results obtained using active seismic source signals prior to and during the STIMTEC experiment. EGU General Assembly, Vienna

Boese, C., Renner, J., Dresen, G. and the STIMTEC Team (2019, April) The STIMTEC experiment at the Reiche Zeche Ulab (invited). EGU General Assembly, Vienna

Cheng, Y., and Renner, J. (2019, December) Hydro-mechanical analysis of pressure recovery after a perturbation of a shut-in phase. AGU Fall meeting, San Francisco

Cheng, Y., and Renner, J. (2019, December) Injectivity and Axial Interference Analysis: Extended Evaluation of Periodic Pumping Tests Using a Double-packer System. AGU Fall meeting, San Francisco

Jimenez, V., Renner, J., Klee, G., Becker, F. and Sebald, F. (2019, April) Using periodic pumping tests to evaluate the hydraulic changes induced by stimulation experiments in the research mine "Reiche Zeche", Freiberg, Germany. Geophysical Research Abstracts Vol. 21, EGU2019-8863-1, 2019 EGU General Assembly

Jimenez, V. and Renner, J. (2019, December) Hydraulic changes induced by stimulation: a three-phase experiment. AGU Fall meeting, San Francisco

Mjakischew, Valerij (1987): Untersuchung des Gebirgsspannungszustandes im Südostteil der DDR.

In: Freiburger Forschungshefte - Beiträge zur Gebirgsmechanik 1987 (A740), S. 7–48.

Rehde, S., Konietzky, H., and Renner, J. (2019). Mit hydraulischer Stimulation kann man unterirdische Wärme als Energiequelle nutzen. Entdecker Unter Tage 1919-2019. H. Mischo (ed.). Halle (Saale), Mitteldeutscher Verlag: 143-146.

Rehde, S., Konietzky, H. (2019, April). Numerical stress field analysis for an underground laboratory in anisotropic crystalline rock as basis for hydraulic stimulation tests. Geophysical Research Abstracts Vol. 21, 2019 EGU General Assembly

Rehde, S., Konietzky, H. (2020, May). Multiscale 3D stress field modelling for the URL 'Reiche Zeche' using a discontinuum model approach. EGU General Assembly, Vienna

Renner, J. and STIMTEC team (under review), STIMTEC – A mine-scale hydraulic stimulation experiment of anisotropic metamorphic rock with evaluation by mine-back drilling, *ARMA Newsletter*

Storage of Production Brine in Rooms of Potash Mines Mining Field Behavior: Modelling and Monitoring

Einstapelung von Produktionslösungen in untertägige Hohlräume von Kaligruben - Baufeldbewertung: Modellierung und Messkonzept

Jan-Peter Schleinig, K+S Aktiengesellschaft, Kassel
Mathias Nest, Institut für Gebirgsmechanik GmbH, Leipzig
Matthias Günther, K+S Minerals and Agriculture GmbH, Philippsthal
Holger Zienert, K+S Minerals and Agriculture GmbH, Unterbreizbach
Stephan Deppe, K+S Aktiengesellschaft, Kassel

Abstract

K+S evaluates the possibilities of storing process wastewater (brine) in rooms of potash and salt mines. One main focus is on rock mechanics studies to proof acceptable rock mechanic conditions by exclusion of mining field collapses and prediction of harmonious underground convergence rates. Latter is the basis to substantiate the integrity barriers between biosphere and mining rooms and to predict acceptable subsidence of the surface.

Based on practical experiences in potash and salt mines, procedures to evaluate the suitability of mining fields are developed and tested under parameter variation to check the plausibility of modelling results. The adaption of techniques to a special mining field show the feasibility of brine storage in these mining rooms. The results are the basis for the development of a monitoring concept to observe the actual rock mechanical behavior. Both the prediction of stable and compatible conditions by special rock mechanical modelling and evaluation as well as the confirmation by a suitable observation program establish the basis for a safe brine storage process in rooms of potash and salt mines.

Zusammenfassung

K+S prüft die Möglichkeit einer Einstapelung von Prozessabwässern in untertägige Hohlräume des Kali- und Steinsalzabbaus. Ein Schwerpunkt sind dabei die gebirgsmechanischen Untersuchungen. Auf Basis numerischer Modellierungen sollen unter Berücksichtigung von Abbauhistorie und Lösungseinstapelung Baufeldzusammenbrüche ausgeschlossen sowie harmonisch verlaufende Konvergenzen und Senkungen mit verträglichen Raten ausgewiesen werden. Die gebirgsmechanische Verträglichkeit bewertend soll nachgewiesen werden, dass die Barrieren über und neben dem Einstapelbereich nicht unzulässig beansprucht sowie die Nutzung der Tagesoberfläche nicht unzulässig eingeschränkt werden.

Basierend auf einer Zusammenfassung verfügbarer praktischer Erfahrungen werden Modellierungstechniken zur Bewertung von geeigneten Baufeldern entwickelt und unter Variation einzelner Parameter zur Prüfung der Plausibilität der Modellierungsergebnisse getestet. Angewandt auf eine konkretes Baufeld wird gezeigt, dass eine gebirgsmechanisch verträgliche Lösungseinstapelung möglich ist. Diese Ergebnisse sind Basis für die Entwicklung eines projektbegleitenden Monitoringkonzepts zur Erfassung des tatsächlichen Gebirgsverhaltens. Die Prognose standsicherer Verhältnisse durch die gebirgsmechanische Modellierung und deren Bestätigung durch geeignete Messungen sind die Grundlage für eine sichere Einstapelung von Lösungen in Grubenfelder des Salzbergbaus.

1 Initial Situation

K+S evaluates the possibilities of storing process wastewater (brine) in mining rooms. One focus is on rock mechanics studies to proof acceptable rock mechanic conditions by exclusion of mining field collapses and prediction of harmonious underground convergence rates. Latter is the basis to substantiate the integrity barriers between biosphere and mining rooms and to predict acceptable subsidence of the surface.

The verification procedure bases on the prediction of the rock behavior by numerical modelling and the observation accompanying the project for confirmation. In case of persistent and significant differences between modelling and observation results the causes can be checked and the models can be adjusted. By this procedure, hazards can be recognized early and countermeasures can be initiated if necessary.

The prediction of the rock behavior bases on a representative modelling of the existing mining situation and the conditions of planned brine storage. The numerical models contain a description and implementation of the mechanical effects of all relevant geological-geochemical, hydraulic and rock mechanical processes and changes caused by the brine storage, i. e. the brine penetration in the excavation damaged zone (EDZ), the dissolution of brine sensitive mineral components in pillars and the hydraulic brine pressure. For this purpose, special modelling procedures and approaches have been developed in recent years. The basic for this, practical experience of brine storage available at K+S and a developed modelling technique for single pillars were already presented at the Geomechanics Colloquium in 2019 (SCHLEINIG ET. AL. 2019).

The following chapters describe (i) the application of the developed modeling techniques to a general mining field situation with varying individual parameters to check the plausibility of the modeling results, (ii) the modelling and evaluation of a special mining field where brine should be stored and (iii) the development of an associated monitoring concept that accompanies the project and observes the actual rock mechanical behavior. Latter includes the spatial extension and the focal points of the rock mechanical effects. If the measurement results show a well agreement between observed and predicted rock behavior, the prediction and thus the rock mechanical suitability of the brine storage will be confirmed.

2 Development and Test of a Mining Field Model

The main objective of this investigation is to transfer the techniques to model the mechanical brine storage effects developed for a single pillar model to a general mining field situation for testing of modelling field geometries, stable calculation runs as well as plausible results. The effect of different pillar situations and the impact of stacked field boundaries on the convergence behavior are taken into account too. For this investigation the central panel situation shown in Figure 1 is used as an example to evaluate the stability of the mining field and the consequences of brine storage to the rock mechanical behavior. The field situation is evaluated with numerical modelling and the following goals (i) exclude dynamic events caused by field collapses and (ii) predict mining field convergences induced by brine storage with regard to their effects on the barrier integrity and surface subsidence.

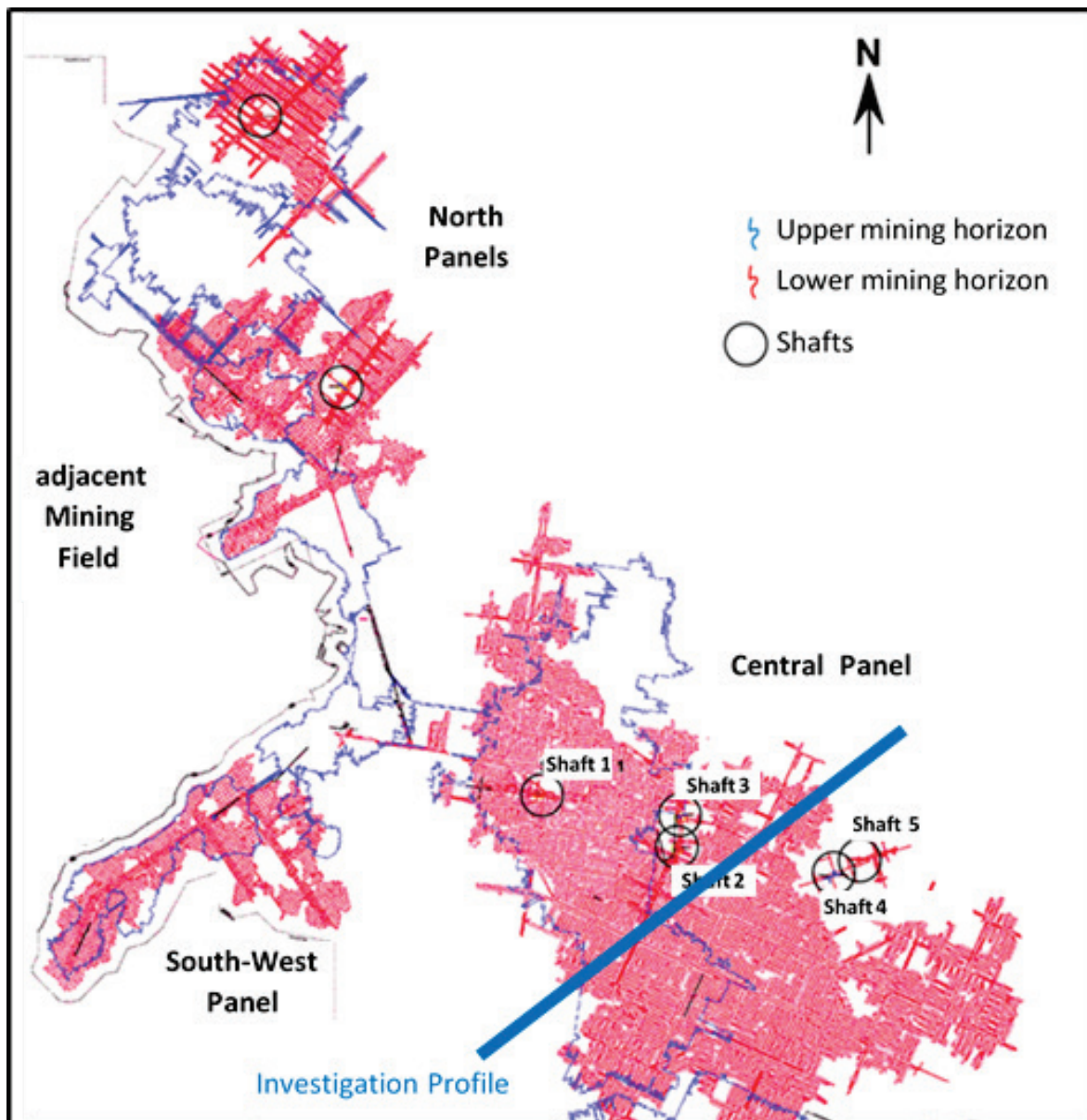


Fig. 1: Mining panels and profile for rock mechanical modelling in the Central panel

The location of the model section is chosen in such a way that the model represents the rock mechanical behavior of the whole mining field in a conservative manner with 2-level mining, characteristic geological formations and pillar design. This includes the minimum barrier thickness above the stacked field boundaries of both mining levels as an unfavorable condition too.

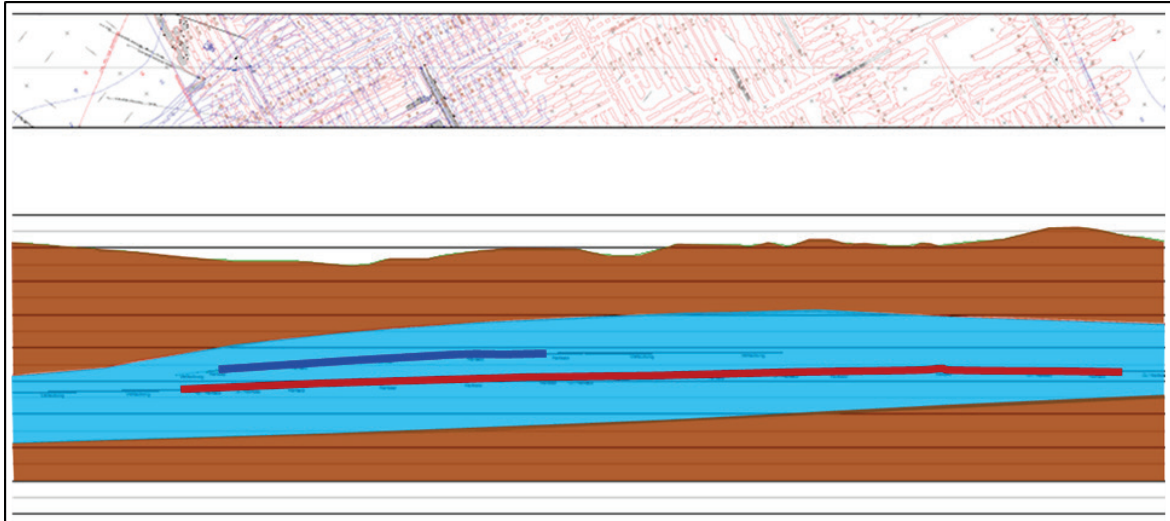


Fig. 2: Detail of mining plan with upper (blue) and lower (red) mining horizon along the profile (above) and geological Model (below: with Overburden and Subsalinar (brown), Salinar (bright blue) with upper (blue) und lower (red) mining horizon)

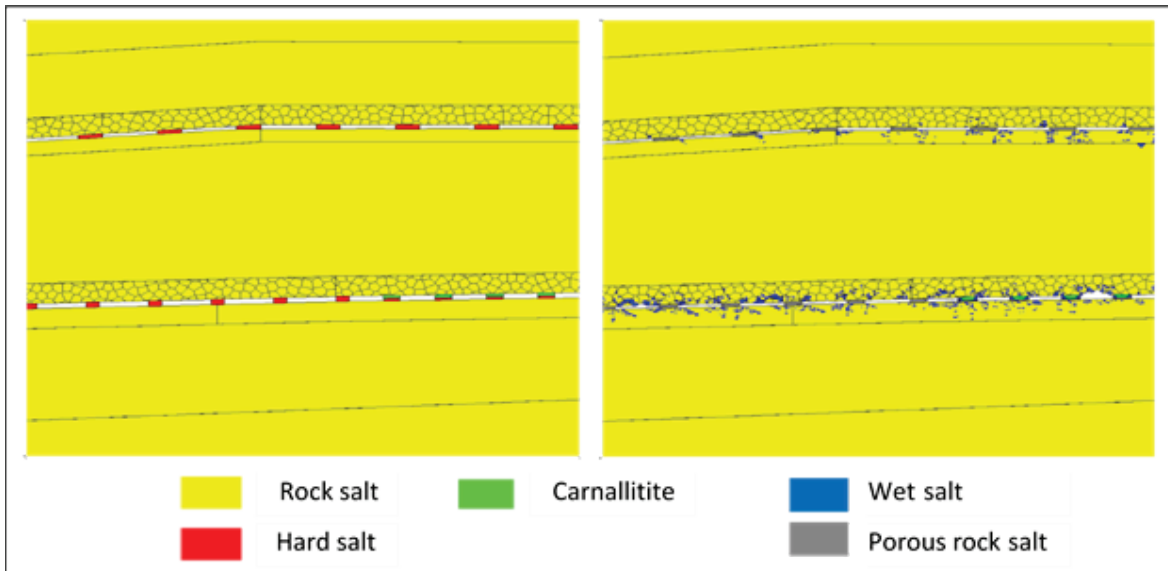


Fig. 3: Detail of the rock mechanical model before (left, year 1980) and 1000 years after filling with brine (right). The area up to 9 m above the roof is modelled with Voronoi-blocks.

The developed model shows Figure 2. Boundary conditions of geology, brine storage and geochemistry are:

- On the 1st level there are mainly pillars of hard salt and on the 2nd level pillars of hard salt as well as carnallitite over hard salt (see Figure 3, left).
- The brine storage begins in 2029 and ends in 2041. The brine rises as a function of time and remains after there permanently. The brine acts to the full pillar height as follow:
 - The excavation damaged zone behind the pillar contour is immediately wetted. Afterwards this wetting follows the advancing plastic deformation with a rate of 20 cm/a. In the wetted rock areas, the MAXWELL viscosity is reduced by a factor of 5, no consolidation is taken into account and the contact surface

strengths between the rock blocks are halved. This significantly reduces the load bearing capacity of the wetted rock areas of the pillars.

- The kieseritic parts of hard salt are dissolved by brine. The solution front penetrates horizontally in the pillar at a rate of 1 cm/a. The dissolution process of kieserite is modelled by changing the rock behavior from intact to porous rock. Subsequently, under the effect of rock stresses the porous rock compacts over time up to intact rock salt conditions in density and mechanical properties. The compaction behavior of porous rock is described by a backfill pressure curve, which was based on empirical values from investigations of salt backfill.

After successful calibration of the model on in situ measurements, several calculations are performed, varying the dissolution rate, the solution pressure and the flooding regime.

The main results of all calculations are the exclusion of any dynamic processes and the harmonious load transfer from the hard salt pillar core, which is becoming smaller due to the kieseritic solution process, to the porous rock. After the load transfer the convergence processes slow down again due to the widening and compacting of the porous rock (see Figure 3, right). At the latest when the last kieserite in the pillars is dissolved, the compacted porous rock in the pillar and the roof falls in the rooms take the load. After completion of the flooding, the brine pressure has a significant damping effect.

The calculated subsidence processes on the surface follow these results for each variation. In the decades to centuries after the flooding the subsidence rate increases and decreases after the load transfer. The integrity of the barriers between the biosphere and the mining rooms was proven in all variations. Likewise, no system condition was predicted that would indicate the beginning of an escalating dynamic process. Even in the case of a stop after partial flooding and conservatively assumed hypothetical pillar failure in the Carnallitite area no field collapse occurs.

The developed model is able to describe the impacts induced by mining and brine storage process to the rock mechanical behavior in a realistic way. All variations show plausible and phenomenologically comprehensible results. The mining field model is suitable for evaluating the rock mechanical situation of a brine filled mining field solution.

3 Existing Experiences

In numerous projects the rock-mechanical compatibility of planned mine closure and repository measures has been proven in air-filled mining rooms with the following investigation steps:

1. Prognosis of the mining induced rock behavior as well as evaluation regarding barrier integrity and tolerable effects on the surface
2. Observation of the rock behavior and evaluation of the measurement results with regard to the predicted rock behavior.

The results of this procedure show that the in situ determined rock movements confirm the prognosis results of the rock behavior and substantiate a safekeeping of the mine workings.

The evaluation procedure is also successfully applied to the flooding of mines with rooms in steep inclined deposits. Here, the mining rooms which are filled with back filling are modelled by a substitute layer to which the convergence behavior of the mining area is assigned. The flooding medium can be fresh and dump water. After their saturation in remote areas by creation of caverns, the brines used in the mining process have no significant dissolving capacity in relation to the surrounding rock. The effect of the moisture penetration in the near-cavity rock is modelled by a specific yielding behavior of the mining areas.

Existing results of flood-accompanying measurements show that the actual rock movements are clearly below the predicted rock behavior and thus also confirm a safe abandonment.

For mines in shallow deposits there is only a little experience available for the brine filling induced rock reactions. The pillars must bulk the vertical loads from the roof and transfer them to the floor. In addition, the moisture penetration in the pillar contours as well as possible dissolving processes have a more intensive effect here than in the case of brine filled steep inclined rooms. Their movement and extension in the surrounding rocks are essentially determined by the geological condition of the pillars, the degree of mining exploitation and the brine chemistry.

A large-scale test of brine storage has been realized in a limited mining room area in the northern part of the Central panel. In preparation for that test convergence and strain measurement points were installed at individual pillars in the brine storage area and a seismic and subsidence monument network was set up in the dry level above. In addition, the air-filled initial situation of the mine workings was modelled and calibrated in a numerical model to reproduce the start point situation. The idea is to measure significant changes in rock behavior due to brine storage and adapt the numerical model in order to make it flexible for the modelling of future projects of brine storage. However, the observing results of the large scale test, which has been running since 2008, shows that the values of in situ measurements do not show any significant changes in rock behavior. All movements are still in the range of air filled conditions and it is impossible to distinguish the rock behavior between air-filled and brine filled excavation areas. Therefore no model adaptation was done. Overall, the accompanying measurements substantiate a safe large-scale test procedure here as well.

These experiences are confirmed by the ongoing flooding of the Volkenroda-Pöthen mine (GESSERT ET. AL., 2019) too. The accompanying seismic measurements show the harmonic convergence behavior of the rock since 1996, whereby the rise in the flood level can be traced by a small increase in energy releases.

The available experience can be summarized as follows. The flooding of salt mining rooms of steep and shallow bedding deposits is compatible with the rock mechanic situation if suitable brine regarding the mine geology is used. All existing accompanying measurements prove a harmonious convergence process. The rock behavior predicted in preliminary rock mechanics studies conservatively overestimates the rock behavior obtained by accompanying measurements.

4 Brine storage in the South-West panel

4.1 Framework and procedure

Based on the experiences discussed above, a special mining field situation of a planned brine storage into the rooms of the South-West panel has to be investigated to prove the rock mechanical compatibility and approvability of this area. The location of the South-West panel is shown in Figure 4.

For this purpose, both the field stability by excluding dynamic failure of pillar ensembles and the induced convergences with regard to their effects on the barrier integrity and the surface subsidence have to be predicted by rock mechanical modelling. Due to the location of the South-West panel the pillar in the North-West is a barrier pillar between the brine-filled and an air-filled mine field. Based on a detailed description of the geological, geochemical and mining situation the behavior and integrity of this pillar is evaluated explicitly.

All rock mechanics investigations for the prediction of the rock behavior are carried out by the Institute of Geomechanics (IfG) by means of numerical modelling. This is done with 3D stripe models along selected section profiles representing the rock behavior of the whole South-West panel. For the investigation of the integrity of the mine safety pillar, a characteristic detailed model is developed that explicitly considers the specific brine penetration behavior. In consideration of these results and based on the in situ measurements already carried out here, a monitoring concept for the observation of the flooding-related rock behavior will be developed.

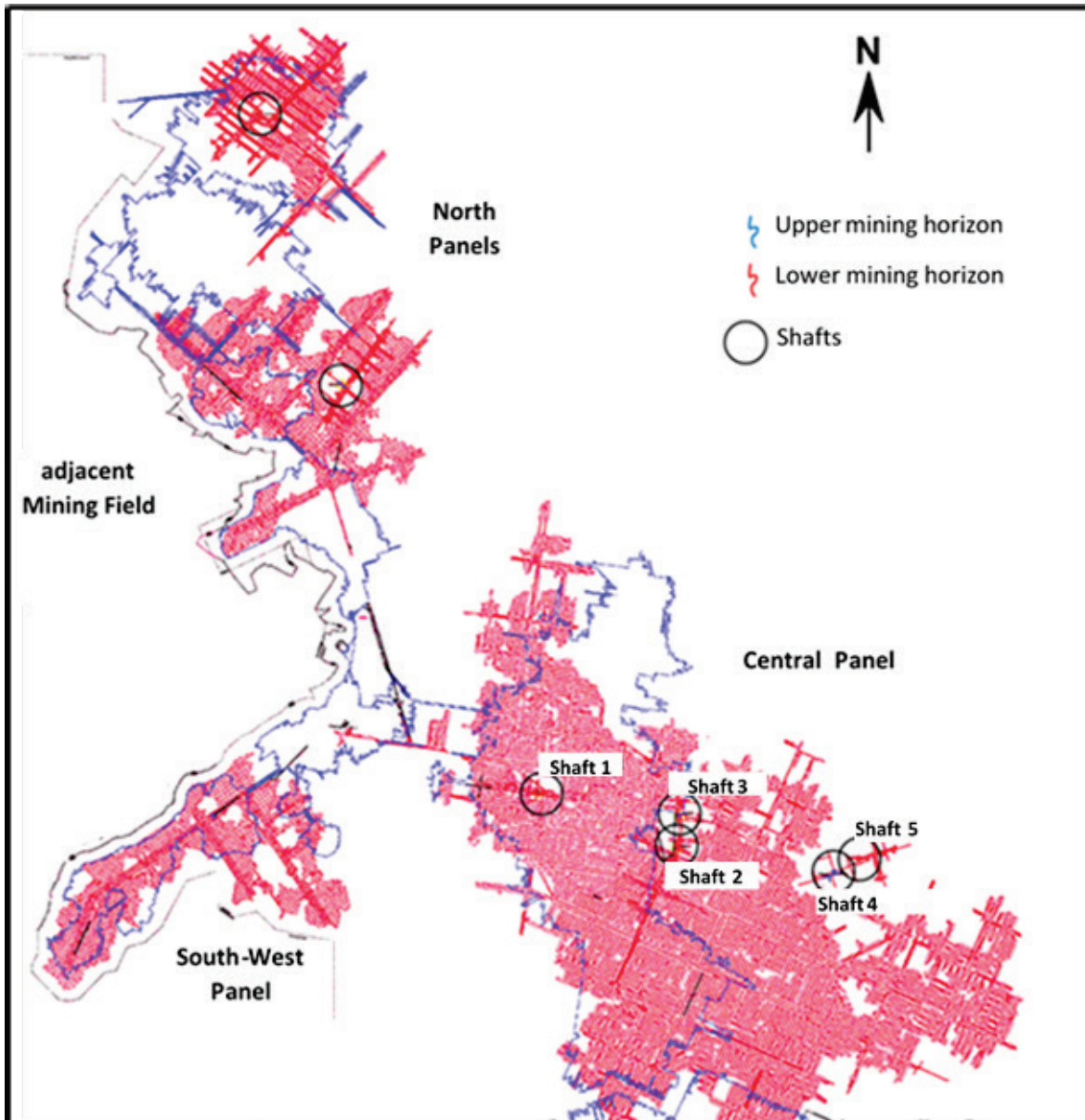


Fig. 4: Mining plan with the South-West-Panel

4.2 Prediction of Rock Behaviour

4.2.1 Evaluation of the Mining Panel Behaviour

Based on the geological and mining situation in the South-West panel, three profile positions are defined which describe the local geological and mining conditions in a conservative sense (Figure 5).

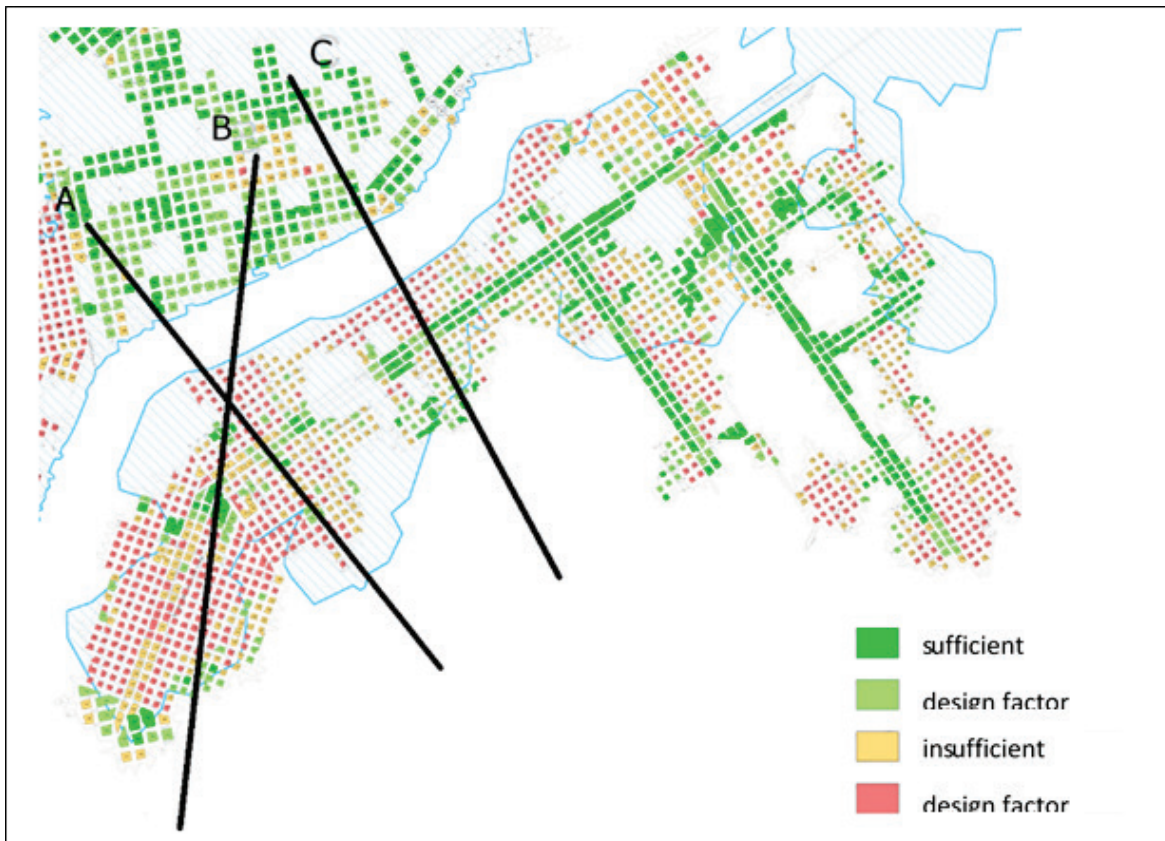


Fig. 5: Detailed mining plan with South-West panel, pillar design factors and profiles of numerical models (A, B, C)

- Section A runs perpendicular to the longitudinal extension of the panel from North-west to Southeast and covers a relatively wide area of small pillars on the second level. To the south, the mine approaches an area with reduced barrier thickness.
- Section B runs from North to South and follows mainly the steepest inclination of the seams. It takes into account the centrally located small pillars on the second level and the local incline gradients in mining rooms of up to 19 %.
- Section C runs like section A perpendicular to the longitudinal extension of the construction field, but at a lower depth and reaches a center of subsidence in the north adjoining mining field.

A three-dimensional, discontinuity mechanical strip model with a width of half a pillar and half a drift was developed for each position based on geological profiles extending from the Subsalinar to the surface. Figure 6 shows the developed rock-mechanical structure model using the example of the profile B.

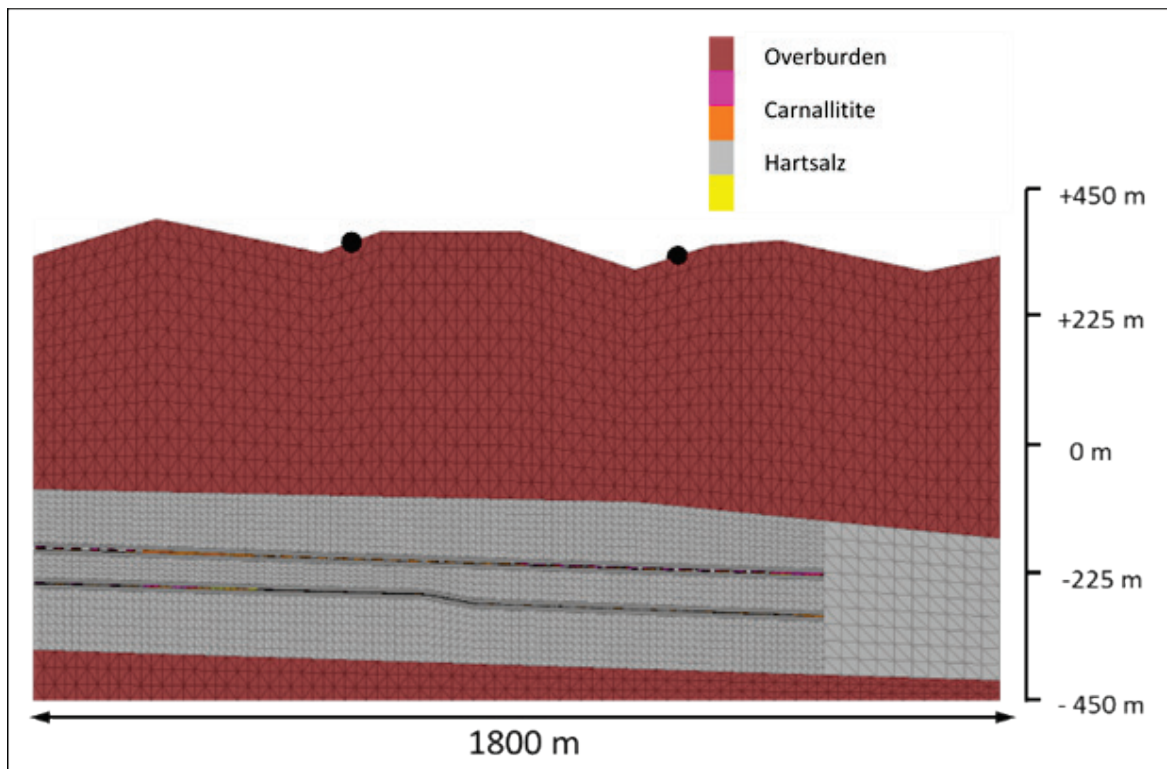


Fig. 6: Model B of the rock mechanical investigations

Starting from the original geological situation the mining history is modelled and the model is calibrated up to the present using available in situ measurement data. The processes occurring in pillars during brine filling are considered as follows:

- After an initial brine penetration of the excavation damaged zones close to the pillar contours the further penetration into salt rocks follow the development of dilatant damage. This process follows with a rate of 20 cm/a and is taken into account in the model by an increased creeping ability of wetted areas. By reducing the viscosity by a factor of 5, this salt can faster deform under load.
- A dissolution of Carnallitite up to a depth of 0.6 m occurs in pillars with Carnallitite.
- In hard salt pillars kieseritic parts are dissoluble. The remaining porous rock gets the mechanical behavior of backfilling which compacts over time up to intact rock salt density and mechanical properties.
- Accompanying to rising brine level a supporting hydraulic pressure acts on the room contours against the convergence and softening process.

The prediction of the rock mechanical behavior is done by numerical calculations up to approx. 1000 years after the start of brine filling. Already after about half of this time, the wetting process reaches a final state and the dissolving process in the pillars is completed. After an increasing phase the convergence rates come back to the order of magnitude of the rates of air-filled cavities and the rooms converges without further, flooding-related changes to the supporting elements. The rock-mechanical compatibility of the entire process sequence is assessed in the following steps:

- Evaluation of mining room convergences and their effects on barrier integrity and surface subsidence. Barrier integrity is assessed using the minimum stress and dilatancy criteria.
- Proof of the stability of the panel by investigating a hypothetical failure of pillars or pillar areas.

The results can be summarized as follows. The convergence behavior caused by the mining and the brine storage processes proceeds harmoniously. Because of moisture penetration and dissolution of brine sensitive minerals the convergence rate increases and - after harmonious load transfer to the remaining porous rock - decreases again to the range of air-filled excavations. After completion of the flooding the brine has a stabilizing effect. The mining field remains stable, the barriers are intact and the subsidence effects on the surface, which is predominantly used for forestry and agriculture, are tolerable. The storage of brine in the investigated South-West panel is possible and compatible from the rock mechanical point of view.

For the planned accompanying observation of the brine storage measuring points for the near-pillar measurement of the drift convergence, a seismic monitoring to observe energy release in the near field rock and surface subsidence measurements are discussed and the following orientation values are predicted.

- The convergence rate increases to twice of the initial rate at the start of brine storage and decreases later to the previous rate again. Due to uncertainties of calculation and measurement process, moderately higher values may occur in situ for a limited time period. The development of the subsidence rates follows the development of the convergence rates with a time delay.
- Experience-based recommendations for the seismic observation are as follows: exceeding of the local magnitude of 1.0 requires a discussion with consultant experts and of a local magnitude of 3.0 requires a general re-evaluation.

4.2.2 Evaluation of the Behavior of the Mine Safety Pillar

In the period of about 1200 years considered in the South-West panel evaluation the brine penetrates only 12 m into the safety pillar between the mining panels. To investigate the pillar integrity, a much longer period is considered in a detailed analysis. The dissolution processes occur in the rock as long as a hydraulic pathway allows to bring fresh brine to original rock. Based on a very conservative description of the geochemical and hydraulic processes the brine penetration is limited to about 20 m to 35 m after several 10,000 years. Beside this these pathways are additionally impacted by the rock convergence behavior. This situation is captured in a detailed rock mechanical model of the safety pillar in order to evaluate the impact of convergence process. After the dissolution of brine sensitive minerals a porous rock remains, which converges more strongly than the neighboring intact rock due to the rock stresses and reduces the pores as a brine pathway. As a result, the integrity of the remaining mine safety pillar, which is unaffected by the dissolution, is also to be evaluated.

The model of the 150 m wide pillar (Figure 7) is 440 m wide and 400 m high. Since the contents of brine sensitive minerals and thus the porosity of the rock after dissolution vary between 20% (in rock banks) and 85% (in single lines), both geometries are considered in detail in the small-scale model.

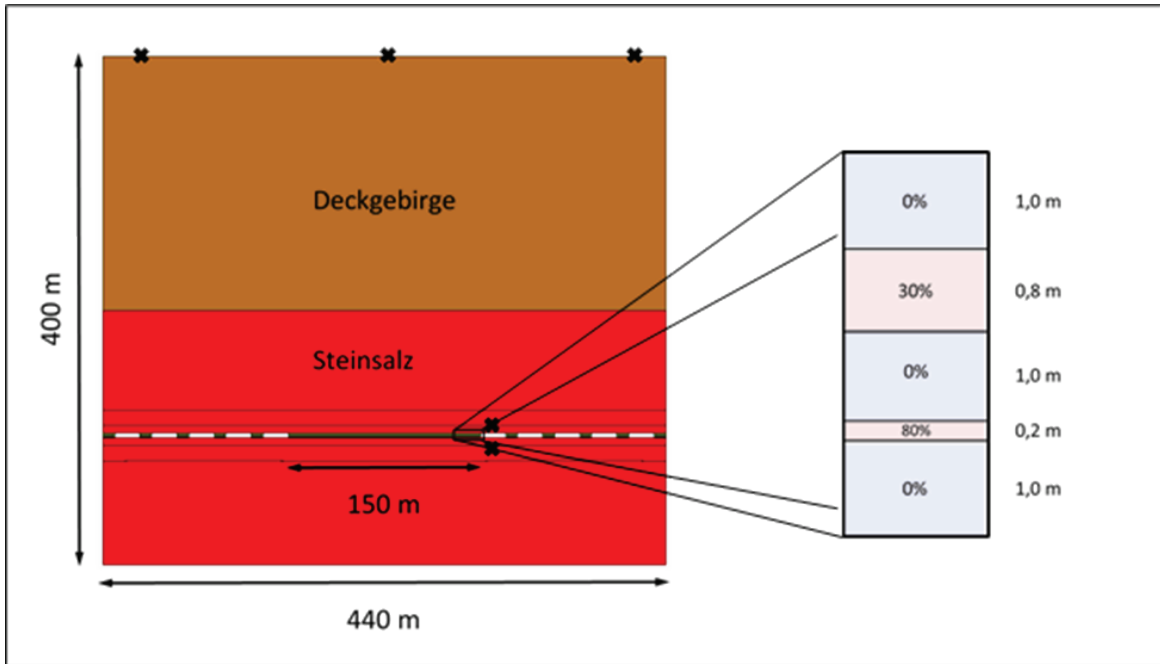


Fig. 7: Generic model with pillar between air filled (left) and brine filled (right) panels and the detail of potash seam (right: Kieseritic seams (red): 0, 8 m (30% Kieserite) and 0, 2 m (80% Kieserite) as well as Rock Salt (blue))

The calculation covers the mining history and an air-filled time of 60 years, followed by the modeling of the brine storage. The behavior of a very soft backfill material (see Figure 8, diagram on the right, black dashed curve) is used for the compaction behavior of the porous rock.

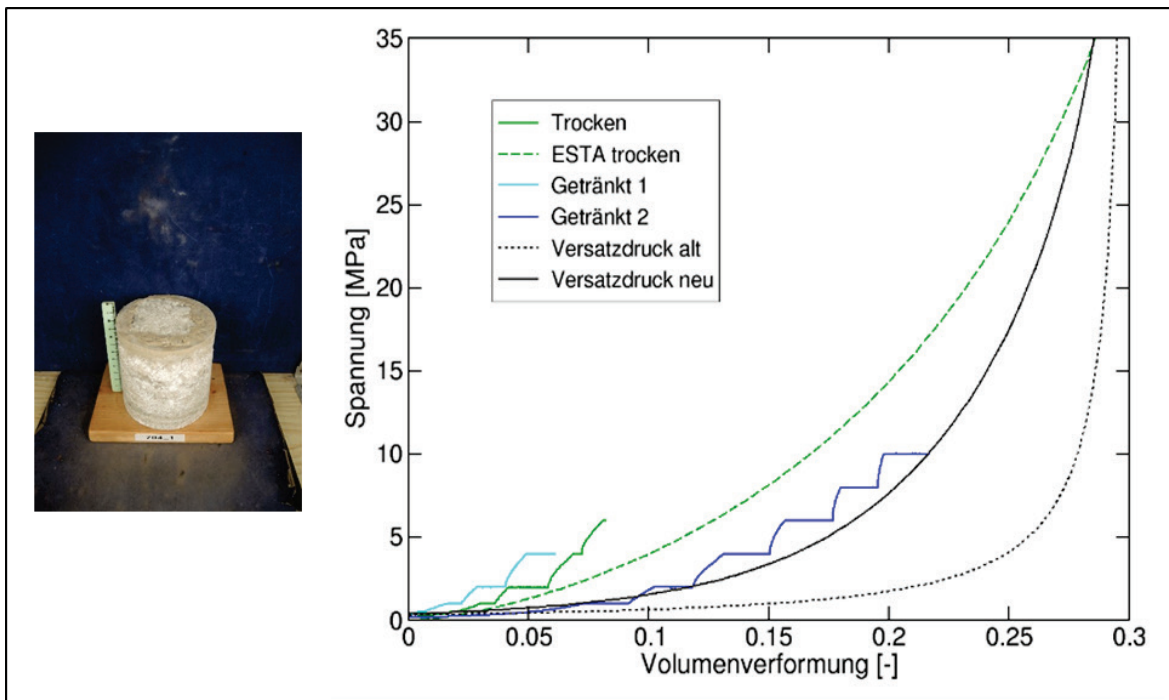


Fig. 8: Porous Rock Salt (after dissolving Kieserite): Sample (left) and stress deformation relationship (right)

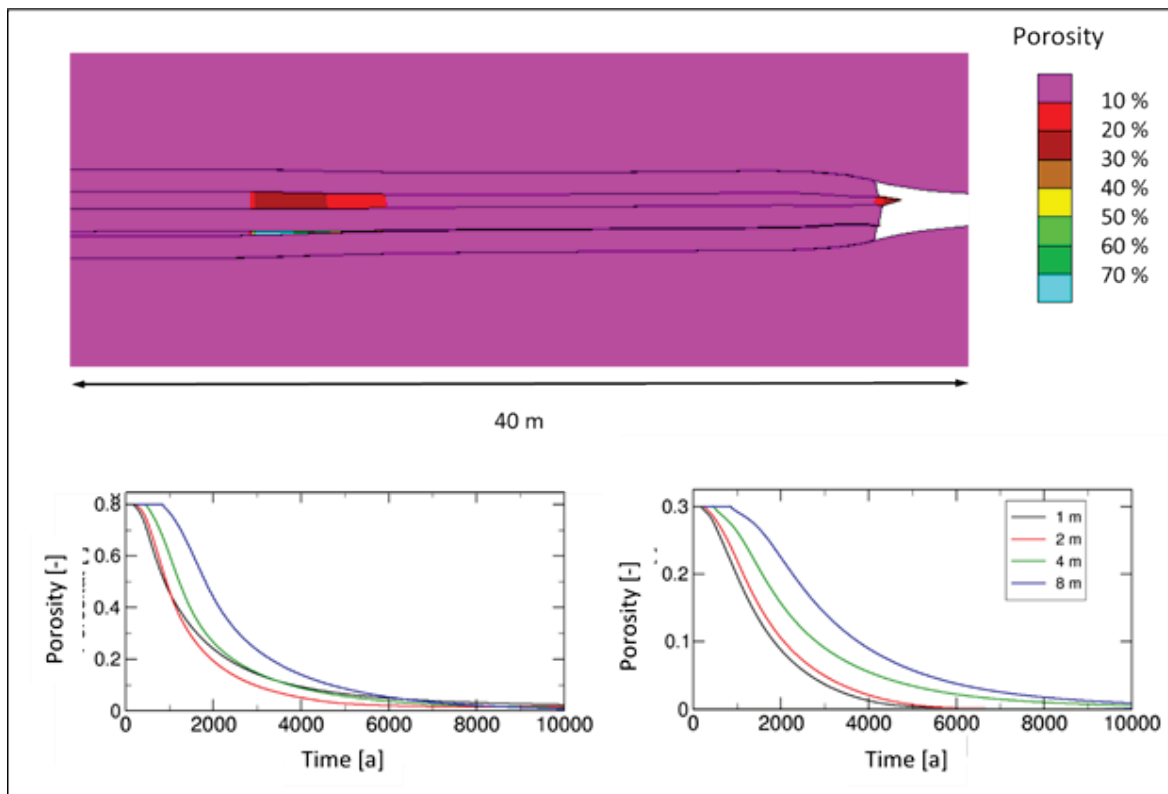


Fig. 9: Development of porosity in the pillar (above) and versus time (below: starting from 80% (left) and 30% (right))

The results show that the porosity of the rock decreases over long periods, starting with 30 or 80 % close to the room contour and decreasing to values below 10 % (Figure 9). The convergence-induced compaction of the porous rock limits significantly the permeation way of the unsaturated brine from the rooms and confirms the conservative nature of the present geochemical and hydraulic investigations. Nevertheless, the remaining intact area of the safety pillar is at least 115 m wide (Figure 10). The minimum stress criterion is safely fulfilled in at least 100 m width and substantiates the integrity of this barrier. These results are consistent with the integrity assessments of the safety pillar as documented in the field models explained above.

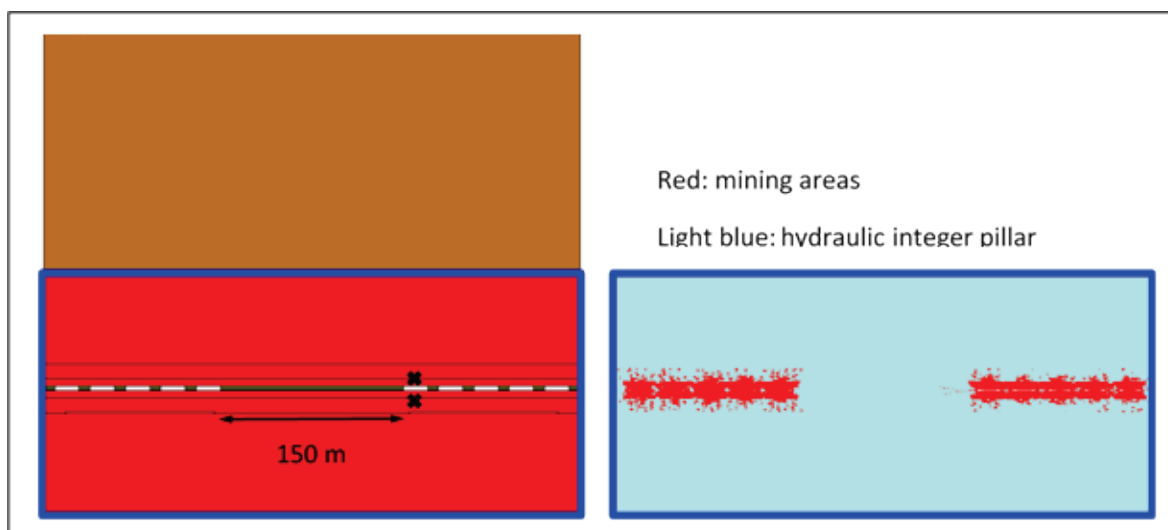


Fig. 10: Model (left) and calculation result (right: fulfilled integrity criterion)

4.3 Rock Mechanical Monitoring Concept

On the basis of the predicted stability of the brine filled mine and the tolerability of the effects on the surface the real behavior of the mining cavities and the rock mass has to be determined and documented spatially and temporally by suitable observation methods. The comparison of the measurement results with the predicted values derived from expert forecasts for stable and environmentally compatible conditions guarantees a safe brine storage process. Significant and persistent exceeding of these values can be detected and evaluated early in time. The following measuring methods are used for monitoring.

- Convergence measuring points will be set up for the recording of the pillar behavior. They observe the real rock behavior of brine filled rooms permanently and autonomously. Such measuring points have already been successfully used in a test field for more than 10 years. For the observation of the convergence in the small pillar area and near to the safety pillar two redundant convergence measuring stations are installed per mining level (stations 1 to 4) (see Figure 11). Initial measurements should be start before brine filling. The evaluation of the measurement results is initially done monthly, but can be adjusted if necessary. Based on experience, a short-term increase in the convergence rate of up to 20 mm/a after the start of flooding is acceptable if the convergence rate drops below 10 mm/a again within 3 years. Exceeding the convergence rate of 20 mm/a as well as exceeding the convergence rate of 10 mm/a in a period of more than 3 years requires a new expert evaluation.

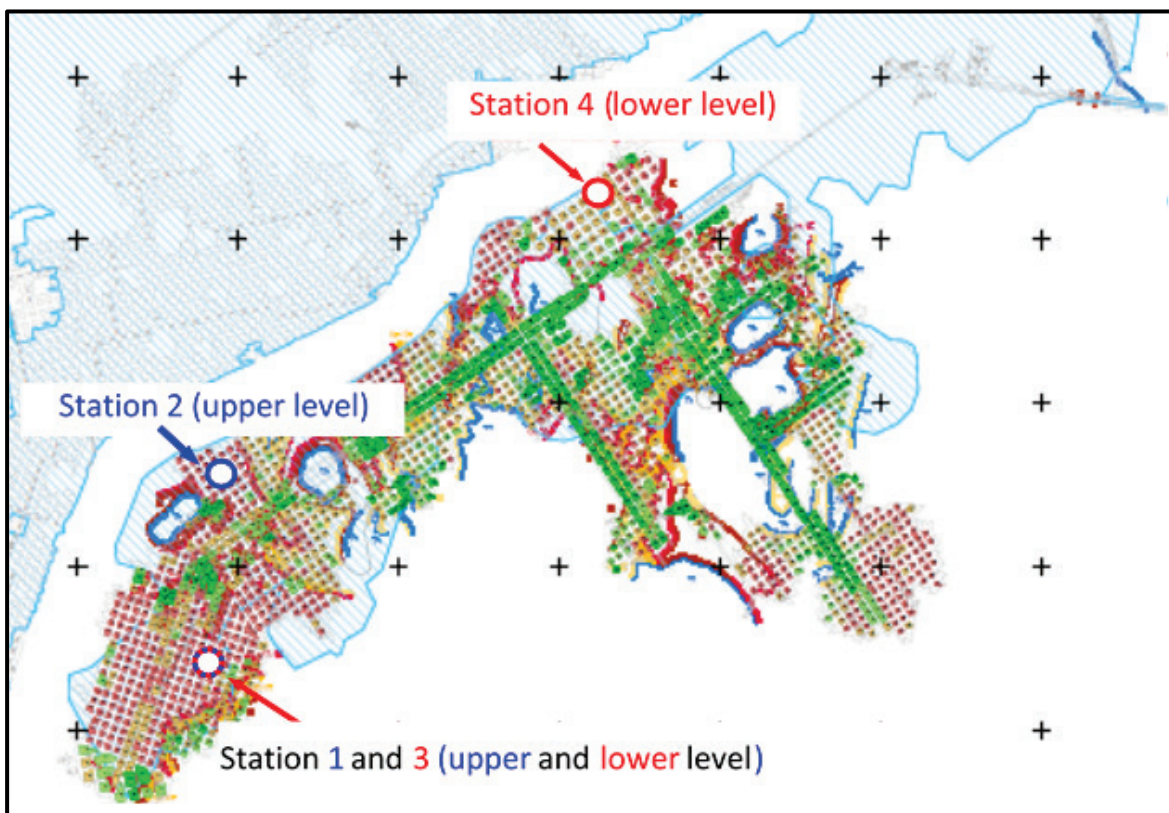


Fig. 11: Mining plan (1. level: blue, 2. level: red) with observation stations for convergence (stations 1 and 2: upper level, stations 3 and 4: lower level)

- The existing seismic monument network is being adapted to ensure the timely recording of temporal, spatial and intensity concentrations of seismic events that indicate a deviation from the expected rock behavior at an early stage. For this purpose, two additional measuring monuments will be set up on the surface above the South-West panel in addition to the existing underground measuring points in order to make the spatial results more precise with regard to the location and depth of seismic events.
The evaluation is initially also planned on a monthly basis, but can be adjusted at any time depending on the measurement results. The seismic system is designed to issue warnings when predefined intensities are exceeded ($M_L > 1.0$). Exceeding the seismic intensity with a magnitude $M_L > 3.0$ leads to a temporary stop of flooding and a new overall evaluation.
- Surface subsidence observation determines the rock mechanical effects of excavation and brine storage across all mining panels. For this purpose, the existing measuring network is supplemented by additional observation points in the area. The measurements are carried out and evaluated annually.

The results of these measurements will be summarized in reports and discussed with the rock mechanical experts. It is expected that the measured values will support the expert's statements and thus confirm the concept of a compatible brine storage process.

5 Conclusions

In preparation of a possible storage of waste water of potash production K+S evaluates the opportunities to fill this brine in rooms of potash and salt mines. Based on practical experiences in potash and salt mines K+S and IfG develop a procedure to investigate the rock mechanical behavior of mine fields under the impact of brine storage. The procedure contains (i) the development of numerical model techniques to investigate the mechanical effects of a brine storage in salt mining rooms, (ii) the application of the model techniques to evaluate the suitability of a special mining field for brine storage and (iii) the development of a monitoring concept to observe the predicted rock behavior of the numerical modelling. The results of the numerical modeling of the special mining field situation show that the storage of brine is possible and compatible from the rock mechanical point of view. Both this prediction by special rock mechanical modelling and evaluation as well as the confirmation by a suitable observation program establish the basis for a safe brine storage process in rooms of potash and salt mines.

6 Quellenverzeichnis

- GESSERT, A., GÖTTERMANN, J., KÖHLER, R., SCHINDLER, A., THOMA, H. & SCHREINER, W. (2019): Die Verwahrung und Sicherung des Bergwerkes Volkenroda / Pöthen durch Flutung mit Haldenlösungen. Vortrag zum 48. Geomechanik-Kolloquium am 15.11.2019 in Leipzig
- SCHLEINIG, J.-P., NEST, M., DEPPE, S. & ZIENERT, H. (2019): Einstapelung von Produktionslösungen in untertägige Hohlräume, Konzeptionelles Vorgehen

und Gebirgsmechanische Modellentwicklung. Vortrag zum 48. Geomechanik-Kolloquium am 15.11.2019 in Leipzig

Problems related to Geomechanics in hard coal mining in the Asturian Central Coal Basin

Geomechanische Probleme des Steinkohleabbaus im zentralasturianischen Kohlebecken (Spanien)

Falko Schmidt^a, Javier Menéndez^b, Jorge Loredó^c

^aSachverständiger, Santander, 39011, Spain

^bHunaser Energy, Oviedo, 33005, Spain

^cDept. of Mining Exploitation, University of Oviedo, Oviedo, 33004, Spain

Abstract

The Asturias region in northern Spain has a history of 200 years of hard coal mining. Because of tectonic movements, coal seams are dipping up to 60°, in extreme cases up to 80°. Sublevel caving and longwall mining is applied, the latter method is subject to this presentation. The mining techniques applied in those mines demands both: high resistance and flexibility from the drift support. Upper and lower drifts are typically excavated for extracting the coal seams. This paper explores the geomechanical problems in the lower drift after the coal extraction. The damage in the lower drift depends on the thickness of the coal seam. To prevent damage, a drift 10 m beneath the seam can be excavated. This drift is using conveyor belt to transport the coal.

Zusammenfassung

Asturien im Norden Spaniens, hat eine 200 jährige Geschichte im Steinkohlebergbau. Wegen tektonischen Vorgängen, weisen die Flöze ein Einfallen von 60°, in Extremfällen 80° auf. Teilsohlenbruchbau und Strebbau wird angewandt, Strebbau wird in diesen Beitrag behandelt. Der Abbau stellt hohe Anforderung an den Ausbau: er muss widerstandsfähig und nachgiebig zugleich sein. Der Kohleabbau erfolgt typischerweise zwischen Kopf- und Fußstrecke. Das Augenmerk liegt hier auf den geomechanischen Problemen der Fußstrecke, nachdem die Abbaufont fortgeschritten ist. Die Schäden am Ausbau hängen stark von der Mächtigkeit des Flözes ab. Um Schäden zu verhindern kann die Fußstrecke in das taube Gestein des Liegenden verlegt werden. Diese wird dann mit einem Förderband zum Kohletransport versehen.

1 Introduction

1.1 Scope

The purpose of this presentation is to inform the audience about the hard coal mining activities in NW Spain, see Figure 1. The mining takes place in the Asturian Central Coal Basin (ACCB) in the southern part of the Asturian province. Some brief aspects about geology, mining method are presented and geomechanical problems and their affection on tunnel support are illustrated in photographs.

1.2 Mining Activity in Asturian Central Coal Basin

There are more than 70 productive coal layers worked during the 200 years of mining in the Asturian Central Coal Basin (Villa and Sanchez, 2009).

It has an extension of about 1400 km². ACCB is an extensively mined area and its network of tunnels covers more than 30 mines. The typical structure of underground coal mines consists of a main vertical shaft for access and extraction of coal, and networks of horizontal drifts at different levels. There are also auxiliary shafts for the ventilation system and to serve as emergency exits. The depth of the mining operations reached 600 m below surface. The diameter of the access and ventilation shafts is 6 m. The cross section of the drifts is between 9 and 12 m². The exploitation drifts normally have a support system consisting of steel sets and wire mesh (Menendez et al., 2019). Longwall mining between tow level is used up to an inclination of 60°. In extreme cases, where the dipping is around 80°, sublevel caving is applied (Díaz Aguado, 2009).

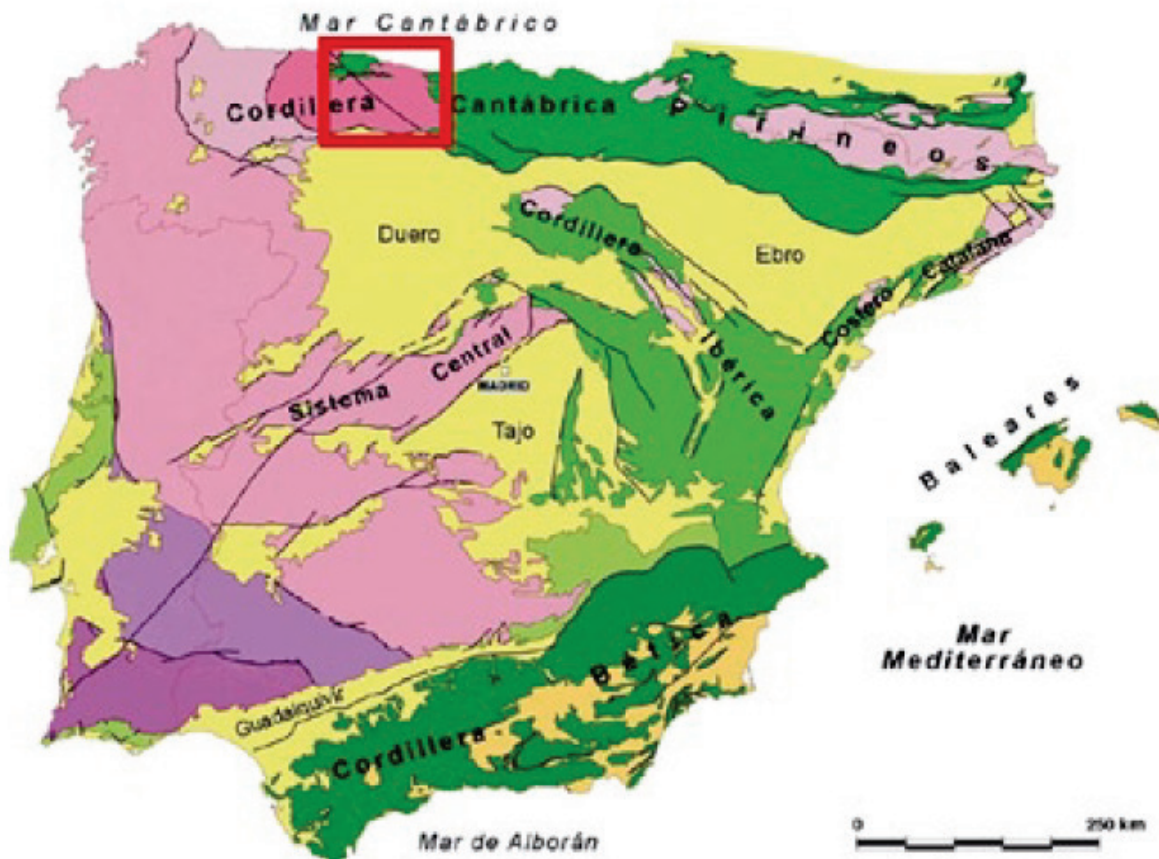


Fig.1: Structural scheme proposed by Vera (2004) of the Iberian Peninsula (Marcos and Pulgar, 1982).

2 Geology

The ACCB is characterized by the so-called Sinorogic succession of the Carboniferous, whose age ranges from Tournaisian to Westfalian D. There are shales and sandstones with abundant layers of exploitable coal and some limestones located preferably close to the base. In the middle and upper part some layers of conglomerates up to 60 m thick are interspersed, with clasts exclusively siliceous in the lower horizons, and siliceous and calcareous clasts in the upper horizons (Menendez et al., 2019).

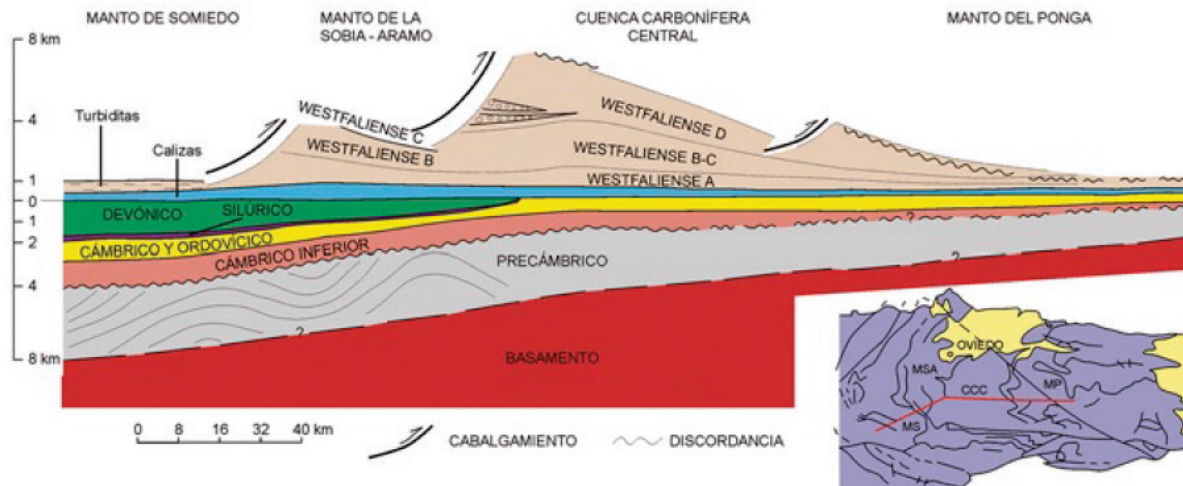


Fig.2: Palinspastic reconstruction of the clastic wedges of the Carboniferous along an east-west cross-section of the Cantabrian Zone (Marcos and Pulgar, 1982).

Due to tectonic actions, coal seams could be found with a dip angle up to 60° in some occasions 80°, see Figures 2 and 3.

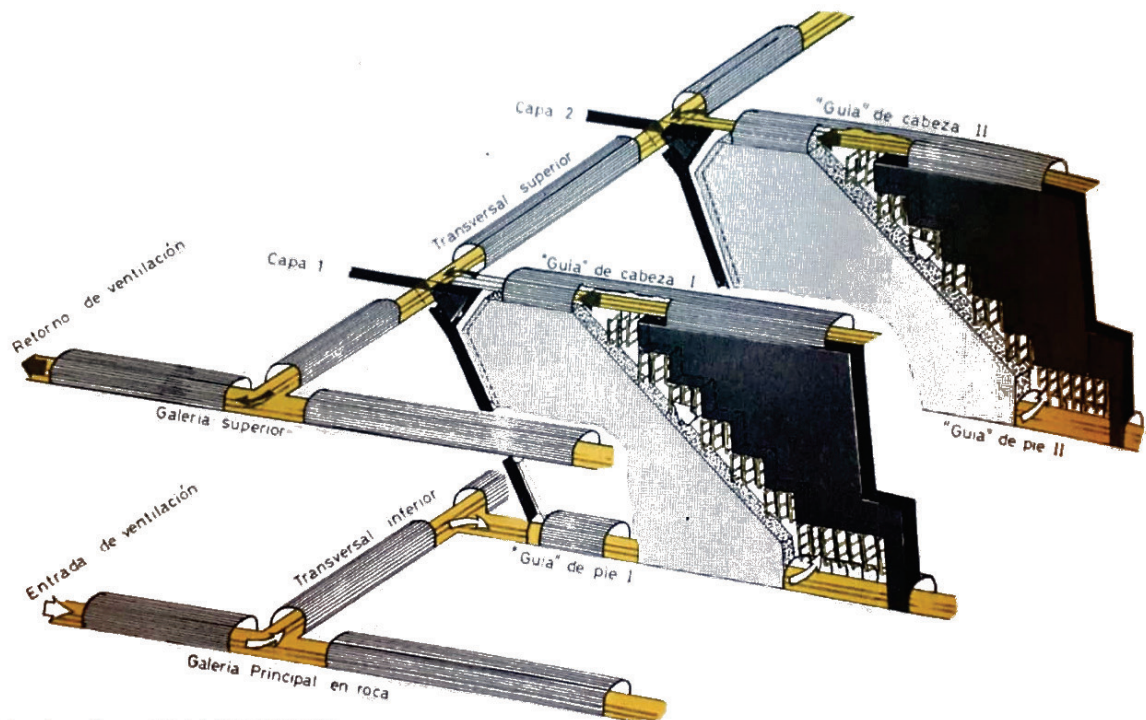


Fig.3: Coal layer developed in a marginal area of an alluvial fan (Sama Group, Carboniferous Central Basin). The layer is in erosional contact with overlying sandstones deposited in a distributary channel (interpretation and photo: C. Salvador, 1993).

3 Mining in steep coal seams

Unlike horizontal seams, where a high grade of automatization with hydraulic chocks, conveyor and shearer is achieved, inclined seams require a different approach regarding support. Figure 4 shows an extraction scheme of two seams of coal, establishing an extraction face between an upper and lower drift. The coal in the roof is supported normally with wood where mining takes place. The mined coal falls because of gravity to the lower drift and is loaded.

The lower drift support “suffers” more deformation due to the collapse once the extraction face passes.



Estructura de un cuartel de explotación.

Fig.4: Steep Longwall Mining scheme with two coal seams.

Figure 5 shows a section of an extraction design using a shearer on a winch the mined area is backfilled in panels separated by metal mesh. The support material in the extraction face is mainly wood. The vertical distance between the upper and the lower drift varies between 80 and 100 m.

From the main drift of two levels, transversal drifts are made in order to cut coal seams perpendicularly. Once the seam is found, drifts are excavated "guided" by the coal. These drifts form the upper and the lower drift. A general scheme of these drifts can be seen in Figure 6.

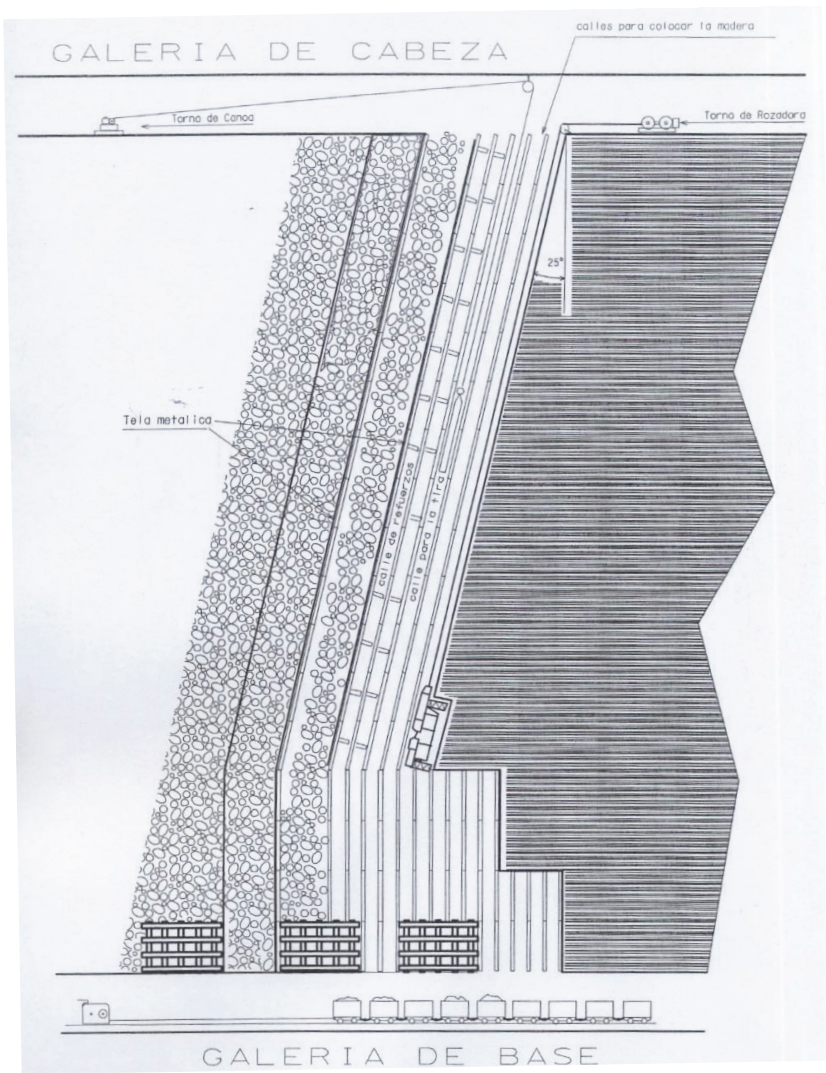


Fig.5: Section view of longwall mining with shearer at 65°.

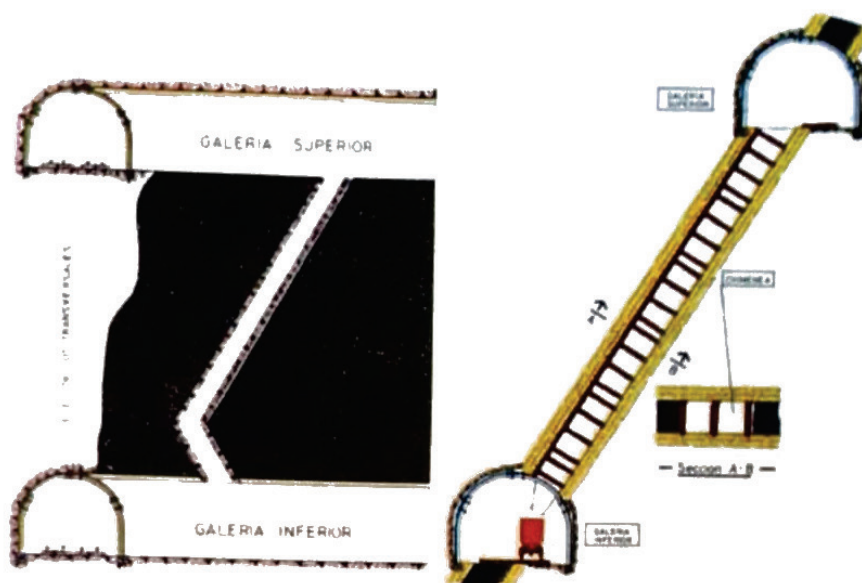


Fig.6: Typical section of upper and lower drift in longwall mining, cutting the coal seam

4 Geomechanical problems

The backfilling and the collapse cause large deformations, redistribution of stresses and heavy asymmetric loads on the drift support. Although the support is designed to be deformable, often, the loads exceed the load bearing capacity of the support. The failure of support leads to a decreasing of the section area (important for ventilation), and loss of serviceability.



Fig.7: Lower drift steel set and wood support, heavily damaged

In some extreme cases, sections became so small, that no passing was possible, see Figure 8.



Fig.8: Drift totally collapsed

Very high loading on the support of the lower drift causes severe damage to tunnel support, see Figure 7.

To prevent damage, a drift 10 m beneath the seam in the foot wall can be excavated, compare Figure 6 with Figure 9. That drift is not exposed too high deformations and is less likely to have stability issues.

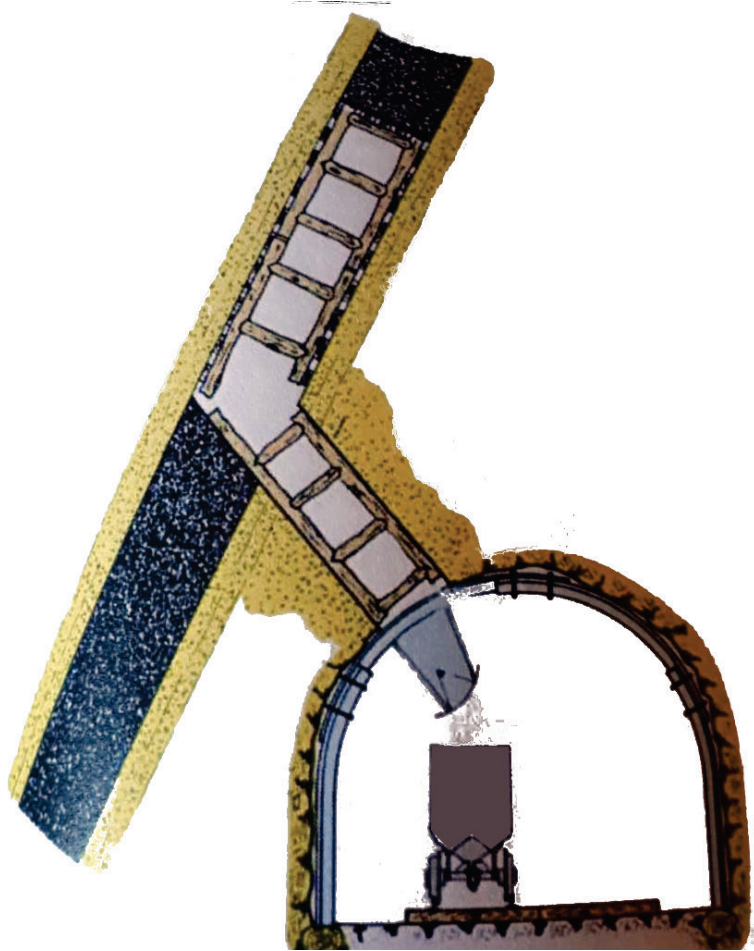


Fig.9: Lower drift located in the wall under the coal seam

When the drift support is already damaged and further load increasing is expected, additional support in form of steel posts connected to the TH profile sets, see Figure 10 A. Timber forming a box are also used, especially for high profiles. The timber in Figure 10 B already reached its load capacity and splintered.

Once a collapse of a drift occurs, the drift will be recovered by loading and hauling the fill and fixing the support. A support combining both: steel sets and wood is applied where heavy loads are expected. In that cases the timber forms part of the drift wall support, where the arcs of the steel sets support the crown.

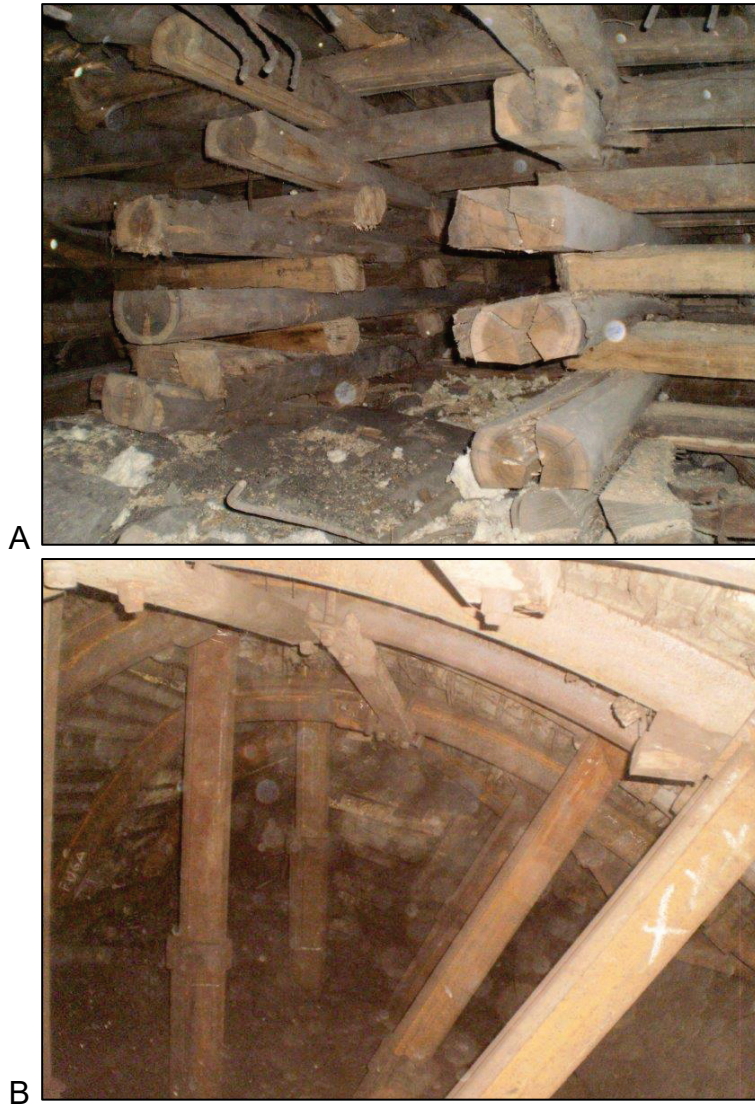


Fig.10: Wooden pillar (A) and Steel post (B) supporting drifts

5 Conclusions

Coal mining in the ACCB is challenging due to the dipping of the coal seam up to 80° in extreme cases. For dipping up to 60° longwall mining between drifts at different levels is applied.

The lower drift suffers, due to the gob and the collapsing of the hanging wall, very high loads. Despite of applying a flexible support of steel sets, wood and wire, the lower drift tends to collapse and need to be recovered in order to maintain the mining operational. Collapsed drifts are often supported by a combination of timber pillars and steel sets. At high depths, where a high support load is expected, the lower drift is located in the foot wall at a safe distance from the coal seam.

6 References:

Díaz Aguado, María B. & González, C., Influence of the stress state in a coal bump-prone deep coalbed: A case study, *International Journal of Rock Mechanics and Mining Sciences*, Volume 46, Issue 2, 2009, Pages 333-345, ISSN 1365-1609, <https://doi.org/10.1016/j.ijrmms.2008.07.005>.

(<http://www.sciencedirect.com/science/article/pii/S1365160908001202>)

Marcos, A. and Pulgar, J.A. (1982). An approach to the tectonostratigraphic evolution of the Cantabrian foreland thrust and fold belt, Hercynian Cordillera of NW Spain. *N. Jb. Geol. Paläont. Abh.*, 163/2, 256-260, Stuttgart.

Menendez, Javier & Schmidt, Falko & Konietzky, Heinz & Oro, Jesús & Vega, Mónica & Loredó, Jorge & Díaz Aguado, María. (2019). Stability analysis of the underground infrastructure for pumped storage hydropower plants in closed coal mines. *Tunnelling and Underground Space Technology*. 94. 103117. [10.1016/j.tust.2019.103117](https://doi.org/10.1016/j.tust.2019.103117).

Salvador, C.I. (1993). La sedimentación durante el Westfaliense en una Cuenca de antepaís (Cuenca Carbonífera Central de Asturias). *Trab. Geol., Univ. Oviedo*, 19, 195-264.

Villa, Elisa & Sanchez de Posada, Luis. (2009). Carboniferous of the Cantabrian Zone. In: *Spanish Geological Frameworks and Geosites. An approach to Spanish geological heritage of international relevance*. http://www.igme.es/patrimonio/GEOSITES/Chapter_03_SGFG.pdf

Die Beurteilung der von Steinschlag ausgehenden Gefahr mithilfe von Prozessmodellen: Stolpersteine und Risiken

Hazard assessment of rockfall using process models: difficulties and risks

Alexander Preh, Emmanouil Fleris, Mariella Illeditsch
Institute of Geotechnics, Vienna University of Technology
1040 Vienna, Karlsplatz 13, Austria

Abstract

For regions with distinct rock-cliffs, rockfall represents a serious hazard due to high propagation velocities. In order to pursue territorial planning with an awareness of rockfall hazard, it is necessary to identify those areas that are or may be affected by this process. Process models play a central role here. Assessing rockfall hazard using process models (at regional or object scale) is a great challenge, because many parameters have to be considered, that can only be quantified with great effort, on site. The biggest challenges in estimating the hazard of rockfall are

- the identification of detachment areas,
- the estimation of relevant block sizes,
- the determination of model parameters relevant for the runout process,
- the calibration of the process models and
- estimating event frequencies.

Zusammenfassung

Für Regionen mit ausgeprägten Felswänden stellt der Prozess Steinschlag aufgrund seiner hohen Ausbreitungsgeschwindigkeiten eine ernsthafte Gefahr dar. Um Raumplanung im Bewusstsein der Steinschlaggefahr zu verfolgen, ist es notwendig, jene Gebiete zu identifizieren, die von diesem Prozess betroffen sind oder betroffen sein können. Hierbei spielen Prozessmodelle eine zentrale Rolle. Eine Beurteilung der Steinschlaggefahr mithilfe von Prozessmodellen (auf kommunaler Ebene oder der Objektebene) stellt eine große Herausforderung dar, da viele Parameter berücksichtigt werden müssen, die vor Ort nur mit großem Aufwand quantifiziert werden können. Die größten Herausforderungen und Stolpersteine bei der Abschätzung der Gefahr durch Steinschlag liegen

- bei der Bestimmung der Abbruchbereiche und
- der maßgeblichen Blockgrößen,
- bei der Festlegung der für den Sturzprozess relevanten Modellparameter,
- bei der Kalibrierung der Prozessmodelle und
- bei der Abschätzung der Ereignishäufigkeit.

1 Der Prozess Steinschlag

Evans and Hungr (1993) beschreiben den Prozess Steinschlag als die Bewegung individueller, voneinander unabhängiger Felsfragmente, die mittels episodischer Ein-

schläge mit dem Untergrund interagieren. Die österreichische Richtlinie zum Technischen Steinschlagschutz (ONR 24810:2017) beschreibt Steinschlag gemäß der Definition nach Kienholz et al. (1998) als das Fallen, Springen und Rollen von isolierten Steinen und Blöcken. Entsprechend den gängigen Definitionen kann der Prozess Steinschlag als die Bewegung individueller, voneinander unabhängiger Felsfragmente (Steine oder Blöcke) beschrieben werden, wobei nach Bozzolo (1987) vier Bewegungszustände der Fragmente zu unterscheiden sind: Fallen, Springen, Gleiten und Rollen. Der dominante Bewegungszustand ist in hohem Maße von der Fallhöhe, der Länge und der Morphologie (Hangneigung etc.) der Sturzbahn, der Beschaffenheit der Oberfläche (Oberflächenrauheit und Dämpfung) und den Materialeigenschaften des vorherrschenden Gesteins (z. B. Einfluss durch Fragmentierung) abhängig. Entsprechend vieler Beobachtungen ist der dominante Bewegungszustand jedoch zumeist das Springen (Abbildung 1), also die Interaktion des Felsfragments mit dem Untergrund mittels episodischer Einschläge. Die übrigen Bewegungszustände (Fallen, Gleiten und Rollen) beobachtet man vor allem am Beginn und am Ende einer Trajektorie. Es kann jedoch beobachtet werden, dass große Blöcke im Vergleich zu kleineren Blöcken während des Sturzprozesses weniger springen und öfters rollen. Sturzversuche an bewaldeten und nicht bewaldeten natürlichen Hängen (Dorren et al. 2006; Smith and Duffy 1990; Usiro et al. 2006) und Rückrechnungen von Steinschlagereignissen haben gezeigt, dass die maximal auftretenden Prozessgeschwindigkeiten im Allgemeinen bei 30 bis 35 m/s liegen. Vereinzelt wurden jedoch auch schon Geschwindigkeiten von über 45 m/s beobachtet bzw. rückgerechnet (Pamminger 2019; Rauscher 2018).



Abb. 1: a) Einschlagkrater b) Bereich des Abbruchs c) Endlage des Sturzblocks

2 Vom Prozess Steinschlag ausgehende Gefahr

Gefahr besteht dann, wenn aus einem Prozess Schaden für Personen und/oder Sachgüter entstehen kann (ÖGG 2014). Die von einem Prozess wie z. B. Steinschlag ausgehende Gefahr wird einerseits durch seine Intensität und andererseits durch seine Eintrittswahrscheinlichkeit bestimmt (siehe Gleichung 1). Die Kombination von Intensität (I, intensity) und Eintrittswahrscheinlichkeit (P, probability) zur objektivierten Beurteilung der Gefahr (H, hazard) macht insofern Sinn, da im Allgemeinen lediglich ein möglicher großer Schaden mit einer subjektiv als hoch empfundenen Eintrittswahrscheinlichkeit als Gefahr wahrgenommen wird. Ein unwahrscheinliches Eintreten eines großen Schadens wird hingegen im Allgemeinen kaum als große Gefahr empfunden. Umgekehrt wird es auch nicht als große Gefahr empfunden, eine Geldmünze zu verlieren, obwohl bei diesem Szenario die Eintrittswahrscheinlichkeit eher hoch ist.

$$H = I * P \quad (1)$$

Durch die hohen Geschwindigkeiten, die herabfallende Blöcke erreichen können, kann die Intensität – selbst von kleinen Steinen – sehr hoch sein. Für Personen kann daher der kleinste stürzende Stein eine große Gefahr darstellen, umso mehr, weil die Eintrittswahrscheinlichkeit für das Fallen kleiner Steine im Allgemeinen höher ist als für große. Für Infrastrukturen besteht erst ab einer gewissen Intensität Gefahr.

3 Prozessmodelle

Prozessmodelle zur Simulation von Steinschlag (Trajektorienmodelle) existieren seit Mitte der 70er Jahre (z. B. Azimi and Desvarreux 1977; Piteau and Clayton 1977). Gegenwärtig steht eine große Anzahl von Modellen, sowohl für zwei als auch für drei Dimensionen, zur Verfügung (für einen aktuellen Vergleich siehe Tabelle 1 nach Volkwein et al. (1997)). Alle gegenwärtigen Modelle beschränken sich auf die Modellierung des eigentlichen Sturzprozesses. Der initiale Abbruch (Disposition) wird in den Modellen nicht simuliert, sondern lediglich durch die Anfangsbedingungen (Anfangsposition und Anfangsgeschwindigkeiten) abgebildet. Daher benötigen alle Modelle als Eingabe die potentiellen Ablösebereiche, welche mit Hilfe anderer Methoden zu ermitteln sind.

Alle Steinschlagmodelle verwenden klassische ballistische Gleichungen zur Beschreibung der Flugbahn der Fragmente. Die Modelle können entsprechend ihrer mathematischen Beschreibung der Gesteinsfragmente (welche eng mit der Berechnung des Rückpralls verbunden ist) in

1. Massenpunktmodelle („lumped mass approach“),
2. Starrkörpermodelle („rigid body approach“) und
3. hybride Modelle („hybrid approach“) eingeteilt werden.

Bei den Massenpunktmodellen wird der Block als form- und dimensionsloser Massenpunkt („lumped mass“) betrachtet. Im Gegensatz dazu wird bei den Starrkörpermodellen der Sturzblock als komplexer Starrkörper („rigid body“) modelliert. Eine Mischform zwischen diesen beiden Ansätzen stellt der sogenannte hybride Ansatz dar, bei dem der Sturzblock als dimensionsloser Block für die Simulation der Flugbahn, bei der Berechnung des Rückpralls jedoch als Starrkörper (Berücksichtigung von Blockgröße und Form) betrachtet wird. Der aktuelle Trend in der Entwicklung geht in Richtung komplexer Starrkörpermodelle, bei denen versucht wird, die möglichen Blockformen

so naturgetreu wie möglich abzubilden (Andrew et al. 2012; Glover et al. 2012; Vijayakumar et al. 2012).

Tabelle 1: Auswahl vorhandener Modelle, Tabelle verändert nach Volkwein et al. (1997)

Modell/ Programm Name	Referenz	2D/3D	Ansatz	Probabi- listisch	Wald
CRSP (4.0)	Pfeiffer and Bowen (1989)	2D (Profil)	Hybrid	Ja	Nein
Rockfall 7.1 (2008)	Spang and Sönser (1995)	2D (Profil)	Starrkörper	Ja	Ja
RocFall 6.0 (2016)	Stevens (1998)	2D (Profil)	Massenpunkt, Starrkörper	Ja	Ja
Sturzeschwindigkeit	Meissl (2001)	2D (x,y)	Massenpunkt	Nein	Nein
STONE	Guzzetti et al. (2002)	3D (x,y,z)	Massenpunkt	Ja	Nein
Rockyfor 3D 5.2 (2014)	Dorren (2012)	3D (x,y,z)	Hybrid	Ja	Ja
RAMMS::Rockfall	Christen et al. (2007)	3D (x,y,z)	Starrkörper (reale Form)	Ja	Ja
THROW	Preh (2015)	2D (Profil)	Hybrid	Ja	Ja
WURF	Fleris and Preh (2016)	3D (x,y,z)	Hybrid	Ja	Ja
Pierre3D	Gischig et al. (2015)	3D (x,y,z)	Massenpunkt	Ja	Nein

Weitere wesentliche Unterschiede ergeben sich bei den Modellen in der rechnerischen Behandlung des Rückpralls (der Dämpfungseigenschaften der Oberfläche) und der Oberflächenrauheit. Die meisten Modelle verwenden zusätzlich probabilistische Ansätze (Streuung von Modellparametern), um dem stochastischen Charakter des Prozesses Steinschlag Rechnung zu tragen. Tabelle 1 zeigt eine Auswahl vorhandener Steinschlagmodelle mit deren zugehörigen Berechnungsansätzen.

4 Modellparameter und Kalibrierung

Auch wenn die unterschiedlichen Modelle unterschiedliche Ansätze zur Berechnung des Rückpralls nutzen, folgen doch alle Berechnungsansätze demselben Prinzip. Mit Hilfe von Restitutionskoeffizienten (oder Dämpfungsparametern) wird versucht, die Energieverluste während eines Anpralls zu berücksichtigen. Restitutionskoeffizienten berücksichtigen die Summe der Energieverluste zufolge Deformation, Bruch und Massenverschiebung (bei der Kraterbildung) und müssen demzufolge für die unterschiedlichen Untergrundarten (blanker Fels, bedeckter Fels, Hangschutt, etc.) für jedes Modell bestimmt bzw. kalibriert werden. All diese Verluste steigen mit der Zunahme der eingehenden kinetischen Energie. Zur Berücksichtigung dieser Gesetzmäßigkeit kann die Restitution anhand der eingehenden Geschwindigkeit oder kinetischen Energie skaliert werden. Die folgenden Gleichungen (2) zeigen exemplarisch die Skalierung

der Restitutionskoeffizienten entsprechend einem Vorschlag von Bourrier and Hungr (2013).

$$k_n = \frac{E_{0.5,n}}{E_n^{in} + E_{0.5,n}} \quad k_t = \frac{E_{0.95,t}}{E_t^{in} + E_{0.95,t}} \quad (2)$$

$E_{0.5,n}$ und $E_{0.95,t}$ in Gleichung (2) repräsentieren Referenzenergien (Eingabeparameter), definiert als die erforderlichen eingehenden kinetischen Energien, die zu einer Restitution von 0,5 (ausgehende Energie 50% der eingehenden Energie) bzw. 0,95 führen. Bild 2 zeigt exemplarisch die Skalierung des Restitutionskoeffizienten k_n entsprechend dem Vorschlag von Bourrier and Hungr (2013), unter Anwendung einer Referenzenergie von $D \cdot v^2 = 5 \text{ m}^3/\text{s}^2$ (D =Blockdurchmesser).

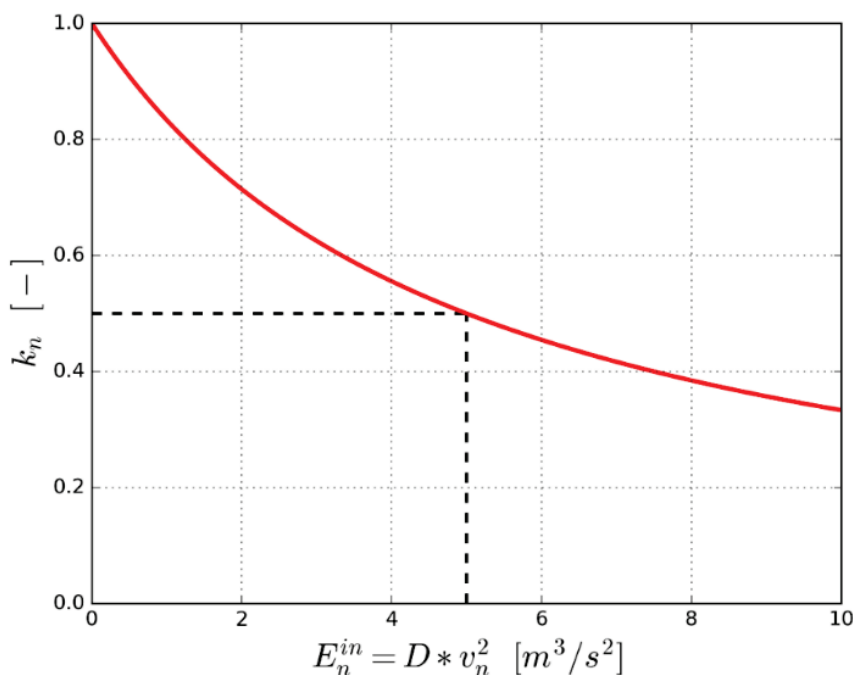


Abb. 2: Hyperbolische Restitutions-Funktion für die eingehende Energie normal zur Geländeoberfläche (nach Bourrier and Hungr (2013))

Einige Modelle, wie zum Beispiel Rockyfor3D (Dorren 2012), bieten die Möglichkeit, ihre erforderlichen Modellparameter (wie Rauheit und Dämpfung) mittels standardisierten Kartierungsmethoden (Kartierungsblättern) festzulegen. Trotzdem sollten alle Modelle für den jeweiligen Anwendungsfall kalibriert bzw. verifiziert werden. Dies kann mittels Rückrechnungen anhand von kartierten Abbruch- und Ablagerungsbereichen, einzelnen stummen Zeugen (Sturzblöcke am Böschungsfuß) und/oder Steinschlagindikatoren, wie Schlagmarken (z. B. an Bäumen) und Einschlagkratern, erfolgen. Sind diese nicht in ausreichender Anzahl vorhanden, können Sturzversuche durchgeführt werden. Abbildung 3 zeigt die Kalibrierung des Steinschlagmodells THROW (Preh 2015) für die Liechtensteinklamm anhand von durch Sturzversuchen ermittelten Geschwindigkeitsverläufen. Die Geschwindigkeitsverläufe entlang der vertikalen Erstreckung der Sturzbahn wurden mithilfe von kartierten Sprungweiten und Videoanalysen (Rauscher 2018) rückgerechnet.

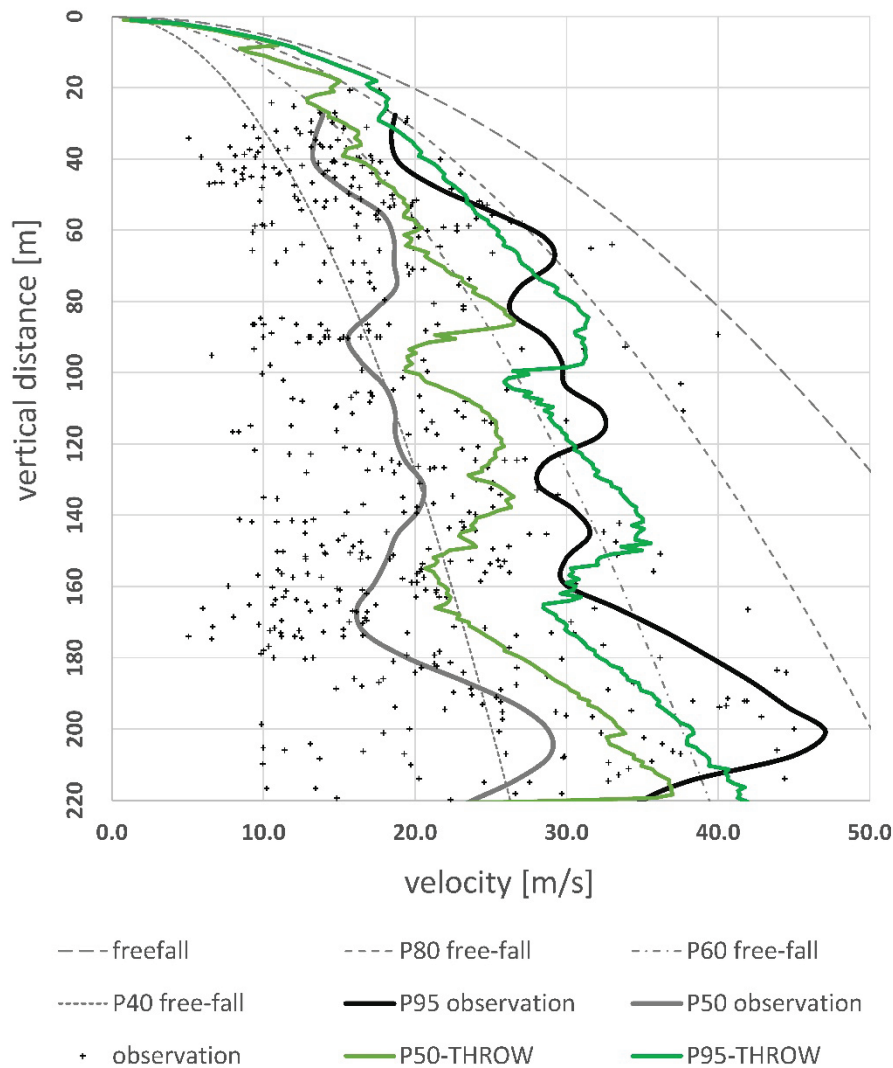


Abb. 3: Beobachtete und berechnete Geschwindigkeiten entlang der vertikalen Erstreckung der Versuchsböschung Liechtensteinklamm im Vergleich zur Geschwindigkeit des Freien Falls. Anmerkung: Pxx = xx Perzentil der Geschwindigkeit

5 Bestimmung der Abbruchbereiche und der maßgeblichen Blockgrößen

Steinschlagmodelle erfordern die Eingabe von potentiellen Ablösebereichen sowie zugehörigen Blockgrößen. Die festgelegten Ablösebereiche und die in den Steinschlagsimulationen berücksichtigte Blockgröße bzw. Blockgrößenverteilung haben einen entscheidenden Einfluss auf die berechneten Intensitäten (Einwirkungen und Sprunghöhen) und somit auf die Festlegung von Gefahrenbereichen und der Bemessung von Schutzbauten.

Potentielle Ablösebereiche können durch die Festlegung von Grenzneigungswinkeln (Melzner et al. 2011), Stabilitätsanalysen und/oder ingenieurgeologischer Kartierung festgelegt werden. Abbildung 4 zeigt die Identifikation von Ablösebereichen in einem digitalen Höhenmodell mit einer Auflösung von 1 m anhand eines Untersuchungsrassters von 5 m und eines Grenzneigungswinkels von 55°. Dabei werden alle Punkte des

Untersuchungsrasters im Höhenmodell mit einer Umgebung steiler als 55° automatisch als Ablösepunkte (bzw. Ablösebereiche) markiert.

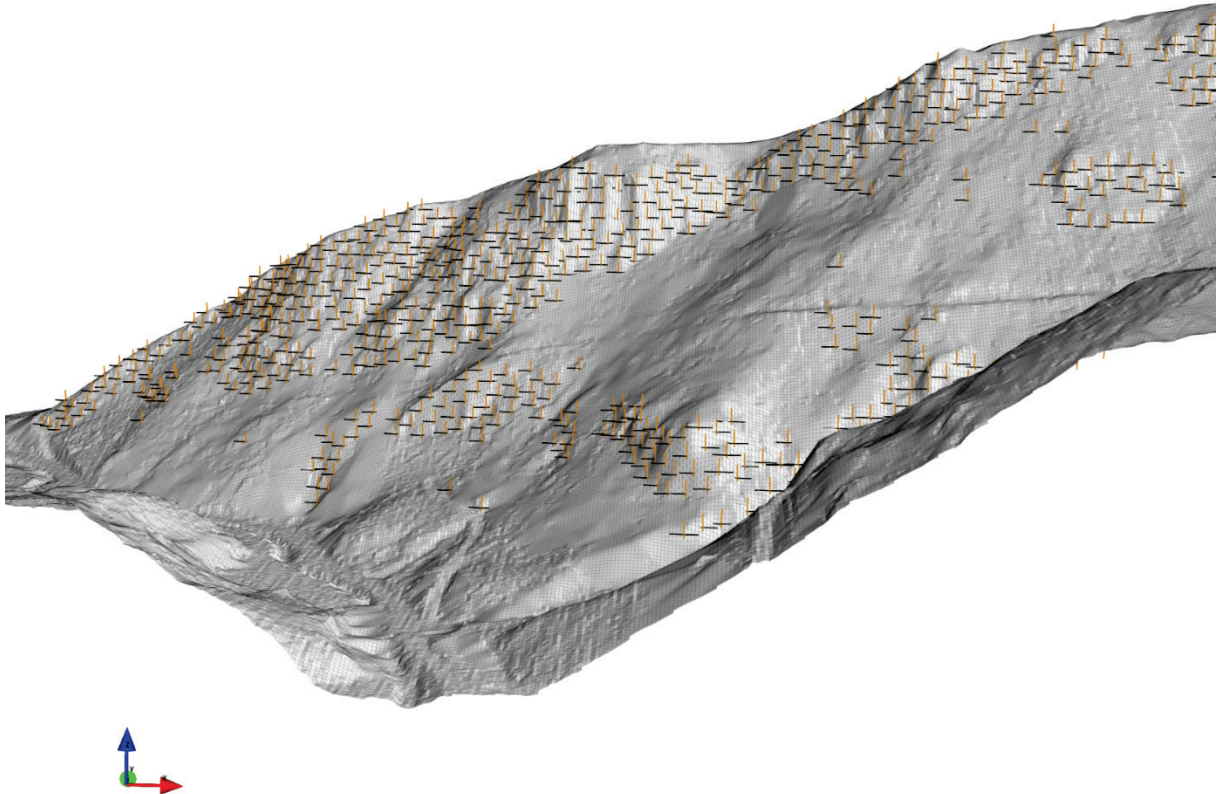


Abb. 4: Automatisierte Identifikation von Ablösepunkten im DHM mithilfe eines Grenzwinkelkriteriums

Die Ermittlung von Blockgrößen stellt eine besonders große Herausforderung dar und wird international sehr unterschiedlich behandelt.

In der Schweiz ist die maßgebliche Blockgröße in das Risikokonzept (RIKO) eingebettet, welches die Risikominderung von Projekten im Verhältnis zu ihren Kosten bewertet. Dies ermöglicht die Priorisierung von Projekten zur Minderung von Naturgefahren nach ihrer Kosteneffizienz. Basierend auf Geländeanalysen, topografischen und geologischen Karten, Luftbildern und Satellitenbildern sowie aus Ereignisinventaren und historischen Chroniken werden verschiedene Gefahrenszenarien gebildet und entsprechende Intensitätskarten erstellt. Szenarien ergeben sich aus der Zuordnung ermittelter Blockgrößen zu bestimmten Jährlichkeiten. Intensitätskarten geben an, an welchem Ort während eines bestimmten Bezugszeitraums eine bestimmte Einwirkung zu erwarten ist.

In Österreich regelt derzeit die Richtlinie (ONR 24810:2017) den technischen Steinschlagschutz. Eines der zentralen Elemente dieser Richtlinie ist die Evaluierung des sog. Bemessungsblocks. Er ergibt sich aus einer im Feld ermittelten Blockgrößenverteilung (Abbildung 5) und einer geschätzten Ereignisfrequenz, wobei beide sehr unsicher sein können.

Die Grundlagenerhebung besteht aus vorhandenen Datengrundlagen (Karten, Pläne), Chroniken und Geländeerhebungen (Wald, Ablösebereiche, Schutthalden) innerhalb eines abgegrenzten Bearbeitungsbereichs. Ablösebereiche müssen durch Kluffkörperanalysen beurteilt werden. Diese werden durch aufgenommene Blockgrößenverteilungen aus zugehörigen Schutthalden plausibilisiert. Dabei sollte der größte Block in der

Halde jedenfalls nicht größer als der aus Klufftkörpern in den Ablösebereichen ermittelte größte Block sein. Blockgrößenverteilungen in Schutthalten werden häufig durch das Linienzählverfahren bestimmt. Andere zulässige Methoden sind die Schätzung der Blockgrößen, die Achsvermessung nach Zufallsprinzip, das Flächenzählverfahren, die Siebanalyse und Fotosieving. Die häufig angewendeten Zähl- und Schätzverfahren sind stark vom Bearbeiter abhängig und können im gleichen Bearbeitungsgebiet zu unterschiedlichen und damit ungenauen Verteilungen führen. In Österreich sind i.d.R. kaum Ereignisinventare oder historische Chroniken vorhanden, sodass Ereignishäufigkeiten oder Bezugszeiträume meist nur sehr ungenau abgeschätzt werden können. Bei häufiger Ereignisfrequenz (EF 4) wird die 98. Volumes-Perzentile (V98) der Blockgrößenverteilung als Bemessungsblock für die Steinschlagsimulation herangezogen. Je geringer die Ereignisfrequenz, umso kleiner der Bemessungsblock (EF 3: V97, EF 2: V96, EF 1: V95, siehe auch Tabelle 2).

Tabelle 2: Ereignishäufigkeiten und zugeordnetes Volumes-Perzentil der Blockgrößenverteilung (ONR 24810:2017).

Ereignisfrequenzklasse	Ereignishäufigkeit n (1/a)	Fraktile für die Bemessungsblockgröße
EF 4 (sehr hoch)	$n \geq 10$ (≥ 10 Ereignisse/Jahr)	V_{98}
EF 3 (hoch)	$1 \leq n < 10$ (1 bis 10 Ereignisse/Jahr)	V_{97}
EF 2 (gering)	$0,03 \leq n < 1$ (1 Ereignis/1 bis 30 Jahre)	V_{96}
EF 1 (selten)	$n < 0,03$ (< 1 Ereignis/30 Jahre)	V_{95}

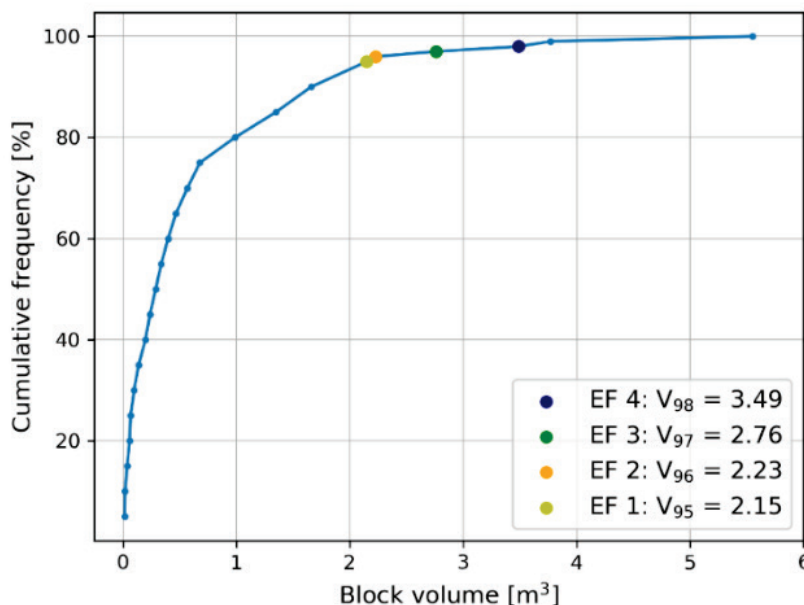


Abb. 5: Kumulierte Häufigkeit von Blockgrößen (= Blockgrößenverteilung) in der Liechtensteinklamm (Rauscher 2018)

Die Vorgangsweise der (ONR 24810:2017) beinhaltet einige Stolpersteine. Zunächst lässt die Bezeichnung „Bemessungsblock“ (in Anlehnung an den Eurocode) darauf schließen, dass dieser gewisse Sicherheiten beinhaltet. Das Gegenteil ist der Fall, indem der Bemessungsblock um zwei bis fünf Volums-Perzentilen kleiner gewählt wird (je nach EF), als der im Feld ermittelte größtmögliche Block (in der Blockgrößenverteilung). Eingangsparameter werden also zu Beginn der Bemessung abgemindert. Eine solche Vorgangsweise sieht der Eurocode nicht vor.

Untersuchungen haben gezeigt, dass die spätere Beaufschlagung von repräsentativen Werten mit Teilsicherheitsbeiwerten Bemessungswerte liefert, die unter den charakteristischen Werten liegen (Illeditsch and Preh 2020).

Durch das Konzept des Bemessungsblocks wird eine einzige Blockgröße für Steinschlagsimulationen verwendet. Durch die Vernachlässigung der größten und aller kleinen Blöcke können maximale Energien und Sprunghöhen übersehen werden.

Durch die Verknüpfung von Volums-Perzentilen mit Ereignisfrequenzen werden Szenarien von großen Blöcken bei geringer Eintrittswahrscheinlichkeit (und umgekehrt) unmöglich.

Ein weiteres Konzept ist die Ermittlung der Einwirkungen/Intensitäten durch die Berücksichtigung der gesamten Blockverteilung in den Steinschlagsimulationen.

Simuliert man Blockverteilungen anstelle eines einzigen Bemessungsblocks, so wirken sich Ungenauigkeiten bei der Aufnahme von Blockgrößenverteilungen weniger erheblich auf die berechneten Intensitäten (Einwirkungen und Sprunghöhen) aus. Die Modellierung der gesamten Blockgrößenverteilung liefert realistischere Energie- und Sprunghöhenverteilungen, als die eines einzelnen Bemessungsblocks. Mit der Verwendung von Blockgrößenverteilungen können Szenarien mit verschiedenen Jährlichkeiten gebildet werden.

6 Bestimmung der Ereignishäufigkeiten

Die Abschätzung der Ereignishäufigkeiten erfolgt auf Basis der Beurteilung der vorliegenden stummen Zeugen (Sturzblöcke im Transport- und Ablagerungsbereich), d. h. aufgrund ihres Alters und der Häufigkeit ihres Auftretens. Diese Alterseinstufung ist aufgrund von zumeist fehlenden objektiven Messungen mit Unsicherheiten aus der gutachterlichen subjektiven Beurteilung behaftet (siehe Abbildung 6).

Ergänzend zur Datierung mittels Kartierung können Ereignischroniken (Archive der Länder und Städte, des geologischen Dienstes, der Straßenmeisterei, etc.) herangezogen werden. Diese liegen aber nur in den seltensten Fällen in ausreichender Qualität vor. Zumeist sind die Angaben zur Lokalisation, zum Volumen, aber auch zum Ereignisdatum zu uneinheitlich und zu ungenau.



Abb. 6: Stumme Zeugen mit verschiedenem Alter; links: frisch, Mitte: angewittert, rechts: alt, starker Bewuchs (Preh et al. 2020a)

Entsprechend der österreichischen Richtlinie (ONR 24810:2017) ist die Ereignishäufigkeit grob gemäß Tabelle 2 zu klassifizieren und dient zur Festlegung des Volumens des Bemessungsblocks (siehe Kapitel 5).

7 Klassifizierung und Darstellung der Gefahr

Entsprechend der von Rouiller and Marro (1997) eingeführten Matterock-Methode kann die Gefahr H an einem bestimmten Punkt x für eine gegebene kinetische Energie E wie folgt berechnet werden:

$$H(E, x) = \lambda_f \times P_p(E, x), \quad (3)$$

wobei λ_f die Ereignishäufigkeit (Abbrüche/Jahr) und $P_p(E, x)$ die Ausbreitungswahrscheinlichkeit (die Wahrscheinlichkeit, dass der jeweilige Punkt x erreicht wird) repräsentiert. Die Eintrittswahrscheinlichkeit eines Events im Punkt x ergibt sich aus dem Produkt $\lambda_f \times P_p(E, x)$. Abb. 7 zeigt eine Visualisierung von (3) nach Jaboyedoff et al. (2005).

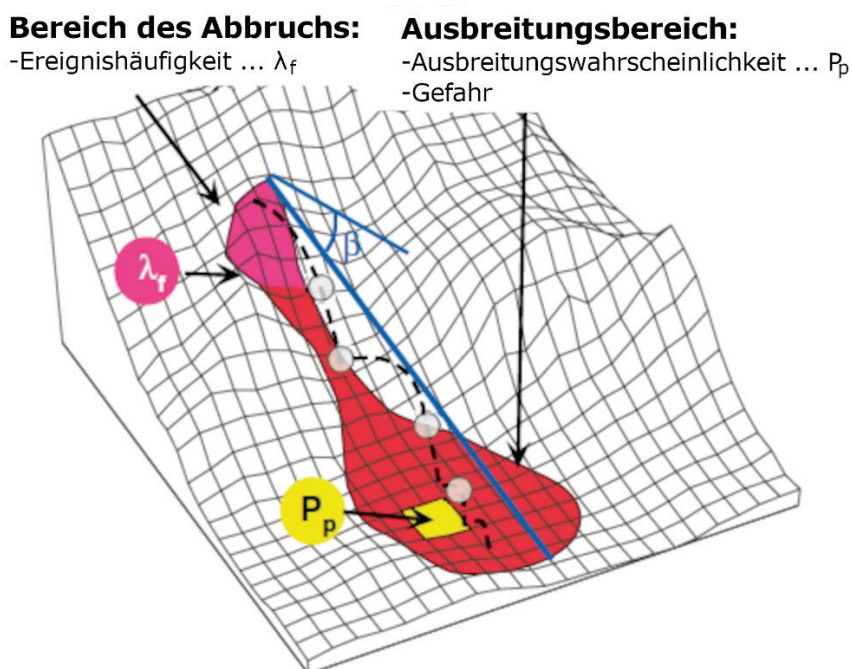


Abb. 7: Darstellung der Steinschlaggefahr nach Jaboyedoff et al. (2005)

Die maximale kinetische Energie E oder ein Perzentil der auftretenden kinetischen Energieverteilung (zumeist E_{90}) und die Ausbreitungswahrscheinlichkeit können mithilfe von Prozessmodellen bestimmt werden. Die Ereignishäufigkeit λ_f muss aber entsprechend den in Kapitel 6 beschriebenen Verfahren abgeschätzt werden und ist, wie beschrieben, eine unsicher zu bestimmende Größe.

Die Wahrscheinlichkeit eines Abbruchs (Ereignishäufigkeit) wird bei der Matterock-Methode auf qualitative Weise, durch eine detaillierte Untersuchung der potentiell gefährdeten Felswände, bestimmt. Dieser Ansatz findet sich in einer Vielzahl von Bewertungssystemen, z. B. Budetta (2004), Pierson (1991), wieder, bei denen die Felswände entsprechend ihrem Trennflächengefüge, der Auflockerung, der Verwitterung etc. durch ein Punktesystem bewertet werden. Entsprechend der erreichten Punktezahl erfolgt dann die Klassifizierung der Wahrscheinlichkeit eines Abbruchs, z. B. in Gering, Mittel und Hoch.

Es existiert eine Vielzahl von nationalen Klassifizierungssystemen zur Zonierung von Gefahrenkarten, welche sich zumeist stark an den in der Schweiz und im Fürstentum Andorra (Copons 2007) entwickelten Systemen orientieren. Diese nutzen ein Ampelsystem als Funktion der Wiederkehrzeit ($1/\text{Häufigkeit}$) und der Intensität (kinetische Energie). Abbildung 8 zeigt exemplarisch das Schweizer Intensitäts-Wiederkehr-Diagramm, das die Definition der Eintrittswahrscheinlichkeit (Gering, Mittel, Hoch) entsprechend der Matterock-Methode nutzt.

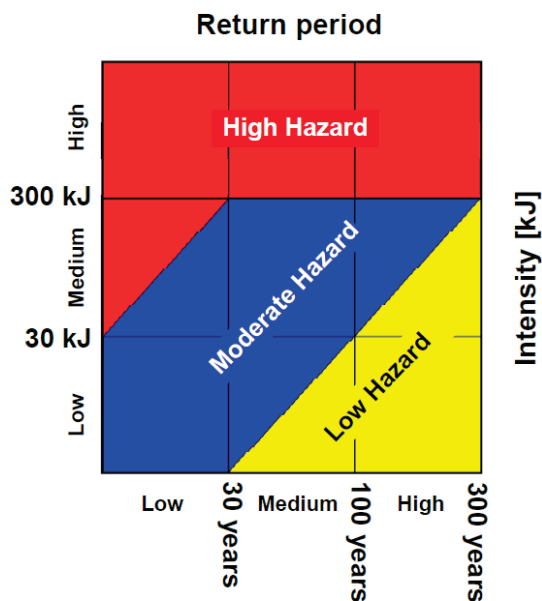


Abb. 8: Schweizer Intensitäts-Frequenz-Diagramm entsprechend den Schweizer Richtlinien (OFAT 1997)

Abbildung 9 zeigt eine mit dem Programm WURF (Fleris and Preh 2016) erstellte Gefahrenkarte, basierend auf der Matterock-Methode und unter Anwendung des Schweizer Intensitäts-Frequenz-Diagramms.

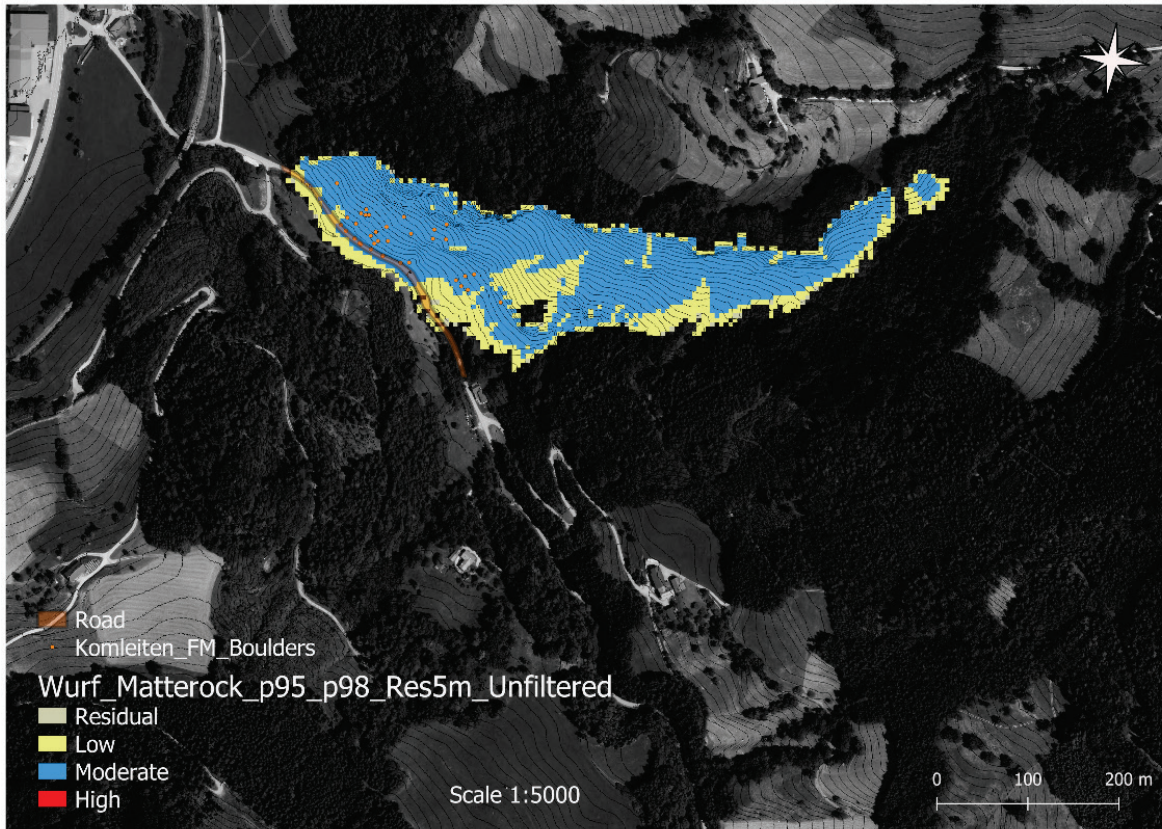


Abb. 9: Gefahrenkarte auf Basis des Matterock-Systems (Preh et al. 2020b)

Die oben beschriebenen Ansätze zur Darstellung von Gefahr beinhalten den Parameter der Eintrittswahrscheinlichkeit (return period), der oft sehr unsicher zu bestimmen ist. Außerdem bleiben Sprunghöhen bei diesen Ansätzen unbeachtet.

Der Rockfall Hazard Vector RHV (Crosta and Agliardi 2003) ist ein Ansatz, der statt der Eintrittswahrscheinlichkeit die Ausbreitungswahrscheinlichkeit c (Anzahl der Trajektorien) berücksichtigt. Der RHV bildet sich aus der Ausbreitungswahrscheinlichkeit c , der kin. Energie k und der Sprunghöhe h , entsprechend Formel (4).

$$|RHV| = \sqrt{c^2 + k^2 + h^2} \quad (4)$$

Abbildung 10 zeigt ein Beispiel für Gefahrenzonierung mit dem Rockfall Hazard Vector (RHV).

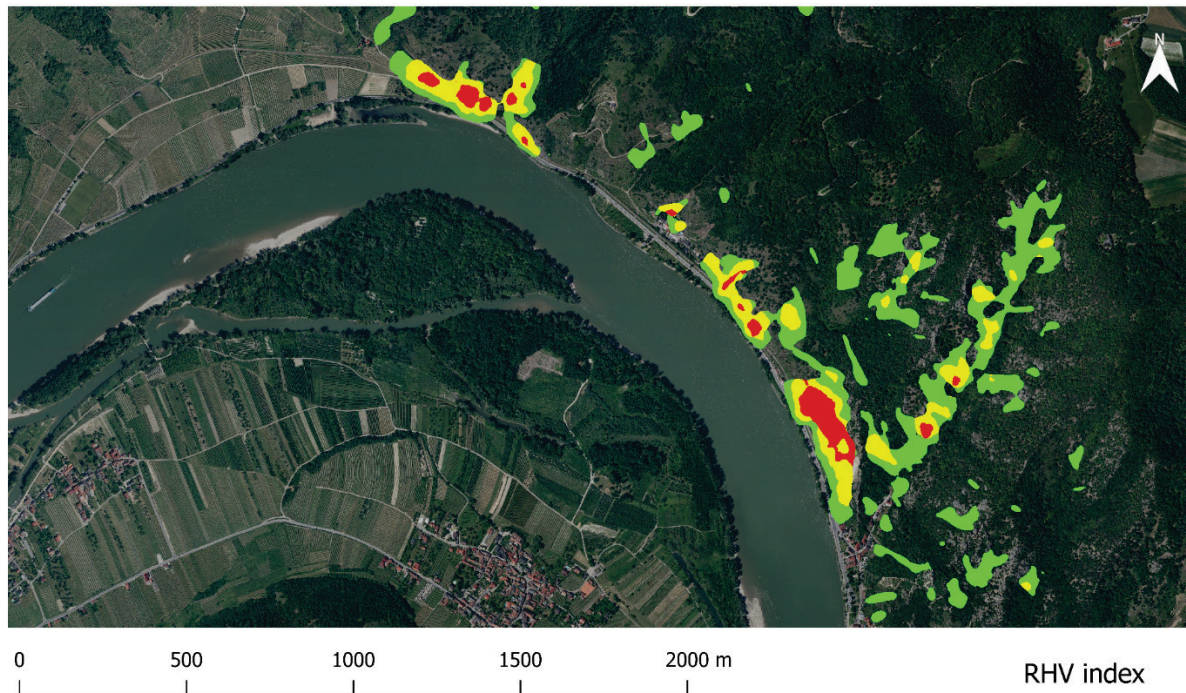


Abb. 10: Beispiel für Gefahrenzonierung mit dem Rockfall Hazard Vector, klassifiziert anhand der RHV Magnitude: grün: $RHV < 1.732$, gelb: $RHV 1.732 - 2.886$, rot: $RHV > 2.886$

In Österreich erfolgt die Gefahrenzonierung auf Basis des Bemessungsblocks nach Mölk and Rieder (2017). Der Bemessungsblock wird in Abhängigkeit einer Ereignishäufigkeit gewählt. Die Eintrittswahrscheinlichkeit steckt also bereits indirekt in den Berechnungsergebnissen. Die Gefahrenkarte ergibt sich durch Klassifizierung der berechneten kinetischen Energie. Sprunghöhen und Ausbreitungswahrscheinlichkeiten bleiben bei diesem Ansatz unberücksichtigt.

8 Schlussfolgerungen

Die Bestimmung der Ereignishäufigkeit stellt den wohl größten Stolperstein bei der Beurteilung der von Steinschlag ausgehenden Gefahr dar. Da die Ereignishäufigkeit meist weder durch Kartierung, noch mit Hilfe von Datenbanken zu bestimmen ist, wurden Bewertungssysteme entwickelt (Budetta 2004; Pierson 1991), deren Anwendung stark vom Bearbeiter abhängt.

Die unterschiedlichen Berechnungsansätze der Modelle zur mathematischen Beschreibung ihrer Gesteinsfragmente sowie zur Behandlung der Dämpfung lassen den Modellfaktor nur schwer abschätzen. Hinzu kommt, dass Modelle oft unterschiedliche Modellparameter benötigen und diese unterschiedlich bestimmt werden müssen.

Viele Ansätze basieren auf der Bestimmung einer Bemessungsblockgröße in Abhängigkeit einer Blockgrößenverteilung und einer Ereignisfrequenz. Beide sind stark vom Bearbeiter abhängig.

Zur Klassifizierung von Gefahr gibt es unterschiedliche Ansätze aus verschiedenen Ländern. Selbst in den Bundesländern Österreichs wird an unterschiedlichen Ansätzen gearbeitet (Mölk and Rieder 2017; Preh et al. 2020b).

Es gibt keinen flächendeckenden und alle Themen (Bestimmung des Ereignishäufigkeit, Bestimmung der Abbruchbereiche und Blockgrößen, Berechnungsansätze, Modellparameter, Klassifizierung von Gefahr) umfassenden Standard. Eine europäische Richtlinie fehlt.

Literatur:

- Andrew R, Hume H, Bartingale R, Rock A, Zhang R (2012) CRSP-3D User's Manual Colorado Rockfall Simulation Program. Lakewood, Colorado
- Azimi C, Desvarreux P (1977) Calcul de chutes de blocs et vérification sur modèle réduit.
- Bourrier F, Hungr O (2013) Rockfall Dynamics: A Critical Review of Collision and Rebound Models. In: Lambert S, Nicot F (eds) Rockfall Engineering. 638 Hoboken, NJ, USA: John Wiley & Sons Inc, pp 175-209.
doi:10.1002/9781118601532.ch6
- Bozzolo D (1987) Ein mathematisches Modell zur Beschreibung der Dynamik von Steinschlag., Eidgenössische Technische Hochschule Zürich
- Budetta P (2004) Assessment of rockfall risk along roads. Natural Hazards and Earth System Sciences 4:71-81 doi:10.5194/nhess-4-71-2004
- Christen M, Bartelt P, Gruber U (2007) RAMMS – a modelling system for snow avalanches, debris flows and rockfalls based on IDL. Photogrammetrie-Fernerkundung-Geoinformation 4:289-292
- Copons R (2007) Avaluació de la perillositat de caigudes de blocs rocosos al Solà d'Andorra la Vella. St. Julià de Lòria-Principality of Andorra, Andorran Research Center Press,
- Crosta GB, Agliardi F (2003) A methodology for physically based rockfall hazard assessment Nat Hazards Earth Syst Sci 3:407-422 doi:10.5194/nhess-3-407-2003
- Dorren L (2012) Rockyfor3D (V5.1) enthüllt - Transparente Beschreibung des kompletten 3D-Steinschlagmodells. ecorisQ,
- Dorren L, Berger F, Putters US (2006) Real-size experiments and 3D simulation of rockfall on forested and non-forested slopes. Natural Hazards and Earth System Sciences 6:145-143
- Evans SG, Hungr O (1993) The Assessment of Rockfall Hazard at the Base of Talus Slopes. Can Geotech J 30:620-636 doi:10.1139/t93-054
- Fleris E, Preh A (2016) WURF_LIVE: Demonstration of a stochastic numerical rockfall code in 3D. In: Abstract Volume of GeoTirol 2016 – Annual Meeting of DGGV and PANGEO Austria, Innsbruck, 25-28 September 2016. H. Ortner, p 69
- Gischig VS, Hungr O, Mitchell A, Bourrier F (2015) Pierre3D: a 3D stochastic rockfall simulator based on random ground roughness and hyperbolic restitution factors. Can Geotech J 52:1360-1373 doi:10.1139/cgj-2014-0312
- Glover J, Schweizer A, Christen M, Gerber W, Leine R, Bartelt P (2012) Numerical investigation of the influence of rock shape on rockfall trajectory. In: EGU General Assembly, Vienna, Austria, 2012. Geophysical Research Abstracts. doi:EGU2012-11022-1
- Guzzetti F, Crosta G, Detti R, Agliardi F (2002) STONE: a computer program for the three-dimensional simulation of rock-falls. Comput Geosci-Uk 28:1079-1093 doi:10.1016/s0098-3004(02)00025-0

- Illeditsch M, Preh A (2020) The Concept of Design Block Size – A Critical Review of ONR 24810 “Technical Protection against Rockfall” Geomechanics and Tunnelling (in press)
- Jaboyedoff M, Dudt JP, Labiouse V (2005) An attempt to refine rockfall hazard zoning based on the kinetic energy, frequency and fragmentation degree Natural Hazards and Earth System Sciences 5:621-632 doi:DOI 10.5194/nhess-5-621-2005
- Kienholz H, Zeilstra P, Hollenstein K (1998) Begriffsdefinitionen zu den Themen: Geomorphologie, Naturgefahren, Forstwesen, Sicherheit, Risiko, Arbeitspapier. Bundesamt für Umwelt, Wald und Landschaft, Eidgenössische Forstdirektion, Bern
- Meissl G (2001) Modelling the runout distances of rockfall using a geographic information system. Zeitschrift für Geomorphologie 125:129-137
- Melzner S, Lotter M, Tilch N, Kociu A (2011) Rockfall susceptibility assessment at the regional and local scales as a basis for planning site-specific studies in the Upper Moelltal (Carinthia, Austria). vol 91.
- Mölk M, Rieder B (2017) Rockfall hazard zones in Austria. Experience, problems and solutions in the development of a standardised procedure. Geomechanics and Tunnelling 10:24-33 doi:10.1002/geot.201600065
- OFAT O, OFEFP (1997) Recommandations 1997 - Prise en compte des dangers dus aux mouvements de terrain dans le cadre des activités de l'aménagement du territoire. OFAT OFEE,
- ÖGG (2014) Empfehlungen für das Schutzziel bei gravitativen Naturgefahren in Österreich. Österreichische Gesellschaft für Geomechanik,
- Pamminger P (2019) Untersuchungen zum Einfluss der Blockfragmentierung am Beispiel der Liechtensteinklamm mit Hilfe des Berechnungsansatzes WURF., TU Wien
- Pfeiffer T, Bowen T (1989) Computer Simulation of Rockfalls. Bulletin of the Association of Engineering Geologists 26:135-146
- Pierson LA (1991) The Rockfall Hazard Rating System. Oregon Department of Transportation,
- Piteau DR, Clayton R (1977) Discussion of paper “Computerized design of rock slopes using interactive graphics for the in-pu and output of geometrical data” by P.A. Cundall, M.D. Voegele, C. Fairhurst. In: 16th Symposium on Rock Mechanics, Minneapolis, 1977. pp 62-63
- Preh A (2015) THROW, ein dynamisch stochastisches Simulationsmodell zur Prognose von Steinschlag.
- Preh A, Mölk M, Illeditsch M (2020a) Steinschlag und Felssturz. In: Thomas G, Mergili M, Katrin S (eds) Extrema 2019. Vienna University Press, p 31
- Preh A et al. (2020b) NoeTALUS - a research project to evaluate methods for the production of rock fall hazard maps in Lower Austria. In: 14th Congress INTERPRAEVENT 2020, Bergen, Norway, 2020.
- Rauscher R (2018) Planung, Ausrichtung und Durchführung eines Steinschlag-Sturzversuches zur Kalibrierung von 3D-Steinschlagsimulationen unter besonderer Berücksichtigung der ONR 24810:2017., Universität für Bodenkultur
- Rouiller J-D, Marro C (1997) Application de la méthodologie “Matterock” `a l`evaluation du danger li`e aux falaises, Eclogae Geologicae Helvetiae. Eclogae Geologicae Helvetiae 90:393–399

- Smith DD, Duffy JD (1990) Field tests and evaluation of rockfall restraining nets. California Office of Transportation Materials and Research
- Spang R, Sönser T (1995) Optimized rockfall protection by "Rockfall". In: Eight congress of the International Society for Rock Mechanics, Tokyo, 1995. pp 1233–1242
- Stevens WD (1998) Rocfall: A tool for probabilistic analysis, design of remedial measures and prediction of rockfalls., University of Toronto
- Usiro T, Kusumoto M, Onishi K, Kinoshita K (2006) An experimental study related to rock fall movement mechanism. Journal of Japan Society of Civil Engineers 62:377-386
- Vijayakumar S, Yacoub T, Ranjram M, Curran JH (2012) Effect of rockfall shape on normal coefficient of restitution. In: 46th U.S. Rock Mechanics/Geomechanics Symposium, Chicago, Illinois, 2012. p 8
- Volkwein A et al. (1997) Rockfall characterisation and structural protection - a review. Natural Hazards and Earth System Sciences 11:2617-2651
doi:10.5194/nhess-11-2617-2011

Cross-border geographic information system and monitoring of rock falls events in the Saxon-Bohemian Switzerland

Grenzüberschreitendes Geoinformationssystem und Monitoring von Massenbewegungen in der Sächsisch-Böhmischen Schweiz

Jörn Wichert

TU Bergakademie Freiberg, Geotechnical Institute, Gustav-Zeuner-Str. 1
09599 Freiberg / Germany

Abstract

In the Saxon-Bohemian Switzerland (Elbe Sandstone Mountains) rock falls regularly occur, causing a higher endangerment in parts of the region. Higher risks concern the general public, buildings as well as roads and rail roads. With the project a no cross-border cooperation between Czech and German professionals in the field of "georisks" was initiated. The project comprises the establishment of a geographic information system, installation of a monitoring- and early warning system, a common rock mass classification and the generation of geotechnical "risk-models". While a monitoring system and regular monitoring of possible risks exist on the Czech side there was not such system on the Saxonian side. Here all determined occurrences are accumulated in the event-database of mass movements by information from public authorities, adjacent private owners and messages of public media. The paper gives an overview of the geographic information system as well monitoring - and early warning system.

Zusammenfassung

In der Sächsisch-Böhmischen Schweiz (Elbsandsteingebirge) führen regelmäßige Felsstürze zu einer erhöhten Gefährdung in Teilen dieser Region. Höhere Risiken betreffen die allgemeine Öffentlichkeit, Gebäude sowie Straßen und Gleise. Mit dem Projekt wurde eine grenzüberschreitende Zusammenarbeit zwischen tschechischen und deutschen Fachleuten auf dem Gebiet von „Georisiken“ initiiert. Das Vorhaben umfasst den Aufbau eines Geoinformationssystems sowie Monitoring- und Frühwarnsystems, eine einheitliche Gebirgsklassifizierung und das Generieren geotechnischer „Risikomodelle“. Während auf der tschechischen Seite an zahlreiche Lokalisationen ein Mess-Monitoring sowie regelmäßige Kontrollgänge durchgeführt werden, wird das Landesamt für Landwirtschaft, Umwelt und Geologie (LfULG) auf sächsischer Seite lediglich durch Archive, Ämter, Eigentümer oder die Presse informiert. Der Artikel hier gibt einen Überblick über das Geoinformationssystem sowie das Monitoring- und Frühwarnsystem.

1 Aim of the project and project area

The project area is the Saxon-Bohemian Switzerland (Elbe Sandstone Mountains) in southeast of Germany and central north of the Czech Republic. Within the Elbe Sandstone Mountains rock falls especially regularly occurs, causing a higher endangerment of the region. Compared to other regions of the Free State of Saxony also the amount of mass movements is exceedingly higher. Higher risks concern the general public, houses, buildings or the general infrastructure like roads and rail roads. Especially if one considers the Elbe valley as a bottleneck within the European railway net, the importance of safety for a working traffic becomes obvious.

There is no cross-border cooperation between Czech and German professionals in the field of georisks. While a monitoring system and regular monitoring of possible risks exist on the Czech side there was not such system on the Saxonian side. Here all determined occurrences are accumulated in the event-database of mass movements by information from geological archive, public authorities, adjacent private owners and messages of public media.

The geological setting, the properties of the sandstones and exposition in the environment lead to different slope stabilities within the different areas. An investigation to determine the properties and possible changes of the rocks does not exist in the project area.

The missing cooperation finds its expression in a missing comprehensive and common strategy to carry out a rock mass classification, to establish a geographic information system and to carry out a monitoring of the area.

The project is the basis for a comprehensive monitoring of the Elbe-Mountain region in respect to the endangerment of the public and infra structure caused by rock-fall events and/or mass movements. The geographic information- and monitoring system will be always up-to-date, i. e. it can consider new environmental conditions which can influence the rock behaviour in respect to safety. With the developed forecast instruments of rock falls a suitable tool for risk prevention will be provided. It will be possible to define countermeasures before a rock fall occurs. The classification of "risk areas" is a reliable base for a risk management as well as to make future investments for roads, buildings and rail roads as well as regional planning safer and economically efficient.

The geological setting is characterised by nearly horizontal orientated sandstone of Upper Cretaceous age. To the northeast the "Elbsandsteingebirge" is bordered by the fault "Lausitzer Überschiebung" from the granitic rocks of the Lausitzer Block" while it is bordered by metamorphic rocks of the "Elbtalschiefergebirge" to the Osterzgebirge. The sandstones from Upper-Cenomanium to Middle-Coniacium can reach a total thickness between 550 m and 650 m (Pälchen & Walter 2011).

2 Geographic information system (GIS) for mass movements

A cross-border bilingual Czech-German geographic information system for mass movements was established for the Elbe Sandstone Mountains. The cross-border geographic information system contains all geo-environmental information of the project

area which already exist and will be gained in the future. A core component in the programming is a comprehensive database of mass movement (events) written in PostgreSQL and a smartphone app to report an event. The data base comprises the following topics:

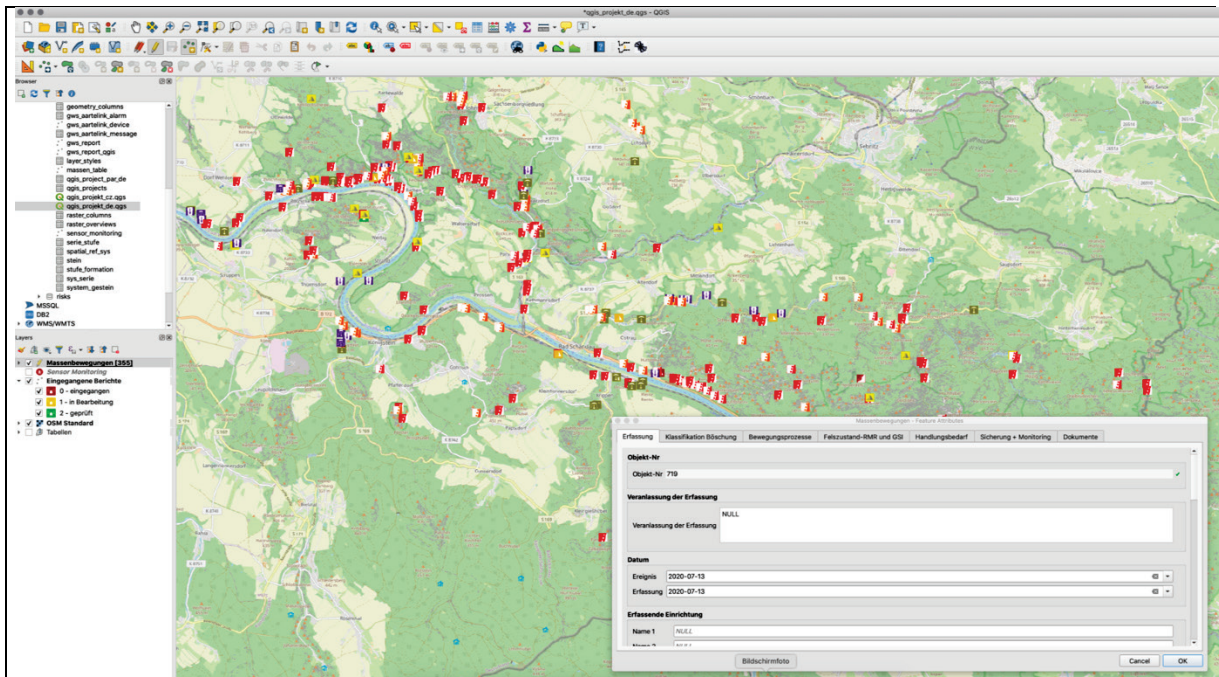
- general information of the recording person and the situation of the location;
- classification of the slope (morphology, inclination, distance from road, mass movements: type, height of the original position of the fallen block, activity, possible trigger process, possible causes, damages);
- Rock mass classification (RMR, GSI) and geological setting;
- assessment of degree of endangerment and definition of counter measures;
- existing monitoring and safety measures;
- safety system/monitoring system: type, principal, installing company, controlling institution
- upload of documents and photographs.

Within the next future, an interface will be written so that the data of the existing Czech monitoring system will be automatically sent to the data base.

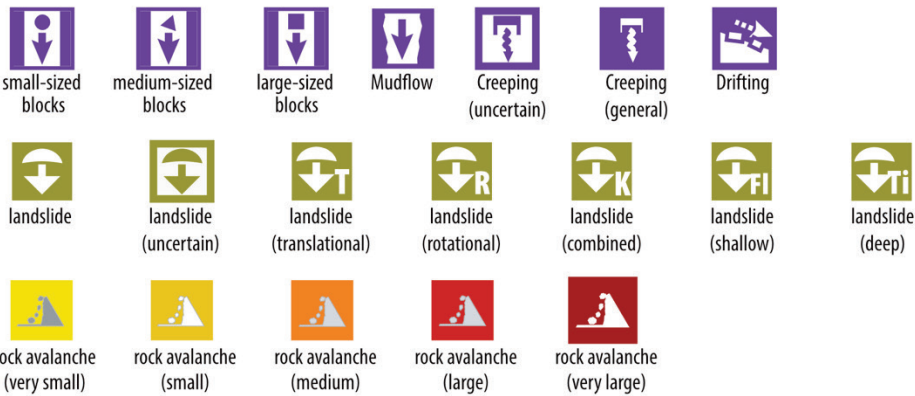
A very important part of the whole system was to find common terms in respect to the different types of mass movements and to translate the technical terms properly.

Furthermore, an appropriate symbology for the different processes had to be designed. We used and adapted the symbology of Kienholz & Krummenacher (1995) for our project area. In the project area, phenomena of rock falls, landslides, creeping and mudflows can be seen, although rock falls are the dominating processes.

First of all, different colours are assigned to the main processes: red/orange to rock falls, brown to landslides and violet to creeping and mudflows to distinguish very quickly the main processes on the map. Within the main processes sub-processes are distinguished (Fig. 2.1).



debrisflow



rock fall (tree = damping by forrest)

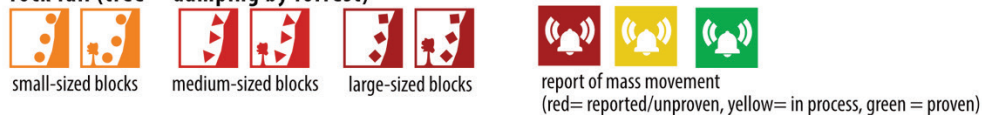


Fig. 2.1: Upper image: Layer with mass movement events and input mask for a new event and (engineering-) geological setting; Lower image: Used symbology adapted by Kienholz & Krummenacher (1995)

The real number of mass movement events is hardly to determine because it would require a regular inspection of the whole area or the specific areas susceptible to mass movements. Since the Saxon-Bohemian Switzerland is a very famous area for trekking and climbing, the idea of “voluntary reporting” arose to collect as many as possible data of mass movement events.

There are two possibilities to report events in a given scheme. Firstly, people can notice what they have seen, take a photograph and add a report over the (Web-) GIS. Secondly, people can report an event via the developed smartphone app at the location of the event. The scheme to report events was designed in a simple manner so that each layman can use this. Since the internet coverage is only punctual given, at least within

the German part, it is possible to download the map of the area in advance for later offline usage. We decided against registration of the user which could hinder the usage of the smartphone app. If there is no internet access, one can work in offline-mode and send it later.

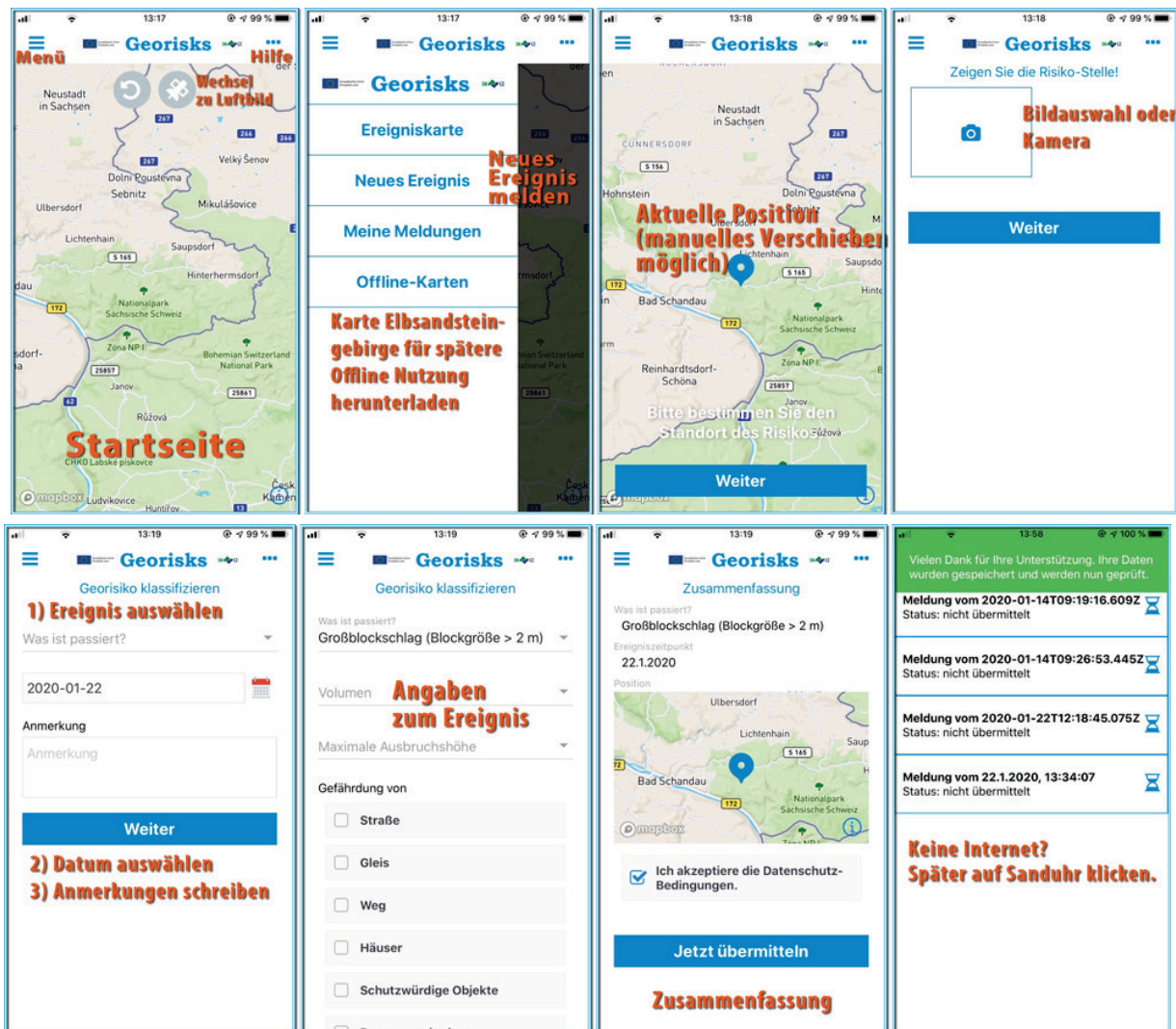


Fig. 2.2: Reporting an event of a mass movement with the smartphone application

A menu guides the person through the App (Fig. 2.2):

- Position of mass movement (automatically but can be manually adjusted);
- Taking photograph of event;
- What happened: type of mass movement or changes of the rock face (the person knows the rock and discovers fractures or other changes on the surface);
- Possible damage of infrastructure.

Afterwards, a possible endangerment of ways, streets, houses etc. and the date reporting as well as a comment can be filled out. The person gets a summary of its report and can send it to our database. If no internet available, the report can be sent later. Once, the report is sent to the database a red bell symbol automatically appears on the map. To verify the report it has to be controlled by experts and the report has three further states with “in processing” (orange bell symbol) and verified/confirmed (green

bell symbol). One aim of this procedure is that the reporting persons see that the other side is active and that they did not it in vain.

3 Monitoring system

For the German part, the monitoring system “Aarte Link” of the Swiss company Aartesys AG was installed on two locations (Fig. 3.1) in September 2019. On location are the Schaarwände within the Kirnitzschtal and the other one in village of Schmilka just at the German-Czech border. For the Schaarwände a geotechnical model was generated in PFC (Itasca) and for Schmilka the works were postponed because of Corona.



Fig. 3.2: Gateway and sensors in the village of Schmilka

With this system a step-wise alarming is possible in a split second and in case of unusual movements the measurements will be carried out in shorter data rate. All data will be automatically sent to the data base by the interface JSON.

The system comprises sensors which send the data to the gateway which send it further to the server. The sensors measure the temperature and the earth acceleration in three vector axis and these values will be used to calculate the deflection. One gateway can communicate with more than 100 sensors over a distance between 5 - 10 km.

With the software AarteLink Monitor (Fig. 3.2) one can manage, monitor and configure the whole system through a web browser. Furthermore, one can define which and how a person will be informed in case of a mass movement (SMS, E-Mail...)

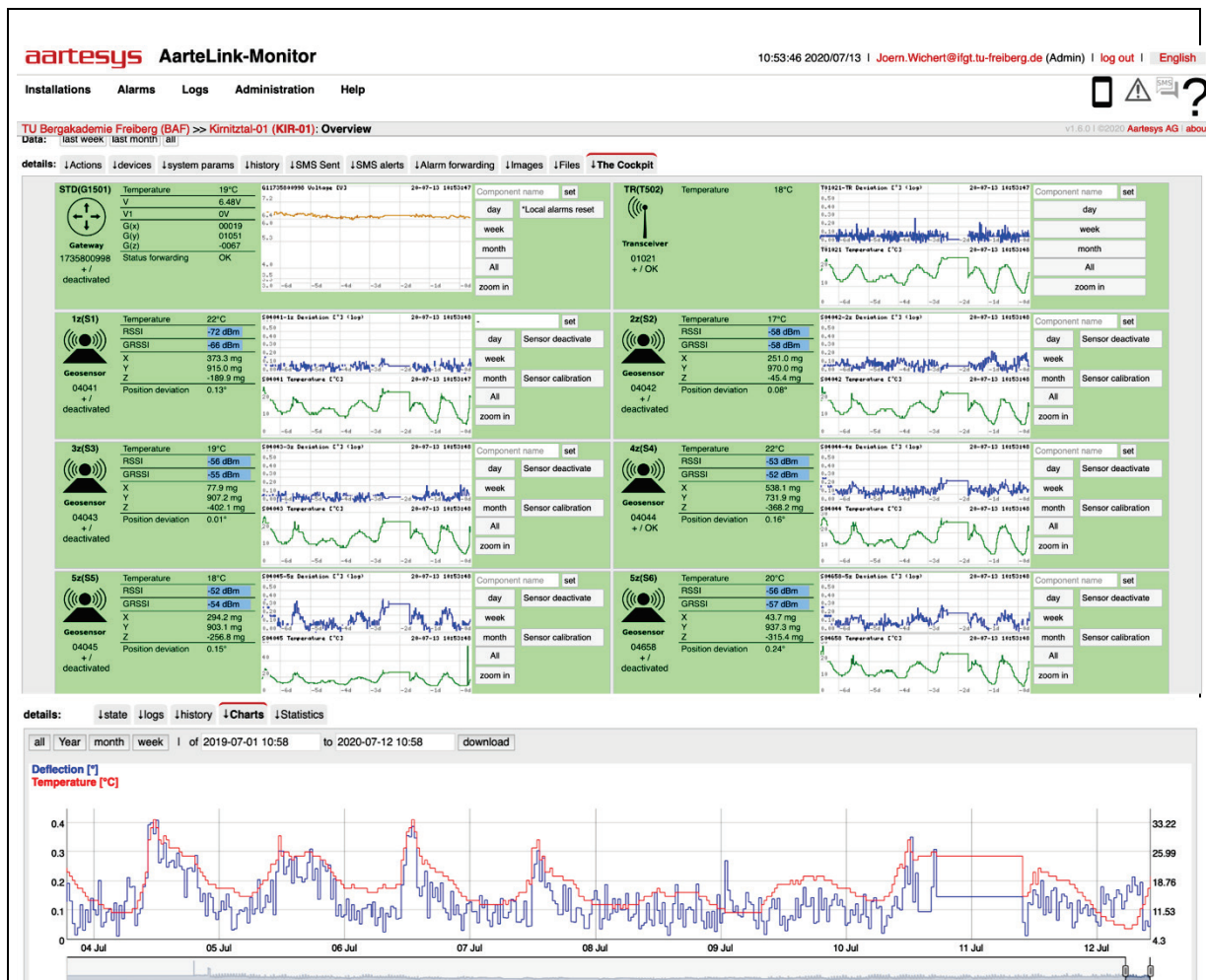


Fig. 3.2: Monitoring with the AarteLink Monitor via Browser

4 References

Kienholz, H. & Kruppenacher, B. (1995): Naturgefahren - Symbolbaukasten zur Kartierung der Phänomene., 79. Bundesamt für Umwelt, Wald und Landschaft BU-WAL, Bundesamt für Wasser und Geologie BWG

Pälchen W. & Walter H. (2011): Geologischer Bau und Entwicklungsgeschichte, 2. Aufl., Stuttgart: Schweizerbart (Geologie von Sachsen, 1), 537 S.

Numerical investigations of fracture interference during hydraulic fracturing

Numerische Untersuchungen zur Rissinteraktion während des Hydraulic Fracturing

Yongjun Yu, Wancheng Zhu, Lianchong Li, Chenhui Wei, Baoxu Yan, Chao Qin
Center for Rock Instability and Seismicity Research, Northeastern University,
Shenyang, PR China

Abstract

During the oil and gas production, ultimate production depends closely on the reservoir regions that have been effectively stimulated, and have the virgin ultra-low permeability evidently enhanced. Multiple closely staged clusters are preset to enlarge the stimulated reservoir volume (SRV), where hydraulic fractures are initiated from the clusters and notched perforations. However, the initiation and propagation of hydraulic fractures may be interfered by preexisting natural fractures throughout the fracturing treatments. Fracture interference diverts the propagation away from originally expected trajectory, particularly leading to complicated fracture network morphologies in post-fracturing periods, which should be studied so as to understand outcomes caused by the fracture interference as well as the related mechanism. In this regard, a coupled stress-seepage-damage model is proposed to simulate the fracture interference when the pre-existing rock discontinuities of beddings are incorporated. The applicability of the model has been validated by reproducing the hydraulic fracturing experiment performed on the bedded shale specimen. Then the proposed model is used to study the multiple fracture interference during hydraulic fracturing in the shale reservoir. Experimental results show that the pre-existing beddings in the shale affect the fracture propagation path to a considerable degree, and the proposed model can favorably reproduce the laboratory result, making it feasible for further studies on mutual fracture interference in fractured reservoirs. Subsequent numerical results show that the fracture interference in shale reservoirs with randomly distributed beddings is such complicated that the fracture propagation direction is controlled not only by the stress shadow effects as described in previous studies in conventional reservoirs, but also by the interference with pre-existing beddings. The configuration of the pre-existing beddings determines the local propagation path of the fractures, but an overall mutual attraction is always found in scenarios where initial perforations are placed with inner perforation ends staggered to some distances, regardless of the number of group beddings. In summary, multiple factors affect fracture interference behavior, thus confirming the significance of incorporating discontinuous structures, e. g., natural beddings, for a precise numerical modeling of fracture interference during reservoir stimulations.

Zusammenfassung

Die Öl- und Gasproduktion hängt stark vom Reservoir und seiner Stimulation ab, wobei die Produktion in ursprünglich extrem gering permeable Reservoirs durch Stimulation erheblich gesteigert werden kann. Mehrere eng gesetzte Cluster vergrößern das sti-

multierte Reservoirvolumen (SRV), wobei die hydraulischen Risse von den Perforationen ausgehen. Die Initiierung und Ausbreitung von hydraulischen Rissen wird jedoch während der Hydrofrac-Operation beeinflusst von existierenden natürlichen Rissen. Die Risswechselwirkung führt zur Abweichung von der ursprünglich erwarteten Rissausbreitungsrichtung und speziell zur Ausbildung von komplexen Rissnetzwerken in der post-fracture Phase. Dies sollte studiert werden, um die Rissinteraktion und die damit verbundenen Mechanismen zu verstehen. Deshalb wird ein hydro-mechanisch gekoppeltes Schädigungsmodell vorgestellt, um die Rissinteraktion mit vorher vorhandenen Diskontinuitäten in Form von Schichtung zu simulieren. Die Anwendbarkeit des Modells wurde validiert durch die Rückrechnung von Hydrofrac-Experimenten durchgeführt an geschichteten Shale-Proben. Danach wurde das Modell eingesetzt, um die Multifrac-Interaktion während des Hydraulic Fracturing in Shale-Reservoiren zu untersuchen. Die experimentellen Ergebnisse zeigen, dass die in Shale existierende Schichtung den Rissausbreitungspfad in einem bedeutenden Maß beeinflusst. Das vorgestellte Modell kann die Laborergebnisse gut nachbilden und eignet sich damit für Studien zur Rissinteraktion in gefracchten Reservoiren. Die numerischen Simulationen zeigen, dass die Rissinteraktion in Shale-Reservoiren mit zufällig verteilter Schichtung so komplex ist, dass die Rissausbreitungsrichtung nicht nur vom Effekt des Spannungsschattens wie in konventionellen Reservoiren, sondern auch noch von der Interaktion mit den existierenden Schichtungen abhängt. Die Konfiguration der vorhandenen Schichtung bestimmt den lokalen Ausbreitungspfad der Risse, aber eine allgemeine gegenseitige Beeinflussung wird immer vorgefunden in Szenarien, wo die initiale Perforationen in den inneren Perforationsenden in einem gewissen Abstand platziert sind, unabhängig von den Anzahl der Schichtungen. Zusammenfassend lässt sich sagen, dass mehrere Faktoren die Rissinteraktion beeinflussen. Damit wird die Bedeutung der Einbeziehung von Diskontinuitäten, wie die natürliche Schichtung, für eine präzise numerische Simulation der Rissinteraktion während der Reservoir-Stimulation deutlich.

1 Introduction

Multi-staged clusters are preset along the wellbore, where multiple induced fractures emanate from the perforations and propagate deeply into the target stratum. Fracture interference due to the closely preset perforations diverts the fracture propagation trajectories and change aperture profiles in height direction^[1]. Fracture interference depends mainly on many factors i.e., intervals of perforations, clusters, stages; and geological aspects as *in-situ* stress anisotropy, distribution of natural discontinuities etc.^[1]. Bungler et al. (2013) quantified effects of perforation spacing on the perforation loss. Subsequently, Cheng and Bungler (2019) emphasized the re-arrangement of the perforation intervals to alleviate negative effects of stress shadow and to get hydraulic fractures with nearly equivalent lengths. Fracture interference in naturally fractured formations with distributed natural fractures is another more complex scenario where repelling and attraction are all ultimate potential patterns of fracture interference. The activated opened beddings and natural fractures in shale change the fracture profile from an ideally elliptical shape, to the one with narrower apertures in vicinity of two fracture tips in the vertical cross-section^[3]. Kresse et al. (2013) confirmed that the relative positions of the initial fracture, or the injection wellbore would have determined the fracture interference pattern, i. e., mutual attraction or repelling. Experimental researches on fracture interference are tougher than conventional hydraulic fracturing experiments, due to that the specimens need to be sawed in half to reveal the interference trajectories among multiple fractures, where artificial turbulence would be inevitably introduced. Rabaa (1989) conducted physical experiment on fracture interferences using gypsum and found that the fracture geometry was influenced by the azimuth between horizontal wellbore axis and minimum *in-situ* stress direction. Crosby et al. (2002) conducted experiments on two hydraulic fracture interference, and found that the breakdown pressure of the second fracture is close to that of a previous induced hydraulic fracture, which indicated that stress shadow effect can be alleviated by appropriate arrangement of wellbores in certain stress regimes.

Even though numerical simulations have already been performed on fracture interference, further improvements considering pre-existing beddings or discrete fracture networks are required. In this study, stress-seepage-damage coupled models were established with attached model validation to laboratory work and thereafter feasible models aimed at modeling shale formations with beddings taken into account, and discussions on mechanical behavior of fracture interference and their effects after hydraulic fracturing performance.

2 Laboratory experiments on hydraulic fracturing

Grown beddings and natural fractures regarded as discontinuities are abundantly developed in shale reservoirs^[3, 7], and they could affect reservoir stimulation results due to the obviously different properties compared to shale matrix.

2.1 Hydraulic fracturing experiment

Shale samples collected from Longmaxi Formation, Sichuan Province, China, and were further processed into cubic specimens of 10 cm × 10 cm × 10 cm with a central hole for pressurized fluid injection (Figs. 1a - 1c). An open hole with length of 2 cm is reserved. By comparison, hydraulic fracturing in a nearly isotropic rock without any layers (i.e., granite) is also performed.

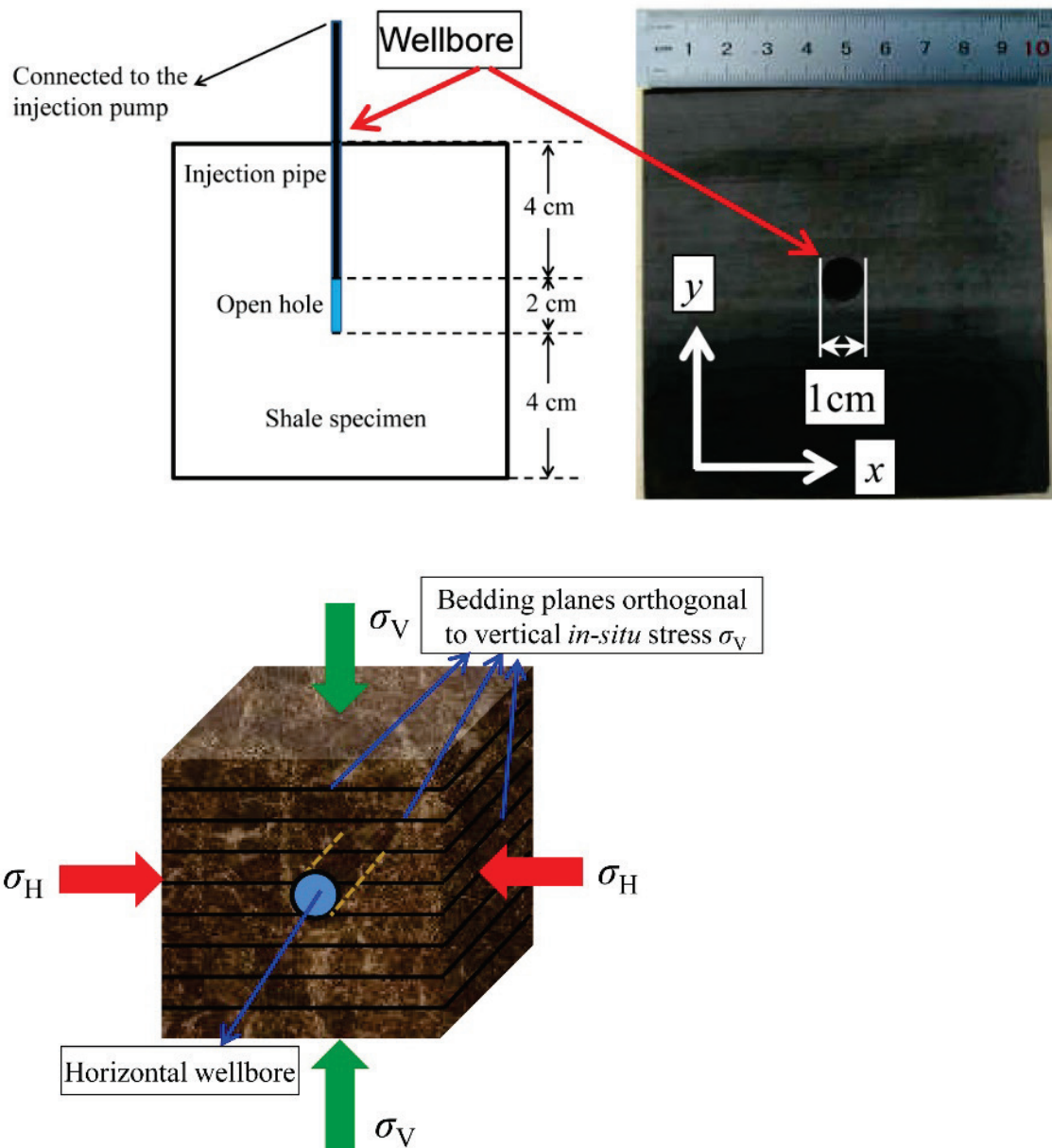


Fig. 1. Schematics of plugged pump pipe configurations (a); and the upper surface of the shale specimen (b); in-situ stress condition and beddings, where vertical in-situ stress σ_v is applied perpendicularly to beddings (c).

Hydraulic fracturing experiments are performed on a biaxial loading apparatus, with systems of fluid injection and AE location monitoring (Fig. 2). A hydrostatic stress regime ($\sigma_H = \sigma_v = 1.0 \text{ MPa}$) is adopted, excluding anisotropic in-situ stress effects. The injection rate is set to $q = 5 \text{ ml/min}$ with injection fluid dynamic viscosity of $1 \text{ mPa}\cdot\text{s}$. Fracture propagation regime is detected by an Acoustic Emission (AE) monitoring device (Fig. 2).

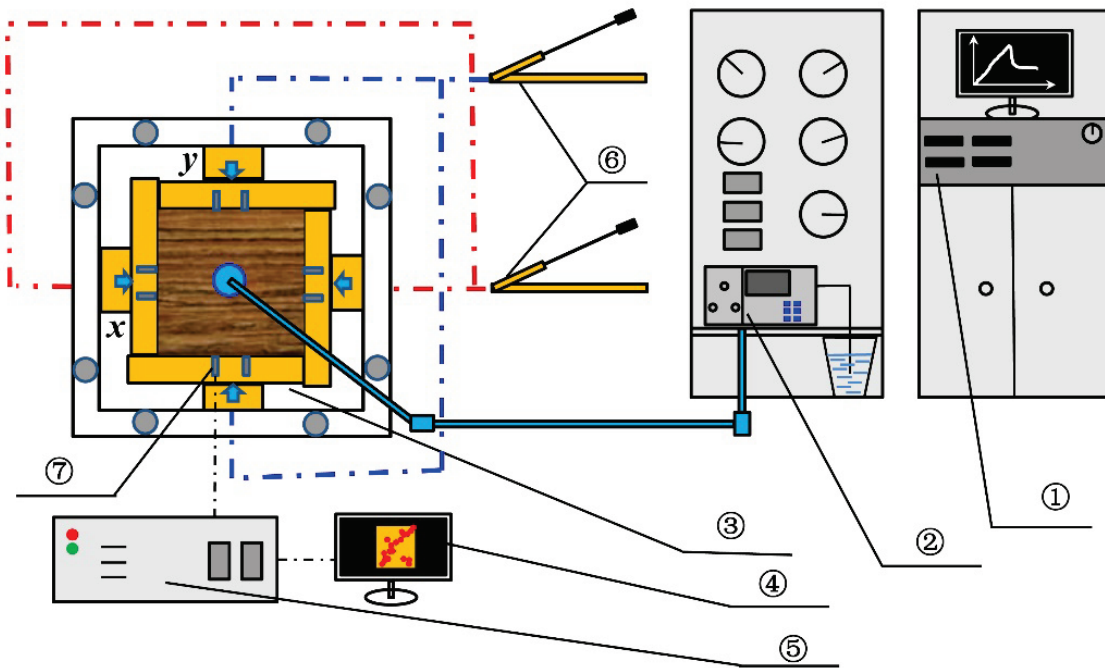


Fig. 2. Schematic diagram of the device for hydraulic fracturing experiment with AE monitor, where ① - computer for recording data; ② - injection pump; ③ - biaxial loading apparatus; ④ - computer for AE location record; ⑤ - AE monitoring apparatus; ⑥ - manual hydraulic pump; ⑦ - AE sensors.

2.2 Observations after hydraulic fracturing performance

Fracturing results of the shale specimen are shown as Fig. 3. As the shale specimen is heterogeneous and anisotropic due to the pre-existing beddings, the induced fracture propagation trajectories would be stochastic and unexpected, analogous findings can be seen at Zhou et al. (2018). Particularly because of the weak interfaces divided by beddings, which are easily to be opened by fluid pressure, thus producing fractures with an distance offset from the injection wellbore (Figs. 3b – 3d). The pump pressure first increases slowly with injection time until it skyrockets to the breakdown pressure at time of 1.89 min, where the acoustic emission energy reaches its maximum simultaneously (Fig. 3e). Followed are drastic decreases of both the pump pressure and acoustic emission energy, reflecting the apparent brittle failure characteristics and a sudden failure during fracturing. The higher breakdown pressure of shale demonstrates the compact and ultra-low permeability properties, from the perspective of hydraulic fracturing effectiveness. The brittleness of shale is so apparent that it leads to observed fracture complexity. The projection of scattered AE events on the horizontal plane shows a similar pattern in comparison with induced hydraulic fractures (Fig. 3d and 3f), where hydraulic fractures aggregate mostly in one side of the specimen within the oxy plane. Accordingly it can be seen by aligning all AE location projections with blue lines. The density of the lines reflects the fracture and/or damage distributions within the specimen in the horizontal plane, which present the analogous fracture evolution by preliminary crack depiction just after hydraulic fracturing (Fig. 3d).

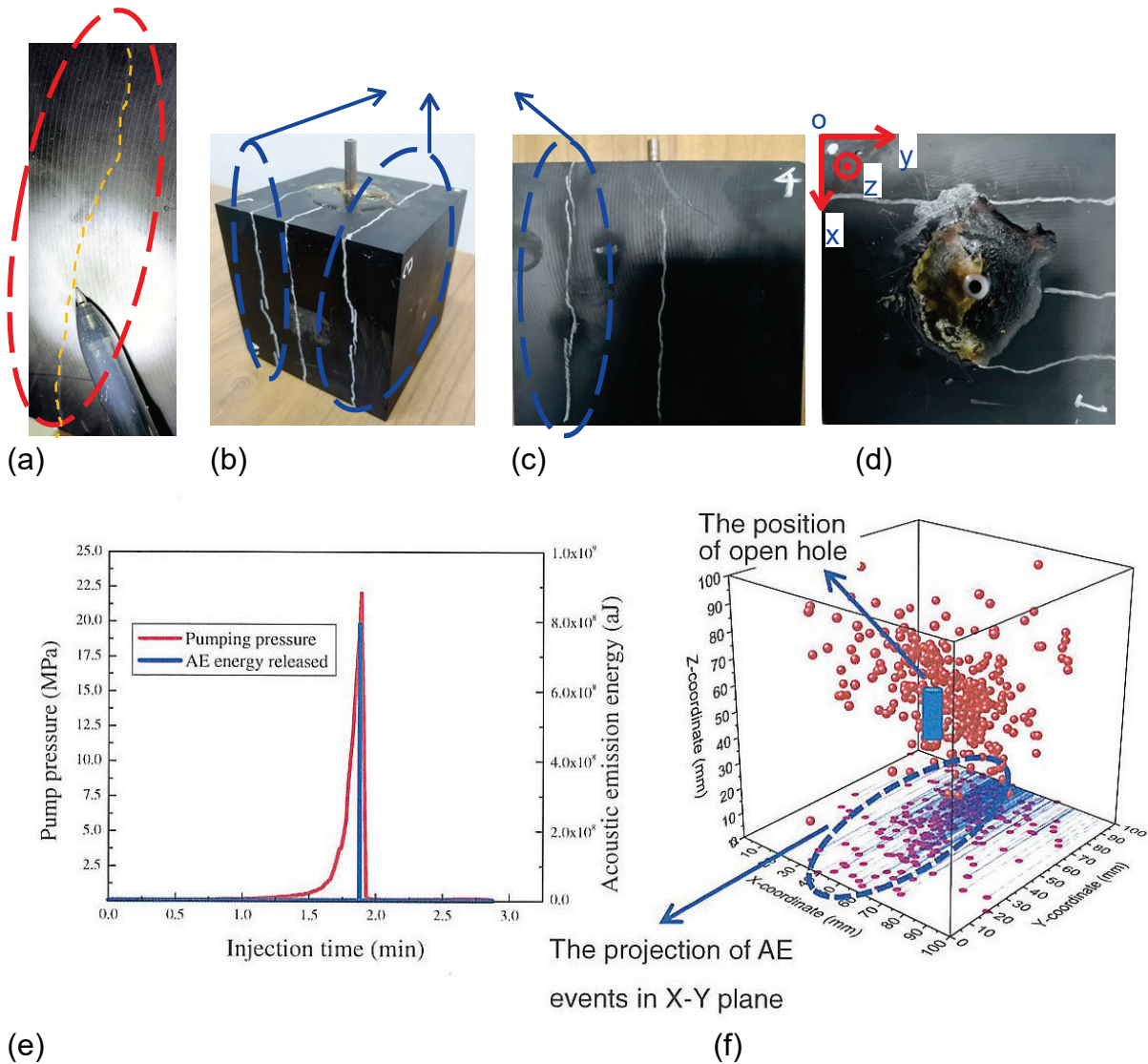


Fig. 3. Fracturing response of the shale specimen with beddings, where the AE location is based on the Cartesian coordinate seen as (d) and (f).

Even though the *in-situ* stresses adopted are hydrostatic stress in which situation all directions are possible for fracture propagation, hydraulic fractures have a predominant direction for propagation (i. e., the direction along the bedding plane). Discontinuous beddings with relatively lower mechanical strengths while the higher hydraulic conductivity and permeability than shale matrix, are beneficial for the pressurized fluid transmission, thus promoting hydraulic fractures propagation.

The X-ray Computed tomography (CT) technology could be used to provide inner structure evolution of shale, without triggering any further disruption or damage. In this study, the shale specimen is subjected to CT scanning after hydraulic fracturing, and the schematic of slice design is shown in Fig. 4a, where slice photos are produced along *oxy* and *oxz* planes and thus the fracture propagation morphologies can be detected. Initially 1500 sliced layers are set both along *y* (layers parallel to *oxz* plane) and *z* (layers parallel to *oxy* plane directions, among which 1099 layers parallel to *oxy* plane, and 1161 layers parallel to *oxz* plane are selected respectively. It can be seen that the slice photo reflect the propagation of hydraulic fractures mainly along the bedding

plane direction (compare Fig. 3d with Fig. 4b, and Fig. 3c with Fig. 4c). Fracture pattern in the central part of the specimen is different from that on the surface, when comparing the direct experimental results (Fig. 3d) with CT scanning results (Layer 550 in Fig. 4b and Layer 581 in Fig. 4c). Only partial fractures can be seen in the middle of specimen and in areas vicinity to wellbore on specimen surfaces, whereas penetrated fractures are found in the middle of specimen, which means that hydraulic fractures formed in inner parts of specimen have different morphology to those formed in specimen surfaces.

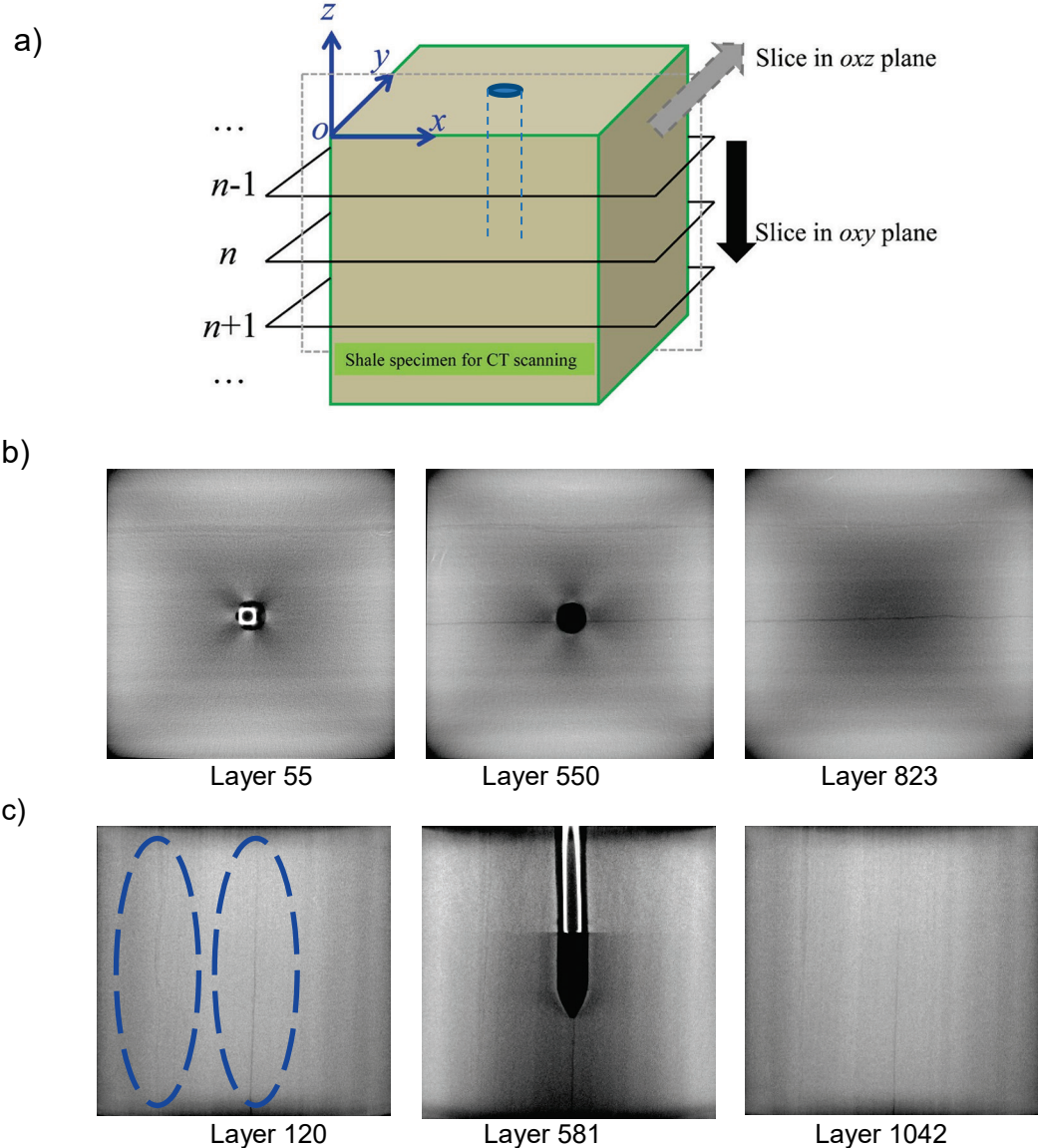


Fig. 4. The CT scanning of the shale specimen after hydraulic fracturing, along with (a) schematic of slice in two orthogonal directions; (b) sliced photos in oxy plane, where the Layer 550 locates at the center of specimen; (c) sliced photos in oxz plane, where the Layer 581 locates at the center of specimen.

The existence of hydraulic fracture tortuosity is mainly due to that the surfaces of the hydraulic fractures are not continuously developed along the wellbore axis. Similar feature can be seen from the AE location result (Fig. 3f) where more AE counts aggregate in the center of the specimen and in areas close to the open hole, several distances

away from specimen surface. Nonetheless the hydraulic fractures leave similar trajectories both on surfaces and the central part of the specimen, as seen by comparing Fig. 3c with Fig. 4c (Layer 120), on side surfaces perpendicular to shale beddings. Above all, it could be concluded that the three-dimensional hydraulic fracture morphology manifests a larger development length in the xoy plane, while less in the zox plane.

3 Numerical modeling

The discontinuous structures make the configuration of induced hydraulic fractures complicated and unexpected, therefore, numerical simulations on the effect of beddings on the fracture interference during hydraulic fractures are conducted further.

3.1 A coupled stress-seepage-damage model considering beddings

The governing equations of solid equilibrium and seepage continuity are expressed as

$$Gu_{i,ij} + \frac{G}{1-2\nu}u_{j,ji} - \alpha(S_w p_{w,i} + S_{w,i} p_w) + F_i = 0 \quad (1)$$

$$S_w(1-\varphi)\frac{\partial \varepsilon_v}{\partial t} + S_w C_w \varphi \frac{\partial p_w}{\partial t} - \nabla \left[\frac{k_j}{\mu} (\nabla p_w - \rho_w g) \right] = \frac{Q_w}{\rho_w} \quad (2)$$

α is Biot-Coefficient

F_i is body force

g is gravity

ρ_w is water density

where G is the shearing modulus; u is displacement vector; ν is Poisson's ratio; S_w is water saturation; p_w is water pressure; ε_v is volumetric strain; C_w is water compressibility; φ is porosity; k is permeability ($j = m$ for matrix; and $j = f$ for beddings; ρ_w is water density; μ is water viscosity, and Q is the source or sink term. The effective stress is expressed as Eq. (3a) with the supplied saturation term expressed as Eq. (3b), depending on the fluid pressure of a representative element volume (REV).

$$\sigma'_{ij} = \sigma_{ij} + \alpha S_w p_w \delta_{ij} \quad (3a)$$

$$S_w = \begin{cases} 1, & p_w \neq 0 \\ 0, & p_w = 0 \end{cases} \quad (3b)$$

Where δ_{ij} is the Kronecker delta and it equals to 1.0 ($i = j$) or 0 ($i \neq j$). The permeability can be expressed as Eq. (4), considering effects of the damage evolution on the change of seepage properties [9-10].

$$k_j = \begin{cases} k_{m0} \cdot (\varphi_m / \varphi_{m0})^3 \exp(\alpha_{km} D_m), & j = m \\ k_{f0} \cdot (\varphi_f / \varphi_{f0})^3 \exp(\alpha_{kf} D_f), & j = f \end{cases} \quad (4)$$

where α_k is a coefficient reflecting the effect of damage on permeability change ($\alpha_k = 5.0$ in this study), and more details about the relationship, and evolution of permeability with damage can be seen at ^[9-11]. The porosity evolution relates to the volumetric strain as ^[12]

$$\varphi_j = \varphi_{0j} + \Delta\varepsilon_v, (j = m, f) \quad (5)$$

where φ_0 is the initial porosity and $\Delta\varepsilon_v$ is the volumetric strain increment. A uniform distribution is adopted when considering the unequal intervals among beddings expressed as Eq. (6a), by which the random locations of the beddings can be provided.

$$f(x) = \begin{cases} \frac{1}{b-a}, & a < x < b \\ 0, & \text{otherwise} \end{cases} \quad (6)$$

The main input parameters of simulation are listed in Table 1, where the different parameters are specified to matrix and beddings in order to represent the heterogeneity and anisotropy of shale.

Table 1: The primary properties of the model used for fracture interference simulations in shale reservoir.

Parameter	Value	Description
E_m	60 / GPa	Young's modulus of matrix
E_j	0.6 / GPa	Young's modulus of bedding
ν_m	0.2	Poisson's ratio of matrix
ν_j	0.3	Poisson's ratio of bedding
k_{0m}	3.4×10^{-9} / mD	Matrix initial permeability
k_{0j}	3.3×10^3 / D	Bedding initial permeability
φ_{0m}	0.05	Matrix porosity
φ_{0j}	0.3	Bedding porosity
μ	1.0 / mPa·s	Water viscosity

3.2 Model verification to the experimental result

The boundary conditions are specified in accordance with the experimental configurations described above and pre-existing beddings with equal intervals are imbedded in the model, where total number of the beddings is assumed to be 83. Numerical simulation results are shown in Fig. 5. It is found that the fracture propagation keeps similar trend with the laboratory observation, illustrating the feasibility of proposed model on hydraulic fracture.

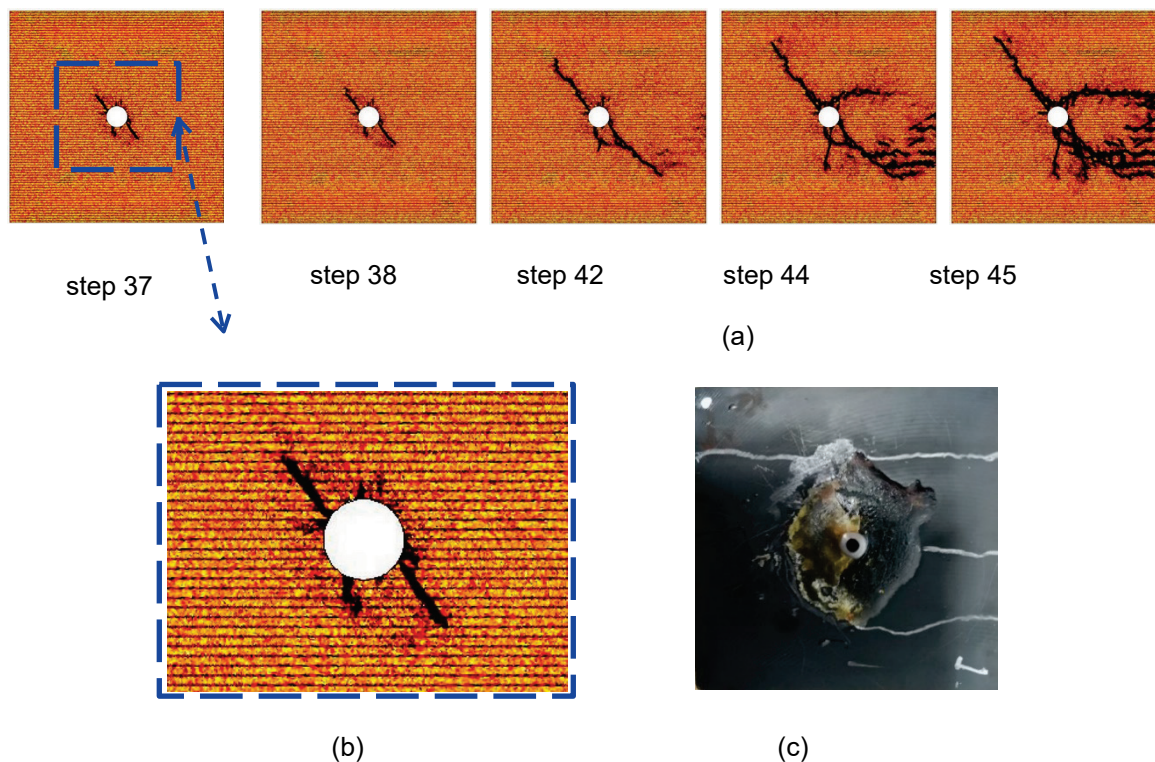
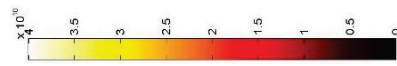
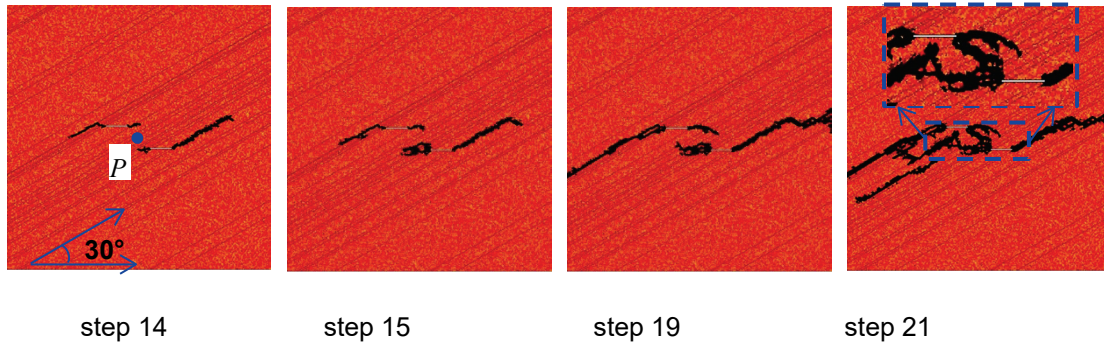


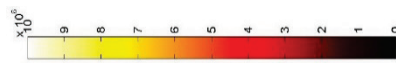
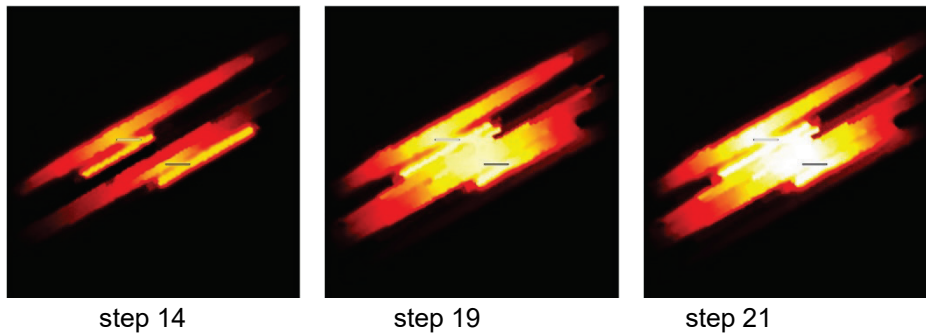
Fig. 5. Model validation with the hydraulic fracturing experiment performed.

3.3 Numerical simulations on fracture interference

A more general scenario where the unequal interval (random locations) among beddings (Eq. (6)) is considered and all beddings are assumed to have an inclination of 30 degree. Two perforations are preset in the model with an initial location offset 5 cm in x direction, and 2.5 cm in y direction, respectively. The *in-situ* stress is 8 MPa in x direction and 4 MPa in y direction, which gives the maximum *in-situ* stress in x direction and the minimum *in-situ* stress in y direction, respectively. Two perforations are fractured simultaneously with a monotonic increase of injection pressure of 0.5 MPa / step, where 1 step represents 3.6 s for seepage process calculation. Fig. 6 shows that at the inner sides of two perforations, hydraulic fractures propagate in opposite directions, and fractures tend to gradually deviate from the maximum *in-situ* stress direction (x -axis), forming a mutual “attraction” and “twining” propagation manner (step 21). Inclined beddings dominate the direction of fracture propagation outside the center perforated regions, due to the weak mechanical while high permeable properties of the beddings as detected in the laboratory work. As for the relatively high permeability of beddings compared to matrix, the profile of water pressure distribution is determined by the bedding configurations to a large degree, which also validates the diverting effects of beddings on the fracture propagation directions.



(a) Elastic modulus (Pa)



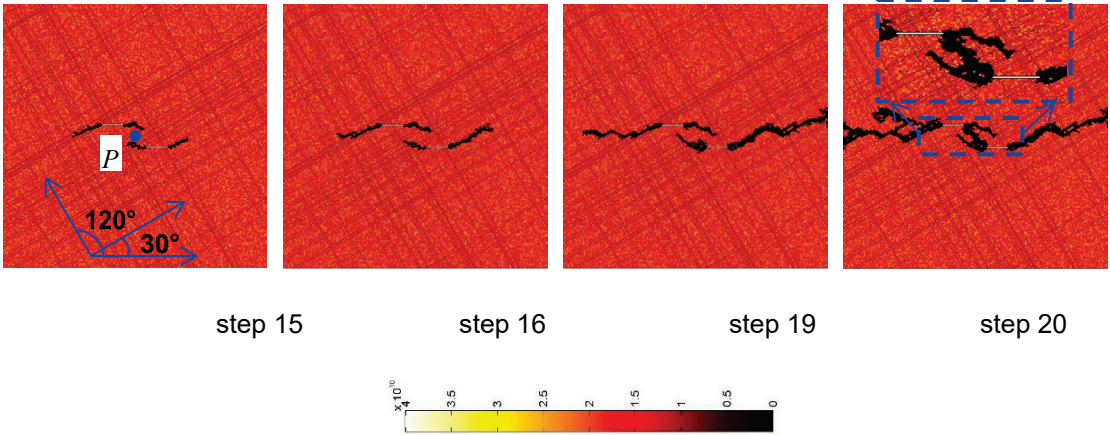
(b) Water pressure (Pa)

Fig. 6. Fracture interference in shale reservoir with beddings of 30 degree inclination.

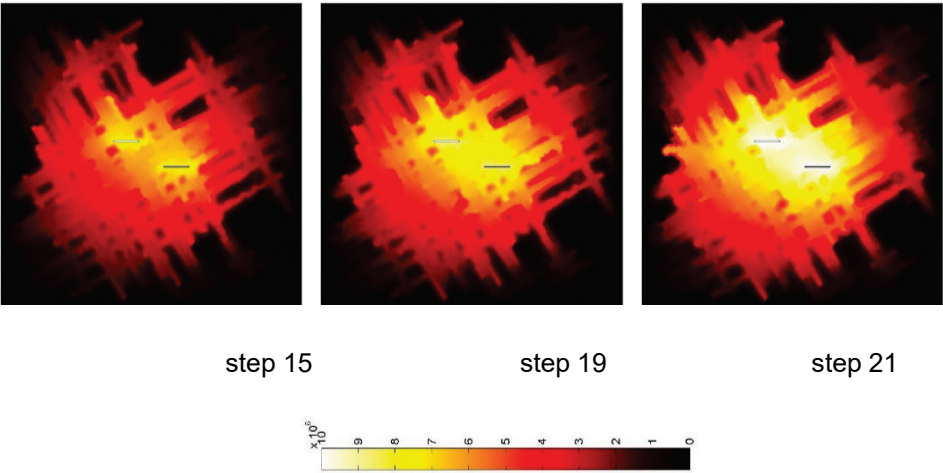
Another numerical simulation gives two groups of mutually orthogonal beddings with 30 and 120 inclination degrees, respectively (Fig. 7). It can be seen that the beddings obvious affect the fracture propagation paths, but the overall formation of the fracture interference remains in the “attraction” and “twining” manners at inner sides of two perforations.

For a discussion of the *in-situ* stress change in the area between two perforations, a point *P* is labeled at center of the model amid two perforations (Figs. 6a and 7a), in order to give the evolution of the local stress (i.e., σ_{xx} , σ_{yy}) evolution that ultimately guides the fracture propagation, as shown in Fig. 8. The positive stress contrast means that the *in-situ* stress reversal occurs at the model center, leading to the diversion of hydraulic fractures from the expected path in original maximum *in-situ* stress direction (x), to the original minimum *in-situ* stress direction (y). The change of *in-situ* stress leads to the consistent propagation reorientation of fractures as shown in Figs. 6 and 7. The contrast of *in-situ* stress is a quantitative estimation of the *in-situ* stress reorientation, which determines the fracture propagation direction. More distinct fracture propagation diversion and fracture complexity were found in scenario of one group of

beddings (Fig. 6), than that of two groups (Fig. 7), which can be directly understood by comparing the changes of in-situ stress contrast of two cases with injection time, shown as Fig. 8, where stress contrast shows more larger positive values in Fig. 8a than that in Fig. 8b. It was attributed to a single predominant bedding direction that can divert and attract the hydraulic fracture propagation, whereas two sets of mutually orthogonal beddings would compensate this bedding predominance as seen overall.



(a) Elastic modulus (Pa)



(b) Water pressure (Pa)

Fig. 7. Fracture interference in shale reservoir with two groups of orthogonal beddings with 30 and 120 inclination degrees, respectively.

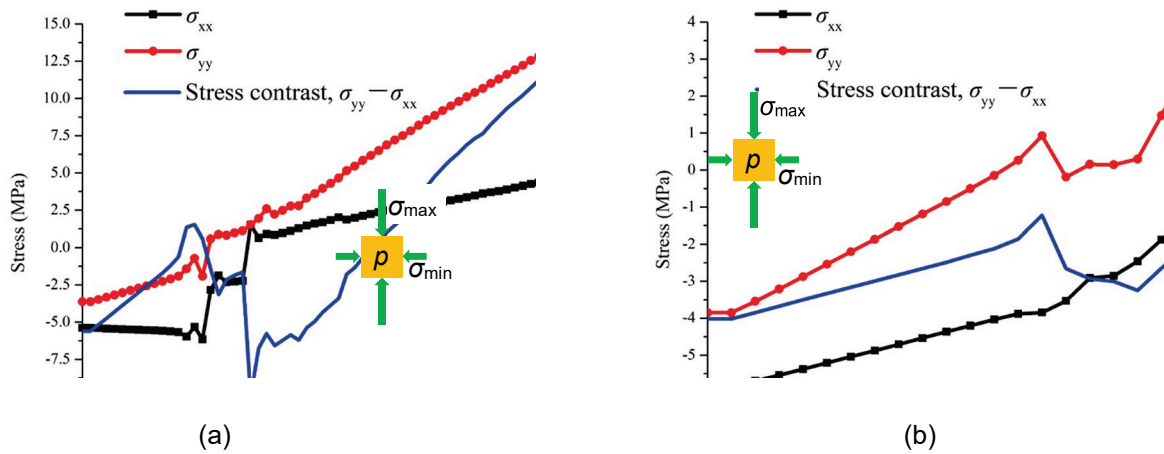


Fig. 8. In-situ stresses (σ_{xx} , σ_{yy}) reversal at point P in center of model in accordance with (a) Figs. 6, and (b) Fig. 7.

4 Conclusions

Fracture interference during hydraulic fractures influences reservoir stimulations, due to the unexpected fracture propagation re-orientations. The experimental results indicated that the pre-existing beddings in shale have apparent influences on the paths of the hydraulic fractures.

Numerical models reflecting multiple fracture interference during hydraulic fracturing are proposed, which are favorably compared with the laboratory works performed on hydraulic fracturing of shale specimen with beddings. Following numerical simulations demonstrate the existence of the mutual interference phenomena among induced fractures, and the obvious effects of beddings on the fracture reorientation during fracturing. The morphology of the beddings determines the hydraulic fracture propagation direction to a large degree, thus reflecting the interference of the multiple fractures.

The mutual “repelling” and “twining” behavior among fractures have been revealed through the numerical simulations, in which the effect of *in-situ* stress is also quantified when it may co-exist with the fracture interference effects.

5 Acknowledgements

This work is supported by the National Natural Science Foundation of China (Grant Nos. 51761135102, 51525402 and 51879041); the National Key Research and Development Program of China (Grant No. 2016YFC0801607) and the Fundamental Research Funds for the Central Universities of China (Grant Nos. N2001034, N180115009). And this work is also part of a joint DFG-NSFC project “PermGas” between the Center for Rock Instability and Seismicity Research, Northeastern University, Shenyang, PR China, and the Chair of Rock Mechanics at the Technical University Freiberg, Germany. These supports are gratefully acknowledged.

6 References

- [1] Bunger AP, Jeffrey RG, Zhang X. Constraints on simultaneous growth of hydraulic fractures from multiple perforation clusters in horizontal wells. SPE Hydraulic Fracturing Technology Conference. The Woodlands, Texas, USA. 2013; 1-17.
- [2] Cheng C, Bunger AP. Reduced order model for simultaneous growth of multiple closely-spaced radial hydraulic fractures. *Journal of Computational Physics*. 2019;376:228-48.
- [3] Tang JZ, Wu K, Zeng B, Huang HY, Hu XD, Guo XY, et al. Investigate effects of weak bedding interfaces on fracture geometry in unconventional reservoirs. *Journal of Petroleum Science and Engineering*. 2018;165:992-1009.
- [4] Kresse O, Weng XW, Gu HR, Wu RT. Numerical modeling of hydraulic fractures interaction in complex naturally fractured formations. *Rock Mechanics and Rock Engineering*. 2013;46:555-68.
- [5] Rabaa WE. Experimental study of hydraulic fracture geometry initiated from horizontal wells. SPE Annual Technical Conference and Exhibition. San Antonio, Texas. 1989.
- [6] Crosby DG, Rahman MM, Rahman MK, Rahman SS. Single and multiple transverse fracture initiation from horizontal wells. *Journal of Petroleum Science and Engineering*. 2002;35:191-204.
- [7] Tan P, Jin Y, Hou B, Zhou YC, Zhang RX, Chang Z, et al. Laboratory investigation of shale rock to identify fracture propagation in vertical direction to bedding. *Journal of Geophysics and Engineering*. 2018;15:696-706.
- [8] Zhou J, Zeng YJ, Jiang TX, Zhang BP. Laboratory scale research on the impact of stress shadow and natural fractures on fracture geometry during horizontal multi-staged fracturing in shale. *International Journal of Rock Mechanics and Mining Sciences*. 2018;107:282-7.
- [9] Zhu WC, Gai D, Wei CH, Li SG. High-pressure air blasting experiments on concrete and implications for enhanced coal gas drainage. *Journal of Natural Gas Science and Engineering*. 2016;36:1253-63.
- [10] Zhu WC, Wei CH, Li S, Wei J, Zhang MS. Numerical modeling on destress blasting in coal seam for enhancing gas drainage. *International Journal of Rock Mechanics and Mining Sciences*. 2013;59:179-90.
- [11] Yu YJ, Zhu WC, Li LC, Wei CH, Yan BX, Li S. Multi-fracture interactions during two-phase flow of oil and water in deformable tight sandstone oil reservoirs. *Journal of Rock Mechanics and Geotechnical Engineering*. 2020;12:821-49.
- [12] Tan X, Konietzky H, Frühwirth T. Experimental and numerical study on evolution of Biot's coefficient during failure process for brittle rocks. *Rock Mechanics and Rock Engineering*. 2014;48:1289-96.

Experimental approaches into process understanding and characterization of georeservoirs - Preliminary results of the GREAT cell poliaxial facility

Experimente zum Prozessverständnis und zur Charakterisierung von Georeservoiren – Erste Ergebnisse von der mehraxialen GREAT-Apparatur

M. Sauter¹, M. Fazio¹, A. P. Fraser-Harris², C. I. McDermott², G. D. Couples³,
A. Lightbody² and T. Frühwirt⁴

¹ Department of Applied Geology, Geoscience Centre of the University of Göttingen, Goldschmidtstraße 3, 37077 Göttingen, Germany.

² School of Geosciences, University of Edinburgh, James Hutton Road, Edinburgh EH9 3FE

³ Institute for Geoenergy Engineering, Heriot Watt University, Edinburgh, EH14 4AS

⁴ Institut für Geotechnik, TU Bergakademie Freiberg, Gustav-Zeuner-Straße 1, 09599 Freiberg, Germany

Abstract

Theoretically accessible everywhere in the world, geothermal energy is one of the most important renewable and sustainable sources of energy. Yet its contribution to the total energy production is low. This is caused by a combination of relatively high drilling costs and potential environmental impacts, particularly the interaction between the injected fluids and the fractured porous rocks, typical of geothermal reservoirs.

To understand this interaction in simulated complex and changing in-situ conditions, crucial for the exploitation of potential geo-reservoirs, a novel Geo-Reservoir Experimental Analogue Technology (*GREAT*) cell has been developed by the collaboration between the University of Göttingen, the University of Edinburgh and Heriot Watt University.

The *GREAT* cell can perform poliaxial experiments, simulating depth up to 5 km in the crust and temperature up to 120°C, on large cylindrical samples (up to 250 mm in diameter), de-facto closing the gap between small scale laboratory and large field scale testing. To approach real conditions during hydraulic fracturing in fractured material, the *GREAT* cell is equipped with a standalone capability: the rotation of horizontal stress via a series of 8 pair of cushions positioned around the sample. This allows the simulation of stress re-orientation observed during the fracturing process.

State-of-the-art fiber optic and Acoustic Emission (AE) monitoring systems allow us to acquire radial strain and microseismic data at high-sampling frequency.

Currently, two *GREAT* cells have been envisioned: a fully operational machine is at the University of Edinburgh, while a second apparatus, at the University of Göttingen, is under construction and should be operative in winter 2020/2021.

Preliminary experiments on both artificial and natural materials shows that this state-of-the-art machine is capable of recreating a variable, poliaxial state of stress on a bench-scale sample, which is validated by numerical simulations.

Zusammenfassung

Theoretisch verfügbar weltweit, ist geothermische Energie eine der erneuerbarsten und nachhaltigsten Energiequellen. Ihr Gesamtbeitrag zur Energiegewinnung ist aber gering. Dies ist bedingt durch die Kombination von relativ hohen Bohrkosten und potentiellen Einwirkungen auf die Umwelt, insbesondere bedingt durch die Interaktion zwischen injiziertem Fluid und geklüftetem porösem Gestein, welches typisch für Geothermiereservoire ist. Um die Interaktion in simulierten komplexen und sich verändernden in-situ Bedingungen zu verstehen, wurde eine neuartige "GEO-Reservoir Experimental Analogue Technology (GREAT)" entwickelt durch Kooperation zwischen der Universität Göttingen, der Universität von Edinburgh und der Heriot Watt Universität. Mit der GREAT-Zelle kann man polyaxiale Experimente, die Teufen in der Erdkruste bis 5 km und Temperaturen bis 120°C simulieren, an großen zylindrischen Proben (bis 250 mm im Durchmesser) durchführen. Damit kann de-facto die Lücke zwischen kleinskaligen Laborversuchen und großen Versuchen in-situ geschlossen werden. Um reale Bedingungen wie beim hydraulischen Aufreißen im geklüfteten Gestein zu erreichen, ist die GREAT-Zelle mit einer einzigartigen Möglichkeit ausgestattet: der Rotation der horizontalen Spannungen durch eine Reihe von 8 Kissen positioniert rund um die Probe. Dies erlaubt die Simulation von Spannungsumorientierungen, wie sie beim Aufreißprozess beobachtet werden. Glasfaseroptische und seismoakustische Sensorik auf allerneuestem Stand erlauben es, radiale Dehnungen und mikroseismische Ereignisse mit hoher Abtastrate aufzunehmen. Gegenwärtiger Stand der GREAT-Zelle ist folgender: eine voll funktionsfähige Maschine arbeitet an der Universität von Edinburgh, eine zweite Maschine an der Universität von Göttingen befindet sich im Aufbau und soll im Winter 2020/2021 in Betrieb gehen. Vorläufige Experimente an künstlichen und natürlichen Materialien zeigen, dass diese hochmoderne Maschine in der Lage ist, variable polyaxiale Spannungen auf Proben im Labormaßstab aufzubringen, was durch numerische Simulationen validiert wurde.

1 Introduction

A geothermal reservoir is an underground, permeable rock body which provides heat to circulating fluids. The high temperature condition is a result of the Earth's internal heat (but temperature can be further increased by the proximity of a magmatic body) and therefore is ubiquitous in the Earth's crust, making geothermal energy a renewable and sustainable source of energy potentially accessible everywhere in the world. The other two characteristics of a geothermal reservoir, namely a permeable rock body and circulating fluids, can be either already existing or alternatively created through hydraulic fracturing and stimulation. In the latter case, pressurized fluids are injected into hot rocks with low permeability to generate fracture networks, hence improving permeability and fluid contents. This is an Enhanced Geothermal System (EGS).

Despite the high potential, the contribution of geothermal energy to the total energy production is marginal, particularly when compared with other renewable sources. In fact, in 2017, its worldwide contribution to the gross electricity generation and gross heat production is 1.4 % and 3.6 % respectively (IEA, 2020). There are a couple of reasons behind this: drilling costs and environmental impacts. Although a similar drilling technique is at the base of both fossil fuel and geothermal field exploitation, costs are covered over the entire productivity range for the former, while only (few) high-flow wells can do so for the latter. In addition to this, the estimation of flow structures at adequate spatial resolution is problematic (Leary et al., 2020). Also, the injection of pressurized fluids and the fracturing of the reservoir rock are not harmless. High noise levels, solid waste disposal, surface water underground, thermal and chemical pollution, induced seismicity are all effects associated with geothermal exploitation (Dickson and Fanelli, 2003). In particular, induced seismicity can occasionally reach magnitudes up to 4-5 and had already caused suspension of EGS projects (e. g. Basel Deep Heat Mining project, Switzerland, Majer et al., 2007). It is therefore clear that to expand the geothermal contribution in electricity and heat production, a better characterization of EGS as well as the reduction of environmental impacts is necessary.

With EGSs, a series of challenges must be investigated. These include: i) fluid flow through fracture networks in highly stressed rocks, ii) rock-fluid thermal, mechanical, hydraulic, chemical and biological (TMHCB) coupled processes and iii) their effects on fluid flow and induced seismicity (Tomic and Sauter, 2018). Laboratory experiments have proven to be invaluable resources to better understand sub-surfaces processes in a quantitative way, as they allow the simulation of complex and dynamic *in-situ* conditions for cracks and fractures typical of georeservoirs.

With the increased interests in alternative, renewable and sustainable energy sources in the last 20 years (following the Kyoto Protocol in 1997) to reduce greenhouse gas, so the experimental studies on geothermal reservoir enhancement techniques also experienced a boost. It has been noticed that the geometry of the hydraulic fractures is controlled by the viscosity of the injected fluid (Chen et al., 2015; Ha et al., 2018; Ishida et al., 2016, 1998; Stanchits et al., 2014) and by rock heterogeneities (e.g. bedding planes, pre-existing cracks, hard grain; Chitralla et al., 2011; Ha et al., 2018; He et al., 2016; Molenda et al., 2015; Renard et al., 2009; Stoeckhert et al., 2015). Permeability of the rock material is increased by the formation of shear fractures, rather than tensile ones (Chitralla et al., 2013), whose generation also depends on fluid viscosity and rock structure (Hampton et al., 2014; Ishida et al., 2016). Paramount to

increase the stimulated reservoir volume (SRV) is the reduction of fluid leak-off through the rock matrix, particularly relevant for porous and permeable materials or in the presence of fractures intersecting the borehole. This can be avoided by either the employment of an impermeable jacket isolating the borehole (e.g. Brenne et al., 2013; Vinciguerra et al., 2004) or by increasing the injection rate/pressurization rate (Diaz et al., 2016; Song et al., 2001; Zhuang et al., 2018). However the drawback of this is the increase of the breakdown pressure up to 6 times when compared to unjacketed samples, which in turn leads to higher AE activity (Stoeckhert et al., 2014). In general, however, precursory AE activity is short (Vinciguerra et al., 2004), making reliable forecasting models difficult to make.

Despite these efforts, the majority of the experiments were performed at room temperature, with pressure conditions representative of maximum 2 km depth and principal stresses kept constant throughout the test. These conditions are hardly representative of an EGS scenario (Dempsey, 2020; Folesky et al., 2016; Majer et al., 2007; Pruess, 2006; Sausse et al., 2008; Zimmermann et al., 2010). Stress rotation has been observed and modeled in the damage zone of faults and fractures (Diederichs et al., 2004; Faulkner et al., 2006; Healy, 2008; Lin et al., 2010), but it has been simulated in a small cylindrical sample (38 mm wide and 76 mm long) only with the SMART cell (Crawford et al., 1995; McDermott et al., 2018; Smart et al., 1999). Large sample size in true triaxial conditions (> 0.1 m), allowing a clear investigation of a fracture network, is usually associated with cubic sample, which requires specialist preparation and handling equipment, and presents issues of stress concentration at the sample edges (McDermott et al., 2018). In addition, AE data has been only analysed in the time-domain in the above-mentioned experiments. Analyses in the frequency-domain can reveal important information about fracture size (Benson et al., 2008; Burlini et al., 2007) and fluids involved (Fazio et al., 2017).

To overcome these issues, the GREAT cell (Geo-Reservoir Experimental Analogue Technology) has been designed and manufactured by combining the SMART cell concept with further technological advance, allowing a larger sample size, more sample displacement and higher loading (McDermott et al., 2018). Thanks to the unique features of the GREAT cell, it is possible to not only characterize and understand the underlying processes of geothermal systems, but also of other significant georeservoirs, such as nuclear waste repositories and CO₂ storage sites.

2 The GREAT cell

Closing the bridge between standard laboratory (up to 100 mm) and field scale, the GREAT Cell allows the simulation of shallow crustal conditions on bench-scale cylindrical samples. Two apparatuses are designed and located respectively at the University of Edinburgh (UoE) and at the University of Göttingen (UoG).

The UoE GREAT cell (Fig. 1) can simulate axial and radial stresses up to 100 MPa, pore pressures up to 40 MPa and temperatures up to 100°C on a 200 mm x 200 mm sample (McDermott et al., 2018). The UoG GREAT cell (also called GREAT cell – 2) can host a larger sample (250 mm x 250 mm) and reproduce axial stresses up to 200 MPa, radial stresses and pore pressures up to 100 MPa, temperatures up to 120°C.

The unique feature of the GREAT cell is the simulation of poliaxial conditions on a cylindrical sample and the rotation of the horizontal stresses. This is achieved through eight pairs of fluid-filled soft cushions (made of Viton in UoE and silicon in UoG), called Pressure Exerting Elements (PEEs). The PEEs are servo-controlled by pumps keeping the symmetrical identical pressures on opposite side of the sample. Dynamic Sealing Strips ensure that one PEE does not influence the pressure in a neighbouring one (McDermott et al., 2018).

To simulate hydraulic fracturing and stimulation, a separate servo-controlled pump injects fluids through a central borehole drilled in the sample. A second port, located at a radius of 50 mm, can be used for re-injection to assess the effect of stresses' rotation and the interaction with the previously generated hydraulic fracture. Electro-resistance heating bands are placed circumferentially around the cell body, providing the desired heat and controlling the temperature (McDermott et al., 2018).

Both apparatuses are equipped with distributed optical fibre sensing (DOFS) to measure the radial strain directly on the sample surface and with Acoustic Emission (AE) systems to monitor AEs and P-wave velocities. The recording of high resolution radial strain through DOFS is ensured by ODiSI-B, produced by LUNA Inc. (Gifford et al., 2007), while the AE system, both hardware and software, is provided by ITASCA Consulting Ltd (Fazio, 2017).

2.1 Materials and experimental procedure

Artificial samples (thermoplastic polymer and polyester resin) were used in the first experiments aimed to validate the experimental data against the numerical simulations modelling the effect of a rotating horizontal stress field on either an intact sample (M1) or fractured samples undergoing fracture fluid flow (HM1 & HM2, McDermott et al., 2018). A further experiment on a fractured Freiberg Grey gneiss (FG, Germany) is performed to investigate fracture permeability under a variable stress field. Samples HM1, HM2 and FG were first hydraulic fractured in a uniaxial apparatus and later placed inside the GREAT cell.

Once inside the GREAT cell, all samples were initially vertically loaded, followed by the application of equal radial confining pressure and then the creation of a poliaxial stress field (Table 1). Apart from M1, all other samples experienced fluid flow at different flow rate and downstream pressure (McDermott et al., 2018).

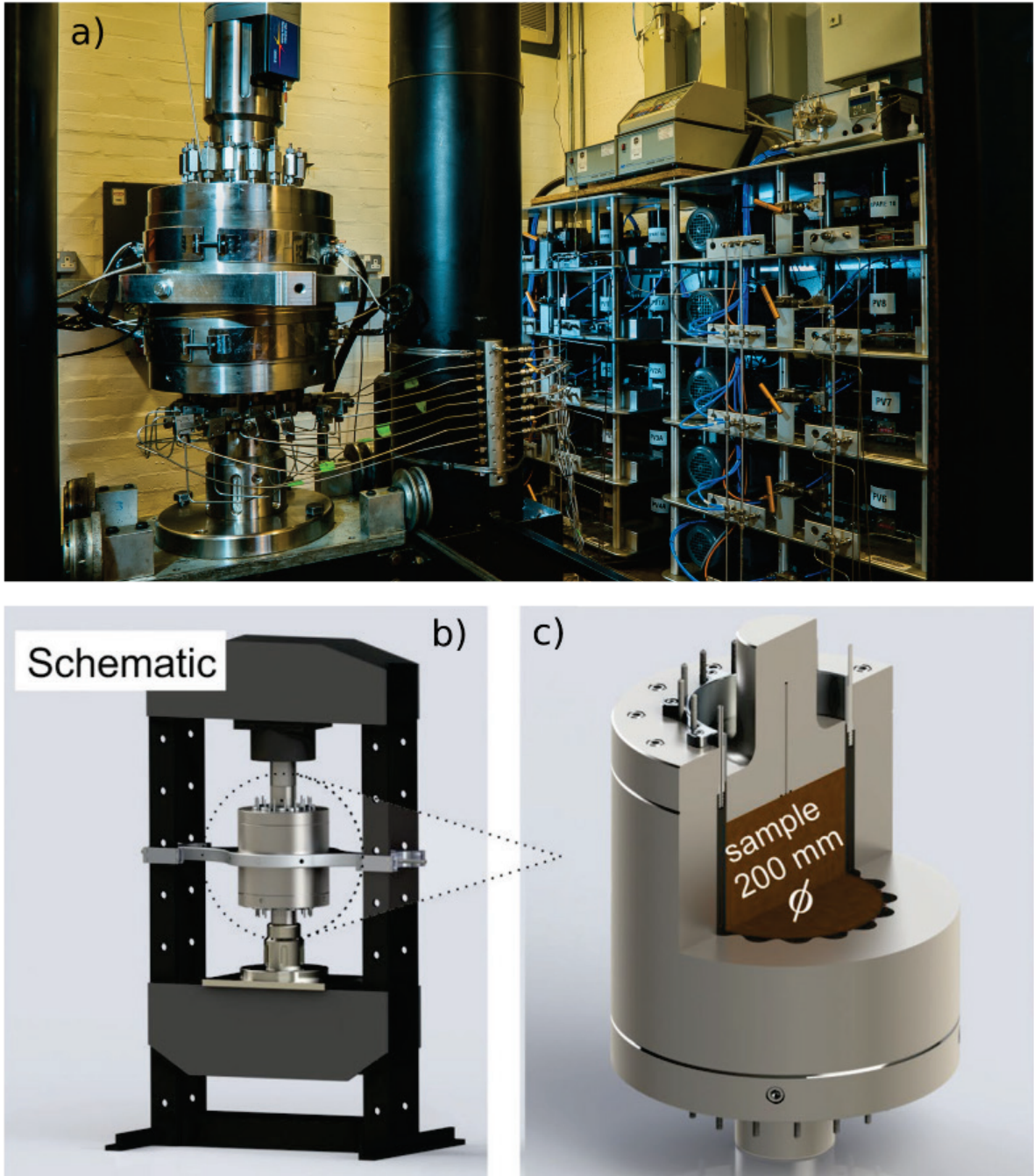


Figure 1: a) the UoE GREAT cell, including pumps and piping. b) Schematic of the cell – frame assembly. c) Schematic of the internal design of the GREAT cell. Modified from McDermott et al., 2018.

Table 1: Stress state field for all experiments

Sample name	Type	σ_1 (MPa)	σ_2 (MPa)	σ_3 (MPa)
M1	thermoplastic polymer, Intact	8.2	8	2
HM1	polyester resin, fractured	10	8	2
HM2	polyester resin, fractured	10	8	2
FG	Freiberg Grey gneiss, fractured	12	12	6

3 Preliminary results

Here only the preliminary results obtained with the GREAT cell at UoE are shown, as it is currently the only apparatus fully operational, while the Great cell – 2 at UoG is under construction.

As shown in Figure 2a, true-triaxial conditions in the sample volume were almost created in M1 test (and therefore we use the term poliaxial instead of true-triaxial), with the small difference between modelled and measured stress due to the impossibility to apply shear traction on the curved sample. However the measured strain data matched up with the modelled data (Fig. 2b). Similar results in strain were achieved for the fractured sample (HM1 and HM2) as both modelled and measured data detected the surface strain expression of the fracture. In addition, a clear fracture permeability change is observed due to the rotation of horizontal stresses (McDermott et al., 2018).

Figure 3 shows the effect of the fracture on the measured strain in FG as the stress field changes from $\sigma_1 > \sigma_2 = \sigma_3$ to $\sigma_1 = \sigma_2 > \sigma_3$. The fracture is parallel to σ_2 (orientated $0^\circ - 180^\circ$) in Figure 3a and is at 45° (orientated $135^\circ - 315^\circ$) in Figure 3b. In both scenarios, as σ_2 increases the surface strain reveals the opening of the fracture parallel to the intermediate stress (Fig. 3a) and the shearing of the fracture inclined to the intermediate stress (Fig. 3b).

Taken together, these results show the capability of the GREAT cell to re-create reservoir conditions under a variable, poliaxial stress state.

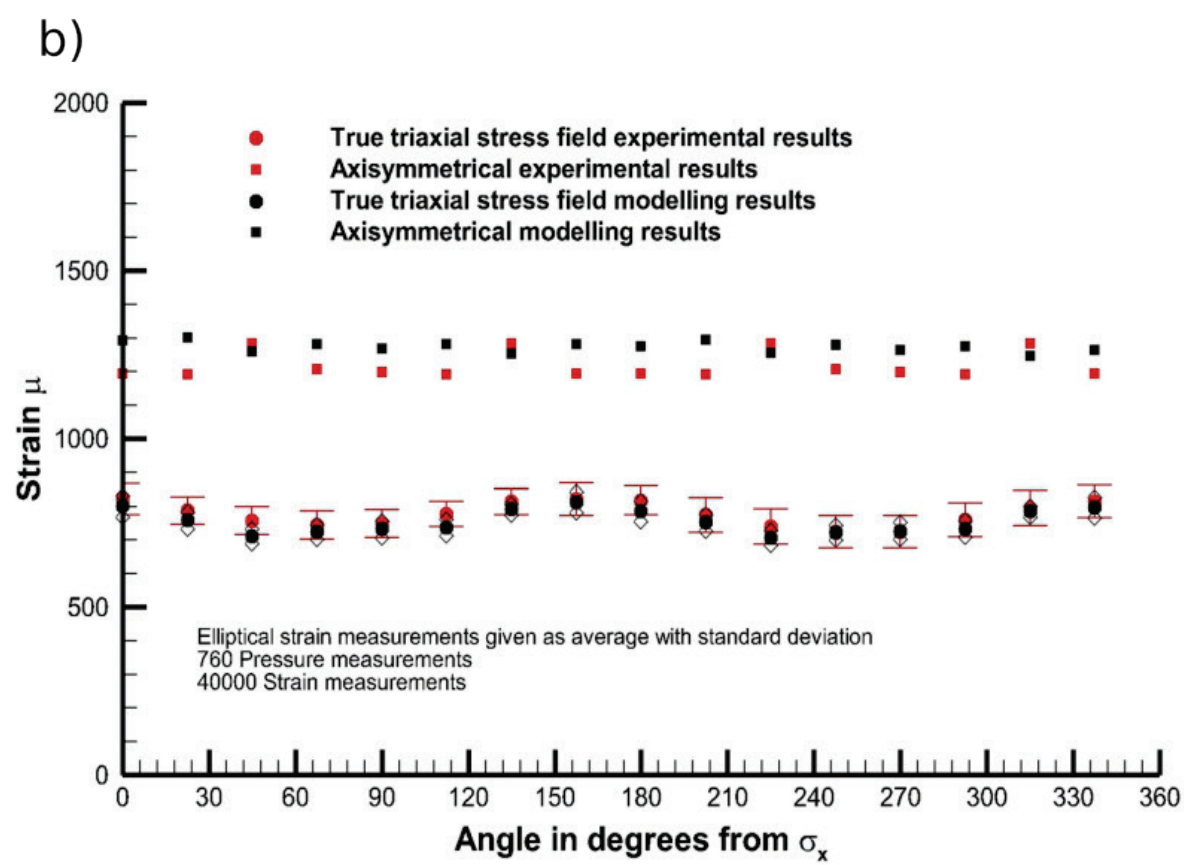
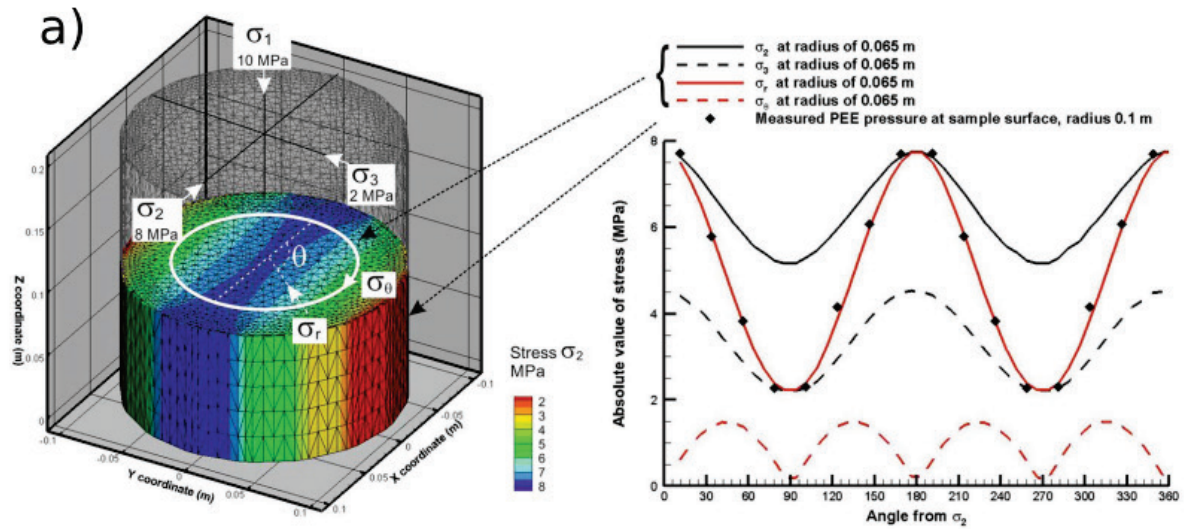
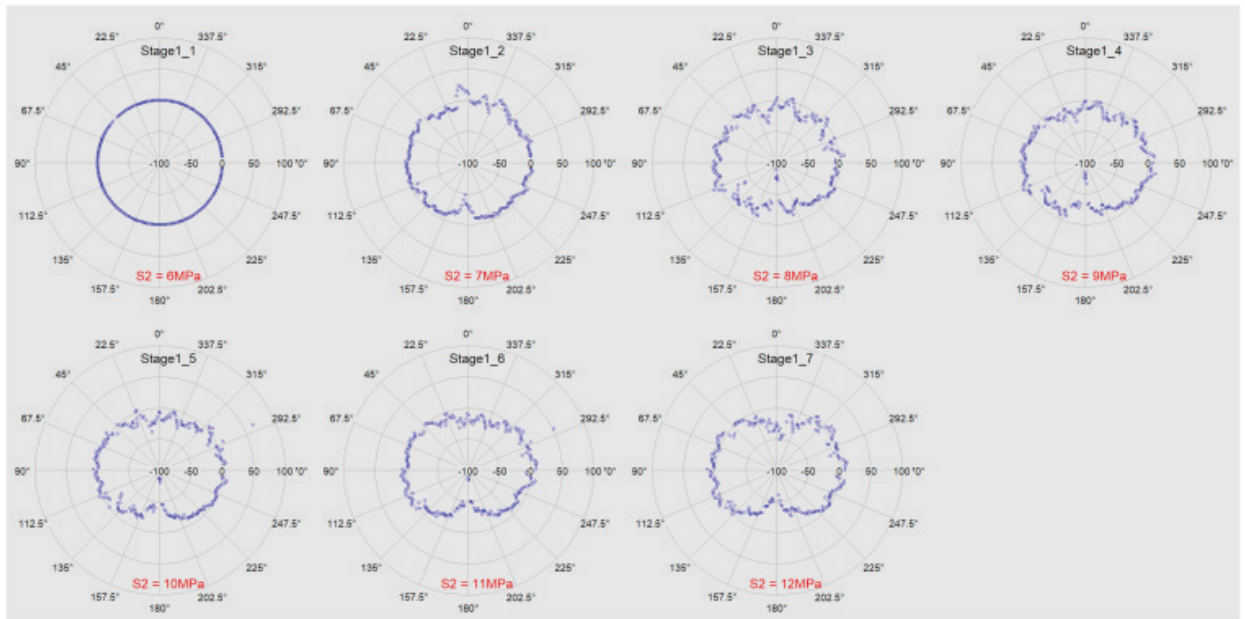


Figure 2: a) Modelled stress field, with graph also showing the PEE measured pressures at sample surface in M1. b) Modelled vs measured strain data in M1. Modified from McDermott et al., 2018.

a)



b)

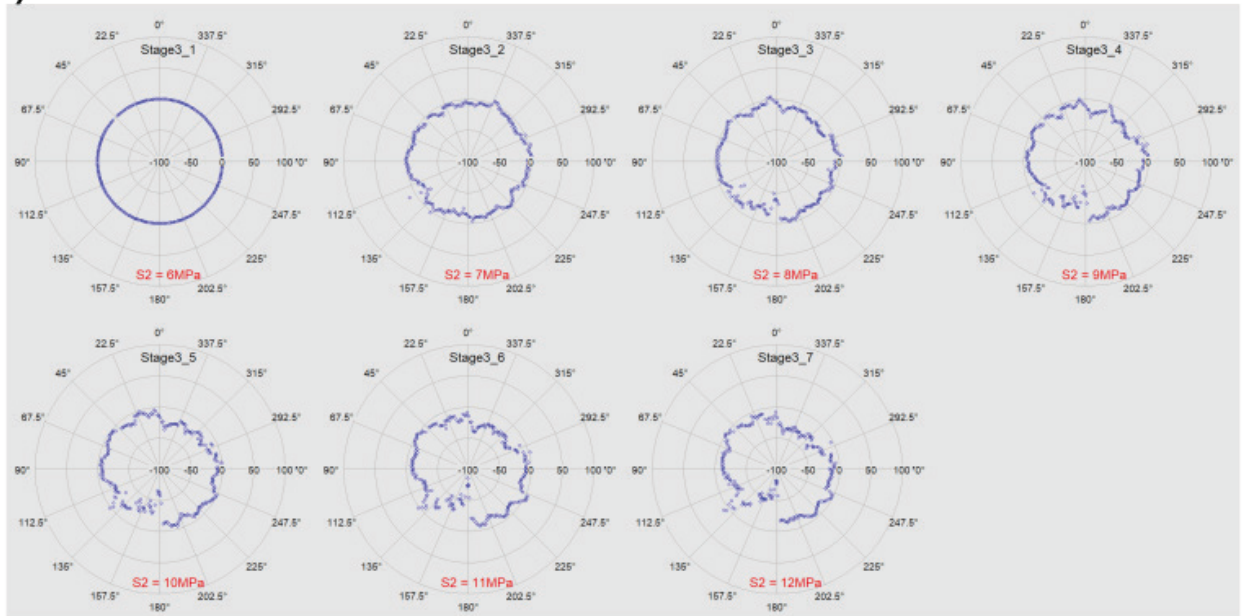


Figure 3: Measured strain in FG as the intermediate stress is increased from 6 (top left) to 12 MPa (bottom right) with fracture parallel (a) and at 45° (b) to σ_2 .

4 Conclusions

With an increased interest in environmental protection, a better understanding of rock-fluid thermal, mechanical, hydraulic, chemical and biological coupled processes is crucial in geothermal energy exploitation, carbon storage and sequestration, nuclear waste repositories. With this in mind, the GREAT cell has been developed to simulate *in situ* conditions representative of up to 5 km deep in the crust, where suitable georeservoirs are mostly located. As never achieved before on a bench-scale sample, the GREAT cell can apply a variable horizontal stress field on a cylindrical sample, recreating the conditions of stress rotation observed near damage zones. The results here presented not only confirmed the numerical simulations but also show how the variable stress field affects the deformation and the permeability of a fractured rock. Considering the gaps observed in the experimental studies, the GREAT cell has the potential to overcome these and to provide paramount data to both the academia and the industry.

5 Acknowledgments

This research was funded by a University of Edinburgh College of Science and Engineering capital equipment grant, internal investment by Heriot Watt University, by the Deutsche Forschungsgemeinschaft (DFG), by the Niedersächsisches Ministerium für Wissenschaft und Kultur (MWK) and by funding from the European Union's Horizon 2020 research and innovation programme.

6 Bibliography

- Benson, P.M., Vinciguerra, S., Meredith, P.G., Young, R.P., 2008. Laboratory Simulation of Volcano Seismicity. *Science* 322, 249–252. <https://doi.org/10.1126/science.1161927>
- Brenne, S., Molenda, M., Stockhert, F., Alber, M., 2013. Hydraulic and Sleeve Fracturing Laboratory Experiments on 6 Rock Types, in: Jeffrey, R. (Ed.), *Effective and Sustainable Hydraulic Fracturing*. InTech, pp. 425–436. <https://doi.org/10.5772/56301>
- Burlini, L., Vinciguerra, S., Di Toro, G., De Natale, G., Meredith, P., Burg, J.-P., 2007. Seismicity preceding volcanic eruptions: New experimental insights. *Geology* 35, 183. <https://doi.org/10.1130/G23195A.1>
- Chen, Y., Nagaya, Y., Ishida, T., 2015. Observations of Fractures Induced by Hydraulic Fracturing in Anisotropic Granite. *Rock Mech. Rock Eng.* 48, 1455–1461. <https://doi.org/10.1007/s00603-015-0727-9>
- Chitralla, Y., Moreno, C., Sondergeld, C., Rai, C., 2013. An experimental investigation into hydraulic fracture propagation under different applied stresses in tight sands using acoustic emissions. *J. Pet. Sci. Eng.* 108, 151–161. <https://doi.org/10.1016/j.petrol.2013.01.002>
- Chitralla, Y., Moreno, C., Sondergeld, C.H., Rai, C.S., 2011. Microseismic and Microscopic Analysis of Laboratory Induced Hydraulic Fractures. Presented at the Canadian Unconventional Resources Conference, Society of Petroleum Engineers. <https://doi.org/10.2118/147321-MS>

- Crawford, B.R., Smart, B.G.D., Main, I.G., Liakopoulou-Morris, F., 1995. Strength Characteristics and Shear Acoustic Anisotropy of Rock Core Subjected to True Triaxial Compression. *Int. J. Rock Mech. Min. Sci. Geomech. Abstr.* 32, 189–200.
- Dempsey, D., 2020. Induced Volcanic Eruptions from Magma Enhanced Geothermal Systems: Theoretical Models, in: *Proceedings World Geothermal Congress*. Reykjavik, Iceland, p. 10.
- Diaz, M.B., Jung, S.G., Zhuang, L., Kim, K.Y., Yeom, S., Shin, H.S., 2016. Effect of cleavage anisotropy on hydraulic fracturing behavior of Pocheon granite, in: *50th US Rock Mechanics/Geomechanics Symposium*. American Rock Mechanics Association, Houston, Texas, USA.
- Dickson, M.H., Fanelli, M., 2003. Geothermal energy: utilization and technology: UNESCO renewable energy series. Earthscan Lond. 205.
- Diederichs, M.S., Kaiser, P.K., Eberhardt, E., 2004. Damage initiation and propagation in hard rock during tunnelling and the influence of near-face stress rotation. *Int. J. Rock Mech. Min. Sci.* 41, 785–812.
<https://doi.org/10.1016/j.ijrmms.2004.02.003>
- Faulkner, D.R., Mitchell, T.M., Healy, D., Heap, M.J., 2006. Slip on “weak” faults by the rotation of regional stress in the fracture damage zone. *Nature* 444, 922–925. <https://doi.org/10.1038/nature05353>
- Fazio, M., 2017. Dynamic laboratory simulations of fluid-rock coupling with application to volcano seismicity and unrest (Doctoral Thesis). University of Portsmouth, Portsmouth (UK).
- Fazio, M., Benson, P.M., Vinciguerra, S., 2017. On the generation mechanisms of fluid-driven seismic signals related to volcano-tectonics: Experiments on Fluid-Induced Seismicity. *Geophys. Res. Lett.* 44, 734–742.
<https://doi.org/10.1002/2016GL070919>
- Folesky, J., Kummerow, J., Shapiro, S.A., Häring, M., Asanuma, H., 2016. Rupture directivity of fluid-induced microseismic events: Observations from an enhanced geothermal system: DIRECTIVITY OF FLUID-INDUCED EVENTS. *J. Geophys. Res. Solid Earth* 121, 8034–8047.
<https://doi.org/10.1002/2016JB013078>
- Gifford, D.K., Kreger, S.T., Sang, A.K., Froggatt, M.E., Duncan, R.G., Wolfe, M.S., Soller, B.J., 2007. Swept-wavelength interferometric interrogation of fiber Rayleigh scatter for distributed sensing applications, in: Udd, E. (Ed.), *Fiber Optic Sensors and Applications*. Presented at the Optics East 2007, Boston, MA, p. 67700F. <https://doi.org/10.1117/12.734931>
- Ha, S.J., Choo, J., Yun, T.S., 2018. Liquid CO₂ Fracturing: Effect of Fluid Permeation on the Breakdown Pressure and Cracking Behavior. *Rock Mech. Rock Eng.* 51, 3407–3420. <https://doi.org/10.1007/s00603-018-1542-x>
- Hampton, J., Matzar, L., Han, Y., Warpinsky, N., Mayerhofer, M., 2014. Laboratory Shear Stimulation and Hydraulic Fracture Characterization Using Acoustic Emission. 31st Conference of the European Working Group on Acoustic Emission, p. 11.
- He, J., Lin, C., Li, X., Wan, X., 2016. Experimental Investigation of Crack Extension Patterns in Hydraulic Fracturing with Shale, Sandstone and Granite Cores. *Energies* 9, 1018. <https://doi.org/10.3390/en9121018>
- Healy, D., 2008. Damage patterns, stress rotations and pore fluid pressures in strike-slip fault zones. *J. Geophys. Res.* 113, B12407.
<https://doi.org/10.1029/2008JB005655>

- International Energy Statistics, 2020. Data and Statistics. <https://www.iea.org/data-and-statistics/data-tables?country=WORLD&energy=Renewables%20%26%20waste&year=2017>. Accessed on 20/07/2020
- Ishida, T., Chen, Q., Mizuta, Y., Roegiers, J.-C., 1998. Influence of fluid viscosity on hydraulically induced crack geometry. *Int. J. Rock Mech. Min. Sci.* 35, 460–462. [https://doi.org/10.1016/S0148-9062\(98\)00046-1](https://doi.org/10.1016/S0148-9062(98)00046-1)
- Ishida, T., Chen, Y., Bennour, Z., Yamashita, H., Inui, S., Nagaya, Y., Naoi, M., Chen, Q., Nakayama, Y., Nagano, Y., 2016. Features of CO₂ fracturing deduced from acoustic emission and microscopy in laboratory experiments: Features of CO₂ Fracturing. *J. Geophys. Res. Solid Earth* 121, 8080–8098. <https://doi.org/10.1002/2016JB013365>
- Leary, P., Malin, P., Saunders, G., Fleure, T., Sicking, C., Pullammanappallil, S., 2020. Flow-Imaging of Convective Geothermal Systems – Obtaining Seismic Velocity Models Needed for Production Well Targeting, in: *Workshop on Geothermal Reservoir Engineering*, Stanford University, Stanford, California. Stanford, California, USA, p. 13.
- Lin, W., Yeh, E.-C., Hung, J.-H., Haimson, B., Hirono, T., 2010. Localized rotation of principal stress around faults and fractures determined from borehole breakouts in hole B of the Taiwan Chelungpu-fault Drilling Project (TCDP). *Tectonophysics* 482, 82–91. <https://doi.org/10.1016/j.tecto.2009.06.020>
- Majer, E.L., Baria, R., Stark, M., Oates, S., Bommer, J., Smith, B., Asanuma, H., 2007. Induced seismicity associated with Enhanced Geothermal Systems. *Geothermics* 36, 185–222. <https://doi.org/10.1016/j.geothermics.2007.03.003>
- McDermott, C.I., Fraser-Harris, A., Sauter, M., Couples, G.D., Edlmann, K., Kolditz, O., Lightbody, A., Somerville, J., Wang, W., 2018. New Experimental Equipment Recreating Geo-Reservoir Conditions in Large, Fractured, Porous Samples to Investigate Coupled Thermal, Hydraulic and Polyaxial Stress Processes. *Sci. Rep.* 8. <https://doi.org/10.1038/s41598-018-32753-z>
- Molenda, M., Stoeckhert, F., Brenne, S., Alber, M., 2015. Acoustic Emission monitoring of laboratory scale hydraulic fracturing experiments. *American Rock Mechanics Association, 49th US Rock Mechanics / Geomechanics Symposium*, San Francisco, USA.
- Pruess, K., 2006. Enhanced geothermal systems (EGS) using CO₂ as working fluid—A novel approach for generating renewable energy with simultaneous sequestration of carbon. *Geothermics* 35, 351–367. <https://doi.org/10.1016/j.geothermics.2006.08.002>
- Renard, F., Bernard, D., Desrues, J., Ougier-Simonin, A., 2009. 3D imaging of fracture propagation using synchrotron X-ray microtomography. *Earth Planet. Sci. Lett.* 286, 285–291. <https://doi.org/10.1016/j.epsl.2009.06.040>
- Sausse, J., Dezayes, C., Genter, A., Bisset, A., 2008. Characterization of Fracture Connectivity and Fluid Flow Pathways Derived from Geological Interpretation and 3D Modelling of the Deep Seated EGS Reservoir of Soultz (France), in: *Thirty-Third Workshop on Geothermal Reservoir Engineering*. Stanford, California, USA, p. 8.
- Smart, B.G.D., Somerville, J.M., Crawford, B.R., 1999. A rock test cell with true triaxial capability. *Geotech. Geol. Eng.* 17, 157–176.
- Song, I., Suh, M., Won, K.S., Haimson, B., 2001. A laboratory study of hydraulic fracturing breakdown pressure in tablerock sandstone. *Geosci. J.* 5, 263–271. <https://doi.org/10.1007/BF02910309>
- Stanchits, S., Surdi, A., Gathogo, P., Edelman, E., Suarez-Rivera, R., 2014. Onset of

- Hydraulic Fracture Initiation Monitored by Acoustic Emission and Volumetric Deformation Measurements. *Rock Mech. Rock Eng.* 47, 1521–1532.
<https://doi.org/10.1007/s00603-014-0584-y>
- Stoeckhert, F., Brenne, S., Molenda, M., Alber, M., 2014. Fracture mechanical evaluation of hydraulic fracturing laboratory experiments, in: Alejano, L., Perucho, Á., Olalla, C., Jiménez, R. (Eds.), *Rock Engineering and Rock Mechanics: Structures in and on Rock Masses*. CRC Press, pp. 1335–1340.
<https://doi.org/10.1201/b16955-232>
- Stoeckhert, F., Molenda, M., Brenne, S., Alber, M., 2015. Fracture propagation in sandstone and slate – Laboratory experiments, acoustic emissions and fracture mechanics. *J. Rock Mech. Geotech. Eng.* 7, 237–249.
<https://doi.org/10.1016/j.jrmge.2015.03.011>
- Tomac, I., Sauter, M., 2018. A review on challenges in the assessment of geomechanical rock performance for deep geothermal reservoir development. *Renew. Sustain. Energy Rev.* 82, 3972–3980.
<https://doi.org/10.1016/j.rser.2017.10.076>
- Vinciguerra, S., Meredith, P.G., Hazzard, J., 2004. Experimental and modeling study of fluid pressure-driven fractures in Darley Dale sandstone. *Geophys. Res. Lett.* 31. <https://doi.org/10.1029/2004GL019638>
- Zhuang, L., Kim, K.Y., Jung, S.G., Diaz, M., Min, K.-B., 2018. Effect of Water Infiltration, Injection Rate and Anisotropy on Hydraulic Fracturing Behavior of Granite. *Rock Mech. Rock Eng.* <https://doi.org/10.1007/s00603-018-1431-3>
- Zimmermann, G., Moeck, I., Blöcher, G., 2010. Cyclic waterfrac stimulation to develop an Enhanced Geothermal System (EGS)—Conceptual design and experimental results. *Geothermics* 39, 59–69.
<https://doi.org/10.1016/j.geothermics.2009.10.003>

Ground movement predictions above coal mines after flooding

Numerische Simulation von Hebungen über gefluteten Kohlebergwerken

G. Lüttschwager, J. Zhao, H. Konietzky

TU Bergakademie Freiberg, Institut für Geotechnik
Gustav-Zeuner-Str. 1, 09599 Freiberg

Abstract

The flooding of abandoned coal mines has several consequences for the environment. The uplift due to the flooding of the goaf and overburden is one aspect which usually has been described by analytical solutions only. These approaches are not sufficient for complex geometries. A 3-dimensional numerical model has been developed for the case study Lugau-Oelsnitz coal mine. An elastic continuum mechanical approach has been used to predict the surface uplift. The chosen method works also in case of limited hydraulic permeability information. Numerical results are in good qualitative agreement with the observed uplift rates. That case study proves the importance of a detailed knowledge of abandoned mines for better risk predictions.

Zusammenfassung

Die Flutung stillgelegter Steinkohleminen hat zahlreiche Einflüsse auf die Umwelt. Hebungen infolge der Flutung des Alten Mannes sowie des Deckgebirges sind ein Aspekt, welcher bisher fast ausschließlich analytisch beschrieben wurde. Entsprechende Ansätze sind für komplizierte Grubengeometrien nicht ausreichend. Ein 3-dimensionales numerisches Modell wurde beispielhaft für das ehemalige Steinkohlenrevier Lugau-Oelsnitz entwickelt. Für die Prognose der Hebungsdaten an der Geländeoberfläche wurde ein elastischer Ansatz gewählt. Der gewählte Ansatz ist auch für Bergwerke mit beschränkten hydraulischen Informationen geeignet. Die numerischen Ergebnisse sind in guter qualitativer Übereinstimmung mit den vorliegenden Messdaten. Diese Untersuchung bestätigt die Notwendigkeit genauer Kenntnisse über stillgelegte Kohleminen zur besseren Risikoabschätzung.

1 Introduction

During the last decades numerous coal mines have been closed. Usually they undergo a more or less controlled flooding. The flooding has several consequences like mine instabilities, shaft instability, infiltration and pollution of ground and surface waters. The flooding of the disturbed underground excavations and the corresponding stress redistributions cause uplift effects at the surface. Such uplifts have been observed, described and evaluated by several researchers (Bekendam, 2017; Bekendam & Pöttgens, 1995; Dudek et al., 2020; Gee et al., 2016; Gee et al., 2017; Heitfeld et al., 2014; Heitfeld et al., 2016). Calculations and predictions of uplift rates are mainly limited to analytical solutions. Numerical approaches are still very rare.

As part of the EU-project GeoMAP, a numerical modelling approach for calculation and prediction of mine water induced surface uplifts has been developed. The abandoned coal mine of Lugau-Oelsnitz located between Zwickau and Chemnitz (Saxony, Germany) has been chosen as case study. The location and extend of the chosen model area are shown in Fig. 1. The mine has been abandoned in 1971, therefore information about the mine and flooding process are very limited. Several studies about the different risks of the mine related to shaft instability, water management and pollution have been published (Bayer, 1974; Eckart & Rüterkamp, 2013; Felix et al., 2007). The surface subsidence as well as the uplift is documented by e. g. Löbel et al., (2015) and John (2019). First 2D numerical simulations for that area have been done by Löbel et al. (2015). That paper extends these first approaches by a more comprehensive 3D modelling including the development of a strategy to deal with limited information.

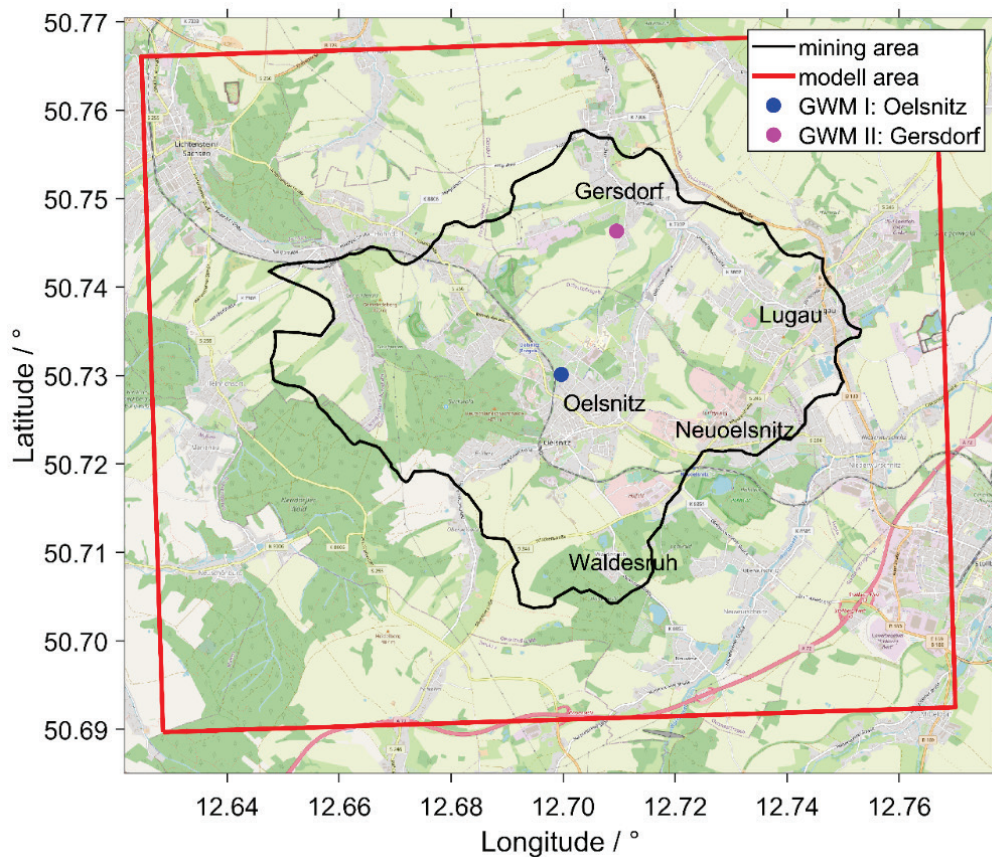


Fig. 1: Overview map of the research area showing main cities, numerical model area, mine water measuring locations and coal mine area.

The main challenges are data preparation and necessary simplifications of the mine geometry and relevant mechanisms. The mine is characterised by high seam offsets (jumps) and a relatively steep dip of the coal seams. First, analytical approaches are shortly discussed for a better understanding of the relevant mechanisms. Furthermore, relevant monitoring data are provided. Finally, the numerical simulation strategy is presented.

2 Surface uplift estimation for abandoned mines during flooding

A raising mine water level and therefore increasing pore pressure in abandoned coal mines results in surface uplift. An first analytical description of these uplifts has been presented by Pöttgens (1985). According to his work, the uplift over flooded coal mines is caused by decompression and extension of the goaf due to pore pressure increase. Depending on the permeability of the overburden rock, that effect can be restricted to the goaf or is also acting in the overburden layers.

Stress redistributions act on the rock mass due to buoyancy (eq. 1). The resulting uplifting effect of the flooded goaf can be described by eq. 2.

$$\sigma' = \sigma - p \quad (1)$$

$$\Delta h = D_m h \Delta p \quad (2)$$

The pore pressure change Δp acting on the goaf height h , results in a vertical extension Δh . Therefore, the extension factor D_m needs to be calibrated. Pöttgens determined the expansion factor for the Südklimburg coal mining area as $D_m = 3.5 \cdot 10^{-9} \text{ m}^2/\text{N}$. The resulting surface uplift is a superposition effect of all flooded goaf parts. The horizontal surface uplift distribution for a single goaf element can be described by the influence function k_z . The resulting total uplift can be calculated as an integration using eq. 3:

$$u_z = \Delta h \int k_z dA. \quad (3)$$

Different approaches have been developed for the influence function. Most often used approaches are those of Geertsma (1973) and Knothe (1984).

The approach of Geertsma has been originally developed for analysing surface subsidence over gas caverns. Pöttgens (1985) first used that approach for uplift determination over flooded coal mines. Therein the uplift is mainly influenced by the before described extension factor and the Poisson's ratio. The uplifting area is horizontally infinite, which is a very theoretical approach and of only limited practical use. Usually a cut-off is applied for a pre-defined distance.

In contrast, the approach of Knothe is using an exponential decay until reaching a defined distance from the goaf element. That distance is described by a critical angle. Sroka & Preusse (2017) used that surveyor approach originally developed for subsidence analysis also for mine water induced surface uplifting. Until now there is no study available, which compares both methods. Fig. 2 shows a simplified synthetic example according to the solution of Sroka & Preusse.

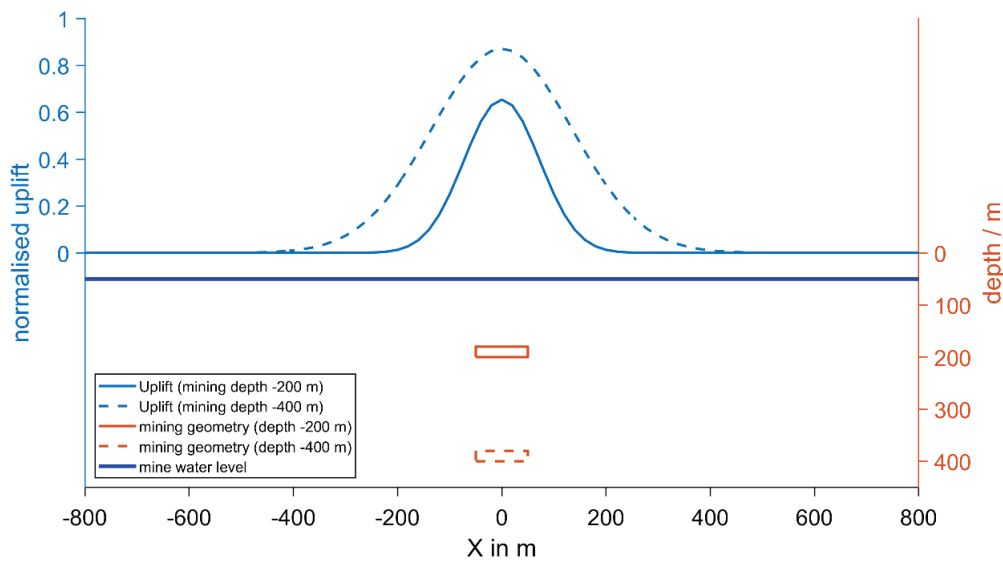


Fig. 2: Analytical solution for the normalised surface uplift above a synthetic flooded abandoned coal mine located in different depths using the influence function after Sroka & Preusse (2017) (dashed line – 400 m below surface; solid line - 200 m below surface).

Due to the simplifications, these analytical solutions are not sufficient for complex mine geometries and complex geological conditions. The saturation process of the goaf is not considered. For complex and inclined mine geometries the stress redistribution during the flooding process needs more detailed consideration. The interaction of different parts of the goaf is not any more a linear superposition. That becomes even more important for overlapping goafs. Generally, the extension of the flooded goaf becomes more inclined oriented for dipping coal seams.

In this paper 3D numerical modelling approaches for a complex mine with inclined seams and offsets is presented. That approach offers a more detailed consideration of mine geometry and variable goaf parameters.

3 Geology, Mining and Monitoring

3.1 Geological background

The research area with the coal deposit Lugau-Oelsnitz is located in the NW-SE oriented Vorerzgebirgs-trough. That trough includes also the coal mining area Zwickau. The geological history is dominated by the Variscan orogenesis of the SE located Ore Mountain crystalline complex. The regional geology has been described in detail by e. g. Berger et al. (2010) and Felix et al. (2007).

The Precarboniferous basement rock is mainly composed of Ordovician phyllite. The high strength of that rock as well as its position directly below the coal seams was useful for the installation of a long-term stable underground infrastructure. The phyllite surface has a pronounced graben structure, which has diverse consequences for the overlying Carboniferous. The top surface of the basement is shown in Fig. 3.

Due to the basement surface roughness, the Upper Carboniferous is very inhomogeneously distributed. It crops out towards SE at ground surface. The thickness varies

between 120 m in the NW and just a few meters along the outcrop. Additionally, the Upper Carboniferous layer underwent much erosion and tectonic deformation. A description of the coal seams is provided in the next chapter.

The Overburden mainly consists of the Rotliegend. In the research area it is structured from oldest to youngest as Härtensdorf formation (HF), Planitz formation (PF), Leukersdorf formation (LF) and Mülsen formation (MF). The thickness thins and outcrops towards SE as well. The geological model for Rotliegend and top basement is available in form of geological horizons (not shown in this paper). These subformations are discussed in more detail, as they are essential for the understanding of the hydraulic behaviour of the overburden above the coal mine:

- The HF is the lowest part of the Rotliegend and can be subdivided into two sedimentation cycles. The Lower HF mainly consists of regular layered fluvial claystone and sandstone. The sedimentation happened along a SW-NE oriented graben structure and reached thicknesses of up to 230 m. Within the Lower HF separated unregular coal deposits are embedded. These very local coal lenses are not worth mining, also due to their low thickness. The Lower HF has been eroded in some area and is therefore not distributed equally. The Upper HF consists of sandstones and varying conglomerates, interbedded by volcanic deposits and underwent erosion processes in many areas.
- The PF has an estimated thickness of about 50 m and consist of sandstone conglomerates and high amounts of volcanic deposits.
- The LF forms the main part of the Rotliegend as well as the whole overburden with thicknesses up to 700 m. It is composed of three main sedimentation cycles, which are typically layered as conglomerates, sandstones, siltstones and claystone in different compositions. Vulcanites are very rare and thin.
- The MF can be found only in the western parts of the research area. It is characterised by highly loosened conglomerates. The MF underwent intensive erosion and has thicknesses up to 200 m towards the western border of the research area.

Younger sedimentary layers from Tertiary to Holocene are only found in valleys and show very low thicknesses of less than 10 m. These layers are not considered in the numerical modelling.

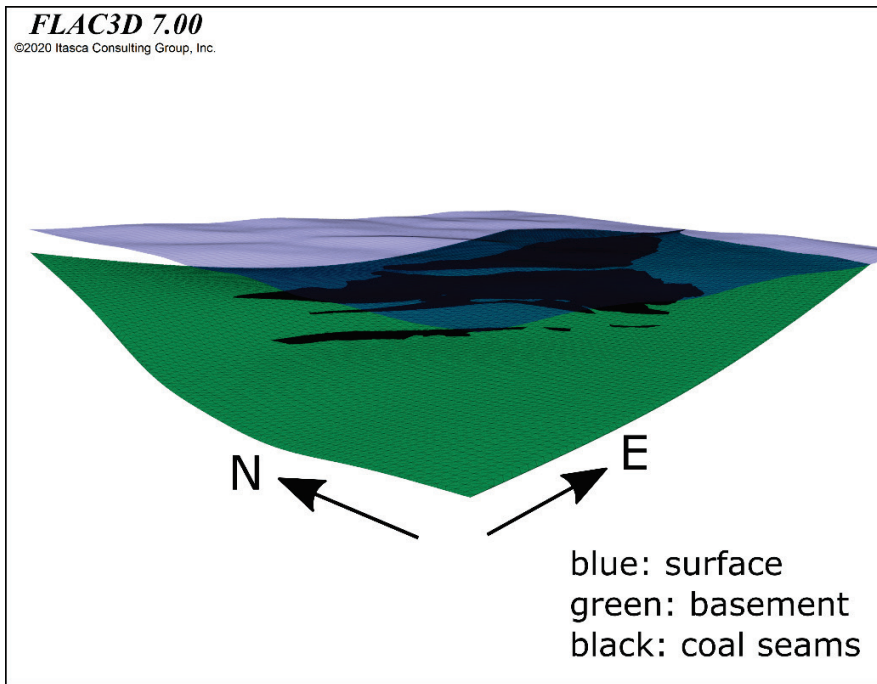


Fig. 3: Simplified geological situation of the abandoned Lugau-Oelsnitz coal mine, including the available coal seams as used for model 1.

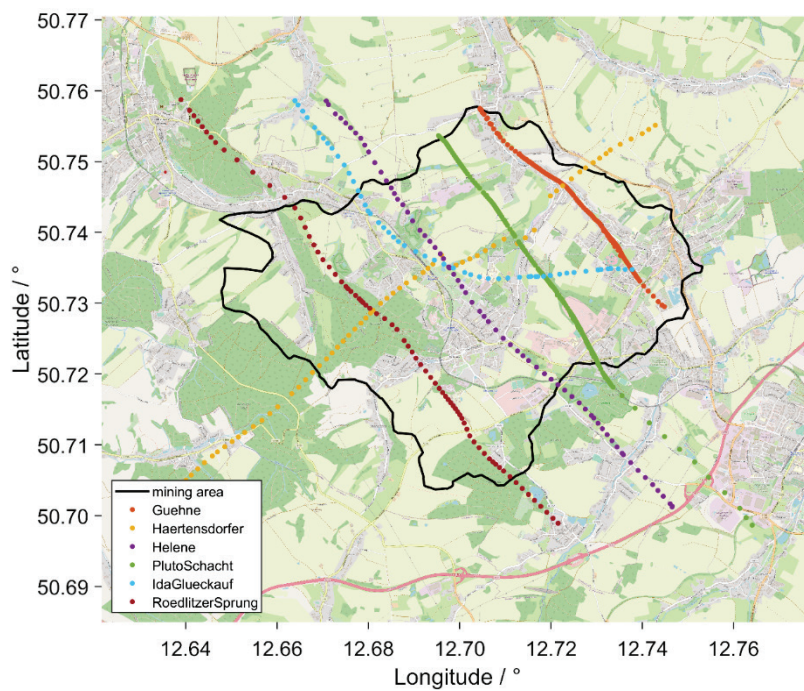


Fig. 4: Location of the main faults in the research area.

Tab. 1: Main Faults with vertical offset and strike direction.

Fault name	Fault offset (max.) / m	Strike direction
Härtensdorfer Störung	50	NW
Rödlitzer Sprung	350	SW
Helene-Hedwig-Schacht-Verw.	80	SW
Pluto-Schacht-Verwerfung	150	SW
Lugauer Verwerfung	65	SW
Carl-Schacht-Verwerfung	50	NE

Due to the orogenesis of the Ore Mountains there has been high tectonic activity until Tertiary. The Middle-Saxonian-Fault-Zone is striking SW-NE and characterized by moderate offsets of usually less than 30 m. Much younger are the Hercynian faults (NW-SE striking). These faults are dominating the mining area. The offsets are up to 350 m and parts of the faults have been reactivated several times, so dip and strike direction vary within one fault. The main faults and their characteristic properties are listed in Tab. 1, the surface location of the faults is shown in Fig. 4. Mainly the blocking and high offsets made mining very challenging. The active period of all faults ended latest with the Tertiary.

The hydraulic properties of the Overburden layers are very important for the numerical modelling of the mine water induced uplift. There are two main questions to discuss: How far does the raising mine water penetrate and saturate the overburden? Is there a continuous and large-scale high permeability in the overburden layers? The near-surface Post-Rotliegend is expected to be widely permeable within the uppermost 50 m. That permeability is dominated by the fault and joint system. Below that erosion layer, the Rotliegend is dominated by horizontal aquifuges. Large scale aquifers do not exist, but local water lenses or confined small scale aquifers are very likely. The faults below depths of 50 to 100 m are clayed or mylonitised and therefore hydraulically impermeable. These assumptions are proven by core analysis and experiences during the active mining period. During the active mining significant water inflow was never observed. The very slow and linear mine water rise proves, that there is no significant water inflow from the overburden. The faults were also not reactivated during the active mining period.

The situation in the Lugau-Oelsnitz mining area is different from mines like Limburg (Netherlands) or Ruhr mining area (Germany). There, a significant inflow from the overburden into the mine as well as large scale uplifting due to pore pressure raise in the overburden is observed. However, local inflow into the Rotliegend is very likely near to the filled shafts with enhanced permeability, but due to the geological situation these areas are locally very restricted. Globally the overburden can be considered as hydraulically impermeable for the numerical modelling. It is recommended to prove that with monitoring wells in the Rotliegend.

3.2 Mining information

During the industrial mining period 1859 to 1971, 142 Mio. t of coal has been quarried. The amount of mined coal during the preindustrial period (1844-1858) and earlier is unknown. The early extensive shallow mining activities along the outcrop of the Upper Carboniferous is unknown as well. These activities have high importance for surface stability and cause serious hazards, however, they are negligible for the uplift process.

Overall 16 at least partially mineable coal seams have been found in the mining area. For the numerical modelling the Grundflötz, Vertrauensflötz, Glück-Auf-Flötz and Oberflötz are used (see Fig. 5). Detailed thickness maps are not available, also not a detailed model of the longwall mining fields. Drifts and headings are often located in the basement. They form 1.5% of the open space in the underground and can be considered as stable or otherwise negligible. More than 100 mining shafts have been sunk. Due to the afore mentioned reasons they will not be considered. Eckart & Unland (2005) estimated the volume of the open underground space (Tab. 2). The still open space is about 45 Mio. m³. Referred to the summed-up coal seam volume (Tab. 3), the averaged open space height can be estimated as 1 m. This value is very low and underestimates the situation due to the unregular mining geometries and missing information for most of the coal seams. Simplified, the open space height has been estimated as 2.0-2.5 m for the considered coal seam geometry.

Over the years very different mining methods have been used. A detailed mining model is not digitally available, moreover the open space and backfill situation in the excavations is unknown. That information is very important for the model generation as well as the estimation of goaf height and loosening. During the last decades open longwall mining with self-backfill and only limited blasting backfill was used. As simplification and due to the limited information, large scale longwall mining with self-backfill is assumed for the numerical modelling. The mining fields are not modelled in detail, but the generally seam distribution is used.

Tab. 2: Volume balance for the mining area Lugau-Oelsnitz.

	Volume in Mio. m ³
Production volume	150
Backfill	8
Subsidence	95
Open drift	2
Residual space	45

Tab. 3: Seam area of the digital model.

Seam name	Area in Mio m ²
Grundflötz	18.1
Vertrauensflötz	15.0
Glück-Auf-Flötz	9.7
Oberflötz	1.6
Sum of all seams	44.4

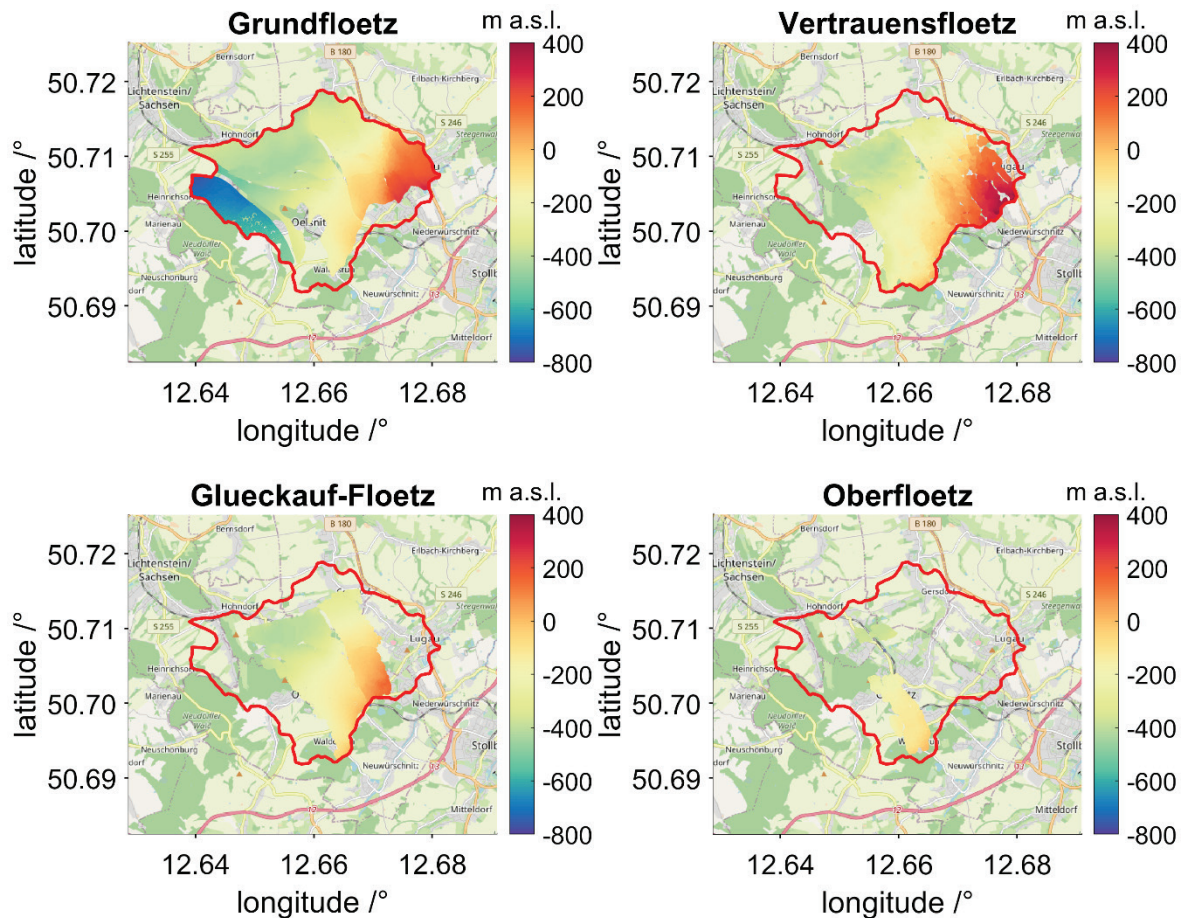


Fig 5: Depth and distribution of the coal seams, used for numerical modelling.

3.3 Water level and uplift monitoring

Two mine water observation wells have been installed. The first station (GWM I) has been drilled in the area of Oelsnitz to a depth of 630 m. The continuous water level monitoring started in June 2006. The monitoring stopped October 2018 due to revision works and did not restart at least until September 2020. Due to the complex geological setting and the unclear mine water passways a second monitoring station (GWM II) has been established in Gersdorf. The water level monitoring started in May 2014. Monitoring results are shown in Fig. 6. The data show a continuous and linear water level raise. Deviations from the linear interpolated trend lines are very small and usually only temporal effects. The mean flooding velocity can be determined as 10.5 m/a (GWM I) and 11.4 m/a (GWM II). In 2018 an increase in the flooding velocity has been detected which seemed to slow down in 2019 again. However, due to the missing data from GWM I this is not sure. For the numerical modelling a linear and constant water level raise of 11 m/a is assumed for the whole mining area. Assuming a future constant water level raise, the mine water is expected to reach the surface in the 2030s. That is an assumption based on recent observations. Due to the different near-surface hydrogeological conditions a future change in flooding velocity is most likely but currently not predictable.

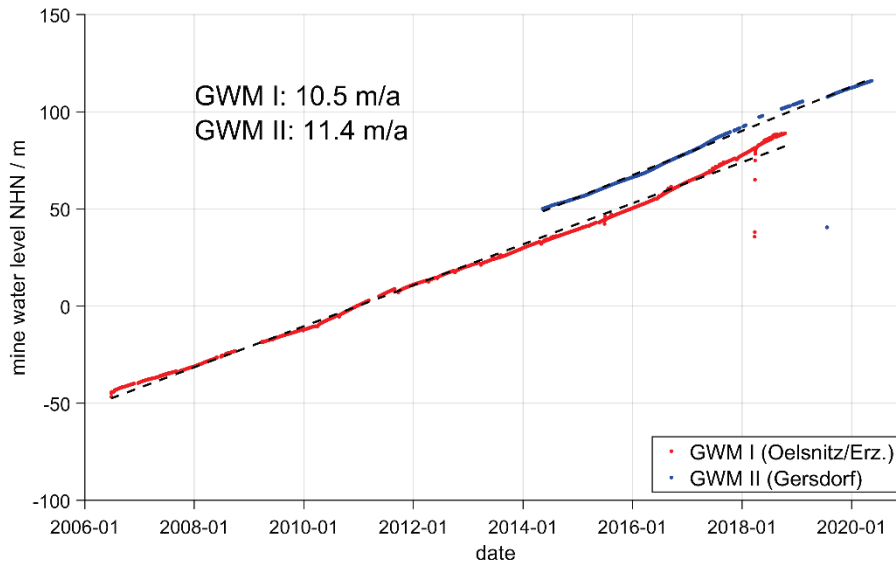


Fig. 6: Water level series for the two observation wells with linear interpolated annual water rise rates. For location of the observation wells see Fig. 1.

During the active mining period between 1900 and 1972 levelling survey has been performed every two years for about 500 measuring points. For that period, total subsidence of about 5-10 m has been detected for most of the area around Oelsnitz. The maximum subsidence of 17 m was detected near to Waldesruh (see Fig. 1). Löbel et al. (2015) published the digitised subsidence data as total subsidence maps as well as 10-year interval maps (e. g. Felix et al., 2007). Comparing these data with the mining activities it can be proven, that the subsidence values correlate directly with the mining intensity (mined seam thickness & depth of the mine). The levelling has not been continued after 1974.

In 1996 the levelling has been continued for app. 50 measuring locations, mainly using old levelling points. Levelling campaigns took place in 1996/1997, 2002, 2006 and 2014. The results are shown as annual uplift rates in Fig. 7. Because uplift has different causes compared with subsidence and because the later subsidence development after the active mining is unknown, the two levelling data series cannot be connected. The uplift rates shown in Fig. 7 are calculated for whole years, as the exact dates of each single measurement are unknown. Therefore, errors of the uplift rates up to 25% are possible. An area-wide interpolation and therefore interpretation is difficult due to large gaps in the levelling network. The southern part of the mine has a bad levelling coverage. An additional east-west oriented levelling line in the north-eastern part would be useful. To improve coverage and shorten the levelling intervals satellite InSAR data have been used (ISBAS DInSAR processing). The InSAR results show similar uplift rates compared with land-based methods. The InSAR results outside of the mining area show subsidence effects which cannot be proven by levelling (processing artefacts). Similar InSAR results for the Lugau-Oelsnitz mining area have been published by John (2019). The above-mentioned gaps in the levelling networks cannot be closed completely by InSAR data. Gaps are either caused by difficult accessible areas (land-based levelling) or thick vegetation (InSAR). For further discussion of that topic see John (2019).

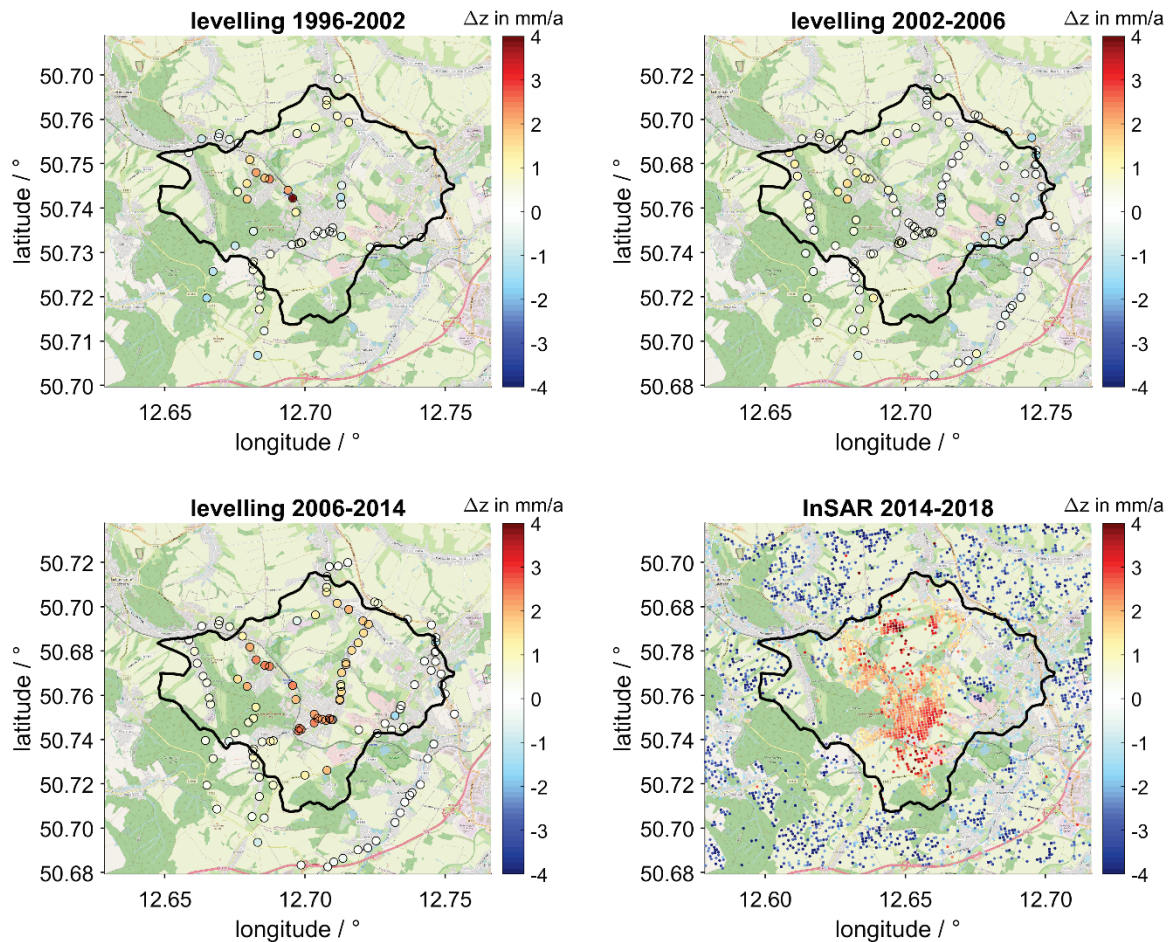


Fig. 7: Annual surface uplift rates for different time periods. Ground based levelling and satellite based remote InSAR data.

However, the data situation is sufficient for a qualitative discussion, especially as the uplifting due to mine water rise are long-term effects. Uplift rates are generally in the range of 1 and 4 mm/a. The maps in Fig. 7 show an eastward shift of the eastern border of the uplifting area. A larger eastward expansion took place between 2005 and 2010. That is caused by the start of flooding the eastern mining fields which are clearly separated by the Pluto-Schacht fault with an offset of 100-150 m. During the last years, similar high uplift rates have been detected in the south. This is caused by the shallower and extensive mining there and coincides with the high subsidence before.

4 Numerical Simulation

4.1 Modelling strategy and setup

The problem of surface uplift due to mine water rise is a hydro-mechanical 3-dimensional coupled problem. It includes aspects like saturation, extension of the goaf and description and possible extension of the overburden (in detail: tectonic behaviour, joints and faults, general permeability but also the existence and influence of ground water lenses). Moreover, the mining related openings like mining tracks and filled or open shafts need consideration. A numerical model in such a complexity is very large and therefore expensive in the sense of calculation time. Therefore, these complex models often need simplifications.

Tab. 4: Comparison of the modelling strategies of the two approaches.

	Modell 1	Modell 2
Faults	Not considered	Mechanical only
Water flow	Not considered	Not considered
Geological layers	2-layer-model with a near-surface-gradient	Multi-layer-model
Coal seam geometries	detailed geometries with constant height	Generalised mining layer
Constitutive model	Pure elastic	Elastic / Mohr-Coulomb

A continuum mechanical approach has been chosen for the numerical modelling, which has been done in FLAC3DTM. The model needed intensive simplification due to the lack of data. Two slightly different models have been used and will be compared. The main focus is on model 1, which gives most reliable results for the research area. Fig. 8 shows the general modelling scheme, focussing on model geometry and parametrisation. In the following, the general model assumptions and the numerical solving process as shown in Tab. 4 are discussed in detail. The discussion focuses on the approach chosen for model 1:

- Faults have not been implemented in model 1 as the mining history revealed that the faults are hydraulically impermeable. Also, mechanical reactivation of the faults during mining has not been observed.
- The hydraulic connectivity and other hydraulic properties are not known in detail for the coal seams or the goaf areas. Further, the water inflow was very low even during the active mining. As discussed before it is most likely, that the overburden is hydraulically tight and will generally not be significantly flooded by the mine water. Therefore, the modelling does not include water flow at all. The influence of water has been implemented as a rising water-level with related pore pressures, reducing the effective stresses and considering the buoyancy effect.
- The geological model has a coarse resolution, whereas the Rotliegend in detail is very heterogeneous and fine layered. The differences of the mechanical properties between the different Rotliegend units are not very significant. Weathering and corrosion effects have been considered by changing the elastic parameters in the uppermost 200 m.
- Coal seams and goaf geometries have the biggest influence in the model. The lateral distribution and depth of the coal seams has been implemented in detail for the available coal seam geometries. Thickness of coal seams as well as goaf height have been set to average values. The coal seam thickness has been estimated as 2 m as discussed before. The height of the disturbed overburden is generally defined by two different approaches. The direct goaf height is often estimated as 3-4 times the seam height (Bekendam, 2017). Usually that is a reasonable value for mechanical analysis. The rising water level usually influences much more overburden, even when the overburden acts as a ground water barrier. (Ahmed et al., 2018) following the suggestions of (Peng & Chiang, 1984), that the influenced height is 28 to 42 times the seam thickness. In model 1 we used 50 m as mining disturbed height for every coal seam.

- For model 1 a pure elastic constitutive model has been chosen. This corresponds to the before discussed analytical solutions. Generally, more research should be undertaken to include the saturation process as well as the widening and developing of cracks in the weakened overburden due to the increasing water pressure. Model 2 is based on the elasto-plastic Mohr-Coulomb constitutive model, because also subsidence is modelled, which is not part of that paper. However, also model 2 uses the linear elastic approach for the decompression of the disturbed and flooded goaf.

For the meshing of the numerical model two different approaches were considered. An irregular mesh forms the model in a natural like manner. The geometries of the layers are represented in detail. The special resolution can be changed continuously over the model, depending on size and structure of the geometrical elements. This meshing scheme has been chosen for model 2, as it allows to implement smooth interfaces (for joint representation) with arbitrary forms. The main disadvantages are very irregular formed zones, which reduce numerical accuracy during the computations. In contrast, Model 1 is based on a regular blocked basic mesh, which has been locally refined. That offers stable numerical modelling with high accuracy, but all non-horizontal or non-vertical structures are staircase-shaped. The influence of these irregularities on the result can be reduced by local refinements. The differences of the chosen approach can be seen in Fig. 9 (model 1) and Fig. 10 (model 2).

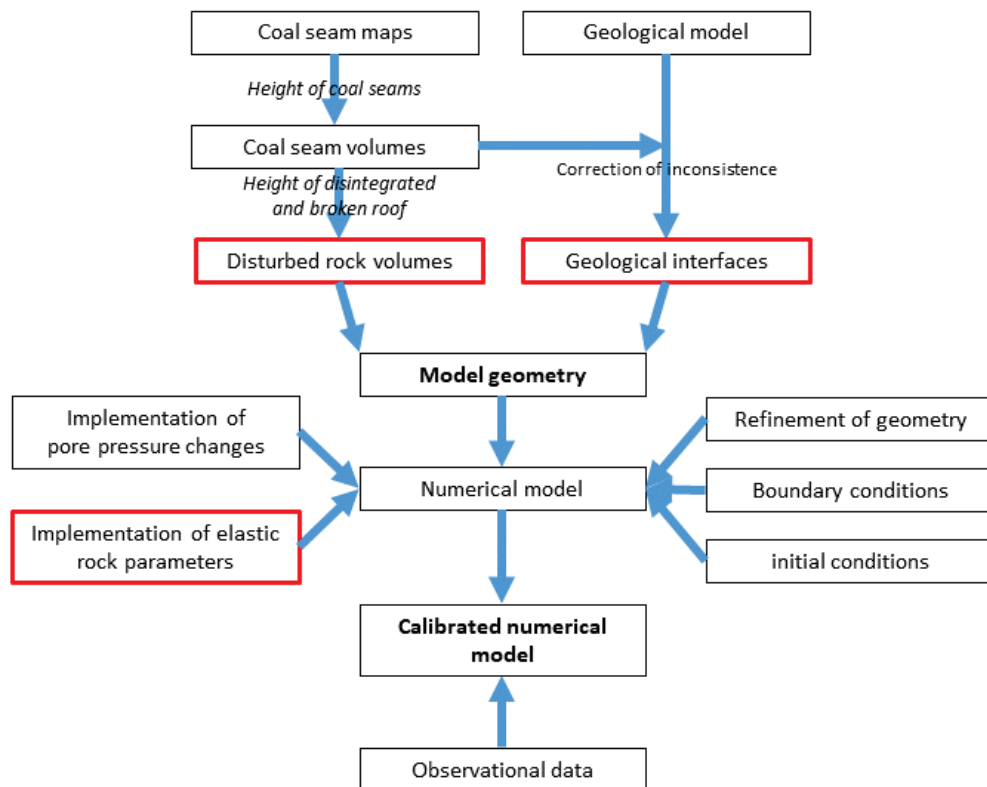


Fig. 8: Workflow for numerical model generation (model 1). Red framed are the main model challenges.

Roller outer boundaries are used, except the surface which is free as it represents the free earth surface. The numerical calculation was divided into two main steps. First the calculation of a dry equilibrium state has been performed, which represents the idealised situation of the dry mine at the end of the active mining. In reality the flooding of the lower mine levels started already during the active mining phase, but this is not considered here. The second part considers the stepwise increasing of water pressure in the model depending on the rising water level.

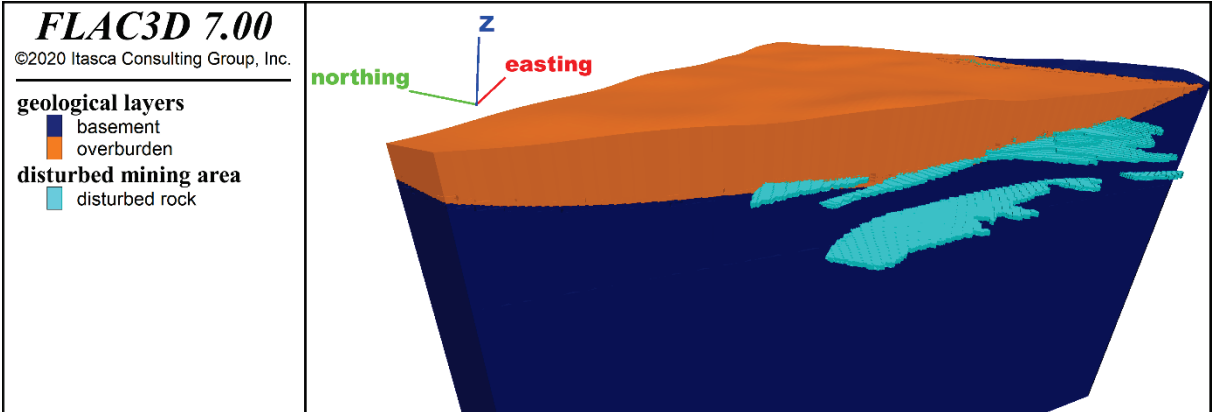


Fig. 9: Model 1: Numerical model geometry, regular mesh geometry with detailed mining area and simplified geology.

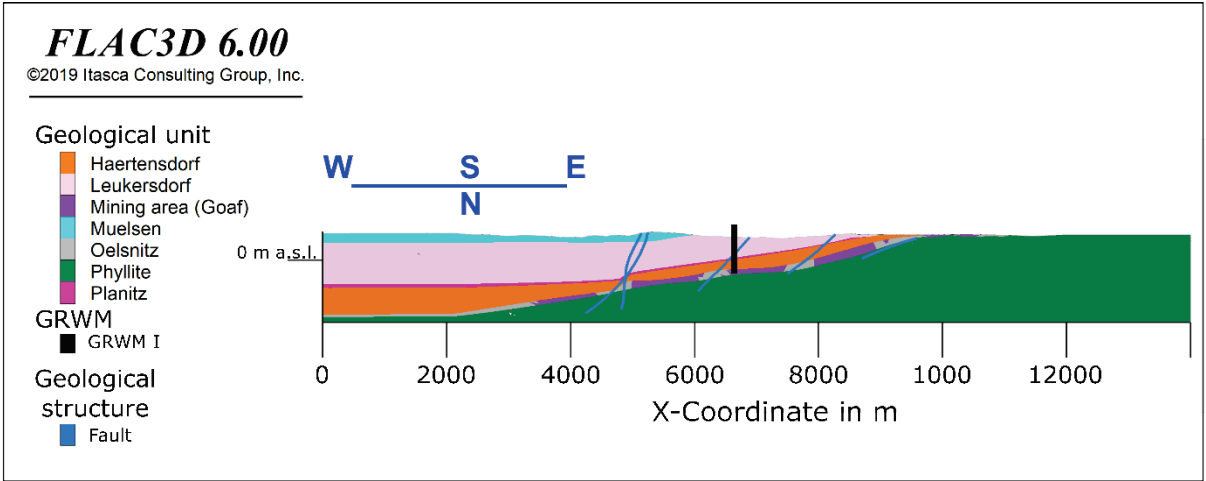


Fig. 10: Model 2: Numerical model geometry (cross section of 3D model), irregular mesh geometry with simplified mining area, faults and multi-layered overburden.

4.2 Model parameters and calibration

A proper parametrisation of the goaf area is essential for the modelling, whereas the exact parameters of the goaf are not known well. The aforementioned two modelling strategies will be discussed separately.

Model 1 is using an elastic constitutive law. The Poisson's ratio is constant for the different geological units and does not change during the flooding. As a sensitivity analysis shows, the Poisson's ratio has no significant influence on the model results. The values have been chosen on the basis of lab results and literature values. The Young's Modulus has the highest impact on the results. The near surface layers of the Rotliegend have been weakened linearly towards the surface from 15 GPa to 5 GPa

to simulate the eroded and weakened surface layers. At lower depths the Young's modulus E is constant for the different layers (see Tab. 5). For the goafs, the methodology proposed by Ahmed et al. (2018) was chosen. E increases from the bottom of the seam upwards until it reaches the surrounding overburden E values. The goaf height was set to approx. 28 times the seam height and E_{seam} to 0.225 GPa. The resulting distribution of the Young's modulus is shown in Fig. 11. An increased density has been used for the flooded goaf areas as the pore space is fully saturated using the porosities of 0.4 for the seam and 0.3 for the Rotliegend. Nevertheless, the assumption for the density in the flooded goaf is just a rough estimation and needs further investigation. The hydrostatic pore pressure in the goaf has been calculated for each flooding step and has been superimposed to the dry stress field.

The second model approach (model 2) considers an elastic constitutive model only for the goaf areas. For other parts the Mohr-Coulomb constitutive model is used. That model has been chosen to consider in more detail the behaviour of the joints/faults. The joints/faults are simulated as interfaces using the Coulomb friction law with peak and residual strength values and corresponding stiffness. Due to the lack of data the parameters were estimated based on experience and appropriate literature values. The implementation of the Poisson's ratio and density has been done the same way as for model 1, the used values are listed in Tab. 5. The pore pressure is again superimposed according to the flooding level. To simulate the ground movement the Young's modulus of the complete Upper Carboniferous (Oelsnitz) layer (virgin rock mass modulus of about 18 GPa) comprising the coal seams and the goaf were adjusted. Based on an assumed GSI value between 20 and 30 and a damage factor between 0.5 and 1.0 representative as an average for the whole Oelsnitz layer at the end of the excavation phase, a value of 500 MPa was assumed for the Young's modulus. These values are used for the prediction of the ground movement during the flooding phase in combination with a reduced density of 1700 kg/m³ (buoyancy effect).

It should be noticed, that there are no indications, that the faults are activated, but the simulations with faults document, that in principle such an approach is able to consider the potential activation of discontinuities like faults and their potential effects.

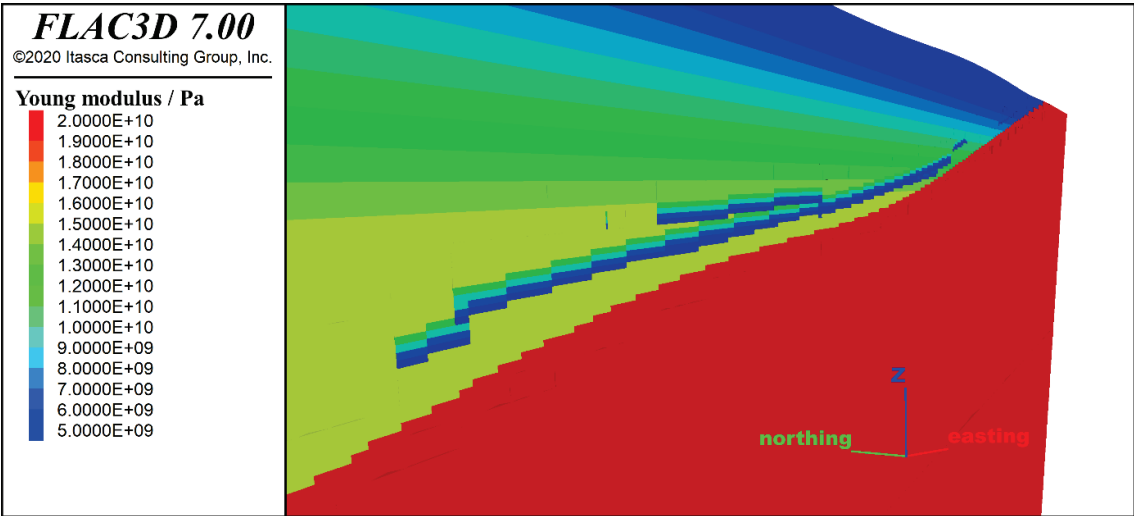


Fig. 11: Model 1: Young's modulus, as implemented in the numerical model. Gradients are applied in the topmost overburden as well as in the disturbed areas above the mined coal seams.

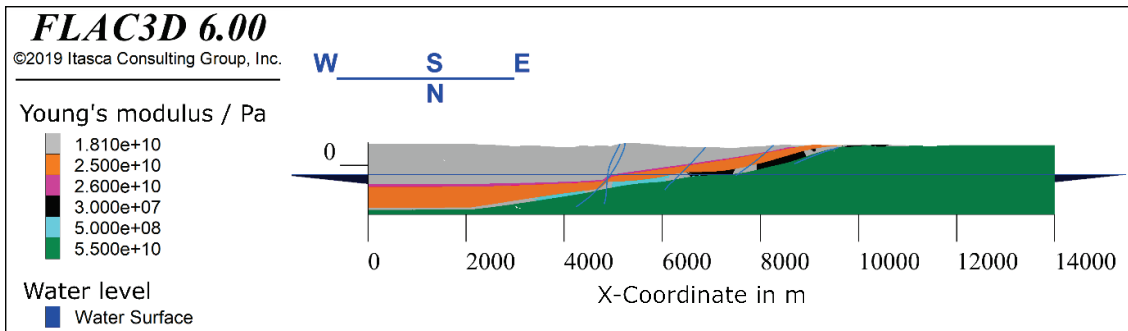


Fig. 12: Model 2: Young's modulus (cross section of 3D model), as implemented in the numerical model. Young's modulus is increased in saturated mine goaf areas in comparison to the subsidence phase (note: this model simulates also the subsidence in a preceding simulation step).

Tab. 5: Main model parameters.

Parameter	Model	Overburden	Goaf (dry)	Goaf (wet)	Basement
Young's modulus / GPa	1	5.0 to 15.0	0.225 to 12.0	0.225 to 12.0	55.0
	2	18.1 to 26.0	0.03	0.5	55.0
Poisson's ratio	1	0.30	0.30 to 0.40	0.30 to 0.40	0.17
	2	0.20 to 0.31	0.40	0.40	0.17
Friction angle	1	--	--	--	--
	2	33° to 45°	--	--	65°
Cohesion / MPa	1	--	--	--	--
	2	3.3 to 5.0	--	--	10.0
Tensile strength / MPa	1	--	--	--	--
	2	4.0 to 4.3	--	--	10.2
Density / kg/m ³	1	2660	2660	2967 to 3070	2750
	2	2600 to 2780	1400	1700	2750
Porosity	1	--	--	0.30 to 0.40	--
	2	--	--	0.30	--

5 Results and discussion

5.1 Results and comparison with monitoring data

The results of the numerical uplift simulations are discussed as annual uplift rates as well as total uplift values. The results of model 1 have been optimised for the levelling and InSAR intervals by simulation of the past mine water levels. The results (Fig. 13) show a very good qualitative agreement between measurements and simulation. The general distribution of the uplifting areas and the eastward shift of the south-eastern flank of the uplift area are well modelled. That shift corresponds to the southwest oriented dip of the coal seams. The relatively high vertical offset in the coal seams due to the Pluto-Schacht fault and the start of the flooding in the eastern side has been expected for the years 2005 - 2010. That is also the reason for the faster uplift in the southern parts. Both can be seen in the field data as well as in the modelling results. It confirms the expected begin of flooding of the southern shallow working fields. The InSAR data confirm the modelling results for the time span 2014-2018. The eastern border of the uplift area is slightly different, which may be caused by inaccurate water

levels as well as missing coal seam information for most of the smaller mined seams. The indicated subsidence around the mining field in the InSAR results are very likely due to inaccurate InSAR processing. John (2019) published also InSAR data based on the PSI method, which show very similar pattern but his results do not show subsidence in the outer areas.

A full quantitative modelling of the uplift rates cannot be presented. The quantitative modelling is very inaccurate due to missing seam information. Seam distribution and depth maps for at least 10 coal seams incl. detailed seam height information is not yet available. The digitalisation of these data is expensive and challenging. Due to these reasons we did not calibrate the numerical model quantitatively.

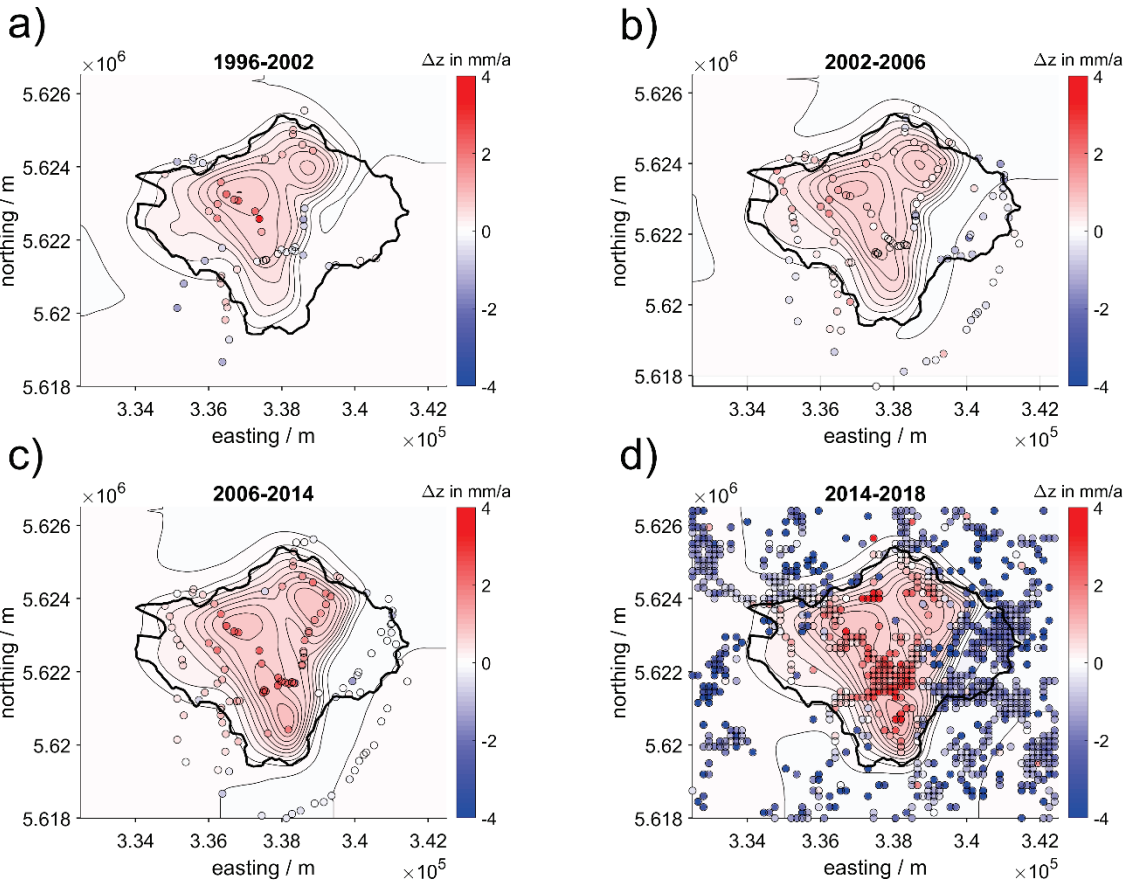


Fig. 13: Numerical modelling uplift rate results (model 1, contours) compared with levelling and InSAR data.

5.2 Uplift prediction and suggestions for future work

The future flooding of the coal mine has been modelled for an extrapolated linear mine water raise until an estimated final water level of 324 m. That water level is expected to be final as for higher mine water levels water outflow starting at the surface in the lowest valleys is expected. Kowarik et al. (2018) suggest an even lower final flooding level of 300 m a.s.l. for safety reasons. More detailed potential hazards and suggested safety measures are intensively discussed by Kowarik et al. (2018).

The extrapolated water levels for the numerical modelling (model 1) are shown in Fig. 14. The resulting uplift rates for the corresponding time intervals are shown in

Fig. 15. Assuming a constant rate of mine water raise the already discussed development of the uplift will continue. Regionally the uplift will slightly fasten in the future. That is caused by the shallower position of the south eastern mine fields. The highest uplift rate will be expected in the southern areas around Waldesruh. The model shows a significant uplift gap between the western and eastern coal fields along the Pluto-Schacht fault. That is expected because due to the high offset of up to 150 m. Mining activities along the fault are very limited. Until now, that gap cannot be proven by field measurements. It is highly suggested to extend the levelling for a west-east directed levelling line in that area. The InSAR data do not cover that area as well. The uplift development in the eastern shallow mining areas is unclear so far. More detailed information about the mining activities is necessary for improving the reliability of the numerical model predictions.



Fig. 14: Water level extrapolation for numerical modelling.

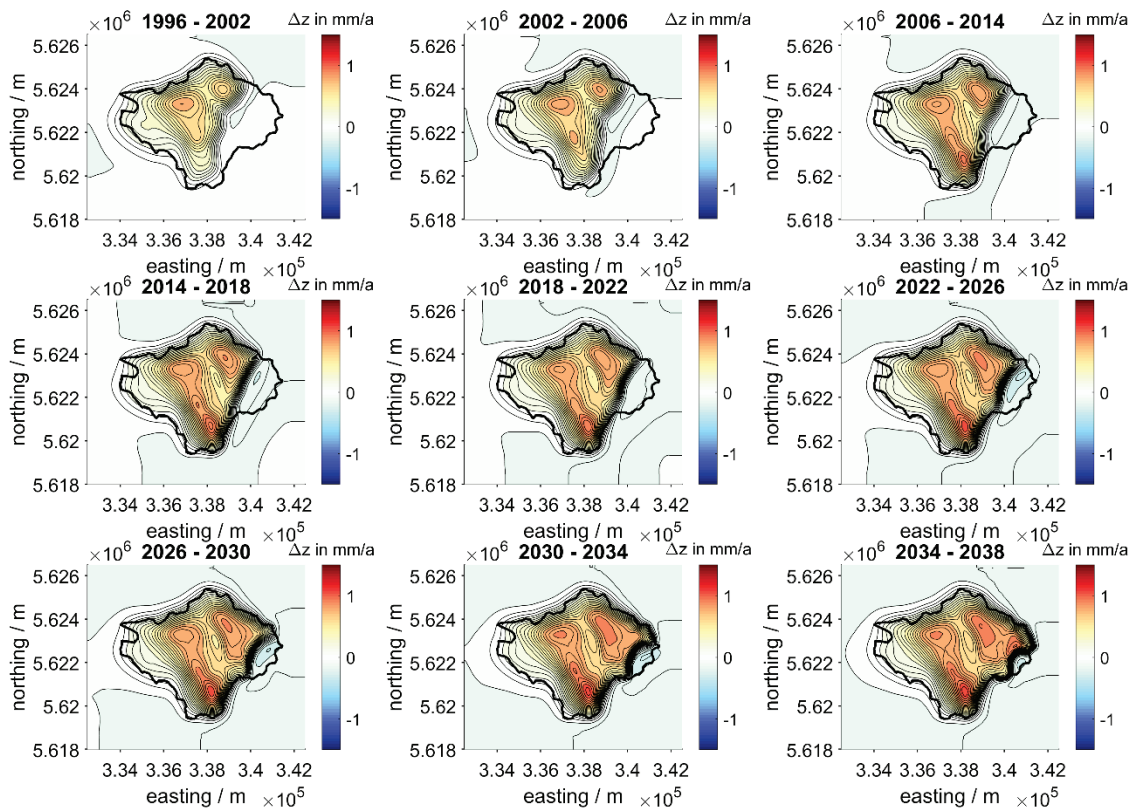


Fig. 15: Model 1: Modelled annual uplift rates for different time (flooding) intervals.

The final total uplift values cannot be predicted precisely. There are two main reasons for that. As already discussed, the mining information does not allow the set-up of a model with detailed geometry. The second important aspect is the flooding and levelling history in the research area. As the flooding of the deepest mine levels started already during the active mining period, subsidence and uplift cannot be separated. Furthermore, the late subsidence events have not been detected as levelling campaigns stopped shortly after closing of the mine.

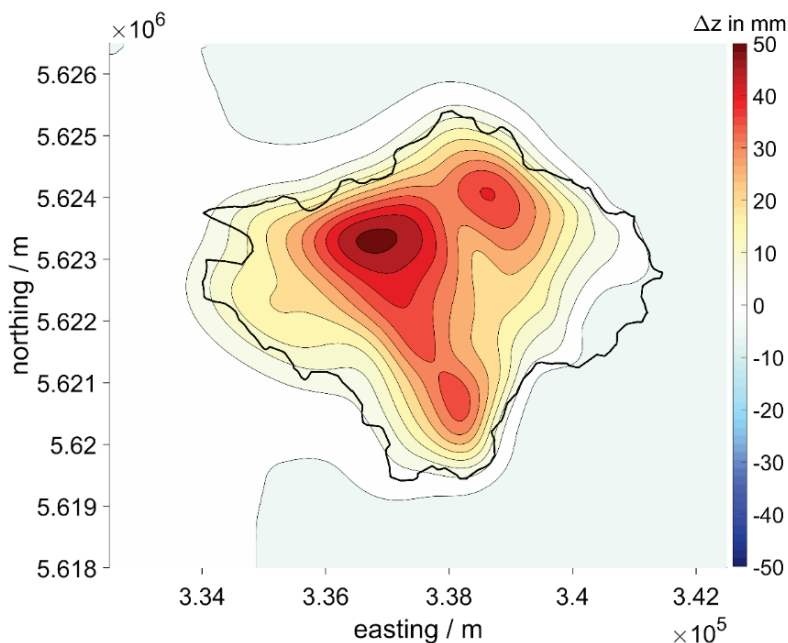


Fig. 16: Model 1: Total modelled surface uplift at maximum flooding level (324 m a.s.l.).

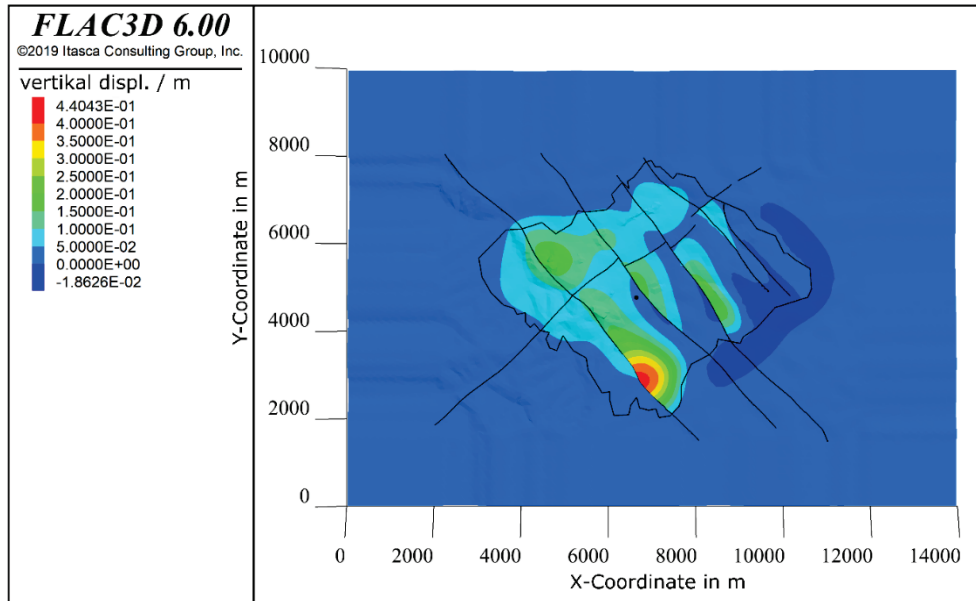


Fig. 17: Model 2: Total modelled surface uplift at maximum flooding level (lowest surface height).

Nevertheless, the uplift simulations provide interesting results. Fig. 1 shows the total uplift for model 1. The highest amplitudes are found in the north-western mining area. They are related to the deeper locations of the mine. Consequently, the highest uplift rates are not directly related to the highest subsidence, as it is often assumed in literature. That can be explained by the strong morphology and the steep dip of the coal seams. As the highest subsidence is mainly located in shallower intensive mining areas, the uplift is higher above areas with deep intense mining, as the higher pore pressure is dominating the uplift. So, there is no general linear relation between subsidence and uplift for dipped coal seams.

The hazard for surface or near-surface infrastructure is directly related to very high horizontal gradients of the vertical uplifts. The numerical modelling as well as the uplift measurements do not show hints for a significance in that respect. The highest risk potential can be found in the southern mining area around Waldesruh, which seems also not to be critical. Generally, the hazard related to mine water raise related uplift is very low. Investigations of other researchers showed that stronger hazards may only be related to reactivated joints/faults in combination with mining only at one side of the joint/fault. As the faults in the Lugau-Oelsnitz mining area have never been reactivated by mining activities stronger hazards are unlikely. Model 2 shows such an event for weakened faults and single sided mining activities. In that model scenario the hazard for surface damages is increased in the southern mining area. However, such a situation is not realistic for the Lugau-Oelsnitz mining area as discussed before.

6 Conclusions

The numerical simulation of the mine water raise related uplifts has shown that:

- Even if data are very limited, the qualitative uplift behaviour over a mine during flooding can be modelled and predicted with a relatively simple numerical simulation approach.

- The used numerical modelling approach seems useful for complex situations in terms of geology and mine structure.

For more detailed numerical modelling and more reliable results the following aspects should be considered.

- For a proper numerical simulation of the uplift process, a continuous monitoring of the water level in the mine, but also in the overburden, is necessary.
- A consistent and detailed model considering geology and mine geometry is necessary. The mine geometry needs information about the mined seam heights and backfilling situation.
- Hydro-mechanical coupled numerical simulations need huge computational resources. The uplift prediction can be simplified by the use of the water levels for discrete points in time.

The stability of the mine shafts and other near surface mine infrastructure during the mine flooding have not been considered in this study. Locally there are high hazard potentials which needs investigation for each location individually. The uplift predictions are based on recent observations and data. For a future changing mine water raise, the surface uplift rate can change significantly and needs therefore corrected numerical modelling.

7 Acknowledgement

This research has been funded by the European Regional Development Fund (EFRE) and the Free State of Saxony in the framework of “Interreg V A – SN-CZ 2014-2020” (project name: “GeoMAP”; project number 100348899). Thanks goes to all contributing project members. Special thanks go to David Gee (University of Nottingham) for processing and providing the InSAR data.

8 References

- Ahmed, S. S., Al Heib, M., Gunzburger, Y. & Renaud, V. (2018). 3D Numerical Simulation of the Goaf Due to Large-Scale Longwall Mining. In H. Shehata & Y. Rashed (Eds.), *Sustainable Civil Infrastructures. Numerical Analysis of Nonlinear Coupled Problems* (pp. 121–131). Springer International Publishing.
- Bayer, J. (1974). *Bergschadenskundliche Analyse „Lugau-Oelsnitz“*. Zwickau. VEB Baugrund Berlin, Produktionsbereich Zwickau & VEB Steinkohlenwerk Oelsnitz.
- Bekendam, R. F. & Pöttgens, J. J. (1995). Ground movements over the coal mines of southern Limburg, The Netherlands, and their relation to rising mine waters. In *FISOLS - Fifth International Symposium on Land Subsidence*. Symposium conducted at the meeting of IAHS & Netherlands Geodetic Commission, The Hague.
- Bekendam, R. [Roland]. (2017). Abschätzung der Bodenhebungen in Folge des Grubenwasseranstiegs über stillgelegten Kohlegruben im Südlimburger Revier. In G. Meier (Ed.), *17. Altbergbau-Kolloquium: 16. bis 18. November 2017, Freiberg* (pp. 118–130). Wagner Digitaldruck und Medien GmbH.
- Berger, H.-J., Steinborn, H., Görne, S., & Junghanns, C. (2010). Stratigraphie und Tektonik im Steinkohlerevier Lugau/Oelsnitz. In Landesamt für Umwelt, Landwirtschaft und Geologie (Ed.), *Geoprofil 13 (2010): Geologie und Bergbaufolgen im*

- Steinkohlerevier Lugau/Oelsnitz* (pp. 15–43). Freiberg: Landesamt für Umwelt, Landwirtschaft und Geologie.
- Dudek, M., Tajduś, K., Misa, R. & Sroka, A [Anton] (2020). Predicting of land surface uplift caused by the flooding of underground coal mines – A case study. *International Journal of Rock Mechanics and Mining Sciences*, 132, 104377.
- Eckart, M., & Rüterkamp, P. (2013, June 3). *Konzeptentwicklung zur gesteuerten Flutung des ehemaligen Steinkohlenreviers Lugau-Oelsnitz und Darstellung technischer Lösungen für die Konzeptumsetzung: EU-Projekt VODAMIN*. Bericht. DMT GmbH & Co. KG.
- Eckart, M., & Unland, W. (2005). *Aufbau eines Grubenwasserwiederanstiegsmodells für das Steinkohlenrevier Lugau/Oelsnitz, Teil II*. unpub. report. Essen. DMT GmbH & Co. KG.
- Felix, M., Berger, H.-J., Köhler, U., Döhner, S., Kauk, S. & Löbel, K.-H. (2007). *Bergbaufolgen im ehemaligen Steinkohlerevier Lugau/Oelsnitz unter besonderer Berücksichtigung des Grubenwasseranstiegs*. Abschlussbericht. Landesamt für Umwelt und Geologie - Oberbergamt.
- Gee, D., Bateson, L., Sowter, A., Grebby, S., Novellino, A., Cigna, F., Marsh, S., Banton, C. & Wyatt, L. (2017). Ground Motion in Areas of Abandoned Mining: Application of the Intermittent SBAS (ISBAS) to the Northumberland and Durham Coalfield, UK. *Geosciences*, 7(3), 85.
- Gee, D., Sowter, A., Novellino, A., Marsh, S. & Gluyas, J. (2016). Monitoring land motion due to natural gas extraction: Validation of the Intermittent SBAS (ISBAS) DInSAR algorithm over gas fields of North Holland, the Netherlands. *Marine and Petroleum Geology*, 77, 1338–1354.
- Geertsma, J. (1973): Land Subsidence Above Compacting Oil and Gas Reservoirs. *Journal of Petroleum Technology* 25(6), 734–744.
- Heitfeld, M., Denys, F., Klünker, J., Rosner, P. & Spaans, J. (2016). Systematische Erfassung und Bewertung von Spätfolgen des Steinkohlenbergbaus in Südlimburg/Niederlande. *BHM Berg- Und Hüttenmännische Monatshefte*, 161(4), 156–163.
- Heitfeld, M., Rosner, P. & Mühlenkamp, M. (2014). Auswirkungen von Geländehebungen im Zuge des Grubenwasseranstiegs im Ruhrrevier - ein Ansatz zur Bewertung der Risiken. In G. Meier (Ed.), *14. Altbergbau-Kolloquium: Vom 6. bis 8. November 2014 in Gelsenkirchen*. Wagner.
- John, A. (2019). Untersuchungen zum Monitoring von Bodenbewegungen in Folge des Grubenwasseranstiegs im ehemaligen Steinkohlerevier Oelsnitz/Erzgebirge mittels Radarinterferometrie. In G. Mayer, C. Butscher, J. Benndorf, K.-H. Löbel, D. Tondera, & W. Busch (Eds.), *19. Altbergbau-Kolloquium: Leoben, 07. bis 09. November 2019* (pp. 127–142). Wagner Digitaldruck und Medien GmbH.
- Knothe, S. (1984). *Prognozowanie wpływów eksploatacji górniczej*. Wydawnictwo Śląsk.
- Kowarik, J., Eckart, M., Rüterkamp, P., Dabrowski, A., Schubert, J. & Beige, H. (2018). *Erarbeitung inhaltlicher Aspekte für ein Rahmenkonzept zu "Bergbaunachfolgen des ehemaligen Steinkohlereviers Lugau-Oelsnitz / Erzgeb."*. DMT-Leipzig.

- Löbel, K.-H., Tamaskovics, N., Eckart, M. & Busch, W [W.]. (2015). Vertikale Bodenbewegungen im Zusammenhang mit dem Grubenwasseranstieg im ehemaligen Steinkohlenrevier Oelsnitz/Erzgebirge. In G. Meier (Ed.), *15. Altbergbau-Kolloquium: Vom 5. bis 7. November 2015 in Leoben, [Montanuniversität Leoben* (pp. 114–129). Wagner.
- Peng, S. S. & Chiang, H. S. (1984). Longwall Mining. Wiley.
- Pöttgens, J. J. E. (1985). Bodenhebung durch ansteigendes Grubenwasser. In *6. Internationaler Kongress für Markscheidewesen*, Harrogate.
- Sroka, A. & Preusse, A. (2017). Technische Abschätzung von Folgelasten des Steinkohlebergbaus. In *9. Aachener Altlasten- und Bergschadenskondliche Kolloquium: "Ende des subventionierten Steinkohlenbergbaus - aktueller Stand und langfristige Entwicklungen"*. Symposium conducted at the meeting of GDMB, Aachen.

Short-Term Pore Pressure Evolution around Tunnels in Opalinus Clay: Lessons Learned from an Overcoring Experiment

Kurzfristige Porendruckentwicklung um Tunnel im Opalinuston: Lehren aus einem Überbohrungsexperiment

K. Khaledi, P. Hamdi, L. Winhausen, M. Jalali, F. Amann

Department of Engineering Geology and Hydrogeology, RWTH Aachen University, Aachen, Germany

Abstract

The paper outlines the results obtained from an in-situ overcoring experiment in Opalinus Clay, which was intended to characterize the unloading-induced pore pressure development under undrained condition. The results observed within the experiment indicated that the pore pressure drop caused by rapid unloading leads to negative pore pressures in Opalinus Clay. The resulted negative pore pressure may contribute to a short-term stability improvement. Based on this observation, a general modeling framework is presented to describe the undrained pore pressure evolution in low permeable porous media considering the effect of desaturation. Then, a 3D numerical model is developed to replicate the pore pressure response observed within the in-situ overcoring experiment. The numerical model includes the most important hydro-mechanical factors contributing to the undrained pore pressure response, such as hydro-mechanical anisotropy of Opalinus Clay and the effect of desaturation. Both experimental and numerical results indicate that the undrained unloading of Opalinus Clay may temporarily generate pore pressures less than the atmospheric pressure. Finally, a large scale tunnel model is developed to investigate the possibility of developing sub-atmospheric pore pressure in the vicinity of tunnels excavated in Opalinus Clay.

Zusammenfassung

Dieser Beitrag skizziert die Ergebnisse eines in-situ-Überbohrungsversuchs im Opalinuston, mit dem die entlastungsinduzierte Porendruckentwicklung unter undrainierten Bedingungen charakterisiert werden sollte. Die im Rahmen des Experiments beobachteten Ergebnisse zeigten, dass der durch die schnelle Entlastung verursachte Porendruckabfall zu negativen Porendrücken im Opalinuston führt. Der resultierende negative Porendruck kann zu einer kurzfristigen Verbesserung der Gesteinsfestigkeit beitragen. Basierend auf dieser Beobachtung wird ein allgemeiner Modellierungsansatz vorgestellt, um die Entwicklung des undrainierten Porendrucks in gering durchlässigen porösen Medien unter Berücksichtigung des Entsättigungseffektes zu beschreiben. Anschließend wird ein numerisches 3D-Modell entwickelt, um die im in-situ-Experiment beobachtete Porendruckveränderung zu replizieren. Das numerische Modell umfasst die wichtigsten hydromechanischen Faktoren, die zur Entwicklung des undrainierten Porendrucks beitragen. Sowohl

experimentelle als auch numerische Ergebnisse weisen darauf hin, dass die undrainierte Entlastung von Opalinuston vorübergehend Porendrücke erzeugen kann, die unterhalb des atmosphärischen Drucks liegen. Schließlich wird ein Tunnelmodell entwickelt, um die Möglichkeit der subatmosphärischen Porendruckentwicklung in der Tunnelumgebung im Opalinuston zu untersuchen.

1 Introduction

Opalinus Clay is recognized as a suitable host rock for nuclear waste disposal in Switzerland. Understanding coupled processes in Opalinus Clay is the key to predict its hydro-mechanical behaviour under various loading and unloading conditions. During recent years, a number of in-situ experiments have been conducted at the Mont Terri Rock Laboratory with the aim to characterize the hydro-mechanical coupled behavior of Opalinus Clay during tunnel excavation (Martin et al. 2004; Corkum and Martin 2007, Yong 2007; Giger et al. 2015; Amann et al. 2017). The in-situ measurements during the excavation have shown an increase in pore-pressure ahead of the tunnel face with a subsequent decrease immediately at the tunnel circumference (Wild et al. 2018). Moreover, it was observed that the monitored pore-pressure values at the vicinity of the tunnel boundary are significantly below the initial pore pressure. For the majority of pore pressure measurements conducted during the excavation of tunnels at the Mont Terri Rock Laboratory, the minimum measured pore-pressure was 100 kPa, indicating that an excavation damaged zone has formed and connected the monitoring interval to the tunnel atmosphere. Amann et al. (2017) presented the results of EZ-B experiment performed at Mont Terri URL. In this experiment, some measurements showed pore pressures in the range of 40 – 50 kPa below the nearest atmosphere (Amann et al. 2017). These pore-pressure measurements demonstrated for the first time that sub-atmospheric pore-pressure could potentially develop during the excavation of galleries in Opalinus Clay, which may provide a considerable apparent cohesion, at least in the short term. To this end, an in-situ experiment entitled “HM-B Experiment” was designed to assess the unloading-induced pore pressure evolution in Opalinus Clay during an overcoring experiment. The present paper highlights the key findings and lessons learned during the HM-B experiment together with the results from numerical modeling conducted to further understand the hydro-mechanical processes in low permeable materials.

2 In-Situ Overcoring Experiment and Results

The HM-B experiment was performed in three main steps including: 1) an installation phase, 2) a saturation phase, and 3) an overcoring phase. In this experiment, the pore pressure response was triggered by overcoring a small diameter pilot borehole equipped with a pressure transducer and a full-range tensiometer. The pilot borehole BHM-B1 (shown in Figure 1) was equipped with a packer system, pressure transducer and full-range tensiometer and was drilled from the Security Gallery towards the Gallery 98 (Figure 1). The BHM-B1 borehole had a length of 11.3 m and a diameter of 56 mm. Upon completion of the BHM-B1 pilot borehole, the tightness of the system was tested and the completed borehole was left for a natural saturation phase. The pore pressure after one year of natural saturation was measured to be approximately 200 kPa.

Following the instrumentation of the pilot borehole and saturation, the overcoring experiment was conducted by drilling a 7.46 m long borehole from Gallery 98 in the opposite direction of the pilot borehole (BHM-B2 borehole in Figure 1). The overcoring borehole had a diameter of 350 mm providing a core with a diameter of 338 mm. Drilling was performed at a constant rate and the core-removal was carried out on average each meter. On November 22nd 2017, the tip of overcoring drill was 1.36 m ahead of the sensor location. The remaining 1.63 m was drilled continuously to a total

depth of 7.73 m (i. e. 0.27 m behind the sensor location). Subsequently, the core and the drilling equipment remained inside the borehole for the following night.

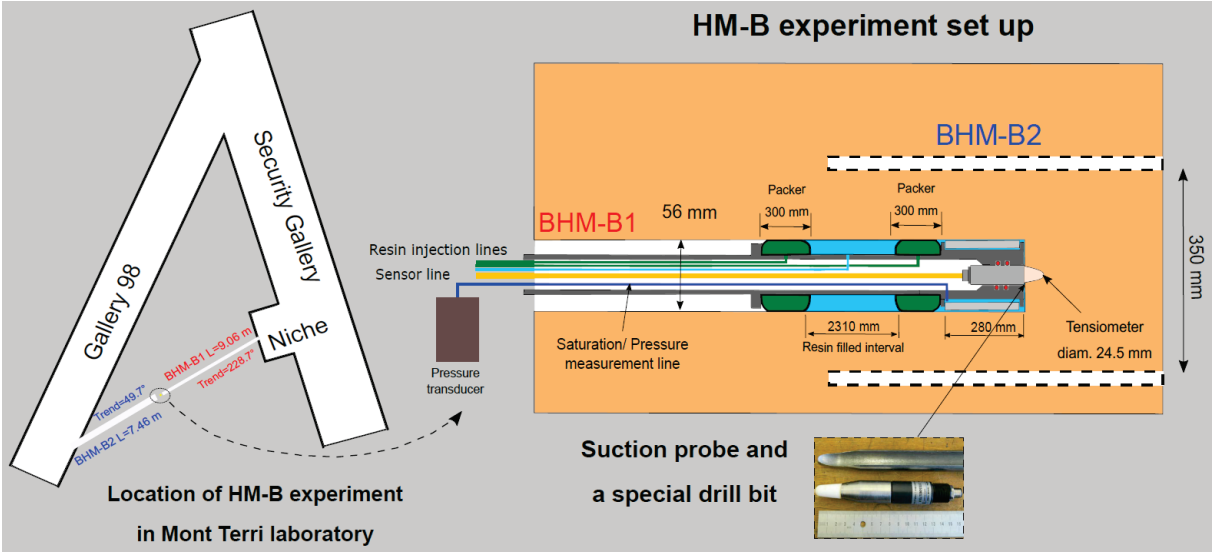


Figure 1: The HM-B experiment setup installed in the BHM-B1 borehole. The pilot borehole is equipped with a resin inflated packer system, a pressure transducer and a full range tensiometer. A special drill bit was used to create a customized-shape hole for the ceramic cup of the tensiometer (modified after Lettry & Roesli, 2017)

Figure 2 shows the pore pressure responses measured during the overcoring process. For distances greater than 1.0 m between the overcoring front and the sensor location (Point A to Point B in Figure 2), the pore pressure remained constant at ~ 200 kPa, corresponding to its initial condition. The pore pressure increased from ~ 200 kPa to almost 300 kPa as the overcoring borehole approached the sensor location and a peak value was reached when the overcoring borehole was about 0.3 – 0.4 diameter in front of the sensor location (from Point B to Point C). As the excavation face passes the sensor location, the pore pressure decreased rapidly from 300 kPa to -755 kPa (from Point C to Point E). In the last step of experiment, all the conditions were kept constant for almost 5 hours. As depicted in Figure 2, the pore pressure dissipated during this time and the recorded pressure increased to 100 kPa (i. e. the atmospheric condition).

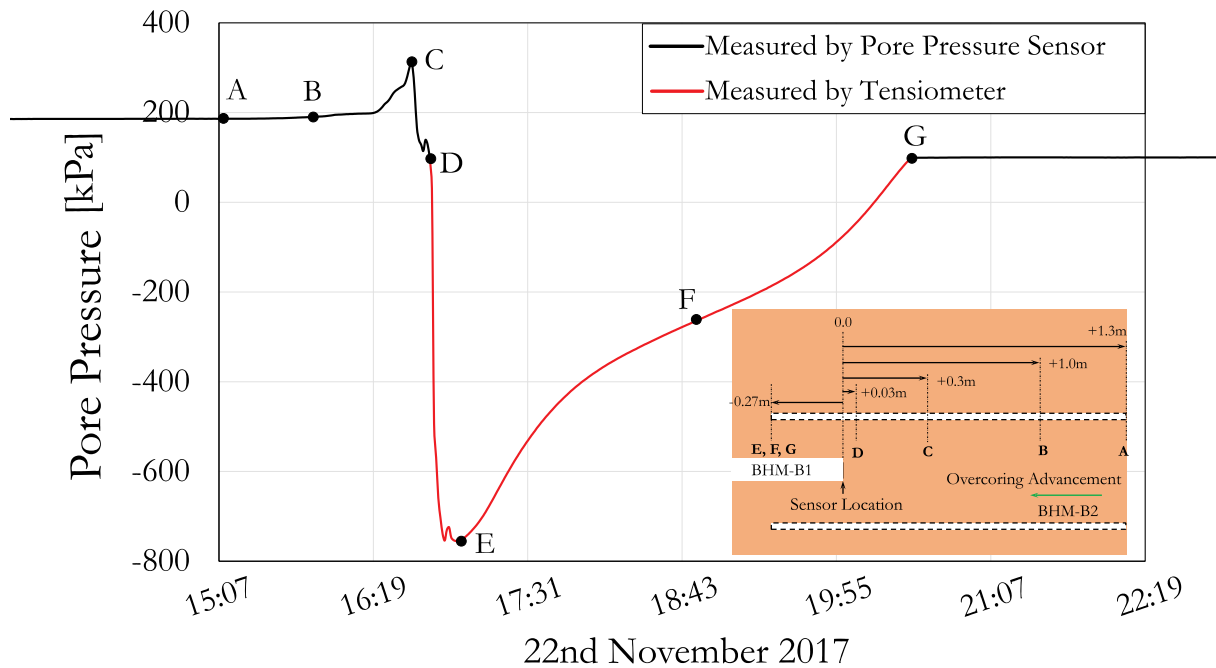


Figure 2: Results of the HM-B experiment. Point B to Point C: shows the rise of interval pressure prior to overcoring. Point C to Point E: shows the subsequent sudden pressure drop resulting from unloading; the sub-atmospheric pore pressure was measured by the tensiometer. Point E to Point G: shows the dissipation of pore pressure.

3 Pore Pressure Development in Porous Media under Undrained Condition

3.1 The monospecies approach to simulate cavitation

Figure 3 shows a complete modeling framework, which is commonly used to simulate iso-thermal hydro-mechanical behaviour of fully and partially saturated porous media in different engineering applications (Hassanzadeh et al. 1979, Olivella et al. 1996). The physical equations to describe couplings between solid, liquid and gas phases are also summarized. Based on this modeling framework, a simplified cavitation model, known as the “monospecies approach“, was proposed by Schrefler et al. (1996) and Gawin et al. (1998). In this approach, the rock mass is initially treated as a fully saturated medium in which all the pore spaces are filled with liquid water (no air exists). However, cavitation may take place if the pore water pressure is equal to or smaller than the saturated vapor pressure at a given temperature (iso-thermal). In this case, the porous medium turns into a two-phase system with the voids filled partly with liquid and partially with vapor. Schrefler et al. (1996) proposed that a number of simplifications can be adopted to model cavitation effects without influencing the overall response of pore water pressure. The underlying balance equations, the governing constitutive equations as well as the relevant simplifications are briefly outlined here for the sake of completeness.

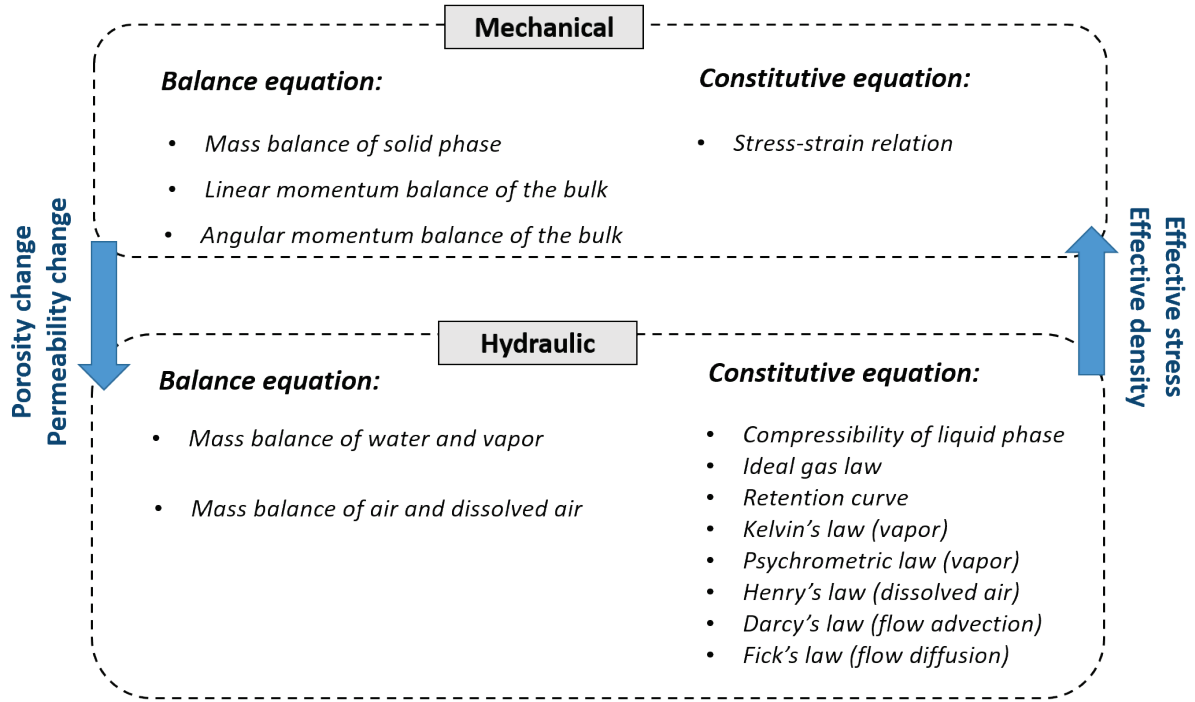


Figure 3: A complete modeling framework to simulate iso-thermal hydro-mechanical behaviour of fully and partially saturated porous media

3.2 Balance equations

In monospecies approach, the undrained hydro-mechanical behavior of porous media is governed by three balance equations, i. e. 1) mass balance of solid phase 2) mass balance of liquid water and vapor and 3) balance of linear momentum. The water mass balance and the vapor mass balance equations are summed as shown in Eq. (1), leading to a single mass balance equation for all water species. In this way, the source and sink terms related to phase change are eliminated. The flux advection and diffusion terms are omitted under the undrained condition. In a fully saturated state, the water saturation S_w is equal to unity and the second term in Eq. (1) is canceled. In this equation, the water saturation S_w , the water density ρ_w and the vapor density ρ_g are three unknown variables that should be determined through appropriate constitutive relations.

$$\frac{\partial(\rho_w S_w n)}{\partial t} + \frac{\partial(\rho_v (1 - S_w) n)}{\partial t} = 0 \quad (1)$$

The balance of linear momentum is shown in Eq. (2). In this equation, the equivalent fluid pressure p_f is an average pressure of the mixture of fluids consisting of liquid water and vapor.

$$\text{div}(\boldsymbol{\sigma}) + \rho \mathbf{g} = 0, \quad \boldsymbol{\sigma} = \boldsymbol{\sigma}' + p_f \mathbf{I}, \quad p_f = S_w p_w + (1 - S_w) p_v \quad (2)$$

3.3 Constitutive relations

A number of constitutive relations are required to form a complete set of equations for the existing unknown variables. These constitutive relations are introduced in the following sections.

3.3.1 Stress-strain relation

Opalinus Clay exhibits inherent anisotropy of their mechanical properties due to its geological structure (i. e. distinct bedding structure). In this paper, a transversely isotropic elastic model is used to describe the mechanical behavior of Opalinus Clay. The stress-strain relation for cross anisotropy reads:

$$\boldsymbol{\sigma}' = \mathbf{D}\boldsymbol{\varepsilon} \quad (3)$$

Where, \mathbf{D} is a fourth order elasticity tensor which is a function of 5 independent elastic parameters, i. e. $E_{||}$, E_{\perp} , $\nu_{||}$, ν_{\perp} , G . The subscripts $||$ and \perp refer to the parallel and perpendicular direction to bedding, respectively.

3.3.2 Soil-water retention

Due to the surface tension of water and very small pore sizes in Opalinus Clay, capillary pressure or suction is generated when the pore water pressure is smaller than the vapor pressure. In this case, the change of water saturation S_w is related to the change of capillary pressure (suction $s = p_v - p_w$) expressed by water-retention curve. In this paper, the van Genuchten model (van Genuchten 1980) is employed to describe the changes of saturation, i. e.

If $p_w \geq p_g$, then $S_w = 1.0$

$$\text{If } p_w \leq p_g, \text{ then } S_w = \left(1 + \left(\frac{s}{p_0}\right)^{\frac{1}{1-\lambda}}\right)^{-\lambda} = \left(1 + \left(\frac{p_v - p_w}{p_0}\right)^{\frac{1}{1-\lambda}}\right)^{-\lambda} \quad (4)$$

here, p_0 and λ are model parameters.

3.3.3 Behavior of water and vapor

Water is assumed to be compressible with a bulk modulus of $C_w = 2.22$ GPa. It is also assumed that vapor behaves as an ideal gas and is described by Boyle's law as follows:

$$\rho_v = \frac{p_v M_w}{RT} \Rightarrow \frac{d\rho_v}{\rho_v} = \frac{dp_v}{p_v} \quad (5)$$

In the presence of capillary effects and surface tension, the vapor pressure in the above equation is described by Kelvin's law:

$$p_v = p_{sv} \exp\left(\frac{-s M_w}{\rho_w RT}\right) = p_{sv} \exp\left(\frac{-(p_v - p_w) M_w}{\rho_w RT}\right) \quad (6)$$

The quantity p_{sv} is the saturated vapor pressure, which is essentially a function of temperature. The following empirical correlation has a good accuracy between 0 C° and 100 C°.

$$p_{sv} = 136075 \exp\left(\frac{-5239.7}{T}\right) \quad [\text{MPa}] \quad (7)$$

3.4 Assumptions and simplifications

Equations 1-7 construct a nonlinear system of equations, which needs to be solved numerically. Schrefler et al. (1996) proposed a simplified approach to model cavitation effects. The following assumptions are made to simplify the abovementioned equation:

- **Simplification 1:** according to Eq. (7), the saturated vapor pressure is equal to 2.96 kPa at a temperature of 25 C°. Therefore, the magnitude of vapor pressure at ambient temperature is significantly less than the pore water pressure (i. e. $p_v \ll p_w$). Similarly, the vapor density ρ_v obtained from Eq. (6) is several order of magnitude less than the water density (i. e. $\rho_v \ll \rho_w$ and $d\rho_v \ll d\rho_w$). Therefore, the last term in Eq. (1) can be omitted.
- **Simplification 2:** Since the magnitude of vapor pressure is negligible compared to the pore water pressure, the suction term in Eqs. 4 and 6 can be written as: $s = -p_w$. Moreover, the equivalent fluid pressure in Eq. 2 is written as: $p_f = S_w p_w$

4 Modelling of In-Situ Overcoring Experiment

A study was carried out to numerically investigate whether the in-situ behaviour observed during the experiment can be replicated. Modelling was performed using the finite element code “Code-Bright” developed by the Geotechnical Engineering Department of the Technical University of Catalonia (Olivella et al. 1996).

Figure 4 shows the geometry and the finite element discretization of the overcoring model. The total size of the model was 4 m × 4 m × 1.8 m. The model boundaries were constrained in all directions (i. e. zero-displacement and no-flow boundaries). The initial pore pressure was set to 200 kPa according to the measured values prior to overcoring. An anisotropic initial stress state ($\sigma_1 = 6$ MPa, $\sigma_2 = 4.5$ MPa, $\sigma_3 = 2.5$ MPa) was considered with the minor principal stress oriented along the core axis. The initial porosity of the Opalinus Clay is assumed to be $n_0 = 0.18$. In addition, a transversely isotropic material model was used to describe the mechanical behaviour of the Opalinus Clay. The material parameters required for the numerical model are summarized in Table 1. According to the data measured during the HM-B experiment, the changes in pore water pressure are negligible when the distance between the overcoring borehole and the tensiometer (i. e. point A in Figure 2) is more than 500 mm. Therefore, in the presented model, the focus was on the hydro-mechanical processes, which take place close to the sensor location. Therefore, the total drilling distance considered in this numerical model is 820 mm (i. e. 550 mm ahead of the sensor location and 270 mm behind the sensor location). Accordingly, the drilling process was modelled in eight steps by gradually removing the excavation rings as shown in Figure 4c (i. e. the elements E1 to E8). The total excavation time for this numerical model was assumed to be 58 minutes, corresponding to drilling speed applied in the experiment. Figure 4d shows the orientation of bedding planes with respect to the core

axis. As depicted in this figure, the bedding planes are almost parallel to the core axis with a dip angle of 45° . During the drilling phase, the hydraulic boundary conditions were modified at those areas, which are excavated. For this reason, during each excavation step, a constant fluid pressure of 0.1 MPa was applied to the boundaries of the excavated ring, indicating a connection to the tunnel atmosphere. When the last segment was excavated, all the conditions were kept unchanged for almost five hours. During this step, the changes of pore water pressure were calculated at the sensor location and the results were compared to the field measurements.

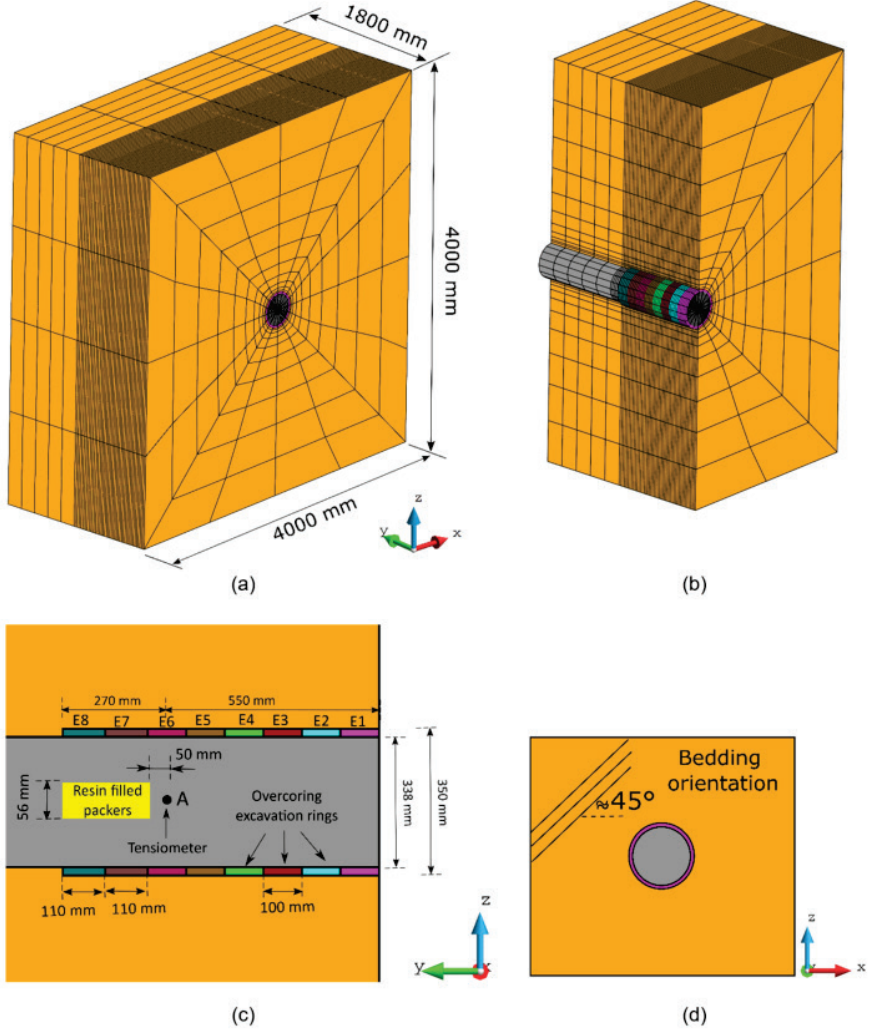


Figure 4: The geometry and mesh of the model; (b) a cross-section of the model in YZ-plane showing the layout of the core and the excavation rings; (c) side-view of the model showing the location of the tensiometer; (d) front-view of the model showing the bedding orientation.

Table 1: Material parameters utilized to simulate the HM-B experiment

Description	Parameters	Value
Stiffness properties of Opalinus clay	Young's Modulus E_{\perp} [MPa]	3000
	Young's Modulus E_{\parallel} [MPa]	1500
	Poisson's Ratio ν_{\perp}	0.2
	Poisson's Ratio ν_{\parallel}	0.2
	Shear Modulus G [MPa]	1400
Properties of water	Bulk Modulus C_w [MPa]	2222
	Surface Tension [N/m]	0.072
Intrinsic permeability of Opalinus clay	Permeability k_{11} [m ²]	1e-18
	Permeability k_{22} [m ²]	4e-18
	Permeability k_{33} [m ²]	1e-20
Water retention curve (Van Genuchten model)	Parameter P_0 [MPa]	15.5
	Parameter λ	0.33

Figure 5 shows the pore water pressure along the borehole developed during the overcoring phase. The pore pressure in front of the excavation face increases when the drilling tool moves toward the tensiometer. It is important to mention that the pore pressure inside the core and around the excavated region reduces to values less than atmospheric pressure. Under such conditions, a transition from a fully saturated to a partially saturated state may take place when the confining pressure applied to the core rapidly drops to zero due to the excavation. Therefore, the effect of capillary suction on the HM response becomes important. A slight desaturation can considerably influence the pore pressure response. This is due to the fact that the existence of a small amount of vapor in the pore spaces can significantly change the poroelastic properties of the material (e.g. Skempton's B, etc.). Figure 5 compares the modeling results with the values obtained during the HM-B experiment. The modelling results are in good agreements with the observed in-situ behaviour and can capture the pore pressure evolution within the experiment.

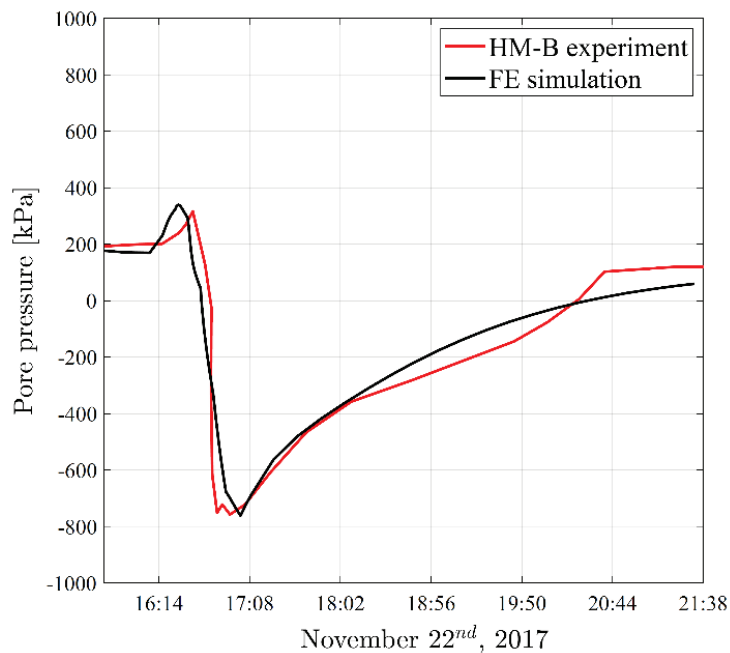


Figure 5: The measured pore pressure versus the obtained values by the employed FE model.

5 Pore Pressure Development around Tunnels in Opalinus Clay

The results of HM-B experiment revealed that negative pore pressures may potentially develop in Opalinus Clay under undrained unloading condition. Similar to the HM-B experiment, the rock mass around an underground tunnel may experience unloading due to excavation. Therefore, a conceptual numerical model is presented to evaluate the pore pressure response in the near-field of tunnels excavated in Opalinus Clay. This numerical analysis relies on the modeling concepts that were established during the HM-B experiment. The geometry of the model is shown in Figure 6. The multi-physics finite element modelling framework Moose was used to simulate the tunneling process (Permann et al. 2020). The tunnel is modeled as an unsupported, circular opening with a diameter of 5 m that is sequentially excavated. The total excavation distance in this model is 7 m starting from point O₁ towards point O₂ (see Figure 6). The entire tunnel length was excavated in 168 hours with an advancement rate of 1 m/day. Thereafter, the excavated area was left unsupported for ca. 190 hours in order to better understand the pore pressure dissipation in the vicinity of the excavation. The initial pore water pressure and in-situ stress are similar to overcoring experiment.

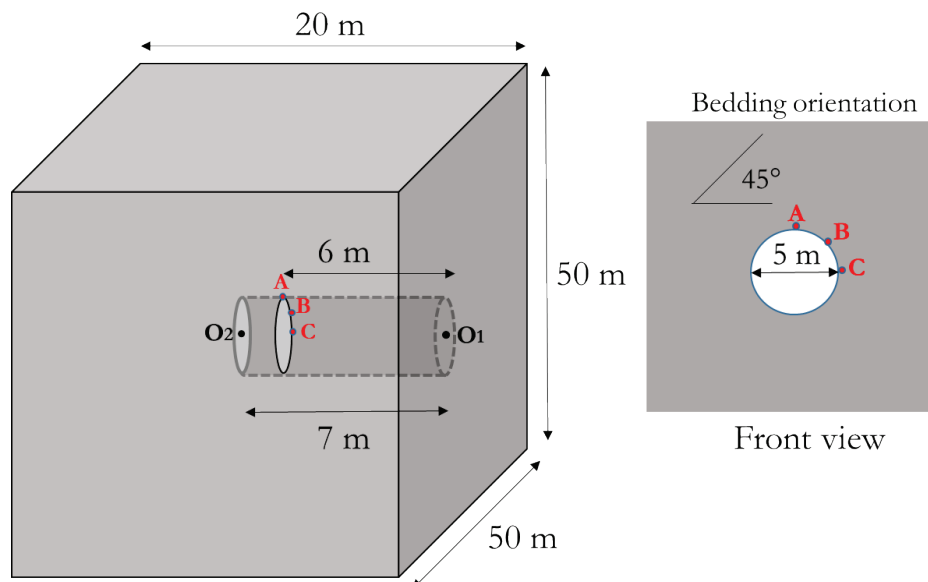


Figure 6: The geometry of a tunnel modeled and the location of the observation points.

Figure 7 shows how the pore pressure development takes place around the tunnel during the excavation process. With tunnel advancement, the short-term pore-pressure increases significantly ahead of the tunnel face. This behavior is due to the coupling of mechanical deformation with the hydraulic response in front of the tunnel face. The pore pressure increase can be observed up to a distance of 2 - 3 tunnel diameter ahead of tunnel face. However, the pore pressure decreases immediately after excavation at the tunnel circumference where the rock mass has experienced stress-relief. This observation is qualitatively in agreement with the field measurement at Mont Terri URL. However, the numerical results show that there might be even “sub-atmospheric” pore pressure in the near-field of the tunnel.

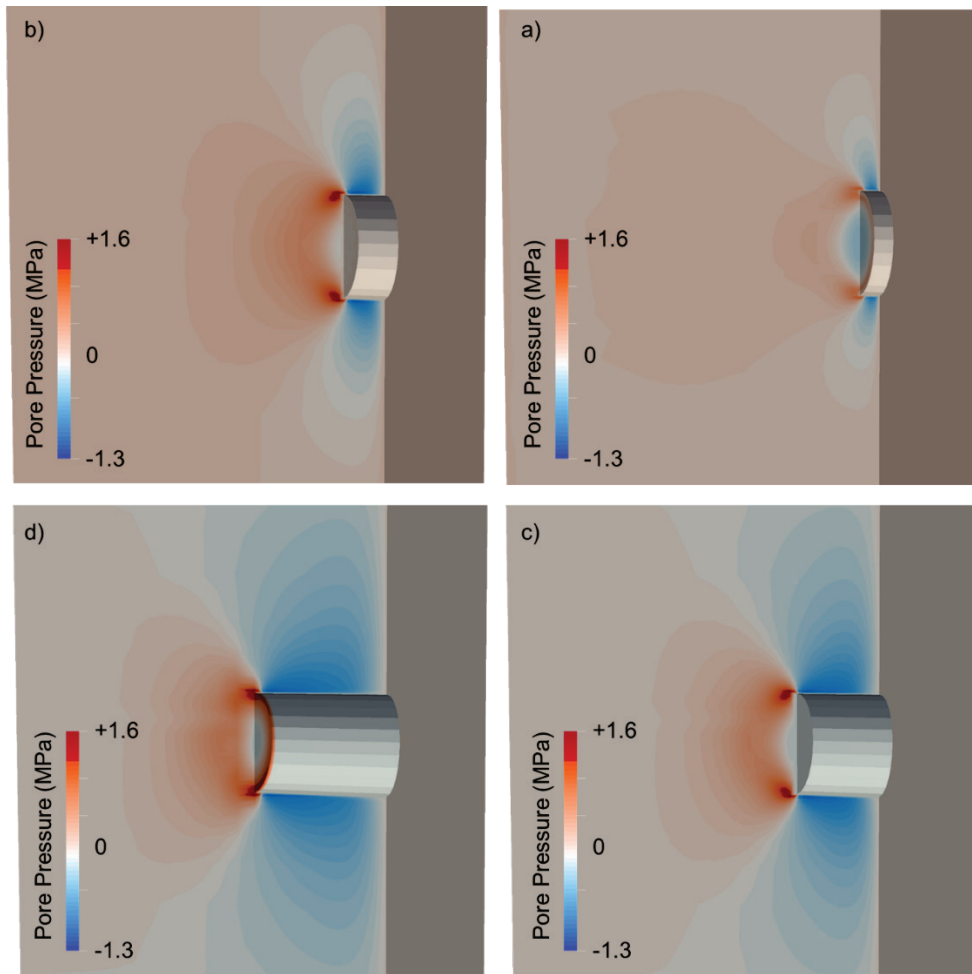


Figure 7: Pore pressure development around the simulated tunnel at four different stage of excavation.

Figure 8 shows the pore pressure evolution at three selected points located close to the boundary of tunnel. The pore pressure starts to decrease rapidly as the excavation face gradually reaches to the observation points (less than ca. 0.5 tunnel diameter). The pore pressure reduction continues even after the excavation face passes the monitoring points due to stress redistribution. Once the face of the tunnel passed the observation points and the stress redistribution is completed, a gradual pore pressure dissipation occurs. The pore pressure at the roof and the sidewall of the tunnel (Point A & C) reduces to a value lower than the atmospheric pressure. The extent of pore pressure reduction at Point B is not as significant as the roof and the sidewall of the tunnel. The observed pattern and distribution of the pore pressure around the tunnel is associated with the material anisotropy, bedding orientation and anisotropy of in-situ stresses.

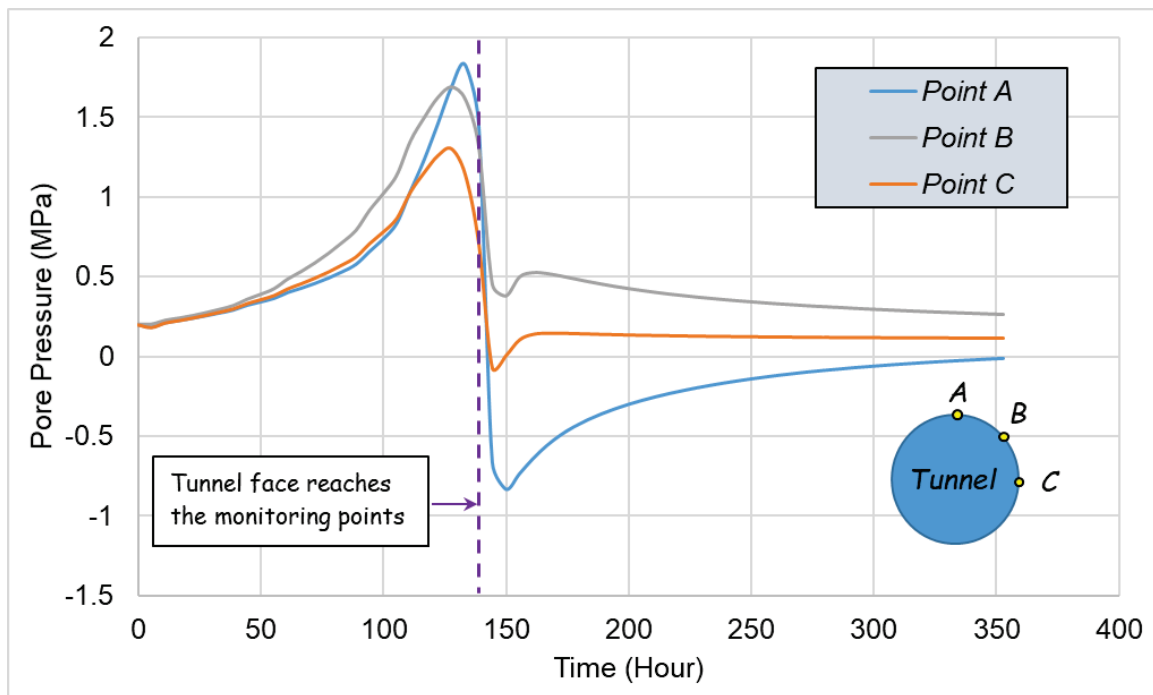


Figure 8: Pore pressure evolution at selected observation points.

6 Conclusions

The HM-B experiment reveals that the negative pore pressure can be developed in Opalinus Clay under undrained unloading condition due to capillary effects. It was shown that the numerical modelling is able to replicate the in-situ behaviour once the effect of desaturation is incorporated. These results suggest that the pore-pressure response typically observed at the Mont Terri Rock Laboratory is a consequence of (1) the anisotropic in-situ state of stress, (2) the transversal isotropic stiffness of Opalinus Clay, (3) the anisotropy ratio and (4) the orientation of bedding with respect to the tunnel axis. In addition, dilatancy accompanying failure may contribute to pore pressure changes within the excavation damage zone typically observed around excavations at the Mont Terri Underground research lab. Plasticity was not considered in the presented models, but is part of ongoing work.

An important outcome of this numerical study is that pore-pressure changes associated with tunnel excavation can lead to development of short-term negative pore-pressures, which may contribute to rock mass strength improvement. In case of a transversely isotropic model, certain zones around the excavation experience sub-atmospheric pore-pressures. The exact location and extension of these zones depends on the assumption of the in-situ stress state, anisotropy ratio and the orientation of bedding with respect to the tunnel axis.

7 Reference

- Amann, Florian, Wild, K. M., Loew, S., Yong, S., Thoeny, R. & Frank, E. (2017). Geomechanical behaviour of Opalinus Clay at multiple scales: results from Mont Terri rock laboratory (Switzerland). *Swiss Journal of Geosciences*, 110(1), 151–171. <https://doi.org/10.1007/s00015-016-0245-0>

- Corkum, A. G. & Martin, C. D. (2007). The mechanical behaviour of weak mudstone (Opalinus Clay) at low stresses. *International Journal of Rock Mechanics and Mining Sciences*, 44(2), 196–209. <https://doi.org/10.1016/j.ijrmms.2006.06.004>
- Giger, S. B., Marschall, P., Lanyon, B. & Martin, C. D. (2015). Hydro-mechanical response of Opalinus Clay during excavation works - a synopsis from the Mont Terri URL. *Geomechanics and Tunneling*, 8(5), 421–425. <https://doi.org/10.1002/geot.201500021>
- Hassanizadeh, M. & Gray, W. G. (1979). General conservation equations for multi-phase systems: 2. Mass, momenta, energy, and entropy equations. *Advances in Water Resources*, 2, 191–203. [https://doi.org/10.1016/0309-1708\(79\)90035-6](https://doi.org/10.1016/0309-1708(79)90035-6)
- Lettry, Y. & Roesli, U. (2017). Mont Terri HM-B Experiment Phase 21 - Saturation. Mont Terri Technical Note TN 2017-70, Solexperts AG, Monchaltorf, Switzerland.
- Martin, C. D., Lanyon, G. W., Bossart, P. & Bluemling, P. (2004). Excavation disturbed zone (EDZ) in clay shale: Mont Terri. Mont Terri Technical Report, TR 01-01. Federal Office of Topography (swisstopo), Wabern, Switzerland. www.mont-terri.ch.
- Olivella, S., Gens, A., Carrera, J. & Alonso, EE. (1996). Numerical formulation for a simulator (Code–Bright) for the coupled analysis of saline media. *Eng. Computation*, 13, 87–112
- Permann, C. J., Gaston, D. R., Andrš, D., Carlsen, R. W., Kong, F., Lindsay, A. D., Miller, J. M., Peterson, J. W., Slaughter, A. E., Stogner, R. H. & Martineau, R. C. (2020). MOOSE: Enabling massively parallel multiphysics simulation. *SoftwareX*, 11, 100430. <https://doi.org/10.1016/j.softx.2020.100430>
- Schrefler, B. A., Sanavia, L. & Majorana, C. E. (1996). A multiphase medium model for localisation and postlocalisation simulation in geomaterials. *Mechanics of Cohesive-Frictional Materials*, 1(1), 95–114. [https://doi.org/10.1002/\(SICI\)1099-1484\(199601\)1:1<95::AID-CFM5>3.0.CO;2-D](https://doi.org/10.1002/(SICI)1099-1484(199601)1:1<95::AID-CFM5>3.0.CO;2-D)
- van Genuchten, M. T. (1980). A Closed-form Equation for Predicting the Hydraulic Conductivity of Unsaturated Soils1. *Soil Science Society of America Journal*, 44(5), 892. <https://doi.org/10.2136/sssaj1980.03615995004400050002x>
- Vietor, T., Armand, G., Nyonyoya, S., Schuster, K. & Wieczorek, K. (2010). Excavation induced damage evolution during a mine-by experiment in Opalinus clay. In *Proceedings of the 4th Int. Meeting on Clays in Natural & Engineered Barriers for Nuclear Waste Confinement*, Nantes, France.
- Wild, Katrin M. & Amann, F. (2018). Experimental study of the hydro-mechanical response of Opalinus Clay – Part 2: Influence of the stress path on the pore pressure response. *Engineering Geology*, 237, 92–101. <https://doi.org/10.1016/j.enggeo.2018.02.011>
- Yong, S. (2007). A three-dimensional analysis of excavation-induced perturbations in the Opalinus Clay at the Mont Terri Rock Laboratory. Ph.D. dissertation, Swiss Federal Institute of Technology, Zürich, Switzerland. <https://doi.org/10.3929/ethz-a-005591763>

Sinkholes over Deep Caverns

Tagesbrüche über tiefen Kavernen

W. Minkley, C. Lüdeling

IfG - Institut für Gebirgsmechanik GmbH
Friederikenstr. 60, 04279 Leipzig, Germany

Abstract

Sinkholes are possible over deep brine-filled caverns; the basic mechanism is the sliding of large columns of rock along overburden joints under the influence of joint fluid pressure. A prerequisite is the loss of salt back integrity, i. e. a hydraulic connection of the brine in the cavern to overburden joints with pressure-driven percolation. We present some examples, conceptual and analytical estimates and results of numerical studies illustrating the mechanism in single-cavern situations and cavern fields with mutual influence.

Zusammenfassung

Tagesbrüche können auch über tiefen solegefüllten Kavernen auftreten. Der zugrundeliegende Mechanismus ist das Abgleiten von großen Gebirgssäulen entlang von Deckgebirgsklüften unter dem Einfluss von Kluftwasserdrücken. Eine notwendige Bedingung ist der Integritätsverlust der Hangendbarriere, d. h. eine hydraulische Verbindung zwischen der Sole und dem Kluftsystem im Deckgebirge mit druckgetriebener Perkolation. Wir diskutieren einige Beispiele, betrachten konzeptionelle analytische Abschätzungen und präsentieren Ergebnisse numerischer Untersuchungen an Modellen von Einzelkavernen sowie Kavernenfeldern mit gegenseitiger Beeinflussung.

1 Introduction

It is often assumed that sinkholes cannot form above solution mining caverns deeper than about 500 m, as in greater depth, the critical span (i. e. the span at which a cavern becomes unstable) is larger than plausible cavern diameters, and overburden strength is sufficient. However, this disregards the effects of fluid pressure and pressure-driven percolation on overburden joints. Rock masses generically contain joints and joint sets, which are considerably weaker than the intact rock, and fluid pressure lowers the effective stress and the shear strength. Thus, the critical spans can be much lower, such that sinkhole with diameters in the order of tens of metres are possible. A necessary condition is a hydraulic connection from the brine-filled cavern to the overburden, such that the cavern pressure can be transferred to overburden joints, and brine pressure in the cavern cannot approach lithostatic pressure.

1.1 Examples of Sinkholes over Caverns

In a review of sinkholes above solution mining caverns, Bérest (2017) concludes that sinkholes can form if the brine gets into direct contact with the overburden. He develops two conceptual models of sinkhole formation, depending on the geomechanical properties of the overburden. Pertinent to our discussion is the “piston” model (see Figure 1), where the cavern moves upwards into the overburden until it reaches a strong layer, which then drops into the cavern as an intact block of rock (the piston). The walls of the resulting sinkhole are thus straight and vertical to a good approximation.

Since the piston itself does not fracture, there is little bulking, and sinkholes can form even over deep caverns, provided the sliding column of rock is sufficiently long.

For a rock sliding instability to occur, the weight of the block must be larger than the maximum retaining forces, which comprise the brine pressure from below and the frictional shear forces along the lateral surface. The latter is determined by the coefficient of friction (assuming a rock block bounded by cohesionless joints) and the horizontal effective stress. Here, it is crucial to note that the horizontal stress is commonly lower than the lithostatic stress, and, crucially, that a joint fluid pressure can significantly lower the acting shear force, and thus facilitate block sliding (Minkley et al. 1990) in situations where it is conventionally considered impossible.

We will briefly review some examples of sinkholes over salt cavities.

The Haoud Berkaoui crater (Morisseau 2000; see Figure 2) was formed over a dissolution cavity created in about 550 m depth by an improperly abandoned oil well that caused a hydraulic connection between two aquifers. The crater has a diameter of about 200 m, with vertical walls. Bérest (2017) considers it likely that the crater was formed by a sudden drop of the rock piston into the cavity.

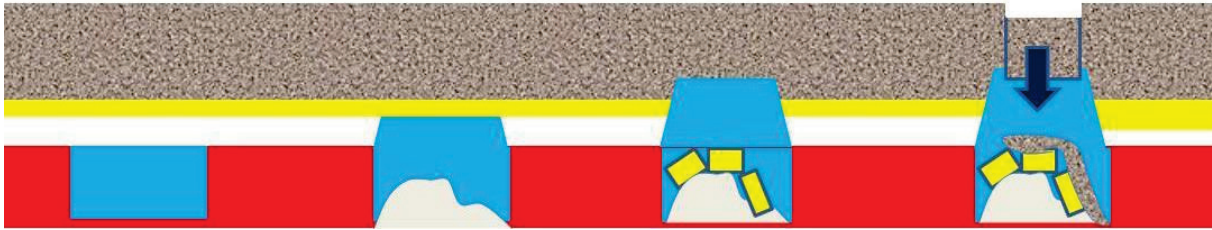


Figure 1: Sketch of the “piston” model of cavern collapse (after Bérest 2017).



Figure 2: The Haoud Berkaoui sinkhole (Morisseau 2000).

In 2012, a sinkhole was discovered in Bayou Corne, Louisiana, near the edge of the Napoleonville salt dome (van Sambeek 2014). It turned out that the Oxy3 cavern, mined in a depth from about 1050 m to 1700 m, was closer to the salt dome flank than previously planned, and its side wall had been breached; sediments flowed into the cavern along the flank. The cavern was essentially filled when the sinkhole appeared at the surface (see Figure 3).

Bérest (2016) raises the question of “How did a 1000-1500 m (3000-5000 ft.) high cylinder of rock with an average diameter of a few dozen meters drop into the cavern along the dome edge?” and concludes that this process requires that cohesion and

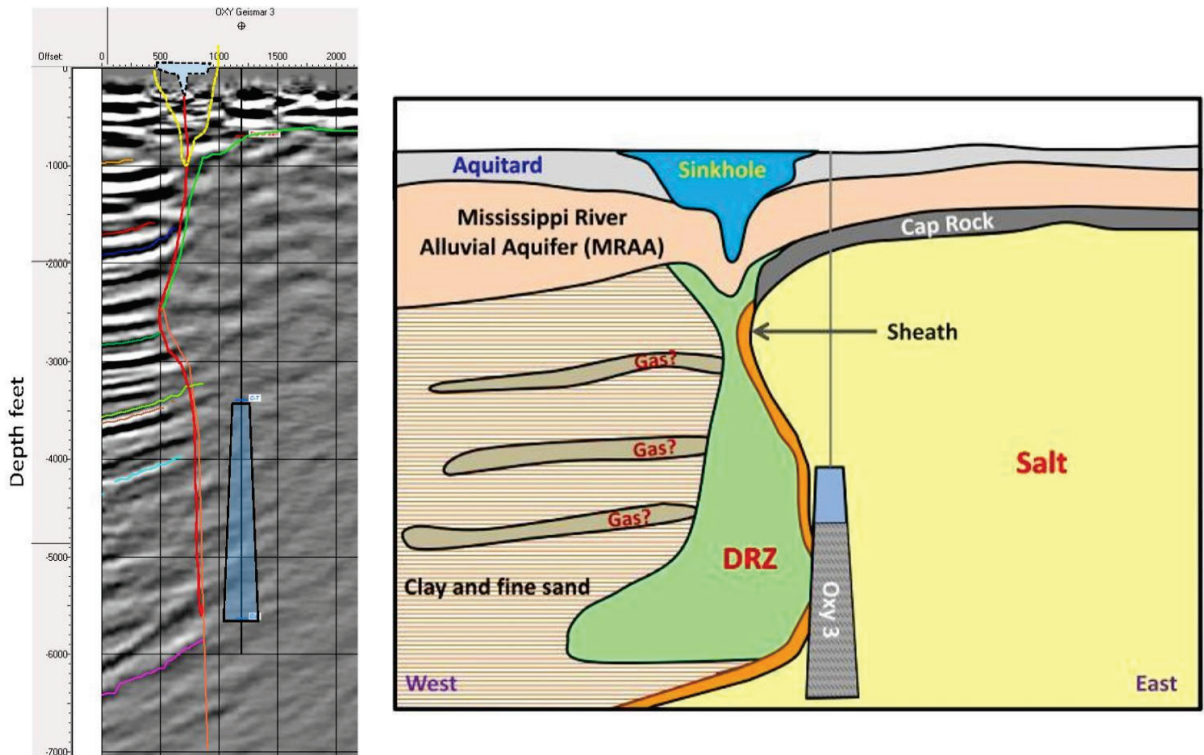


Figure 3: NW-SE Seismic Line with the Oxy3 cavern and the flank of the Napoleonville salt dome (left panel); geological sketch (right panel, van Sambeek 2014).

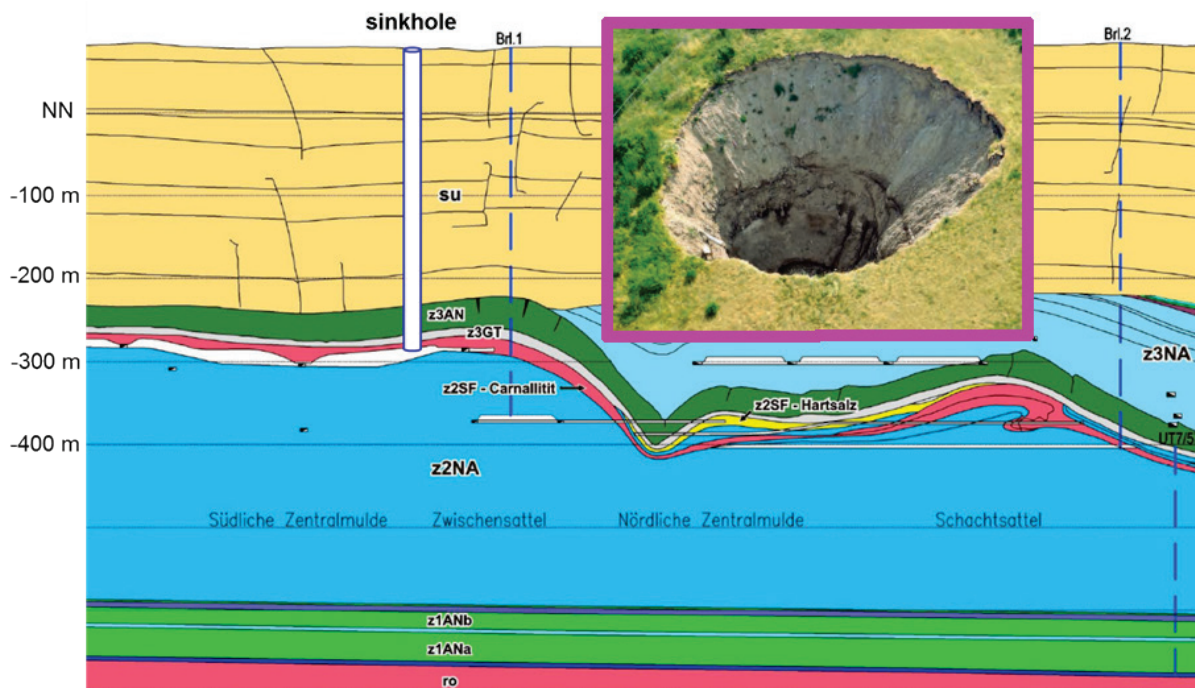


Figure 4: Sketch of the Solvayhall mine and location of the 2010 sinkhole over the southwestern panels where there is no salt back above the potash seam.

friction angle need to be very small or zero. However, taking into account the, plausibly mineralised, water along the edge of the salt dome (see Section 2.2), movement is possible for realistic values of the friction angle. The almost vertical edge of the salt dome is a prime candidate for pressure-driven sliding.

Similar sinkholes can appear over conventional mines if the salt back is lost, or not present at all. The Solvayhall mine in central Germany excavated rock salt, Carnallite and hard salt from the Staßfurt member of the Zechstein formation in a depth of 350 m to 480 m (LAGB, 2012; see Figure 4). Over the southwestern part of the mine, the Leine rock salt which provided the salt back in most parts, was missing, and the Carnallite excavations was covered just by anhydrite and the Buntsandstein overburden. First fluid inflows were observed in 1962, and the mine was abandoned in 1967. Until 1971, three sinkholes formed, and in 2010, a fourth one was discovered, with a narrow chimney from the surface to the flooded Carnallite field.

We finally consider an example of a cavern field in a larger depth of more than 1000 m. The caverns are located in a salt stratum of moderate thickness which includes other evaporitic and sedimentary intercalations. The overburden consists of sedimentary rocks, mainly sandstones. The field was operated for brine production over decades and had been shut down for some time, caverns filled with brine. Due to the leaching process, some pillars and portions of the salt back have been partially or completely dissolved. As a result, a number of caverns are hydraulically connected, and several of those have joined into a large void space. Many caverns were not accessible anymore because of well damage in the overburden when operation was ended, and the field could not be properly abandoned. In summary, the cavern field contains an unknown void volume in a configuration with hydraulic connection to the overburden and a weak support system.



Figure 5: Sinkhole over the edge of a cavern field in a depth of more than 1000 m (Photo: OrthoPixel).

Two decades after the field was closed, a sinkhole appeared near the edge of the cavern field, see Figure 5. This came as a surprise since earlier geomechanical studies had come to the conclusion that the thick overburden would preclude sinkhole formation.

2 Conceptual Geomechanical Model of Sinkhole Formation

2.1 Basic Prerequisites

The development of sinkholes, as presented in the previous section, generically proceeds along the following failure sequence:

1. In the salt formation, cavities with sufficient volume and span are generated.
2. The salt back, i. e. the hydraulic barrier to the overburden, loses its integrity, gets dissolved or breaks into the cavity, or is not present at all.
3. The overburden cannot span the brine-filled cavity without fracturing anymore and starts to collapse into the cavity.

The further progress of the collapse process depends on the hydromechanical properties of the overburden rocks. Bérest (2017) distinguishes two general mechanisms, the “piston” and the “hourglass” model. In both cases, the cavern roof progresses upwards until it reaches a strong layer of rock (stoping). If that layer is breached, soft material above will flow into the cavern (the “hour-glass” model), while in jointed stronger rock, a larger chunk will slide as a single block (the “piston”).

The latter mechanism is particularly important for deep caverns, because block sliding is not associated with significant bulking (i. e. volume increase of the fracturing and falling material), so that the cavern volume can more or less directly translate into sinkhole volume at the surface. Since such rock blocks are supported by the lateral stress, sinkhole formation is aided by low lateral confinement (e.g. over mining edges or other extension zones) and low shear strength on vertical joints, faults or weakness planes in the overburden.

We should stress the crucial rôle of fluids, in particular for brine-filled caverns:

- If the cavern is contained in intact rock salt, which is impermeable to fluids, brine pressure will support the salt back and overburden, and sinkhole cannot form. On the other hand, if the integrity of the cavern is lost, fluids can migrate into porous or jointed overburden.
- If the brine is in contact with overburden joints and their joint water, brine pressure will propagate along the joints and lower the effective stress. The brine can also move along joints by pressure-driven percolation.
- This effect will be particularly pronounced if initial fracture processes generate dynamic overpressures that can rupture rock bridges similar to a hydrofrac.

2.2 Analytical Estimate of Limit Equilibrium

Load limit equilibrium theory allows us to develop a conceptual model of the failure (Minkley et al. 1990): If the span of an underground cavity exceeds a critical value, the weight of the overlying column of rock cannot be balanced by the load-bearing forces, which comprise

- the frictional (shear) force along the circumference of the block, and
- the supporting force at the lower face of the block provided by the brine pressure in the cavern.

We assume that the joints that delineate the rock column are vertical and completely traverse the overburden. This is the most critical case and provides a conservative lower bound on stability.

Consider a column of rock with density ρ , cross-sectional area A , circumference U and height z_D , so that its weight is $W = g\rho A z_D$.

The cavern has an internal brine pressure p_{int} at the roof; the horizontal stress in the rock mass is given, as function of the lithostatic pressure σ_{lith} , by $\sigma_{\text{hor}} = \lambda \cdot \sigma_{\text{lith}} = \lambda \cdot g\rho z$ with the lateral stress coefficient λ . Along the circumference of the rock column, the shear resistance is determined by the coefficient of friction μ , the horizontal stress and the joint water pressure $p_{\text{joint}} = g\rho_{\text{fl}}z$ with fluid density ρ_{fl} .

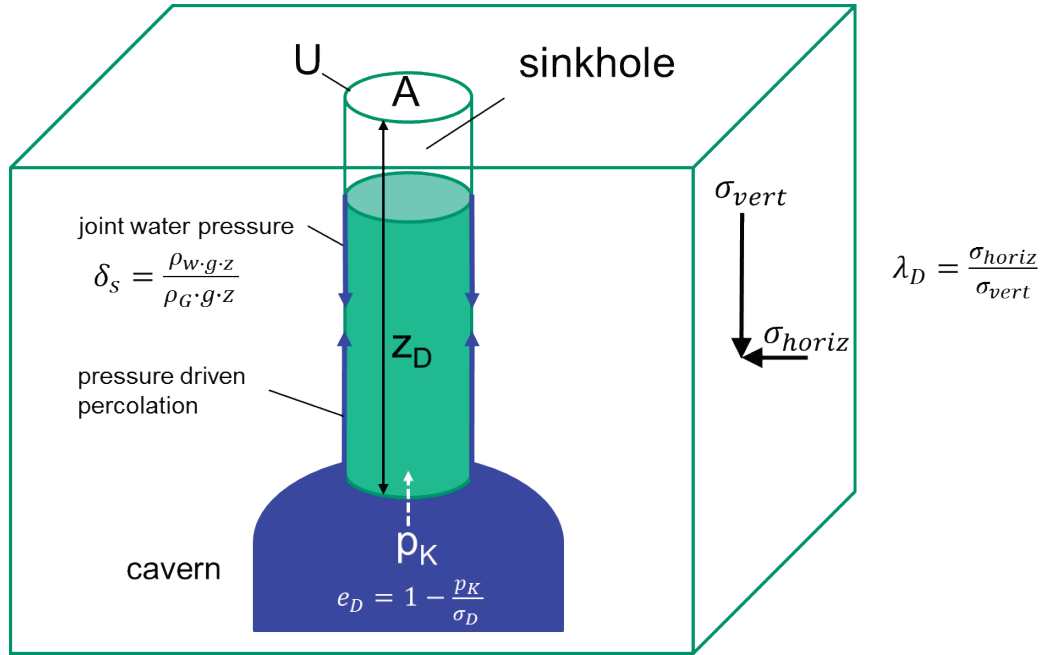


Figure 6: Conceptual model of sinkhole formation.

Hence, the supporting force is the sum of the brine force from below, $A \cdot p_{\text{int}}$, and the frictional force $\frac{1}{2} U g \mu \rho (\lambda - \delta) z_D^2$, where $\delta = \rho_{\text{fl}} / \rho$ denotes the ratio of joint fluid and rock densities.

For a given shape, the weight of a rock column scales as the square of the circumference, so small columns will be stable while large ones are not. Rearranging terms, the critical ratio of area to circumference is found to be

$$\left(\frac{A}{U}\right)_{\text{crit}} = \frac{1}{2} \mu \frac{\lambda - \delta}{1 - \frac{p_{\text{int}}}{\sigma_{\text{lith}}}} z_D.$$

It is immediately apparent that for a properly abandoned cavern, where the brine pressure at the roof approaches the lithostatic pressure, the critical circumference goes to infinity. In other words, over a tightly shut cavern in salt rocks, no sinkhole can form. On the other hand, sinkhole formation is favoured by low lateral stresses and large fluid pressures in the overburden (i. e. low effective stress).

Clearly, sinkhole formation is inhibited by a large lateral stress coefficient, as the lateral stress provides the frictional force holding up the rock column. Generally, there is an elastic and a tectonic component to the lateral stress,

$$\lambda = \frac{\nu}{1 - \nu} + \text{tectonic.}$$

For rocks with Poisson ratio of $\nu = 0.33$, the elastic contribution is $\lambda = 0.5$. Large-scale stress surveys show that bedded salt formations tend to decouple the overburden from the recent tectonic stresses in the basement (Groß et al. 1986), since the viscous salt layer mechanically isolates the overburden from the basement. The overburden stress is mainly controlled by the lithology of the rocks, elastic stiffness contrasts and the regional geology, i. e. (syn)clines and fault zones (Röckel, Lempp 2003).

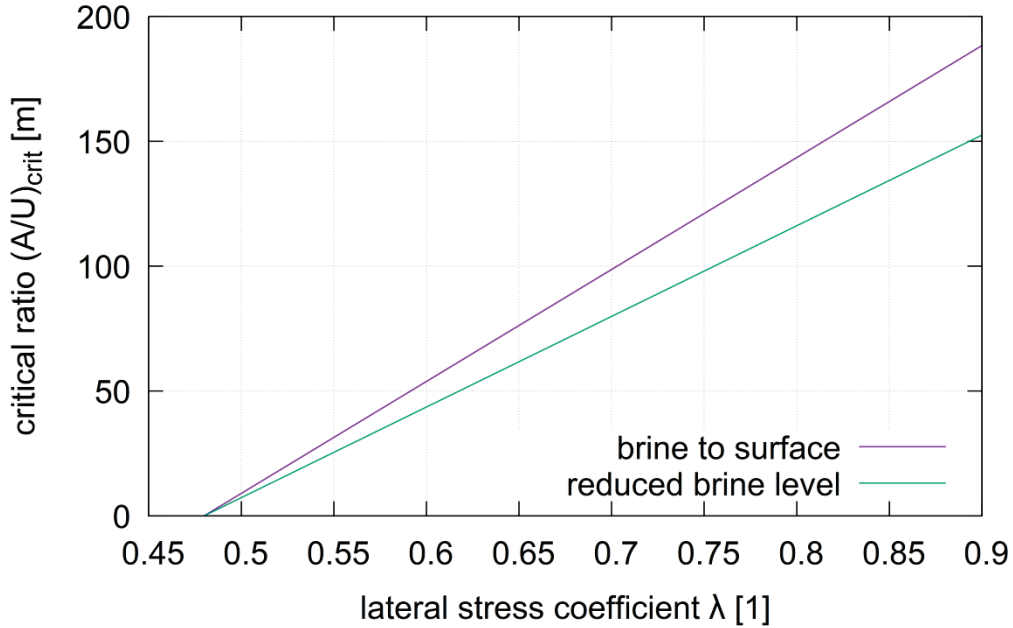


Figure 7: Critical ratio of area to circumference as a function of the lateral stress coefficient for a cavern with brine column up to the surface (violet) and with internal pressure reduced by 3 MPa (green) (cavern in 1000 m depth, angle of friction $\phi = 25^\circ$, $\rho = 2.5 \text{ t/m}^3$).

The ratio of area to circumference depends on the shape of the sinkhole and its size. For a circle of diameter D , we have

$$\left(\frac{A}{U}\right)_{\text{crit,circle}} = \frac{1}{4}D.$$

An ellipse with major and minor diameters D and $d = D/2$ has

$$\left(\frac{A}{U}\right)_{\text{crit,ellips}} \approx \frac{1}{6}D.$$

Finally, for a rectangular sinkhole of width W and length L

$$\left(\frac{A}{U}\right)_{\text{crit,rectangle}} = \frac{W}{2\left(1 + \frac{W}{L}\right)}.$$

In the limit of $W/L \rightarrow \infty$, corresponding to a two-dimensional model, this tends to $W/2$.

In Figure 7, we have plotted the critical ratio of area to circumference as a function of the lateral stress coefficient λ for different internal cavern pressures. As an example, for a cavern without salt back in a depth of 1000 m and a lateral stress coefficient of $\lambda = 0.5$, both lines in Figure 7 give a critical ratio of $(A/U)_{\text{crit}}$ slightly below 10 m. For an elliptic sinkhole under these boundary conditions, we can estimate major and minor diameters of $D \approx 60$ m and $d \approx 30$ m, similar to the example in Figure 5.

The block sliding mechanism does not generate significant porosity. Hence, surface sinkholes can appear even for thick overburden.

The conceptual model discussed here corresponds to the piston model of Bérest (2017). It is crucial that effective lateral friction is reduced by the joint water pressure and pressure-driven percolation (effective stress concept) – only this fluid pressure effect enables sinkhole with diameters of a few tens of metres.

One can plausibly assume that during the sliding process itself, pressure in the joint water and brine changes dynamically, hydraulically fractures joints and further lowers or completely lifts the shear resistance. Thus, pressure-driven processes cause the chimney-like cylindrical fracture surfaces.

Due to the crucial importance of fluid pressure effects along joints, a numerical study of such sinkholes requires discontinuous models and coupled hydromechanical simulations.

3 Discontinuous Modelling and Hydromechanical Coupling

In contrast to many situations that are well described by a continuum model, sinkhole formation and block sliding instabilities in overburden are discontinuous processes. The overburden usually is not viscous, but often brittle, rocks slide along fractures with adhesive peaks and softening and hydromechanical coupling is crucial for a stability analysis. Hence, adequate constitutive models for rocks and joints, as well as a consistent discontinuous modelling approach.

3.1 Constitutive Models for Rocks and Joints

The deformation and fracture properties of saliferous rocks are not adequately described by the usual constitutive models include with numerical codes. For example, rock salt behaves plastically and ductile under load, with strongly nonlinear strength properties, hardening and softening. On the other hand, it is distinguished by pronounced viscous deformation, i. e. ongoing deformation under constant loading.

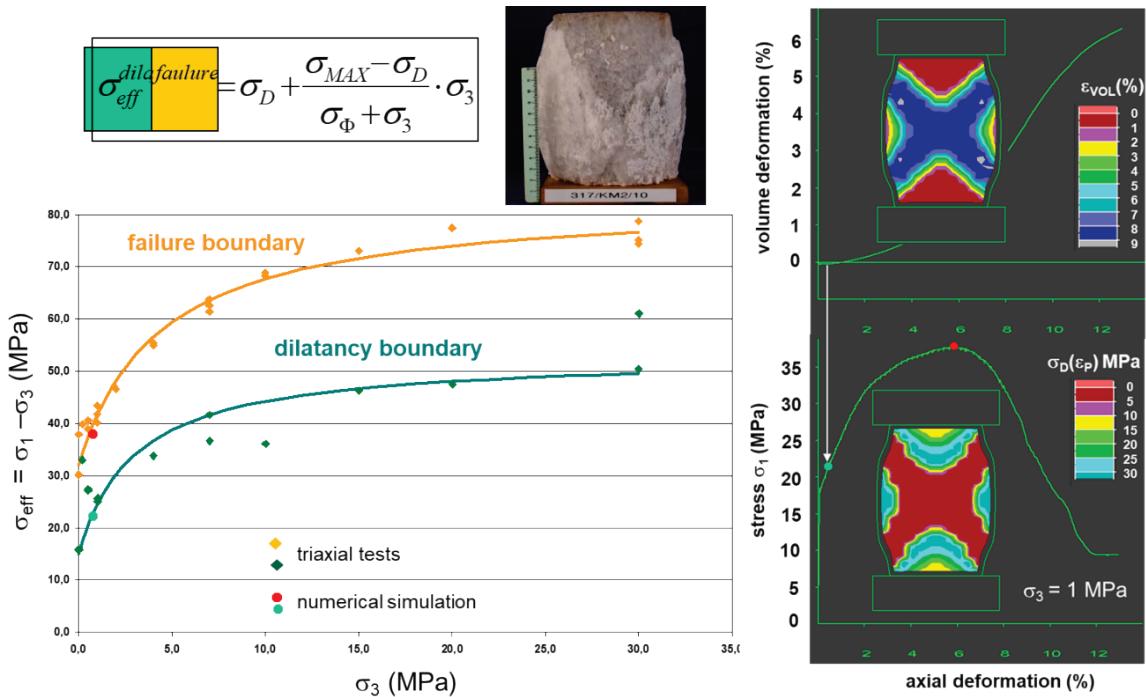


Figure 8: Sketch of the visco-elasto-plastic model of the IfG with yield boundary (left) and recalculation of triaxial tests (right)

The common Mohr–Coulomb fracture criterion, for which the yield or failure boundary is a function of minor principal stress only, is a well-established empirical approach for shear and tensile failure of rocks. The intermediate principal stress does not influence the yield boundary in this model. True triaxial testing confirms the dependence on the minor principal stress, but the linear relationship is shown to be incorrect, in particular for greater depths. Hence, the Mohr–Coulomb criterion should be regarded as a rough approximation, appropriate for high-strength rocks or low confining stresses.

On the other hand, salt rocks can soften and fail under load. In this context, softening implies that the rock strength decreases with increasing deformation (strain softening), associated with the localisation of deformation in shear zones. Depending on the properties of the rock mass and the loading conditions, softening can proceed in various ways. Sudden softening, where the load-bearing capacity strongly decreases when a certain strain is exceeded, is called brittle failure, while ductile behaviour, i. e. gradual softening, is typical for e.g. sylvinitic. Ideal plastic flow corresponds to deformation without softening.

Physically, softening is caused by the formation and accumulation of tiny fractures and defects in the salt grains. With progressing deformation, microcracks coalesce into macroscopic fractures and shear bands, until the rock approaches a residual strength determined by friction on the macroscopic shear surfaces. The formation of these is associated with an increase in volume known as dilatancy.

The visco-elasto-plastic model (Minkley 2004; see Figure 8), originally developed for saliferous rocks, is based on the rheological concept sketched in Figure 4-1 and includes elastic, plastic and viscous behaviour.

The nonlinearity of the yield boundary cannot be neglected in the depth and stress regimes that are common in conventional and solution mining of salt rocks. The yield boundary is given by a nonlinear generalisation of the Mohr–Coulomb criterion (Min-

kley, Mühlbauer 2007): The yield boundary, expressed as the differential stress at failure, is given by

$$(\sigma_1 - \sigma_3)_{\text{fail}} = \sigma_D + \frac{\sigma_{\text{MAX}} - \sigma_D}{\sigma_\phi + \sigma_3} \cdot \sigma_3.$$

Here, σ_1 and σ_3 are major and minor principal stress. The failure curve is parametrised by the uniaxial compressive strength σ_D , the maximal strength σ_{MAX} and the curvature parameter σ_ϕ . These parameters are functions of plastic shear deformation ϵ to account for strain-dependent softening.

While plastic strain requires the stress to reach a boundary, viscous or creep strain develops at any nonzero shear stress. Creep deformation under constant stress is generally divided into three phases: Primary or transient creep occurs directly after the load is applied and is characterised by decreasing deformation rates. In the model, it is described by a Kelvin element. (Primary creep is of minor importance for sink-hole formation and will be neglected in the following). In the ensuing secondary or stationary phase, the creep rate is constant and the material can accrue essentially arbitrarily large deformations. The rate is controlled by the Maxwell viscosity η^M . Tertiary or accelerated creep is associated with dilatant softening and ends in creep rupture.

In the model, the strong stress dependence of secondary creep is included by a stress-dependent modified Maxwell viscosity,

$$\eta^M = \eta_0^M e^{-m\sigma_V}$$

Here, the von Mises effective stress $\sigma_V = \sqrt{3J_2}$ is defined in terms of the second invariant of the deviatoric stress.

The visco-elasto-plastic model is based on (and generalises) proved models of continuum mechanics and can be applied universally to saliferous and other sedimentary rocks. Both ductile and brittle material behaviour can be modelled.

Situations such as block sliding are fundamentally discontinuous and crucially depend on the shear properties of joints and bedding planes. Hence, a comprehensive description of the mechanical behaviour of jointed rock masses requires adequate models for shear behaviour along interfaces.

The adhesive shear model of the IfG (Minkley, Mühlbauer 2007) is based on a frictional approach similar to a Mohr–Coulomb criterion relating maximal shear stress τ_{max} and normal stress σ_N . However, the parameters are not constant: The coefficient of friction receives contributions from static and dynamic frictions, and both are subject to strain- and stress-dependent softening, as is the cohesion. Altogether, the maximum shear stress is given by

$$\tau_{\text{max}} = (1 + \Delta\mu_{\text{max}} e^{-k_1\sigma_N}) \tan(\phi_R + i_0 e^{-k_2\sigma_N}) \cdot \sigma_N + c.$$

The adhesive component $\Delta\mu_{\text{max}}$ depends on shear velocity. The adhesive shear model is thus characterised by a shear strength behaviour with an adhesive peak that occurs for fast shearing motion, with a subsequent drop in shear resistance. After failure, the shear strength decreases as a function of shear motion due to the razing of asperities.

Assume the yield function is given by a functional relation between major and minor principal stress, $\sigma_1 = \sigma_1(\sigma_3)$, with derivative

$$\sigma_1' = \frac{d\sigma_1(\sigma_3)}{d\sigma_3}$$

As shown in Nádai (1950), this implies shear and normal stresses of the failure surfaces of

$$\tau = \frac{(\sigma_1 - \sigma_3)\sqrt{\sigma_1'}}{1 + \sigma_1'}, \quad \sigma_N = \frac{\sigma_1 + \sigma_1' \cdot \sigma_3}{1 + \sigma_1'}$$

For the yield function of the visco-elasto-plastic model, we have

$$\sigma_{1(\sigma_3)} = \sigma_D + \left[1 + \frac{\sigma_{MAX} - \sigma_D}{\sigma_\phi + \sigma_3} \right] \cdot \sigma_3, \quad \sigma_1'(\sigma_3) = 1 + \frac{(\sigma_{MAX} - \sigma_D)\sigma_\phi}{(\sigma_\phi + \sigma_3)^2}$$

Using these expressions together with the maximum shear stress τ_{max} , the parameters for the adhesive shear model can be derived from laboratory strength tests. Thus, the approach provides a consistent way to model the creep and strength properties of saliferous rocks.

The fluid transport properties have been implemented in the distinct-element codes based on the underlying physical model of the generation of flow paths by opening and connecting grain boundaries. Along opened interfaces, fluid transport is modelled as joint flow. From the Navier–Stokes equations, a laminar flow between parallel plates is described by the familiar expression

$$Q = \frac{1}{12\eta} w^3 b \Delta p,$$

where Q is the flow rate, η is the viscosity of the fluid, b and w are width and opening height of the fracture, and Δp is the pressure difference between the ends. Due to the dependence on the third power of h , this relation is commonly known as “cubic law”. The flow model is modified to account for the fluid transport properties of viscous rocks such as salt: The interfaces are closed, i. e. impermeable, in the undisturbed state, and only allow fluid flow in a failed state: The interfaced need to be opened by either a sufficiently high hydraulic pressure (percolation threshold), i. e. a fluid pressure p_{fl} exceeding the normal stress plus a possible tensile strength σ_T , or by a shear stress exceeding the shear strength, leading to plastic shear strain ϵ_{plas}^S along the interface (damage threshold):

- $Q = 0$ for $p_{fl} < \sigma_N + \sigma_T$ and $\epsilon_{plas}^S = 0$,
- $Q > 0$ for $\epsilon_{plas}^S > 0$,
- $Q > 0$ for $p_{fl} > f \cdot (\sigma_N + \sigma_T)$.

The additional factor f is equal to one in undisturbed salt rock, corresponding to a Biot factor of $\alpha = 0$.

It is plausible that fluid flow starts when $p_{fl} = \sigma_N$, i. e. without considering a tensile strength, at least for wetting fluids such as brine. Additionally, the factor f can be smaller than one, allowing flow for fluid pressures below the normal stress, e.g. along faults or discontinuities.

In a continuum analysis of barrier integrity, pressure-driven percolation is conservatively captured by the familiar minimal stress criterion which does not consider the directional nature of fluid motion by pressure-driven percolation.

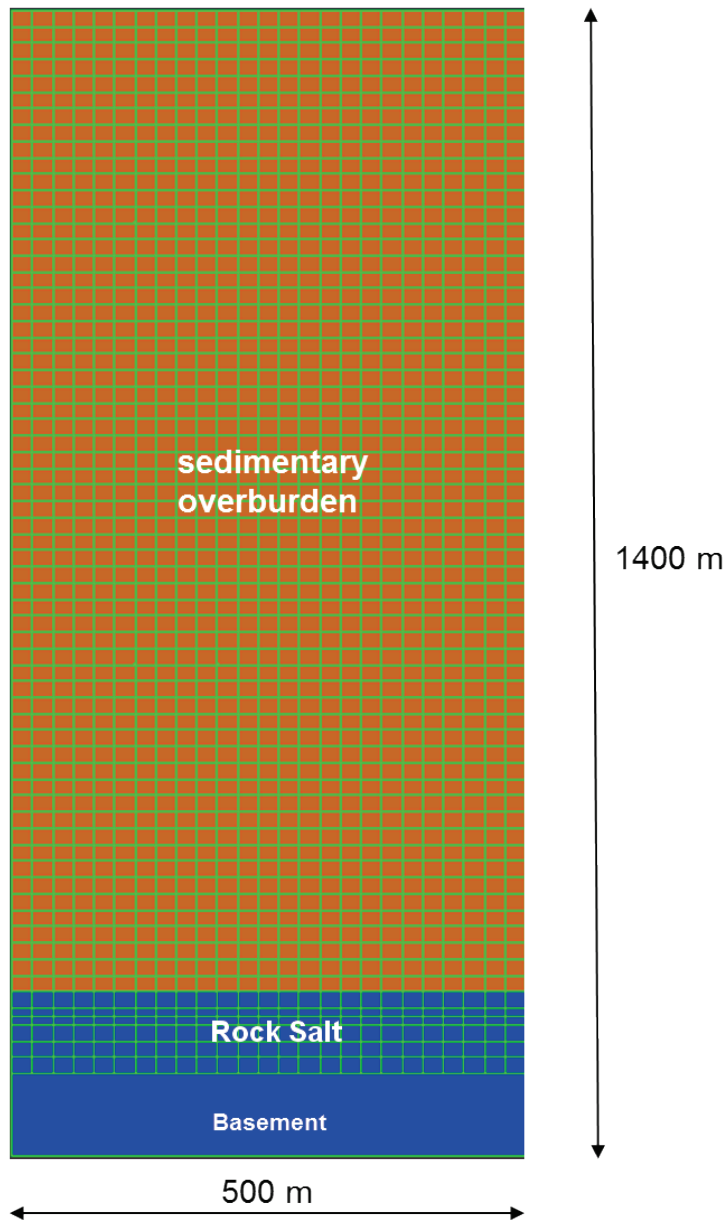


Figure 10: Simplified geomechanical model: The rock salt layer is covered by 1200 m of overburden. Modelled with an orthogonal joint system of 20 m spacing.

4 Examples from Numerical Studies

We will now present a number of examples from numerical simulations that illustrate the mechanism. As previously discussed, block sliding is a fundamentally discontinuous process and is, for relevant depth and rock mass conditions, only possible if fluid

pressure on joints is taken into account. Hence, all simulations presented here are hydromechanically coupled discontinuous, using the discrete-element code UDEC 6 (Itasca 2018). Rock salt and all joints are modelled with the visco-elasto-plastic constitutive model and the adhesive shear model (see Section 3.1), respectively; the overburden is treated as an elastoplastic (Mohr-Coulomb) material.

4.1 Sinkhole over a Single Cavern

We first discuss a simple model with a single cavern. Figure 10 shows the outline of the model: Dimensions are 500 m horizontally and 1400 m vertically; the salt layer is 100 m thick and covered by 1200 m of overburden. The jointing in the overburden is approximated with two orthogonal joint sets (horizontal and vertical) with spacing of 20 m. Continuous vertical joints form the salt horizon to the surface represent a conservative approximation to an in-situ joint system which the friction angle on the overburden joints was comparatively low with $\phi_R = 23^\circ$.

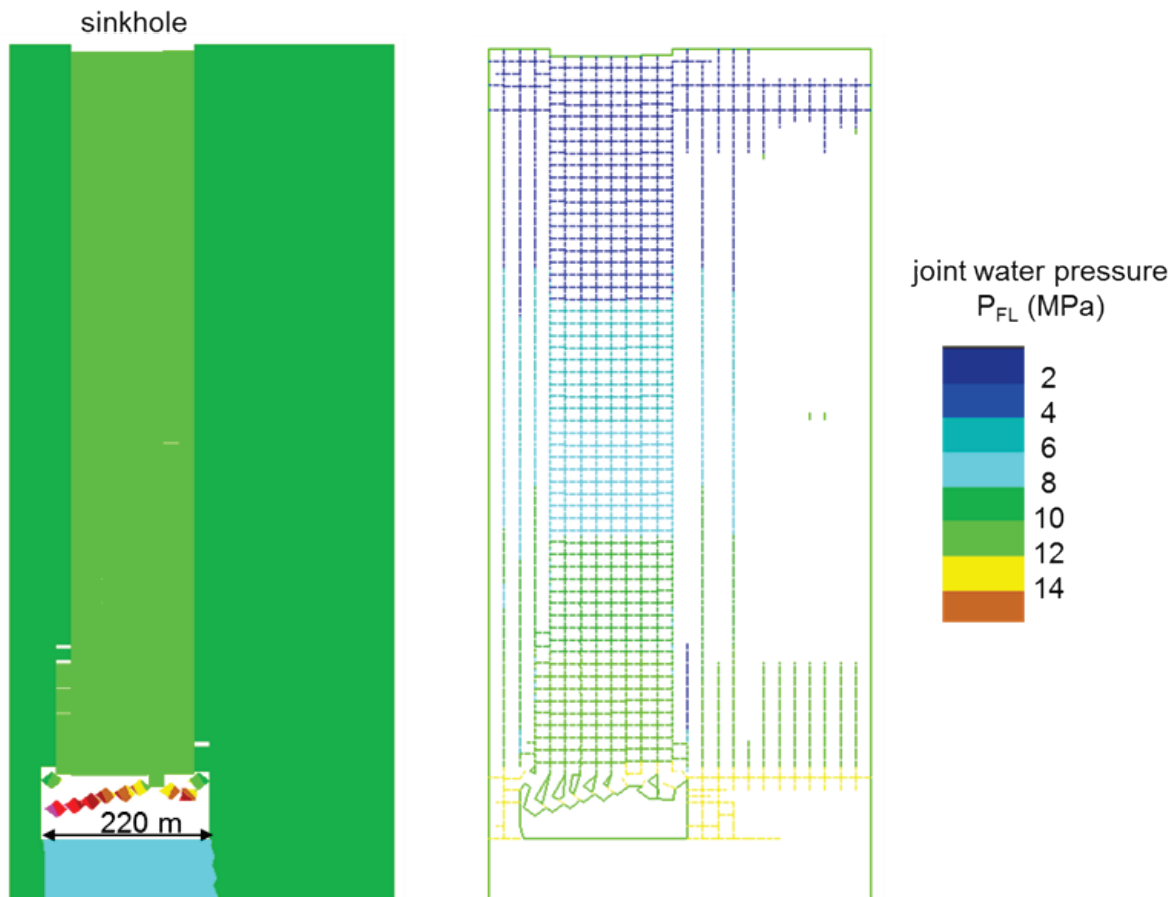


Figure 11: Basic scenario of sinkhole formation with a large-span cavern after the loss of the salt back: A rock column in the overburden has started to slide (left) is modelled with horizontal and vertical joint sets; brine from the cavern percolates along the joints and lowers the effective stress, allowing the rock column to slide.

Figure 11 shows the result for a cavern with a span of 220 m and a lateral stress coefficient of $\lambda = 0.5$. The salt back above the cavern has fractured and failed, allowing the brine from the cavern to penetrate along the overburden joints. Brine pressure has developed along the entire joint system above the cavern up to the surface. Consequently, the shear strength is lowered. A column of approximately 160 m width

has started to slide down in a piston-like motion. There is essentially no bulking, so the movement in the cavern roof directly translates into sinkhole volume at the surface. (Note that the sliding rock column does not disintegrate although the horizontal joints are inundated.)

The block sliding instability requires on the confining stress and the cavern span, i. e. the critical area-circumference ratio. To assess the dependence on model conditions, the lateral stress coefficient and the cavern span were varied. The plots in Figure 12 show that block sliding with a width of 160 m still occurs for $\lambda = 0.6$, while for $\lambda = 0.5$, smaller caverns are unstable as well. The minimal sinkhole width in the model variations was 60 m. For lateral stress coefficients larger than $\lambda = 0.6$, block sliding did not occur.

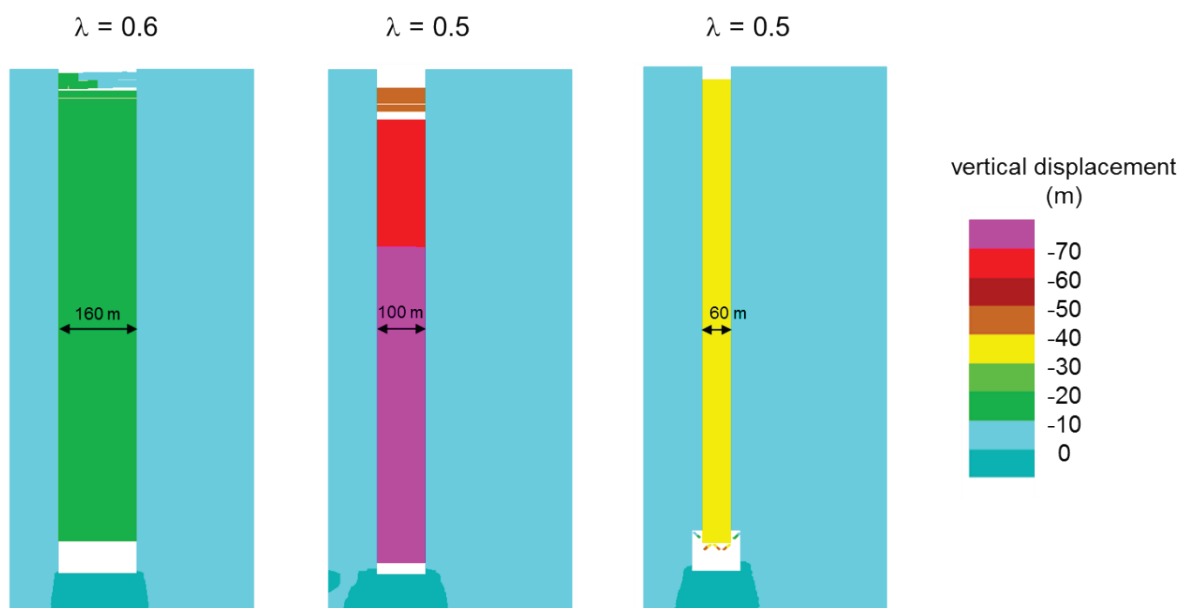


Figure 12: Basic scenario with variations of lateral stress coefficient and cavern span.

In general, the overburden properties will not be uniform from leaching horizon to the surface. In the model shown in Figure 13, a more competent layer has been included. The block sliding instability starts at the cavern roof, but stops at the stronger stratum, so that no sinkhole forms at the surface. A new cavity forms below the competent layer, and the initial cavern volume is partially transferred to the new void. Note that the geomechanical evolution sensitively depends on the strength properties of the competent layer. Thus, stability may be temporary, and the formation of a sinkhole cannot be excluded in the future.

The simplified and conservative models allow to derive necessary conditions for sinkhole formation via block sliding over brine-filled caverns:

- A sufficiently large cavern without salt back, i. e. with hydraulic connection between the cavern and the overburden.
- A jointed overburden with moderate to low shear strength.
- Moderate to low horizontal (confining) stresses in the overburden.
- Fluid pressure on the overburden joints.

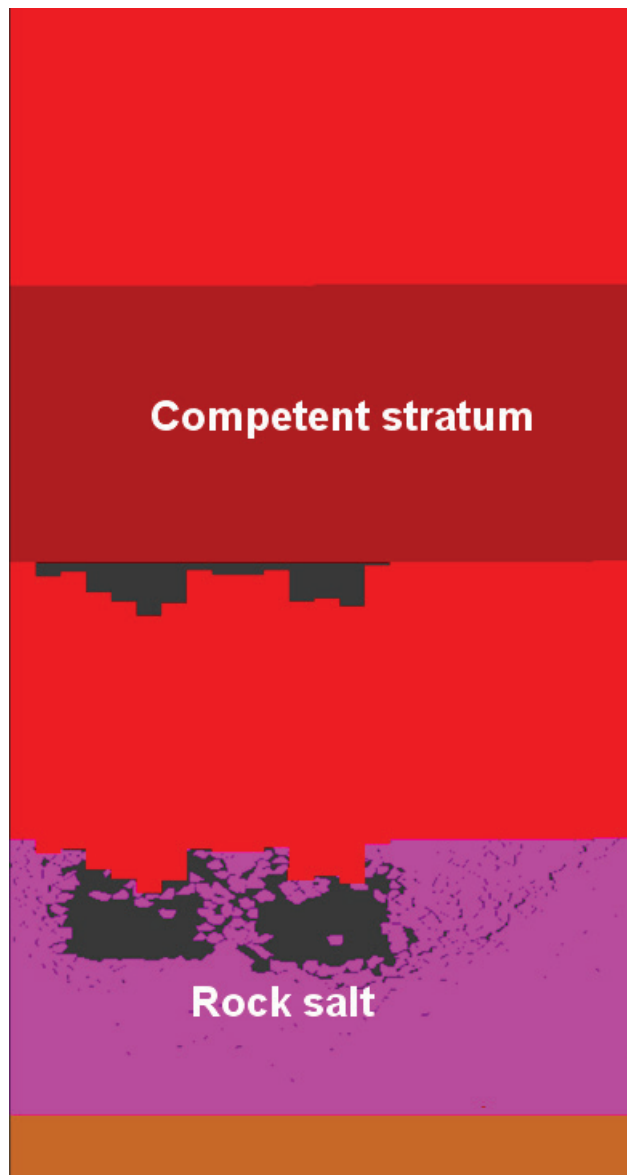


Figure 13: Extended model with several overburden strata: Block sliding starts, but stops at a more competent layer, so that no sinkhole forms at the surface. Further evolution sensitively depends geological and geomechanical details; sinkhole formation in the future cannot be excluded.

4.2 Interactions of Several Caverns

In a cavern field, caverns exert mutual influence due to deformations, stress changes and the alteration of hydraulic conditions. These interactions of neighbouring caverns can contribute to sinkhole formation. The models presented in this section contain several caverns; stratigraphy and parameters are similar to the model discussed in the previous section. The overburden is again equipped with joint sets of 20 m spacing.

In the model shown in Figure 14, the lateral stress coefficient has been increased to $\lambda = 0.55$, such that a narrow sinkhole would not form by itself. We assume that all caverns have lost their hydraulic barrier, but the two caverns on the left have been closed. Thus, the internal pressure is increased by 3.5 MPa. However, due to the hydraulic connection between the caverns and the overburden, the overpressure is transferred to the overburden joint system. Here, it has to be assumed that the over-

pressure can be sustained despite the outflow along the joints, at least temporarily, possibly due to brine injection during the closure process.

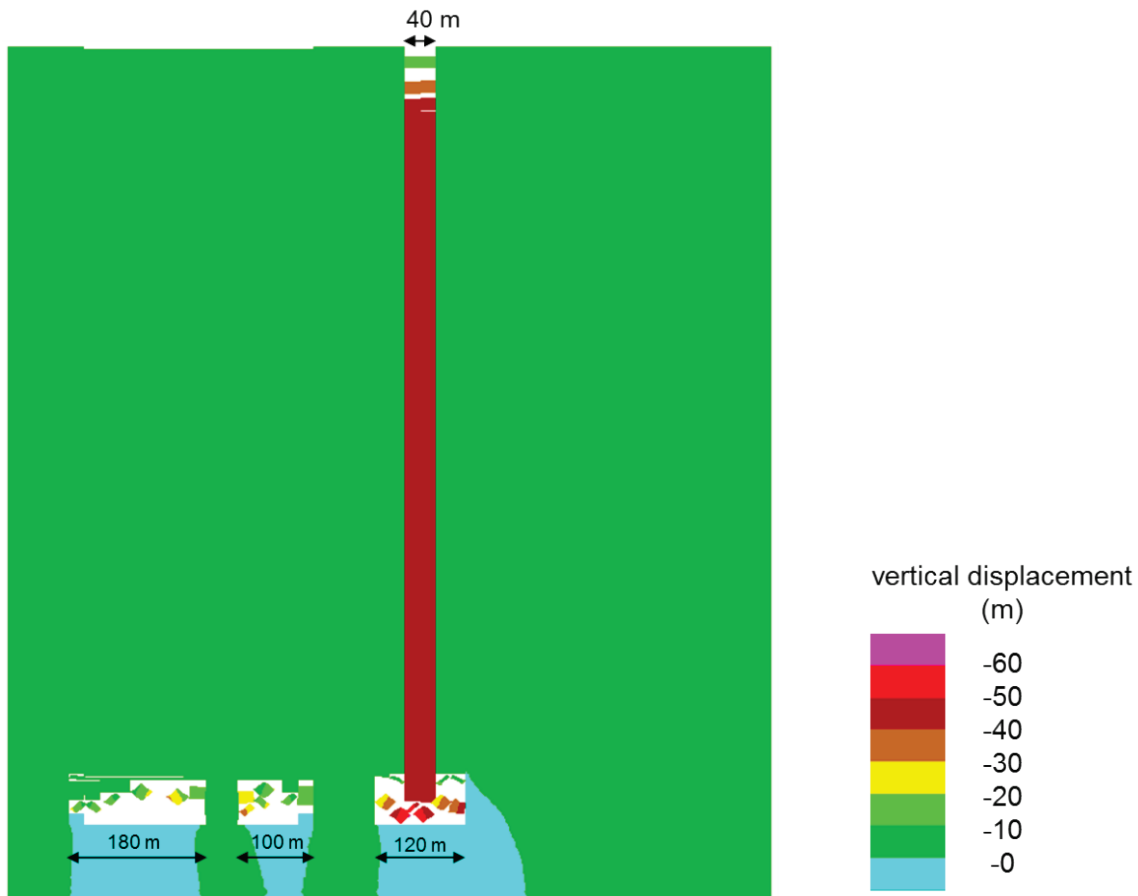


Figure 14: Narrower sliding column due to overpressure in closed caverns with hydraulic connection to the overburden.

As a consequence, the shear resistance is lowered further, and previously stable rock configurations can start to slide – a narrow sinkhole of width 40 m forms above the third cavern. Recall that in the single-cavern model, minimum sinkhole width was 60 m; the overpressure generated by the closed but hydraulically open caverns has lowered the critical rock block size.

In a second example (see Figure 15), a cavern field is modelled with a central group of three caverns with narrow pillars (left side of the plot) and a fourth cavern with a larger distance. A near-surface aquifer is modelled with hydrostatic pressure, as may occur after strong rainfall. Inundated joint with fluid pressure are indicated with dashed lines. In the dynamical simulation, two potential sinkhole positions become apparent:

- The central group of caverns with underdimensioned pillars and large subsidence, and
- the edge of the cavern field, where the subsidence contrast between the field and the unmined area creates extensional strains and thus lowers the horizontal stress. In particular, this shows that the condition of low lateral stress is not necessarily very restrictive, since the edge of a subsidence bowl naturally is a region of lowered horizontal stress.

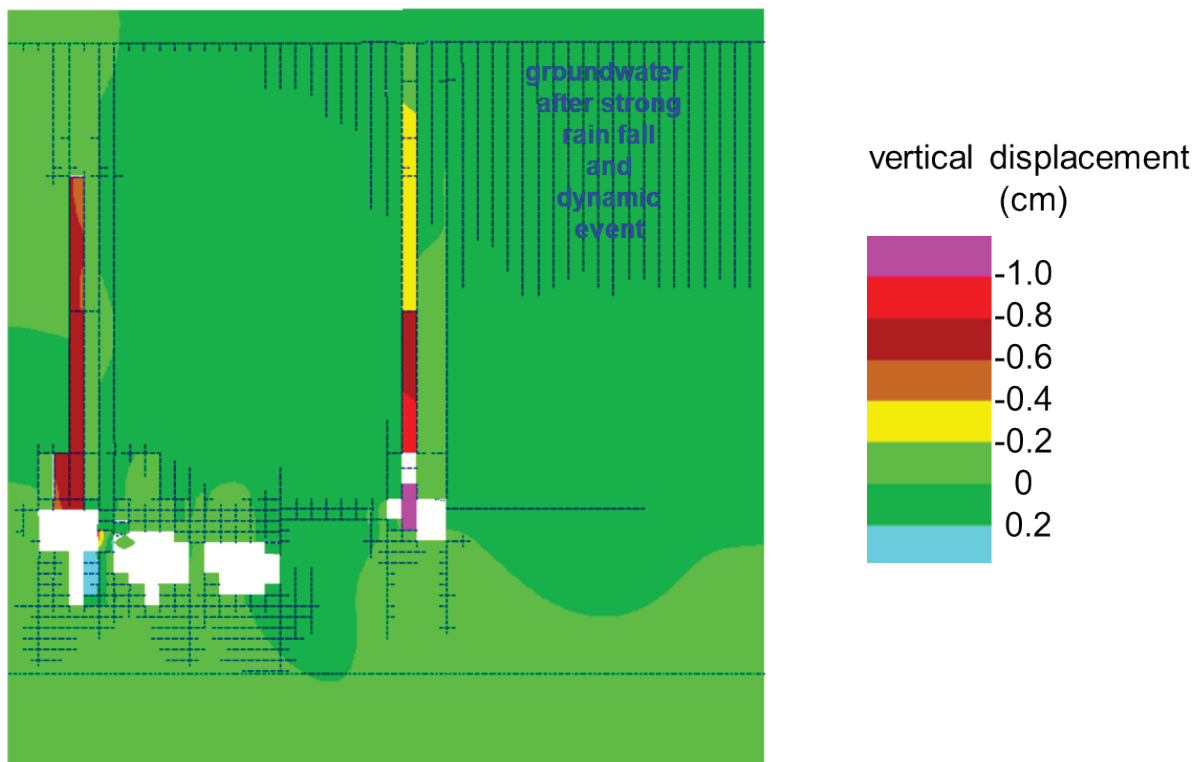


Figure 15: Beginning sinkhole formation over cavern at the edge of a cavern field – the extensional strains due to the cavern field lower the lateral stress. In this simulation, heavy rainfall and a dynamic event increased ground water penetration into the joint system down from an aquifer close to the surface.

5 Conclusions

We have shown that sinkholes are possible for caverns in depths exceeding 1000 m. We have presented in-situ examples, analytical estimates and numerical simulations which give a consistent picture of the mechanism.

The block sliding instability is a hydromechanical process that requires fluid-filled joints in the overburden, where the fluid pressure lowers the effective stress and thus the shear resistance. A necessary condition is the loss of the hydraulic barrier, i. e. a hydraulic connection between the cavern and the overburden, so that brine can penetrate the joint by pressure-driven percolation (Minkley et al. 2015).

The process may be aided by dynamic overpressures, e.g. due to rock fall or tectonic events, which fracture remaining rock bridges. Microseismic monitoring systems possibly can track the evolution of the overburden in the cavern roof.

Note that while the general mechanism is understood, the evolution of specific potential sinkholes, where the system is close to a boundary of stability, depends on geological and geotechnical details and cannot be predicted reliably.

In our models, the joint properties (geometry, shear strength) were generally chosen conservatively. On the other hand, we have not considered chemical alterations in the overburden due to brine, such as weathering and dissolution or the lubrication of clay-filled joints. A detailed rock mass assessment is required in each specific case.

6 References

- Bérest, P. (2017). „Cases, causes and classifications of craters above salt caverns“. In: International Journal of Rock Mechanics and Mining Sciences 100, pp. 318–329. DOI: 10.1016/j.ijrmms.2017.10.025.
- Groß, U., W. Minkley and M. Penzel (1986). „Ergebnisse zur Untersuchung von Gebirgsspannungszuständen und ihre Anwendung für die Hohlraum- und Ausbaudimensionierung“. In: Proc. Int. Symp. on Rock Stress and Rock Stress Measurement, Stockholm, pp. 531–536.
- Itasca Consulting Group (2018). UDEC: Universal Distinct Element Code, Version 6. Minneapolis, Minnesota, USA. URL: <https://www.itascacg.com/software/udec>.
- Jousset, P. and J. Rohmer (2012). „Evidence for remotely triggered microearthquakes during salt cavern collapse“. In: Geophysical Journal International 191.1, pp. 207–223. ISSN: 0956-540X. DOI: 10.1111/j.1365-246X.2012.05598.x. eprint: <https://academic.oup.com/gji/article-pdf/191/1/207/5893839/191-1-207.pdf>.
- LAGB (2012): Rohstoffbericht Sachsen-Anhalt 2012. Mitteilungen zu Geologie und Bergwesen von Sachsen-Anhalt • Band 17
- Minkley, W. and U. Groß (1990). „Sliding of blocks in the top rock, a model for rockburst of the regional type“. In: Gerlands Beiträge Geophysik 99.5, pp. 487–491.
- Minkley, W. (2004). Gebirgsmechanische Beschreibung von Entfestigung und Sprödbrecherscheinungen im Carnallit. Schriftenreihe des Institutes für Gebirgsmechanik – Band 1. Aachen: Shaker Verlag. ISBN: 3-8322-3495-0.
- Minkley, W. and J. Mühlbauer (2007). „Constitutive models to describe the mechanical behaviour of salt rocks and the imbedded weakness planes“. In: The Mechanical Behavior of Salt – Understanding of THMC Processes in Salt. Ed. by M. Wallner, K.-H. Lux, W. Minkley and H. R. Hardy Jr. CRC Press. ISBN: 978-0-415-44398-2
- Minkley, W., M. Knauth and U. Wüste (2012). „Integrity of salinar barriers under consideration of discontinuum-mechanical aspects“. In: The Mechanical Behavior of Salt VII. Ed. by P. Bérest, M. Ghoreychi, F. Hadj-Hassan and M. Tijani. CRC Press. ISBN: 978-0-415-62122-9. DOI: 10.1201/b12041.
- Minkley, W., Knauth, M., Fabig, T., Farag, N. (2015): Stability of salt caverns under consideration of hydro-mechanical loading. Mechanical Behavior of Salt VIII, Rapid City, USA, 26-28 May 2015, 217 – 227
- Morisseau, J. (2000). Uncontrolled leaching of salt layer in an oil field in Algeria. Tech. rep. SMRI Fall Meeting, San Antonio, TX, USA. Solution Mining Research Institute.
- Nádai, A. (1950). Theory of flow and fracture of solids. New York: McGraw-Hill.
- Röckel, T. and C. Lempp (2003). „Der Spannungszustand im Norddeutschen Becken“. In: Erdöl Erdgas Kohle 119.2.
- Sambeek, L. van (2014). Selected Examples of Sinkhole Formation in the United States: Natural and Man-Caused. SMRI Spring 2014 Technical Class. San Antonio, Texas, USA.

Investigations of the thermal impact on Elbe sandstone: real fire experiments, laboratory tests and numerical simulations

**Untersuchungen zum Verhalten von Elbsandstein unter Brandeinwirkung:
Beflammungsexperimente, Laborversuche und numerische Simulationen**

N. Freudenberg, T. Frühwirt, F. Wang
TU Bergakademie Freiberg, Geotechnical Institute
Gustav-Zeuner-Str. 1, 09599 Freiberg, Germany

Abstract

Heat-induced short-term decay of dimension stone on buildings and monuments caused by fire is a well-known phenomenon. Most of the scientific studies about thermal behavior and thermal changes of building stones are carried out in laboratory ovens by stepwise heating of stone samples to different stages of temperature. However, real conditions of fire attack on stone elements of buildings might differ considerably from the relatively slow, even heating of small samples in ovens. Therefore, more realistic fire scenarios were designed to test the behavior of sandstone specimens such as cylinders. The samples comprise the Posta type of the Cretaceous Elbe sandstone. They were exposed to a real scale fire test, applying the room corner test in accordance to the ISO 9705 standard. The specimens were mounted in a fire container at a height of 170 cm above the fire source, a wood crib in accordance to DIN EN 3-7. The standard defines a known theoretical heat release rate, producing a maximum air temperature of approx. 900 °C for about 15 minutes. The temperature in the container as well as on the surface and within the stone specimens was monitored by thermocouples during the tests. The measured surface temperatures vary between 350 and 600 °C, whereas the temperatures at 9.5 cm below surface vary only between 200 and 350 °C. After the fire tests, different crack patterns were observed on the specimens. In contrast, smaller specimens heated in a laboratory oven did not reveal any macroscopic cracks, although they were exposed to the same or even markedly higher temperatures (1000 °C in the sample core). Simulation results show that the large samples under real fire experienced high thermal gradients during both heating and cooling processes. However, thermal gradients inside of the small samples were always very small due to slow heating and cooling rate in the oven. Although triggering quite different modes of failure of impacted stone specimens, both treatments are needed for a better understanding of fire damages on stone buildings since the material behavior of sandstone on grain size scale (fabric and mineralogy) corresponds to macroscopic crack patterns such as fragmentation and scaling. The difference in thermal gradients depending on heating rates is identified as a dominant factor for the difference in cracking behavior of sandstone samples.

Zusammenfassung

Thermisch bedingte Beschädigung von Naturstein an Gebäuden und Denkmälern, verursacht durch Feuer, ist ein bekanntes Phänomen. Die meisten wissenschaftlichen Untersuchungen zum thermischen Verhalten und thermischen Veränderungen von

Bausteinen werden in Laboröfen bei stufenweisem Heizen von Steinproben hin zu verschiedenen Temperaturstufen durchgeführt. Allerdings können sich reale Bedingungen der Brandbeanspruchung von Steinelementen an Gebäuden erheblich von dem relativ langsamen, gleichmäßigen Aufheizen kleiner Proben in Laboröfen unterscheiden. Daher wurden realistischere Brandszenarien entwickelt, um das Verhalten von Proben aus Sandstein, wie z. B. Zylindern untersuchen zu können. Die Proben, welche den Posta-Typ des Kreide-Elbsandsteins umfassen, wurden Beflammungsexperimenten im realen Maßstab ausgesetzt, wobei ein Standard-Brandraum des Room-Corner-Tests (ISO 9705) Anwendung fand. Die Proben wurden in einer Brennkammer in einer Höhe von 170 cm über der Feuerquelle, einer Normholzkrippe nach DIN EN 3-7, befestigt. Die Norm definiert eine bekannte theoretische Wärmefreisetzungsrate, die eine Maximaltemperatur von 900 °C für einen Zeitraum von ca. 15 Minuten erzeugt. Die Temperatur in der Brennkammer sowie auf der Oberfläche und im Inneren der Steinprobekörper wurde von Thermoelementen während der Brandtests überwacht. Die gemessene Oberflächentemperatur variierte zwischen 350 und 600 °C, während in einer Tiefe von 9,5 cm nur Temperaturen zwischen 200 und 350 °C erreicht werden konnten. Nach den Beflammungsexperimenten konnten verschiedene Rissbilder beobachtet werden. Im Gegensatz dazu zeigten die kleineren im Laborofen geheizten Proben keine makroskopisch sichtbaren Risse, obwohl diese gleichen oder auch deutlich höheren Temperaturen ausgesetzt waren (bis zu 1000 °C im Probekern). Die Resultate der numerischen Simulation zeigten, dass die großen Probekörper in den Beflammungsexperimenten große thermische Gradienten während des Heiz- und Abkühlungsprozesses erfahren. Dahingegen sind die thermischen Gradienten innerhalb der kleinen Probekörper aufgrund der geringen Heiz- und Abkühlungsrate im Laborofen stets sehr gering. Trotz der unterschiedlichen Auswirkungen auf die Probekörper werden beide Verfahren für ein besseres Verständnis von Brandschäden an Steingebäuden benötigt, da das Materialverhalten von Sandstein im Korngrößenbereich (Gefüge und Mineralogie) mit den makroskopischen Rissmustern, wie Fragmentierung und Abschälung korrespondiert. Hierbei sind die Unterschiede in den thermischen Gradienten eine Ursache für das unterschiedliche Bruchverhalten der Sandsteinproben.

1 Introduction

Due to firestorms caused by heavy bombardments during the Second World War, lots of buildings and objects made of sandstone were massively damaged. These damages became probably more severe by extinguishing fire by water, leading to another short-term temperature change. The typical damage observed is fragmentation, thus reducing the load-bearing capacity of architectural elements, as shown by the examples of the Church of Our Lady (Frauenkirche) and the altar in the Church of the Three Kings (Dreikönigskirche) in Dresden, Germany (fig. 1.1).



Fig. 1.1: Fire damages of historical buildings in Dresden a) Church of Our Lady (Frauenkirche) 1971 (Wikimedia, © Lencse Zoltán) b/c) altar in the Church of the Three Kings (Dreikönigskirche).

Numerous studies (e. g. Chakrabarti et al. 1996, Hajpál & Török 2004, Gómez-Heras et al. 2006, Hager 2014, or Lintao et al. 2017) deal with methods to record material changes of different sandstones caused by high temperatures. However, most of these studies investigate the thermal behavior of small samples with laboratory heating regimes in high temperature ovens. In contrast, there are only few studies dealing with small scale real fire scenarios of sandstones, e. g. Koser & Althaus (1999), Ehling & Köhler (2000), Pohle & Jäger (2003), McCabe et al. (2007), or Smith & Pells (2008). Obviously, the damage patterns of heat-treated laboratory samples and fire-affected objects and buildings (see fig. 1.1) are different.

This study on Posta sandstone compares the behavior of oven-heated with flame-treated samples, the latter corresponding to a more realistic fire scenario.

Compared with the studies in laboratory investigations on fire effects on rocks, the corresponding numerical simulation is rare. Numerical models can achieve results that cannot be obtained in laboratory tests due to technical limitations. For example, the temperature distribution in sandstone samples under different thermal scenarios can be observed conveniently in numerical models. Therefore, the finite difference code FLAC3D (Itasca 2020) is used in this study to present the different 3D temperature distribution of the sandstones in oven heating and real fires. The simulation results can help to understand the difference in failure behavior of the samples in these two different heating scenarios (i.e. oven heating vs. real fire).

2 Materials and testing procedures

2.1 Laboratory tests and real fire experiments

The investigated material comprises sandstone of the Posta type which is one of the two main varieties of the Upper Cretaceous Elbe sandstone, occurring south of Dresden (Saxony, Germany). The color of the Posta type varies between light grey and yellowish-brownish. It is a fine- to medium-grained, occasionally coarse-grained, porous and siliceous quartz arenite (quartz nearly 100 %) without organic matter and with very small amounts of kaolinite (Grunert 2007, Grunert & Szilagyı 2010).

For the laboratory heating experiments cylindrical specimens with different dimensions of 50 mm x 25 mm and 50 mm x 100 mm (fig. 2.1a) were used. The specimen axis was orientated normal to bedding. The dimensions of the specimens for the real-scale fire exposure tests were significantly larger with cylinders with diameter of 19 cm and height of 58 cm. To imitate real shapes of architectural elements such as pillars, cylinders were carved normal to bedding from Posta type sandstone blocks.



Fig. 2.1: Investigated specimens of Posta type Elbe sandstone: a) small cylinders (50 mm x 100 mm) b) large cylinder (19 cm x 58 cm).

The small sandstone specimens (see fig. 2.1a) were treated in a laboratory oven (Nabertherm LT24/12) at the Institute of Geotechnics, Technische Universität Bergakademie Freiberg (TU BAF) at 6 different temperature levels (400, 500, 600,

700, 800, 1000 °C) with a heating rate of 10 K/min and a cooling rate of 1 K/min after a holding time of 6 hours at each target temperature level.

The large cylinders (fig. 2.1b) were marked for drilling boreholes to mount thermocouples (fig. 2.2a/b) which monitored the temperature on the stone surfaces and within the stones during fire exposure over time. In the cylinder samples, 4 boreholes with a diameter of 8 mm were drilled to a depth of 9.5 cm. Flowable mortar was used to fix the thermocouples in the boreholes and to guarantee undisturbed heat transfer.



Fig. 2.2: a) Scheme of drill holes on a cylinder specimen, b) cylinders with mounted thermocouples. Those thermocouples, on the stone surfaces and within the stones, were indicated with "S".

For the real scale room fire tests a fire container (height: 2.40 m, width: 2.35 m, depth: 4.13 m) was used in accordance to the room corner test of the standard ISO 9705 at the Institute of Fire Protection and Disaster Control (IBK) in Heyrothsberge (fig. 2.3). In the fire container, the cylindrical sandstone specimens were placed at a height of 1.7 m above the fire source (fig. 2.4a), achieving a direct flame treatment. The fire source consisted of a wood crib according to DIN EN 3-7 which provided a known theoretical heat release rate with a maximum temperature of approx. 900 °C for about 15 minutes. N-heptane acted as a fire accelerant which was ignited in a pan below the wood crib.

TOP VIEW

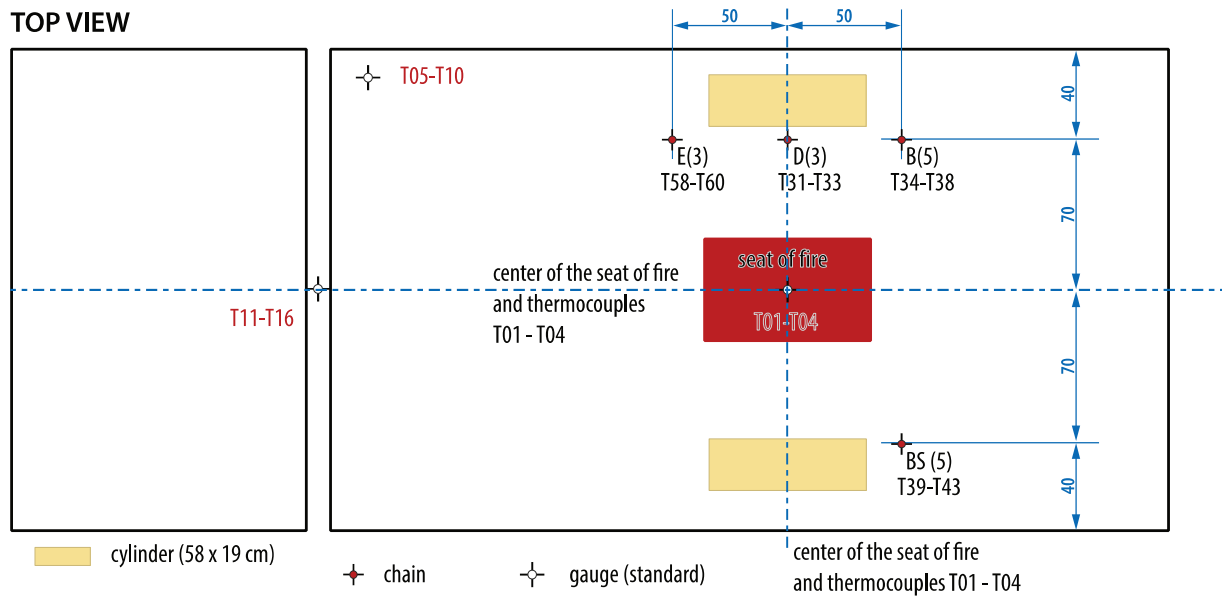


Fig. 2.3: Sketch of the fire container (top view) with sample and thermocouple positions; red: wood crib in accordance to the DIN 3-7 standard as fire source, T01 to T60 indicates the position of thermocouples either mounted on standard positions inside the container or on flexible chains close to the specimens.

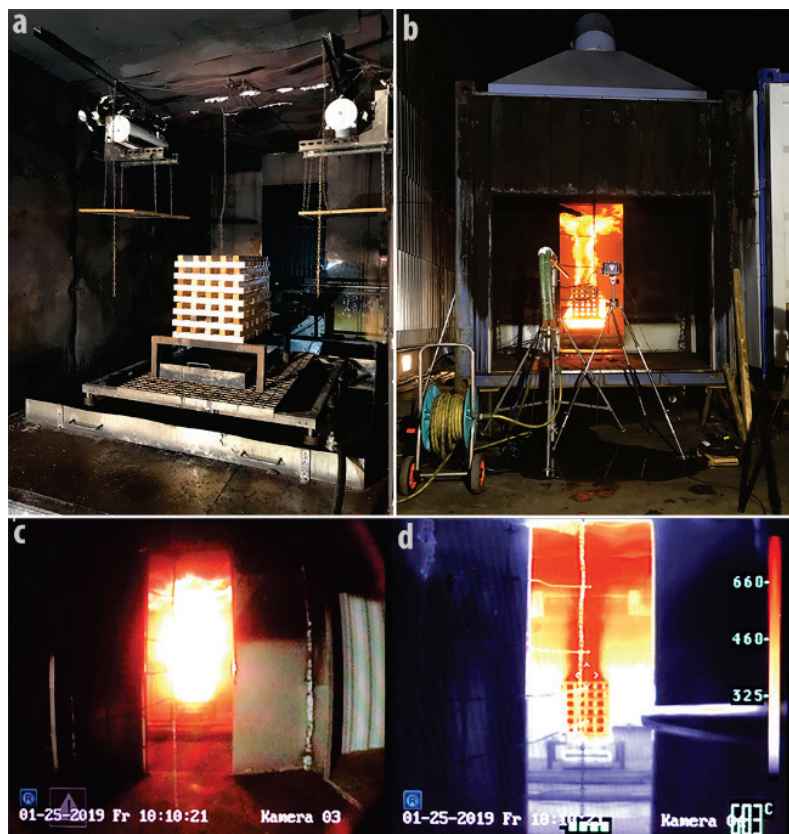


Fig. 2.4: a, b) View inside the fire container before and during testing b) positions of video and infrared camera c) record of video monitoring d) record of infrared monitoring.

The temperature in the container was monitored by thermocouples over time. An infrared and a video camera (fig. 2.4b) recorded the heat distribution and the fire behavior in the container which could be followed in real-time on a monitor in the nearby laboratory (fig. 2.4c/d).

2.2 Numerical model set-up

According to the lab test design, a small cylinder (50 mm x 100 mm) and a large cylinder (19 cm x 58 cm) were built as illustrated in fig. 2.5. An isotropic heat conduction model was used as the thermal constitutive law. Since the numerical model was only used for investigating the temperature distribution, an ordinary Mohr-coulomb model was used for mechanical calculations. Thermal and physical-mechanical properties were assigned according to table 1. For simplicity, homogenous thermal loads were applied onto all the outer surfaces (skin and ends) of the two models. For the small model, the heating rate was 10 K/min as in lab tests. The sample was heated to target temperature of 600 °C and then kept at this temperature until the homogenous temperature distribution across the sample was reached. Afterward, the sample was cooled down with a rate of 1 K/min. For the large model, the temperature development of the fire curve from thermocouple S18 (see fig. 3.1) was applied as thermal boundary condition to the outer surfaces.

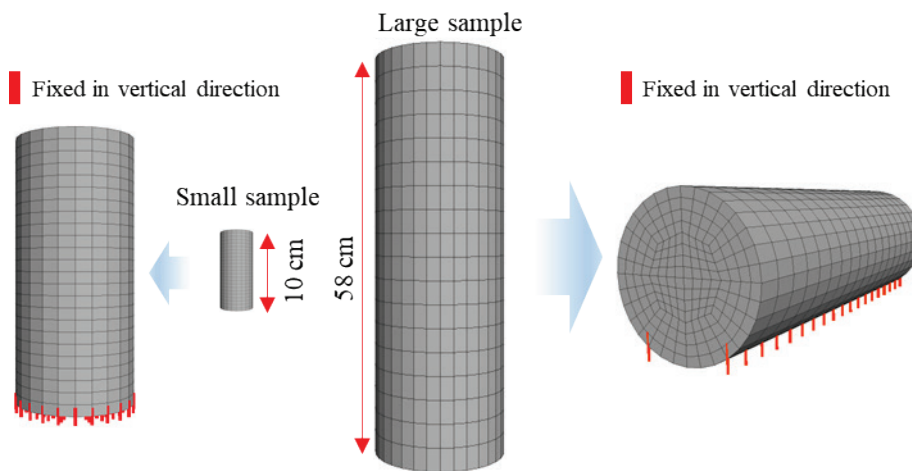


Fig. 2.5: Numerical model set-up of small and large samples.

Table 1: Thermo-mechanical properties of Posta sandstone at room temperature (Robertson 1988, Clauser & Huenges 1995, Grunert 2007).

Pro- perty	α_t ($10^{-6}/^{\circ}\text{C}$)	C_p ($\text{J}/\text{kg}^{\circ}\text{C}$)	k ($\text{W}/\text{m}^{\circ}\text{C}$)	E (GPa)	φ ($^{\circ}$)	c (MPa)	ν (-)	σ_t (MPa)	ρ (kg/m^3)
Value	10.2	684	2.0	15.8	45	11.4	0.2	3.65	2080

α_t : coefficient of linear thermal expansion; C_p : specific heat; k : thermal conductivity;
 E : Young's modulus; φ : friction angle; c : cohesion; ν : Possion's ratio; σ_t : tensile strength;
 ρ : density

3 Results and discussion

The macroscopic results for the stone samples after heating are shown in fig. 3.1a/b. There are significant differences between heating in the laboratory oven and in the fire container. In fig. 3.1a the small Posta type sandstone specimens with axis normal to

bedding (PS_N) are displayed. They are arranged according to their temperature treatment levels (from left to right: 25, 400, 500, 600, 700, 800 and 1000 °C). The specimens appear more reddish with higher temperatures. These color changes are related to mineral transformations, namely of iron-bearing minerals (see Hajpál & Török 2004). Within the brownish to yellowish Elbe sandstones, mainly limonite changes to the red hematite at elevated temperatures (fig. 3.1a). Slight color changes to red can be detected for all sandstone types already at 400 °C (see Gómez-Heras et al. 2009). The cylinders treated in the oven did not reveal any macroscopic cracks. The treated and untreated specimens were stored in plastic bags after cooling down. After moving these sample bags for further investigations, loose single sand grains, increasing in number with temperature, were detected in the bags for those samples heated above 500 °C. They manifest decreased cohesion of sand grains in the respective sandstones.

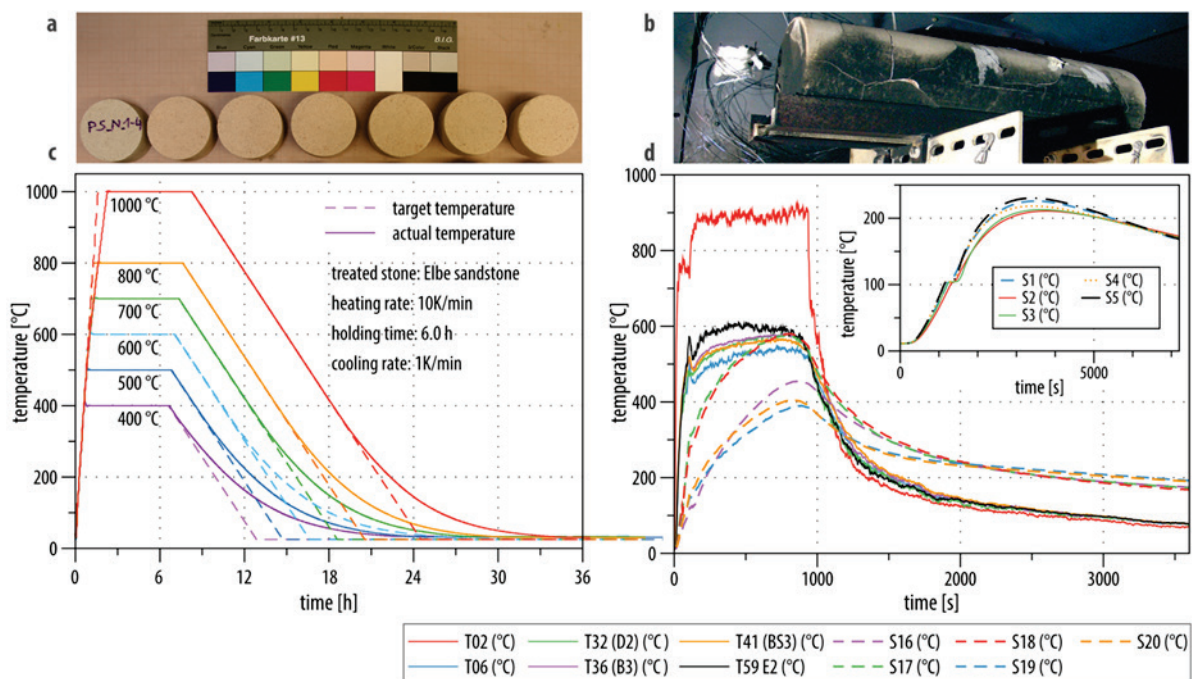


Fig. 3.1: a) Small specimens (50 mm x 25 mm) of Posta sandstone normal to bedding (PS_N) after treatment at different temperature levels in the laboratory oven at the TU BAF, from left to right: 25, 400, 500, 600, 700, 800 and 1000 °C b) significant cracks and heavy sooting on the Posta type sandstone cylinder after the fire test at the IBK in Heyrothsberge c) temperature curves of the small sandstone specimens (50 mm x 25 mm) heated in the laboratory oven at the TU BAF for different temperature levels d) temperature curves of the thermocouples in the fire container at a height of 1.8 m (solid lines) and at the stone surface (dashed lines), the small diagram shows the temperature curves of the thermocouples inside the Posta type sandstone cylinder.

All cylinder specimens exposed for heating in the fire container show macroscopically visible cracks (fig. 3.1b). Moreover, they reveal heavy sooting on the surfaces. Discoloration of the sandstone or crack surfaces could not be detected by the naked eye.

The temperature curves for the small sandstone specimens (50 mm x 25 mm) are shown in fig. 3.1c. They were heated to different temperature levels of 400, 500, 600,

700, 800 and 1000 °C in the laboratory oven at the TU BAF. The set-point temperatures (dashed lines) and the actual temperatures measured (solid lines) show a good correlation. It is recognisable that the heating experiments in the laboratory oven are precisely reproducible.

In contrast, the temperature curves in the fire container at a height of 1.8 m (solid lines) illustrate that the temperature increased very fast (after approx. 3 minutes) to max. 900 °C (fig. 3.1d). After a dwell time of about 15 minutes (= the time the wood crib takes to burn through), the temperature in the fire container decreased rapidly.

If one compares the slow and even heating in the laboratory oven to the dynamic heating in the fire container, the differences between both treatments become obvious. According to the temperature curves measured by the thermocouples in the real fire experiment displayed in fig. 3.1b/d, on the stone surfaces (dashed lines), even in one and the same experiment, the temperatures range between 400 and 600 °C indicating significant spatial differences in thermal loading (fig. 3.1d). The maximum temperature of about 600 °C is reached after approx. 14 minutes. The heating of the air in the container is faster and reaches higher maximum temperatures than the stone surfaces. However, the stone volume is cooling down much slower than the surrounding air. The upper right diagram in fig. 3.1d shows remarkable lower temperatures within the stone compared to the stone surfaces. The maximum temperature of about 230 °C is reached only after approx. 55 minutes, i. e. long after the rapid decrease of the temperature of the surrounding air.

Although the absolute temperatures measured may differ between single experiments, the general patterns of temperature development in the air, on the stone surface, and within the stones are similar. Thus the direct fire impact results in very unequal spatial and temporal distribution of temperature in the specimen within a short time of heating. These differences in temperature may lead to material tension caused by different thermic dilatation between the outer and the inner parts of the objects, resulting in cracks (Gómez-Heras et al. 2009). Many authors refer to the transformation of α -quartz to β -quartz at around 573 °C and the related volume increase to explain deterioration and damage of quartz-rich building stones (e. g. Chakrabarti et al. 1996, Hajpál & Török 2004). In the presented example, heavy damages (cracks) occur, although this temperature is hardly reached on the sandstone surface (see fig. 3.1d).

In the oven-heated smaller specimens, tension due to temperature gradients does not occur due to slower, even heating. From this point of view, this kind of experiment does not reflect real, dynamic fire scenarios on buildings. However, these experiments give insight into effects of temperature on mineral grains and intergranular matrix. In case of long-lasting fire events, these effects may additionally affect building stones and their material properties.

Fig. 3.2 shows the temperature distributions in an axialcutting plane of the large and small samples at different heating stages, respectively. For the large sample under fire temperatures, the temperature differences from surface to inside (i. e. thermal gradient) are very high. When the surface reaches the maximum temperature at about 865 s, the temperature difference between the outmost surface and the core center is up to 442 °C. However, the difference in the small model is very small with a maximum value of only 18 °C. During cooling, thermal gradients in the large model remain remarkable until a uniform temperature distribution across the whole sample is reached. For the

small sample, thermal gradients during cooling are even smaller compared to heating since the cooling rate is 10 times smaller than the heating one.

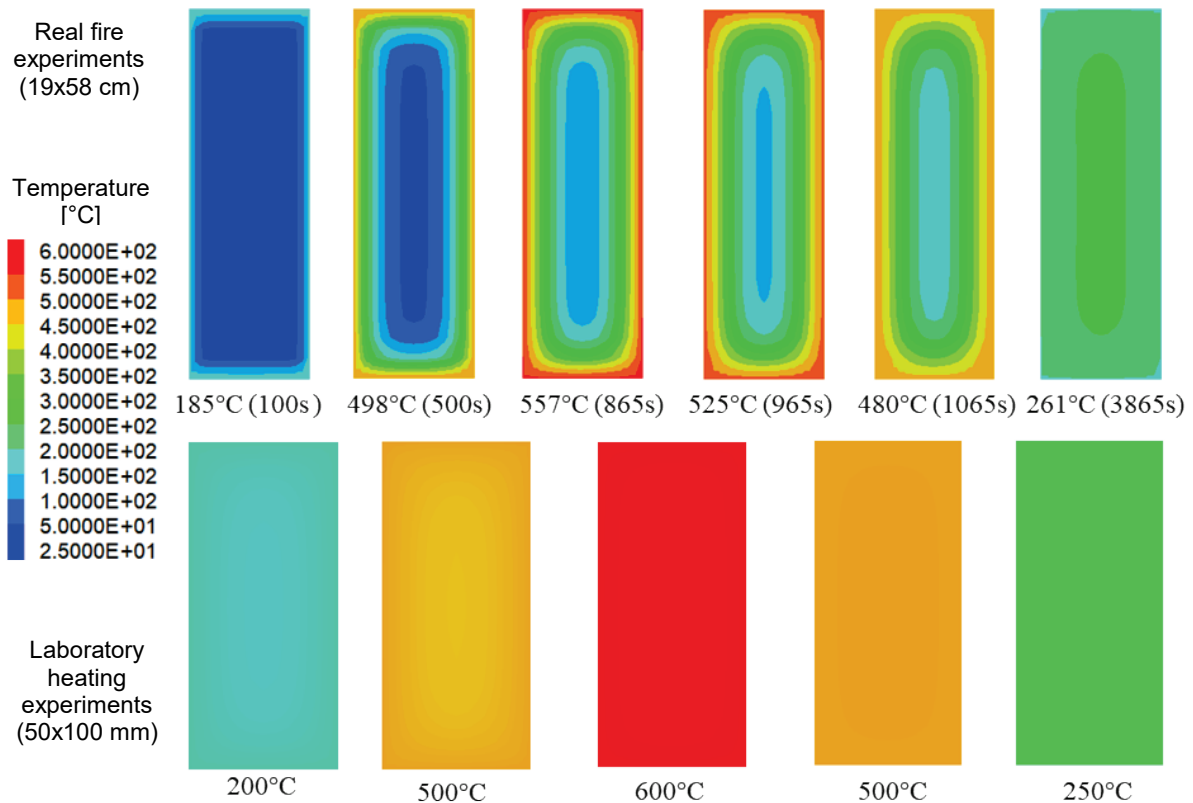


Fig. 3.2 Temperature distributions in the axis cutting plane across the large (19 cm x 58 cm) and small (50 mm x 100 mm) samples at different temperatures during heating and cooling process.

4 Conclusion

This study compares two different heating scenarios which are both necessary to investigate fire damages on sandstone objects or monuments.

The realistic fire scenario with the exposure of architectural sandstone elements to a burning wood crib within a fire container for a short time results in damages comparable to those observed on monuments which suffered from fire attack. The temperatures measured on stone surfaces and within the inner core of the objects indicate high gradients, resulting in material tension and subsequent cracking. Mineralogical changes due to phase transformation of single grains (e. g. transformation of α -quartz to β -quartz at around 573 °C) may be an accompanying, secondary effect, albeit with a spatial extent which is restricted to near-surface volume.

In contrast, smaller specimens of the same sandstone material heated in a laboratory oven show relatively homogeneous decay of matrix strength indicated by loosening of cohesive binding of single grains. A network of microcracks which is manifested typically as “sanding”-effect is triggered. However, even after treatment at higher temperatures up to 1000 °C no significant single cracks can be observed. Such tests and the respective test specimens which will be further investigated, will be needed

for further enlightening the change of petrographic and material properties during heating.

Although triggering quite different modes of failure, both treatments are needed for a better understanding of fire damages on stone buildings since the material behavior of sandstone on grain size scale (fabric and mineralogy) corresponds to macroscopic crack patterns such as fragmentation and scaling.

The continuum code FLAC3D was used to simulate the temperature distribution of different samples under fire and oven heating conductions. Simulations reveal the differences in thermal gradients across the small and large samples during both heating and cooling process. This helps to explain the observed differences in the cracking patterns due to the thermally induced stresses and material deformation.

5 Acknowledgement

The authors thank the Free State of Saxony (Sächsische Aufbaubank - Förderbank - SAB) for funding the work within the project *Simulation zur Rissentwicklung in Architekturteilen und Objekten aus Naturstein infolge hoher thermischer Belastung zur Erarbeitung von Berechnungsroutinen für Aussagen zur Restfestigkeit (WI631)*.

References

- Chakrabarti B., Yates T., Lewry A. 1996. Effect of fire damage on natural stonework in buildings. *Construction and Building Materials* 10(7):539-544.
- Clauser C., Huenges E. 1995. Thermal conductivity of rocks and minerals. In: Ahrens T.J. (Ed.), *Rock Physics & Phase Relations: A Handbook of Physical Constants*, American Geophysical Union 105-126.
- Ehling A., Köhler W. 2000. Fire damaged natural building stones. *Proc. 6th Int. Congr. on Applied Mineralogy ICAM 2*:975-978. Göttingen.
- Gómez-Heras M., Álvarez de Buergo M., Fort R., Hajpál M., Török Á., Varas M.J. 2006. Evolution of porosity in Hungarian building stones after simulated burning. In: Fort R., Álvarez de Buergo M., Gómez-Heras M., Vazquez-Calvo C. (eds) *Heritage, Weathering and Conservation*. Taylor & Francis, London, 513-519.
- Gómez-Heras M., McCabe, S., Smith, B.J., Fort, R. 2009. Impacts of Fire on Stone-Built Heritage. *Journal of Architectural Conservation* 15(2):47-58.
- Grunert S. 2007. Der Elbsandstein: Vorkommen, Verwendung, Eigenschaften. *Journal of Central European Geology* 52/53:3-22.
- Grunert S., Szilaghy J. 2010. Petrophysikalische Eigenschaften einer Auswahl von Baugesteinen aus Deutschland und ihr Bezug zur Petrographie dieser Gesteine. *Journal of Central European Geology* 56(1):39-82.
- Hager I. 2014. Sandstone colour change due to the high temperature exposure. *Advanced Materials Research* 875-877:411-415.
- Hajpál M., Török Á. 2004. Mineralogical and colour changes of quartz sandstones by heat. *Environmental Geology* 46:311-322.
- Itasca 2020. *FLAC3D. Fast Lagrangian Analysis of Continua in Three Dimensions*.
- Koser E., Althaus E. 1999. Brandschäden an Bauwerken aus Naturstein - Hohenrechberg und andere Objekte im Laborexperiment. *Internationale Tagung des SFB 315 Heft 16/1999*.

- Lintao Y., Marshall A.M., Wanatowski D., Stace R., Ekneligoda T. 2017. Effect of high temperatures on sandstone - a computed tomography scan study. *International Journal of Physical Modelling in Geotechnics* 17(2):75-90.
- McCabe S., Smith B.J., Warke P.A. 2007. Sandstone response to salt weathering following simulated fire damage: a comparison of the effects of furnace heating and fire. *Earth Surface Processes and Landforms* 32:1874-1883.
- Pohle F., Jäger W. 2003. Material properties of historical masonry of the Frauenkirche and the masonry guideline for reconstruction. *Construction and Building Materials* 17:651-667.
- Robertson E.C. 1988. Thermal properties of rocks. United States Department of the Interior Geological Survey 88-441.
- Smith A.G., Pells P.J.N. 2008. Impact of fire on tunnels in Hawkesbury sandstone. *Tunnelling and Underground Space Technology* 23:65-74.

Crude oil storage caverns in India and their design aspects

Unterirdische Rohöllagerstätten in Indien und deren Planungsaspekte

A. Kaltenböck

Geoconsult ZT GmbH, Austria

F. Krenn

Geoconsult India Private Ltd.

O. Sigl

Geoconsult Singapore PTe Ltd.

Abstract

The paper deals with aspects of design criteria for crude oil storage caverns and gives an overview how design risks are valued and considered during the construction. During the construction stage are continuously investigations to acquire geological / geotechnical data for the rock mass for a global valuation of the design. The construction of a crude oil storage includes the principal aspect as geological / geotechnical investigation, stability assessments, designing of temporary rock support measures, excavation and side works and permanent re-designing according to the observational approach.

The interdisciplinary relations will be explained on the experience of the cavern design works and during the construction stage of the projects SSCO Vishakapatnam and SSCO Padur in India.

Zusammenfassung

Die Nutzung der Kavernen unter Berücksichtigung der Aspekte der Errichtung der Kavernen stellen besondere Anforderungen an die Bemessung dar. Im Zuge des Ausbruches werden Daten laufend über die geologischen, geochemischen, hydrogeologischen und geotechnischen Eigenschaften erfasst und mit der Planung abgeglichen, um eine gesamtheitliche Evaluierung der geologisch – geotechnische Aspekte des Projektes zu erhalten. Die Errichtung eines Rohöllagers umfasst folgende wesentliche Projektphasen wie die geologisch – geotechnische Erkundung, Stabilitätsberechnungen, Planung der temporären Stützmaßnahmen, den Ausbruch inklusive begleitender Arbeiten und die laufenden Anpassungen der permanenten Stützmaßnahmen an die Ergebnisse des geotechnischen Messprogramms.

Die oben ausgeführten Zusammenhänge werden anhand der erfolgreich umgesetzten Projekte SSCO Vishakapatnam und SSCO Padur in Indien erläutert.

1 Underground Storages

Due to its cost-effectiveness, environmental feasibility, safety and security, underground rock cavern technology is quite popular and widely accepted. Underground caverns can potentially be used for shelter and recreational centers, water collection storage and treatment, sewage treatment, oil and gas storage, cold and dry storage, power stations, underground pumped hydroelectric storage, military installations, and industrial waste repositories [1]. Countries like Japan [2], Singapore [1], South Korea [3], Greece [4] amongst others have been reported. The principle of storage of crude oil in underground unlined rock caverns essentially makes use of confinement by groundwater pressure to contain the stored products. The storage of crude oil in underground unlined rock caverns is based on the following basic principles:

The stored oil is lighter than water and is not soluble in water.

The storage cavern is located below the surrounding groundwater level. When the cavern is excavated below the surrounding groundwater level, water continuously percolates towards the cavern through natural fissures in the rock, thus preventing oil from leaking out [9].

1.1 Projects

All the proposed projects were tendered through electronic reverse auction, i.e. the lowest bid at the deadline gets the job. Out of four EPC contracts (civil works), namely Vishakhapatnam (Vizag), Mangalore and Padur (Part A and B), Hindustan Construction Company (HCC) were able to bag two. These two projects (Vizag and Padur-Part A) are going to be described in detail as Geoconsult is rendering detailed design and site support services there for HCC.

The services basically covered detailed design services for the underground works with emphasis on the support system and site support services for the implementation of the design, support recommendation and geological documentation as per contracts. Since the basis for support selection in all projects is the Q system, modifications were introduced later on to overcome shortcomings, which became evident during the execution of Vizag project. These modifications were then also introduced into the Padur project.

1.1.1 Containment principle for oil storage in unlined rock caverns

The basic principle of oil storage in unlined rock caverns is hydraulic confinement as there is no concrete lining to create a barrier between the stored product and the groundwater outside. Due to the large size of the storage caverns, lining them with concrete would be expensive; hence hydraulic confinement is used. The caverns are constructed at such a depth that they are well below the natural water table and consequently there is sufficient hydrostatic pressure to counter the vapour pressure build-up of the stored hydrocarbons. Furthermore, the stored oil is lighter than water and is not soluble in ground water. When the cavern is excavated below the surrounding groundwater level, water continuously percolates towards the cavern due to natural fissures within the rock, thus preventing oil from leaking out. In order to ensure this ground water flow from the rock mass towards the caverns, a water curtain tunnel system is provided. Water recharge boreholes of 102 mm diameter and 75 m length are drilled horizontally at 10 m intervals from both side walls of the water curtain galleries to cover the caverns and to intersect all discontinuities within the rock mass [13]. During excavation works, the boreholes were connected to a continuous recirculating pumping system injecting water at a pressure of 6 bar in order to keep the rock mass saturated.

Saturated rock mass and groundwater flowing into caverns ensures proper containment of the stored oil during operation. Water seeping into the caverns through the rock mass joints during operation eventually flows along the cavern floor slope into the pump pit and is pumped out at regular intervals and, after proper treatment, re-injected into the water curtain galleries [5], [10], [12].

1.1.2 Typical cross sections

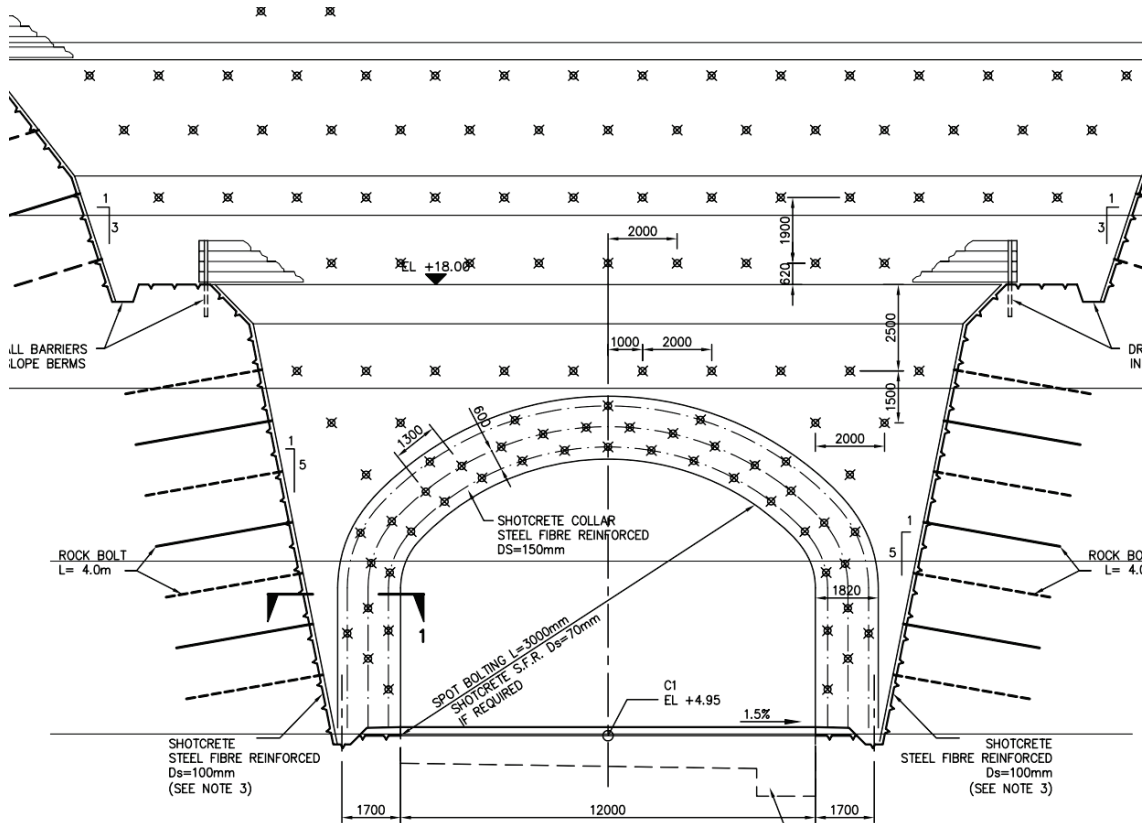


Figure 1: Portal area with access tunnel

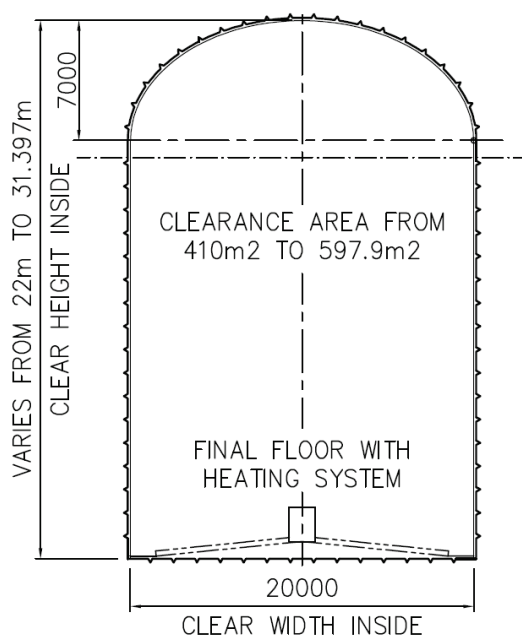


Figure 2: Typical cavern cross section with final floor structure (incl. heating system)

The cross section of a storage cavern is up to 30 m high and 20 m wide. The excavation benches are typically 7 m high. Figure 2 shows a typical cavern cross section within the storage complex. The main access tunnel (Figure 1) is typically about 8 m high and 12 m wide. The water curtain tunnels are typically about 6 m high and 6.5 m wide. In the permanent final condition, all operation and maintenance of the storage facility will be performed down the vertical shafts (two pump shafts and three intake shafts). Therefore, on completion, the access tunnel will be permanently plugged and flooded with groundwater to form part of the permanent water curtain containment system. Operations through the shafts include installation and operation of pumps for handling crude oil and groundwater seepage water, piping for steam injection, vapour connection of the cavern void above the oil level as well as monitoring of operational parameters such as pressures and product levels. The caverns were excavated in the sequence: top heading or gallery pilot tunnel, gallery widening (side slashing), then excavation of the 1st, 2nd and 3rd benches (Figure 3). Benching is carried out again with a pilot excavation in the centre of the bench, followed by side slashing in each case.

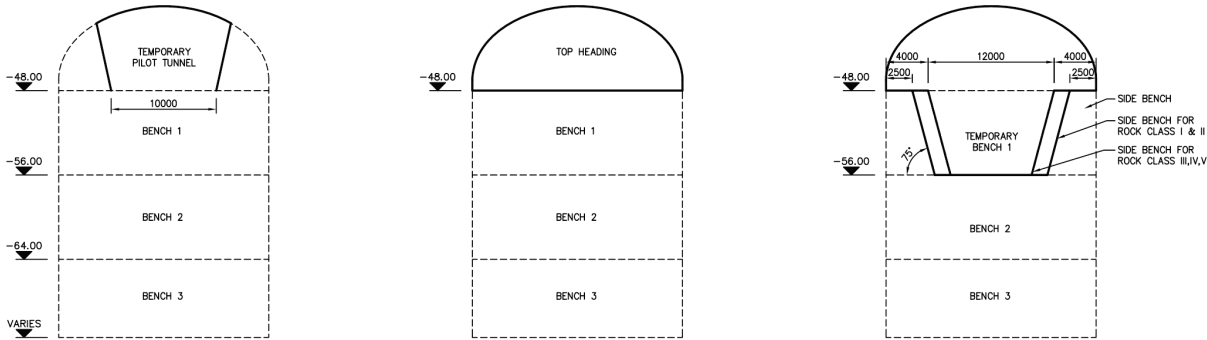


Figure 3: Typical geometry of a bench excavation

For construction purposes, access and cross-cavern connection tunnels with a total length of more than 1,400 m were built. The access tunnels were designed to allow for two-way traffic of heavy plant and excavation equipment and were generally constructed with a slope of 1:8 (Figure 4). The vertical alignment of the access tunnels was de-signed with horizontal curves in order to improve traffic flow and reduce wear on truck tires during construction.

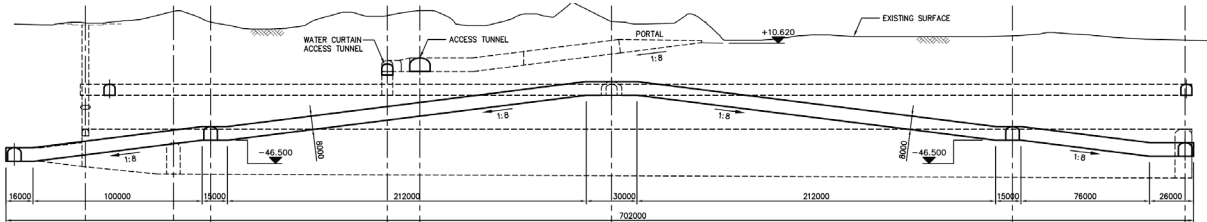


Figure 4: Long section – access tunnel

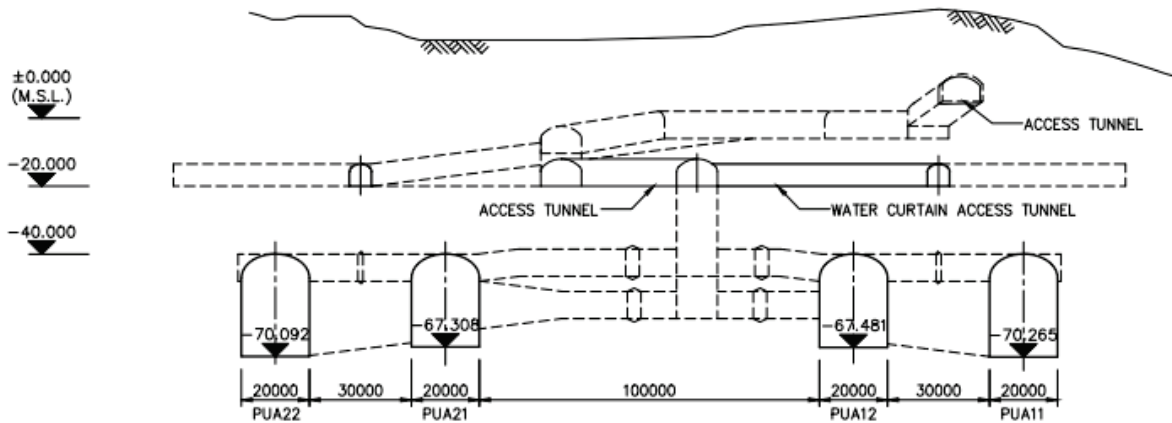


Figure 5: Cross section – access tunnel and cavern complex

The cross section of the access tunnels is typically between 59 to 79 m², and the cross-cavern tunnels have a cross section of about 59 to 159 m². Their actual size depends at what stage of excavation they are connected into the caverns. Full face drill and blast excavation was used for the construction of the tunnels. In the final operational stage of the storage facility, the cross-cavern access tunnels will be plugged. As mentioned above, the main access tunnel will be permanently plugged and then filled with groundwater up to a level of +10 m a.s.l. (equal 40 m above cavern crown level). Such an arrangement is intended to ensure hydraulic confinement of crude oil and the maximum design vapor pressure in the caverns of 150 kPa.

Although the storage caverns are generally unlined (shotcrete and rock bolts only), the cavern floor is paved with concrete placed on a layer of crushed gravel (Figure 2, Figure 5). Within each storage unit, the permanent cavern concrete floor is inclined from the intake to the pump pit, not only to facilitate and enhance flow at lower filling levels but also to optimize the interface between the stored oil and the seepage water, on which the storage product (crude oil) floats. The level of seepage ground water within the caverns below the product is controlled by the water pumps located in the pump shaft (Figure 6). The floors of the caverns are therefore sloped between -53.5 m a.s.l. at the intake down to -60 m a.s.l. at the location of the pump shaft.

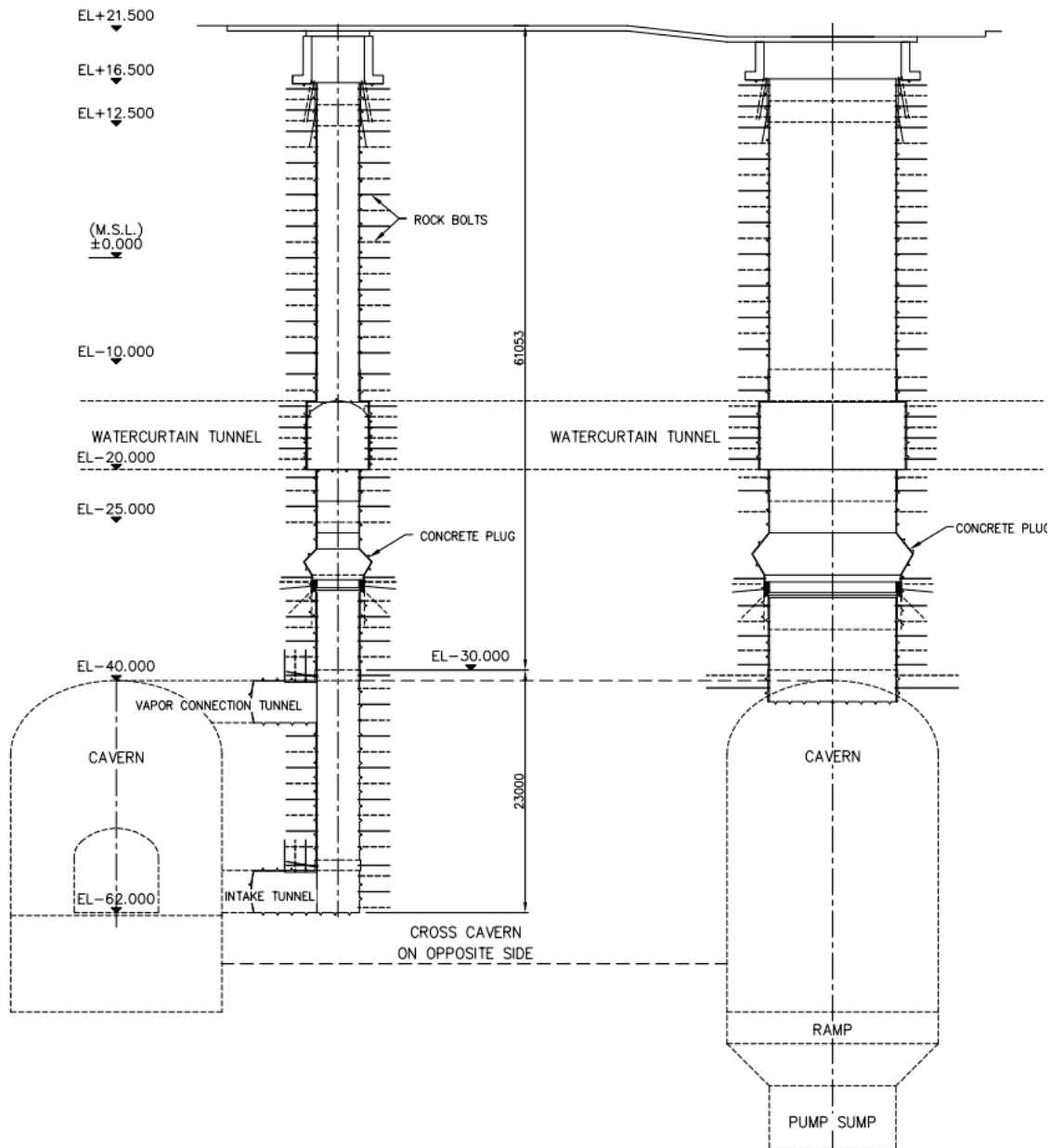


Figure 6: Typical cavern cross section with inlet and outlet shaft structures

While the crude oil storage caverns were built underground using conventional drill and blast methods, all associated operation facilities are located above ground. Therefore, the underground storage scheme is designed to be eventually sealed without any permanent access into the storage area.

The only underground structure to remain theoretically accessible will be the water curtain tunnels, although they will be permanently flooded with groundwater in order to form part of the water curtain system, which provides the necessary product containment. The water curtain system used on this project consists of two water curtain tunnels or galleries running parallel above each storage unit with a systematic series of horizontal boreholes. The total excavated length of water curtain tunnels is 1,140 m with atypical cross section of 35.5 m² (Figure 4, Figure 7).

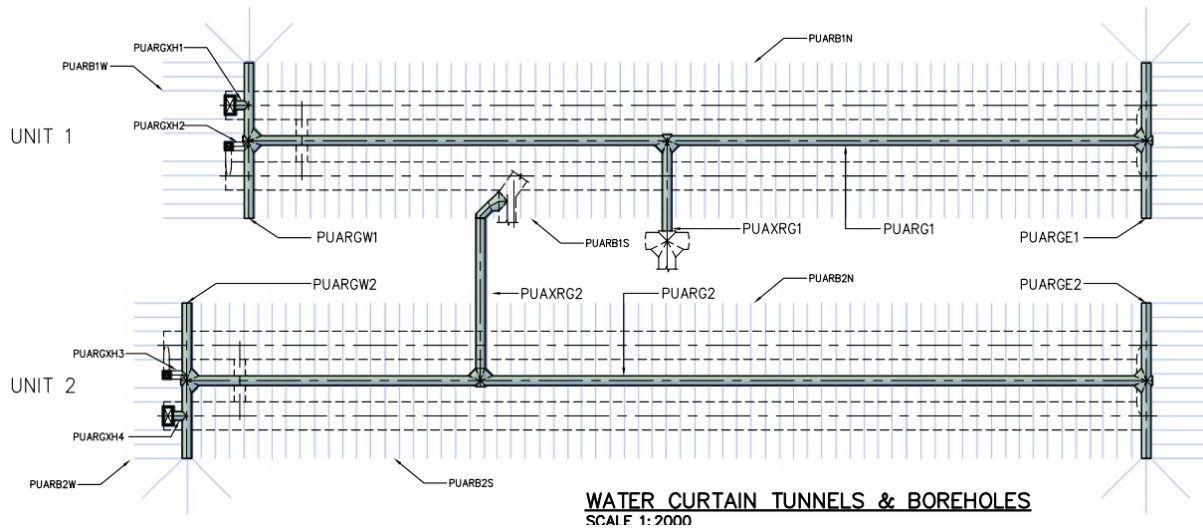


Figure 7: Layout of water curtain tunnel and boreholes

1.2 SSCO Vishakhapatnam (Vizag)

The underground storage facility, aligned in N250-N070 direction, comprises two separate storage units in the proportion of 70:30; the caverns are W- and U-shaped with two product intake shafts at the end of outer legs and one pump installation shaft at the end of middle leg, and with one product intake shaft at the end of one leg and one pump installation shaft at the end of other leg respectively.

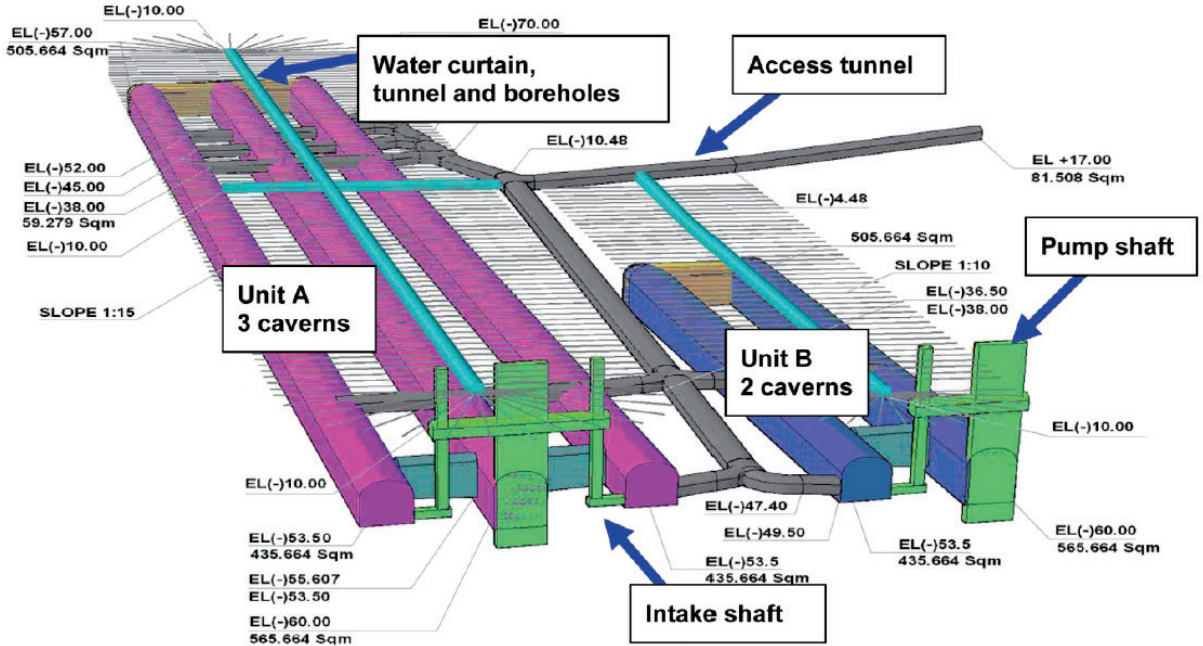


Figure 8: SSCO Vizag layout of Unit A and Unit B

1.2.1 Project outline

The storage facility consists of storage units A and B for storage of 1 and 0.33 MMT of high sulphur crude oil respectively. Storage unit A consists of three caverns (840 m × 20 m × 30 m), two vertical shafts for product intake at the end of outer legs and one main shaft for pump and instrumentation at the end of middle leg, whereas storage unit

B consists of two caverns (320 m × 20 m × 30 m), one vertical shaft for product intake at the end of one leg and one main shaft for pump and instrumentation at the end of other leg. The inverts of storage units are inclined from the intake to the pump pit to minimize the interface between product and water and to make possible the circulation of crude oil. Cross tunnels are provided between storage units for construction purposes (Figure 8).

1.2.2 Geological Situation

The Indian Peninsular Shield is formed of a mosaic of tectonic blocks welded together in the Late Archaean (Tamilnadu block, Karnataka block, Singhbhum block and Bastarblock), which was grouped together with the northern continent during the Early Proterozoic. The dividing line corresponds with the Narmada-Sone-Brahmaputra Lineament. Andhra Pradesh forms the north-eastern part of the Indian Peninsular Shield and is sub-divided into the Eastern Block of Dharwar Craton, Marginal Transition Zone (MTZ) between Dharwar Craton in the west and Eastern Ghat Mobile Belt to the east, Godavari Graben (GG) and the Eastern Ghat Mobile Belt (EGMB) that passes through coastal parts. [9]

The Visakhapatnam region belongs to the Eastern Ghat Orogenic or Mobile Belt of India and is represented by granulitic grade rocks, which are classified into khondalite and charnockite group of Archaean age. The khondalite group is dominantly made up of garnet-sillimanite gneisses with minor bands of quartzites, calc-granulites, and occasionally with cordierite-sappherine granulites and the charnockite group of hypersthene bearing gneisses and mafic granulites. The project area is predominantly represented by garnet-sillimanite-gneisses or garnet gneisses (Sensu-Stricto Khondalite) of Late Archaean to Early Proterozoic age formed during high-grade regional metamorphism [9].

1.3 SSCO Padur

The SSCO Padur cavern complex (Figure 9) is designed as unlined rock caverns for storage of 2.5 MMT of high and low sulphur crude oil at Padur in Karnataka State are proposed to be carried out in two major parts, Part A / Part B and Part C. Parts A and B include the civil works for underground rock caverns, and shaft and caverns mechanical works. Part C includes above ground facilities.

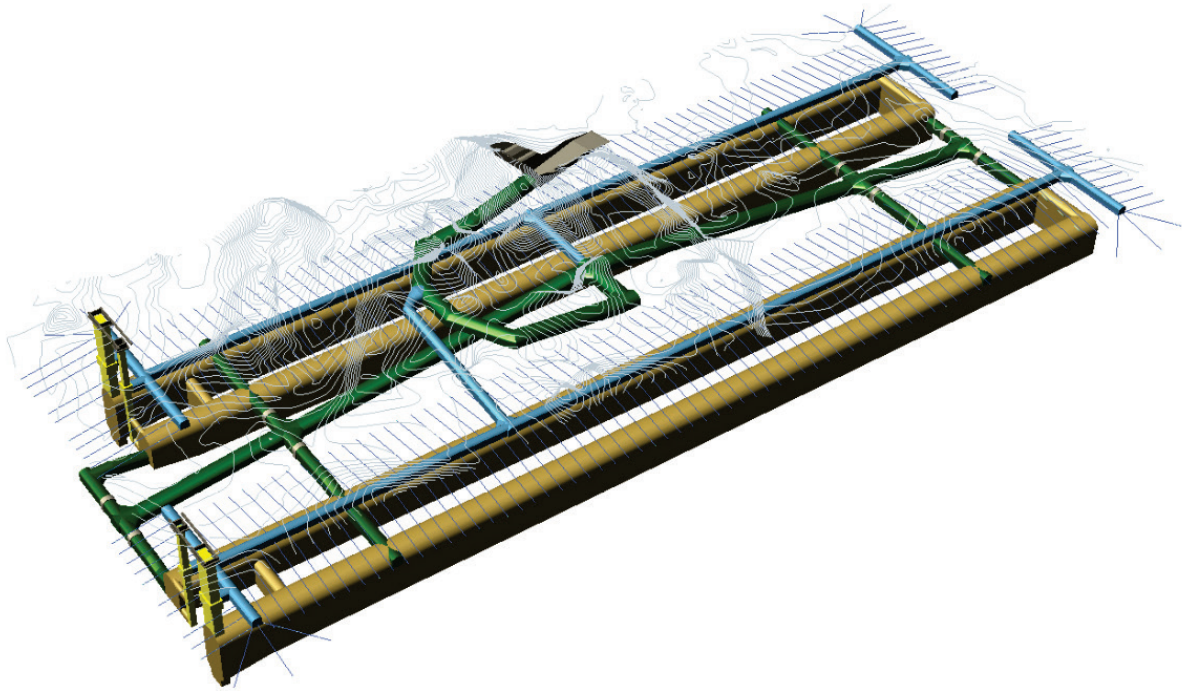


Figure 9: SSCO Padur layout of Part A and Part B

1.3.1 Project outline

The underground storage consists of storage A, comprising three U-shaped storage caverns namely units 1, 2 and 3 ($700\text{ m} \times 20\text{ m} \times 30\text{ m}$ each), for storage of approximately 1.875 MMT high sulphur crude oil and storage B, comprising one U-shaped storage cavern namely unit 4 ($656\text{ m} \times 20\text{ m} \times 30\text{ m}$ each), for storage of approximately 0.625 MMT of low sulphur crude oil i.e. with proportions of approximately 3:1.

Each U-shaped cavern, with an approximately D-shaped cross section, is designed to have a shaft with pump installations and pump pit located at the end of one leg; a separate intake shaft will also be provided at the end of the other leg. The cavern roof is horizontal along its full length and the invert is inclined from the intake to the pump pit to ensure free flow (Figure 9).

1.3.2 Geological Situation

The project area lies within Dharwar craton and is composed of various types of rocks. Granitic gneiss, in other words Peninsular Gneisses, belonging to this region are the most widespread group of rocks in Karnataka and many parts of southern India. They include granites, granodiorites, gneissic granites and banded or composite gneisses, the granitic constituents of which show distinct signs of intrusion. The banded gneisses consist of light bands composed of quartz, feldspar (felsic bands) alternating with dark bands composed of hornblende, biotite and minor accessories (mafic bands). During the construction stage, basic intrusions/mafic dykes have been encountered and have an impact on local stress redistribution [9].

2 Design and Risk management

2.1 Cavern Design Aspects

Rock mass assessments with respective classification were carried out by engineering geologists during the feasibility stage (Q system classification) [12].

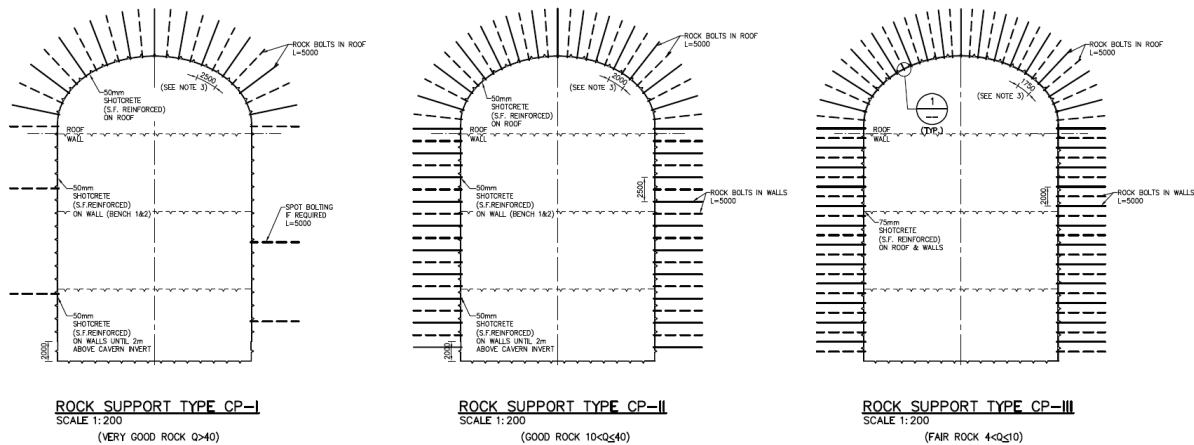


Figure 10: Typical rock support types based on the Q-value system

At the detailed design stage, the following design procedure was used:

- Assessment of rock mass behaviour to Austrian Standard B2203-1 [6] and the Guideline for the geotechnical design of underground structures with conventional excavation [11], and definition of relevant rock mass behaviour types,
- Verification of rock mass behaviour using numerical analysis methods and calibration to the Q value,
- Determination of rock bolting patterns using rock wedge analyses,
- Definition of designed rock support classes for the various sizes of excavation cross sections linked to a Q value,
- Continuous verification of applied rock support during construction on the basis of a continuously updated geological model derived from excavation rock mapping results, Geotechnical monitoring to verify rock mass behaviour during excavation.

For more information on design aspects and geotechnical assessment refer to [8] [9] [10].

2.1.1 Design phase 1

During design phase 1, the design specified by the Owner for typical rock support, as presented in the tender documents such as the Basic Engineering Design and the tender drawings, was evaluated and verified according to the following objectives:

- Design calculations to support and verify the rock support design and proposing rock classes based on the Q System. Calculations, analyses and assessments were based on the relevant construction stage.
- Typical rock support systems derived from the Q System were checked with numerical methods in order to verify that excavation-related rock mass deformations were adequate.
- If necessary and justified by the design, rock support classes were defined, which deviated from the support suggested by the Q system.

- Based on the envisaged rock support, wedge analyses were carried out considering the effects of the various joint sets present in the rock mass and their orientation with respect to the specific tunnel/cavern/shaft structure.
- Preliminary numerical analyses were performed of the effects of primary and secondary rock stresses around the storage caverns, tunnels and shafts. Areas were identified where the rock stress situation needed to be analysed in more detail during the subsequent design stage.
- Principle drawings with main dimensions.
- If applicable for a particular design package, a review of storage capacity requirements was carried out.

2.1.2 Design phase 2

During design phase 2, the designs were fully developed into the required detail such that the designs reached a status fit for construction.

- Implementation of comments on Phase 1 submission,
- Review of assumptions and design philosophies adopted during previous design phases,
- Development of the Phase 1 designs into the final details, especially with respect to the drawings,
- Additional rock support design calculations were done as required,
- Include structural designs, if applicable for a particular design package,
- Final design documentation presenting results and summary of detailed design analyses,
- Analyses of the effects of primary and secondary rock stresses around the storage caverns, tunnels and shafts were performed for critical areas identified during design phase 1,
- Detailed design drawings for construction,
- Review and update of the risk register,
- If applicable for a particular design package, the storage capacity requirements are reviewed.

2.2 Inputs for design

The basic aim of any design for an underground opening should be to utilize the rock itself as the principal structural material, creating as little disturbance as possible during the excavation process and adding any concrete, shotcrete or steel supports in the smallest possible quantities.

The design of rock support is based on adequate design parameters and the assessment of anticipated rock mass behaviour. The analyses carried out recognize appropriate aspects of rock mass behaviour, both during construction and in the long term over the entire service life, together with the construction sequence and processes.

The rock support measures are essentially intended to:

- Limit and control rock mass deformation to achieve safe and stable excavation conditions in the roofs, side walls and floors in caverns, tunnels and shafts,
- Ensure adequate rock mass support adjacent to particular underground openings to maintain global stability of the underground works,
- Provide permanent support for identified weak layers or wedges to achieve more or less permanently stable rock mass conditions for long term load cases,
- Control deformation in the rock mass to limit water seepage.

- All excavated openings are supported by the provision of systematic rock support measures designed to accommodate the design loadings. It is recognized that unfavourable geomechanical or geometrical conditions require particular consideration and that localized special rock support solutions may be necessary in some areas. The rock support system comprises shotcrete, rock bolts, rock anchors and strengthening ribs of steel/concrete/ shotcrete.
- The following loads are considered as part of the analysis:
 - o Static load caused by overburden weight and horizontal initial stresses.
 - o Dynamic load i. e. earthquake loading (In most analysis models, seismic force is applied as an equivalent static load).
 - o Water pressure as per the requirements of water curtain system.
- Block analysis (using the program Unwedge) to investigate stability of potential wedges and numerical analysis of rock deformation and rock support interaction (using the program Phase 2.0) are carried out. Rock support design is carried out based on limit state considerations. A range of rock support measures, specifically shotcrete (either plain or fibre reinforced) and rock bolting, are considered (Figure 11, Figure 12).

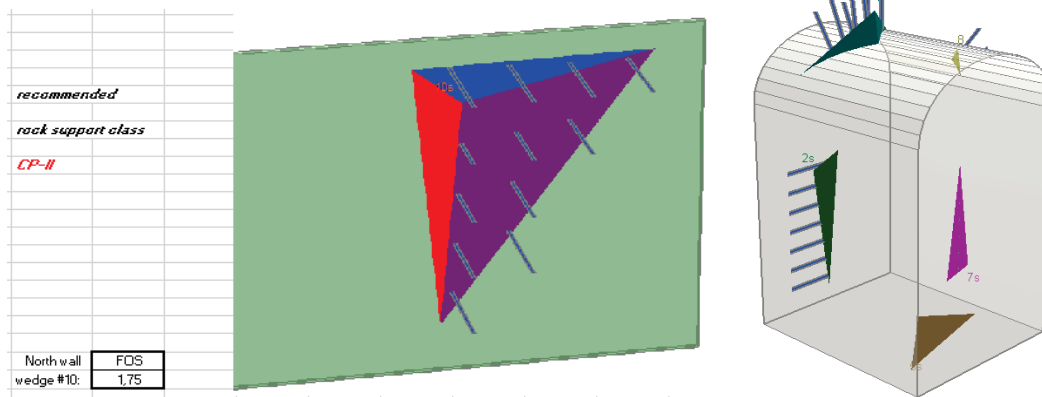


Figure 11: Typical block analyses (software: Unwedge)

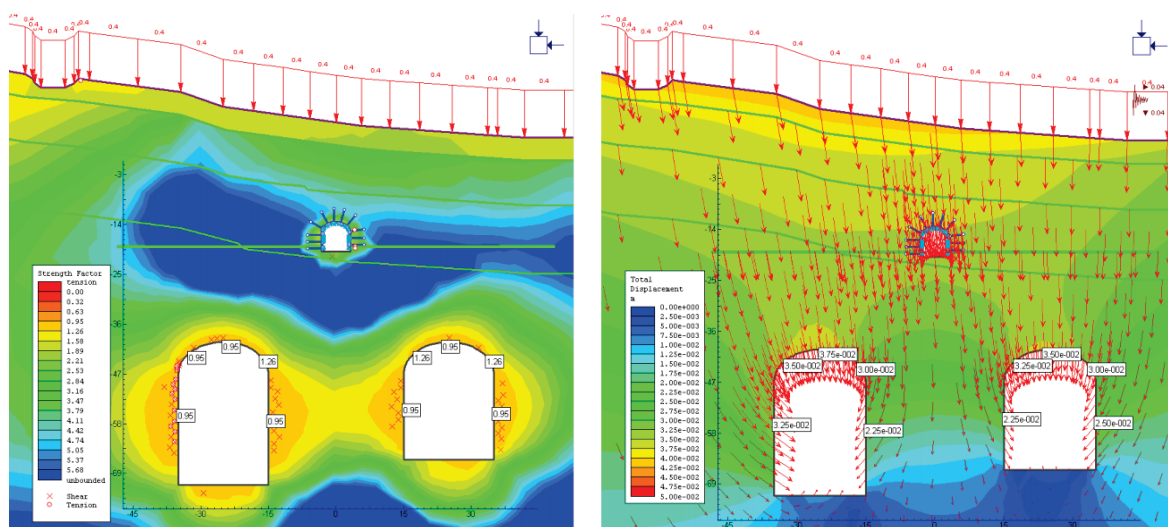


Figure 12: Typical FEM analysis (software: Phase 2 (RS2))

2.3 Design safety philosophy

Construction of underground structures involves several risks which are more or less absent in typical surface construction projects. Although most of the hazards and risks appear to be related to construction processes, some risks and safety issues can be identified and addressed during the design process itself.

As part of the design, the following critical key points are highlighted during design development:

- To use design input, which is moderately conservative,
- Construction sequence to be reviewed (followed by design review) to avoid temporary interruption or obstruction of escape and rescue ways,
- To consider excavation sequence and size of intermediate excavation steps such that the excavation stages are manageable with the intended equipment without exposing personnel and equipment to unnecessary risks and hazards,
- To assess the excavation activities at and around special local features, such as intersections with shafts and caverns regarding construction practicality, so as to reduce the potential risks. Further, the safety concept applied in this project is based on the use of load factors, overall factors of safety and partial factors for material strengths. In addition, monitoring records from underground locations during construction are studied against the results of numerical analyses.

In certain cases, are also large wedge studies are carried out for identifying and validating critical joint combinations along the side walls (Figure 13).

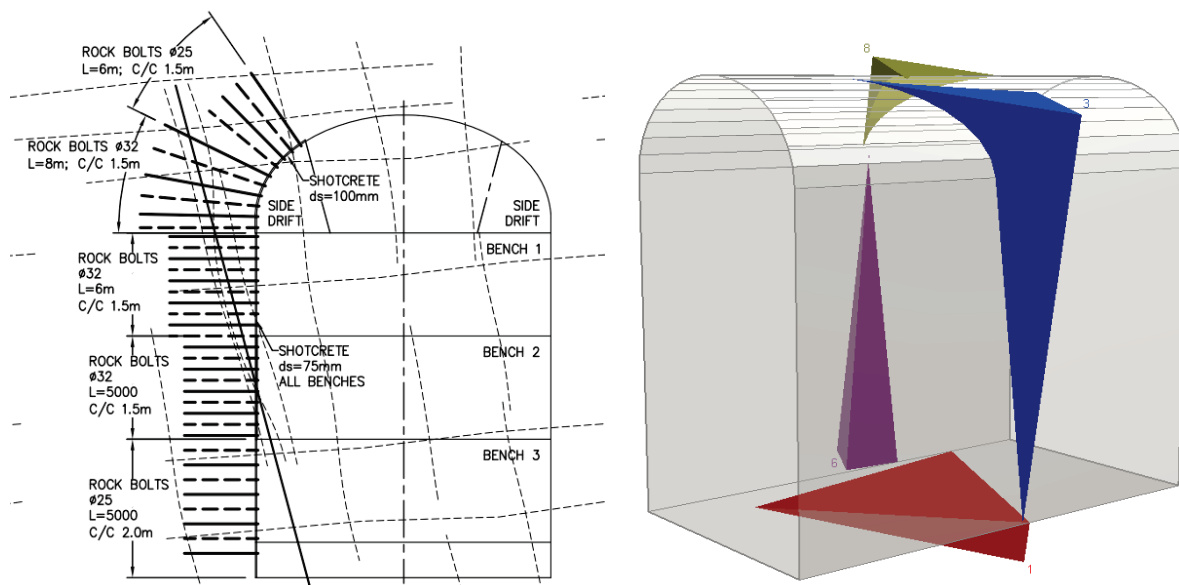


Figure 13: Large wedge formation in sidewalls and wedge analyses (Software: Unwedge)

According to the original basic design, the distinction between the support classes has to be based on the Q value derived from face mappings (Figure 14).

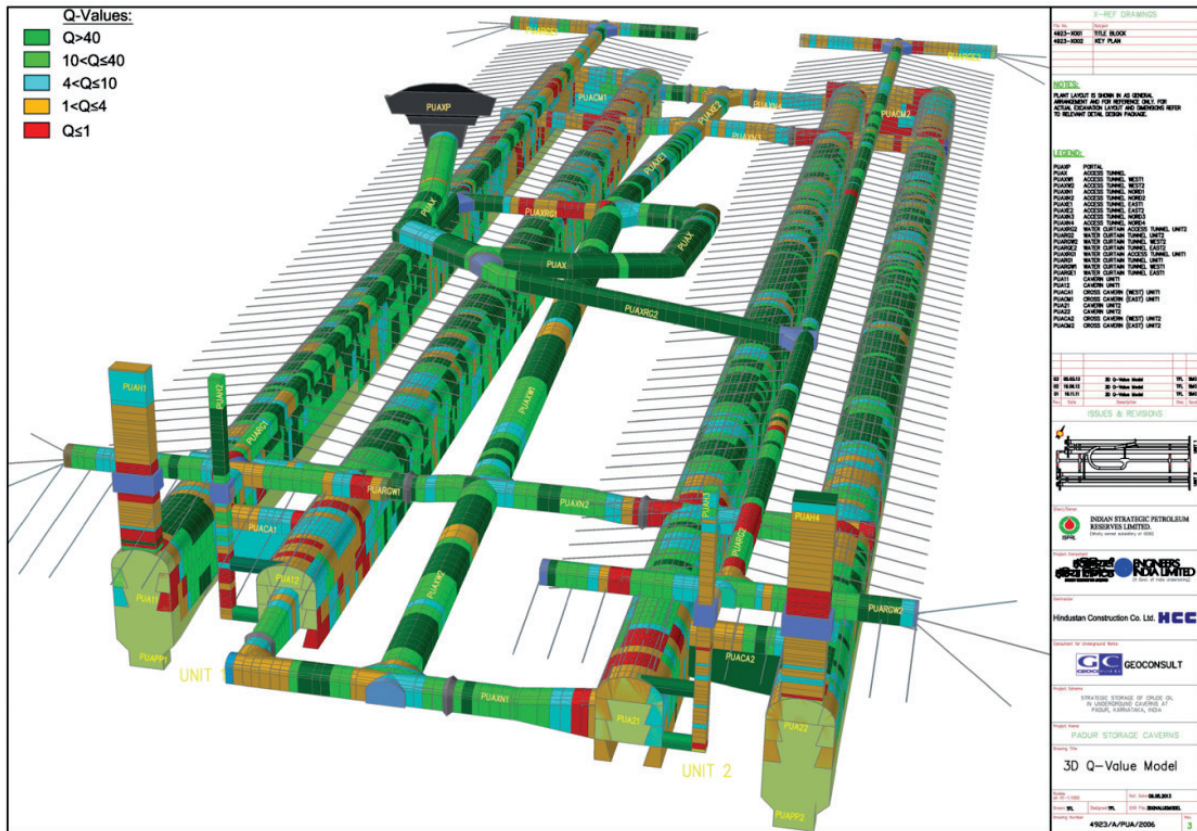


Figure 14: 3D model of the Q value distribution

As an additional measure, so-called bench release procedures were introduced to take care of the scale effects for caverns and the inherent inability of an index system like the Q system to cater for large single structures (Figure 2). These procedures are a structured review wherein the encountered ground conditions are assessed against the basic design and cross checked systematically for deviations, which are then supplemented by further analyses.

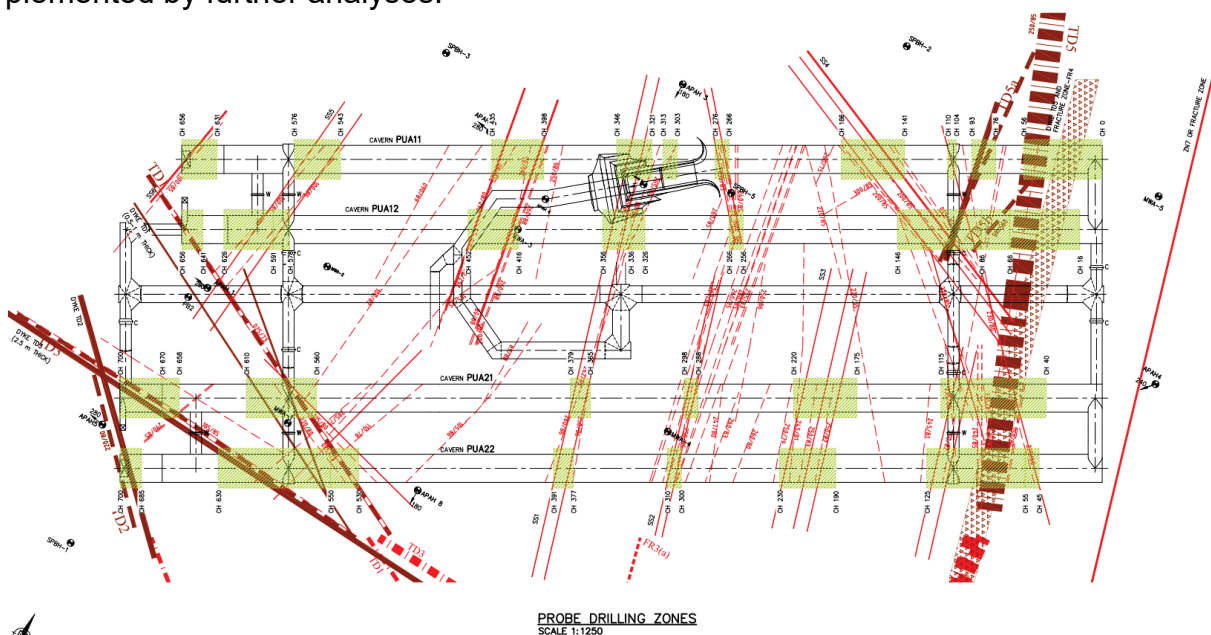


Figure 15: Plan view of the cavern complex with investigated large single structures

2.4 Risk management

Right from the early stages of detailed design, a rigorous risk management approach was implemented on the project with frequent reviews and updates during construction. This started with the assessment of risks at the design stage and was seamlessly carried over into the construction stage. An on-site risk review team integrated the risk management between the design and the construction team.

The risk management processes were used for the assessment of all risks. All identified risks were listed in an open risk register and continuously updated and used for further risk management during construction. Although the assessment of design risks may appear to be different from the assessment of construction risks, it has to be stated that the methods are principally very similar in both cases and based on the very same methodologies and assessment approaches. Therefore, risks arising from a variety of hazards were identified and quantified by risk assessments throughout all stages of the project, using the principle methods and approaches presented in the following sections.

The management of risks on this project were carried out as a systematic process, involving the following principle steps:

- Identify through risk assessments hazards and associated risks that impact on the project's outcome in terms of costs and programme as well as health and safety effects,
- Quantify risks including their programme and cost implications,
- Identify control measures to be implemented to eliminate or mitigate the risks,
- Identify who owns a particular risk and who is responsible for the implementation of the required mitigation measures.

The continuous updating of the risk register, both design as well as construction-related, and the development of risk assessment tools and procedures was carried out throughout the entire construction period in order to achieve the final objective of capturing and adequately addressing risks related to the design and all construction activities on the project.

2.4.1 Risk assessment methodology

Risk is defined as the combination of consequence (or severity) of a hazard and its likelihood, and it can be quantified using the methods presented in this paper. The product of the risk assessment process is a risk register, which is considered as a "live document" similar to databases that are frequently maintained, reviewed and revised, as appropriate.

Although most of the hazards and risks appear to be related to construction processes, some, even some significant risks and safety issues can already be identified and addressed during the design process. Ideally, this results in the elimination of some hazards and/or risks or at least results in reducing the potentially negative consequences related to some risks.

The general approach to the methodology of risk assessment and mitigation of risks is, after their identification, to suppress and control the causes of hazards such that either their occurrence frequency, or, if they do occur, the severity of their consequences is reduced. Therefore, the assessment is carried out for each cause of a hazard. By controlling or eliminating the causes of a particular hazard, the hazard itself can be controlled or eliminated.

Risk should be managed by the persons, who can influence it. Therefore, the assessment of risks follows the design and construction process step-by-step, involving staff

and personnel involved in the actual construction process, not only managerial staff. The assessment is carried out according to the following procedure:

- Identification of hazards: As the first step, particular design or construction hazards are identified. In this process it is also important to identify an owner of the particular hazard. The owner will in the future be responsible for organising and supervising the implementation of control and mitigation measures or reporting difficulties related to the implementation process to the risk management group.
- Identification of hazard causes: A hazard may be triggered by one or more causes. In order to assess the causes, the hazard needs to be seen in its specific environment, either design or construction related.
- Determine incident/accident: If one or more causes of hazards occur and materialise, related incidents or accidents occur. During the assessment process, incidents/ accidents need to be identified in order to be able to later assess the magnitude of potential consequences.
- Initial control measures: The next step in the sequence is listing of control measures, which have already been considered and which address and affect a specific hazard.
- Assessment of initial risk index: Using the assessment tools, the likelihood (occurrence frequency) and severity (magnitude of consequences) are determined. Combining the likelihood with the severity of a hazard cause and using the tools presented in this paper, the related risk can be quantified into a risk index.
- Additional control measures: If the initial risk index is unacceptable, additional control measures have to be identified and implemented in order to bring the risk into the acceptable range.
- Assessment of residual risk index: After consideration of the additional control measures, the risk is quantified again, and a residual risk index determined. The residual risk index should be related to a risk within the acceptable range.

2.4.2 *Design risks*

As mentioned above, both design and construction risks are assessed, quantified and managed using the same risk assessment tools. The assessment of design risk is carried out by analysing each step in the design process, reviewing both input as well as calculation approaches. The claimed use of conservative input parameters may already be a major risk if the assumption is incorrect. Parameter studies are a feasible checking measure.

In the initial phases of design development for each major design package, the following issues are addressed:

- Construction sequences proposed in the design match the intended construction equipment and method, appropriate sequencing avoids interruption or obstruction of escape and rescue ways,
- Excavation sizes (also of intermediate excavation steps) are manageable with the intended equipment without exposing personnel and equipment to unnecessary risks and hazards,
- Excavation activities at and around locations with special conditions, such as intersections with shafts and caverns, etc. are assessed for constructability in order to reduce the potential hazards,
- Design of slopes around the shafts is reasonably conservative considering that major construction activities (shaft construction, equipment staging) occur at the bottom of the slope, involving significant numbers of work force and sensitive operational equipment.

2.4.3 Construction risks

An essential part of the risk assessment is breaking down each construction activity into its constituent elements and components. With respect to the assessment of construction risks, the following considerations will be taken into account:

- Step-by-step analysis and breakdown of the work activity,
- The persons involved in the work,
- The duration of work,
- The type of equipment/machinery,
- The type of material handled,
- The working environment.

Next, the hazards associated with each step are identified. In order to identify the types of hazards in the work activity, the following guidelines can be applied:

- The hazards a person is exposed to at every step of the
- work activity, e.g. falling from height, material falling
- from height, slipping, equipment operating nearby, etc.,
- The hazards associated in operating equipment and machinery,
- The hazards associated in handling materials,
- The hazards relating to the work environment,
- The hazards related to environmental impact.

2.4.4 Approach

Addressing and quantifying the likelihood of a hazard cause becoming a reality is based on the judgment of the assessors and was supported by experience from past projects of similar magnitude (Table 1). Table 2 provides guidelines for the categorization of consequences resulting from the occurrence of hazardous elements and incidents in terms of injuries or losses.

Risk is defined by combining the likelihood of incident occurrence with the severity of consequences. The risks on this project were quantified into risk indices A to D according to the risk matrix presented in Table 3. The shaded cells in Table 3 identify acceptable risk indices (“C” or “D”) and therefore characterise tolerable and acceptable risks. Table 4 presents the proposed definition of the Risk Index.

Table 1: Likelihood of incident occurrence

Likelihood	Rating	Description
Frequent	I	Likely to occur 12 times or more per year
Probable	II	Likely to occur 4 times per year
Occasional	III	Likely to occur once a year
Remote	IV	Likely to occur once in a 5-year project period
Improbable	V	Unlikely, but may exceptionally occur

Table 2: Severity of consequences

No.	Consequence	Rating	Description ¹
1	Catastrophic	I	Single or multiple loss of life from injury or occupational disease, immediately or delayed; and/or Damage to works or plant causing delays of more than 1 month; and/or total loss in excess of 2 % of contract sum.
2	Critical	II	Major injury, occupational disease or dangerous occurrence ² ; and/or Damage to works or plant causing delays of more than 1 week but less than 1 month; and/or total loss in excess of 0.5 % but less than 2 % of contract sum.
3	Marginal	III	Reportable injury, occupational disease ³ ; and/or Damage to works or plant causing delays of less than 1 week; and/or total loss in excess of 0.05 % but less than 0.5 % of contract sum.
4	Negligible	IV	Minor injury, no lost time or the person involved returns to work during the shift after treatment; and/or damage to works or plants does not cause significant delays; and/or total loss is less than 0.05 % of contract sum.

¹ If more than one of the descriptions applies, the severity rating would be increased to the next higher level. Applicable to item numbers 2 and 3 only.
² For more than 7 man-days lost.
³ For between 2 and 7 man-days lost

Table 3: Risk Matrix with risk indices

			Accident severity category			
			I	II	III	IV
			Catastrophic	Critical	Marginal	Negligible
Accident frequency category	I	Frequent	A	A	A	B
	II	Probable	A	A	B	C
	III	Occasional	A	B	C	C
	IV	Remote	B	C	C	D

Table 4: Definition of the risk index

Risk index	Risk description	Definition
A	Intolerable	Risk shall be reduced by whatever means possible.
B	Undesirable	Risk can only be accepted if further risk reduction is impracticable.
C	Tolerable	Risk can be accepted subject to demonstration that the level of risk is as low as reasonably practicable.
D	Acceptable	Risk is acceptable.

2.4.5 Control measures

Control measures are proposed to reduce the identified and evaluated risks to acceptable levels. Examples of such control measures are detailed work procedures for all work activities, continuous training of staff at all levels, emergency stop devices found in certain equipment and the use of skilled tradesmen such as a lifting supervisor for lifting operations.

With the control measures in place, the risks are re-assessed, and the residual risk index re-evaluated. This step is essential in monitoring the reduction of the risk after the implementation of the control measures.

3 Conclusion

These projects are highlighting the importance of a flexible engineering approach which can be valued and adjusted on the investigated geological and geotechnical information during the construction stage.

A brief overview has been given on the nature of the ongoing cavern projects for Strategic Storages for Crude Oil and the services rendered by Geoconsult at the Padur and Vizag Cavern project. The civil works of these challenging projects have been finished successfully.

4 References

- [1] Zhao, J., Choa V., Broms, B. B.: Construction & Utilization of Rock Caverns in Singapore. Part B: Development Costs & Utilization. *Tunnelling & Underground Space Technology* 11 (1996), No. 1, pp. 73–79.
- [2] Tezuka, M., Seoka, T.: Latest Technology of Underground Rock Cavern Excavation in Japan. *Tunnelling & Underground Space Technology* 18 (2003), No. 2–3, pp. 127–144.
- [3] Lee, C. I.: Stability of Underground Oil & Gas Storage Caverns in Korea-Mechanical & Hydrological Aspect. In Saito, Murata (eds.): *Environmental Rock Engineering*. pp. 61–72. Rotterdam: Balkema, 2003.
- [4] Benardos, A. G., Kaliampakos, D. C.: Hydrocarbon Storage in Unlined Rock Caverns in Greek Limestone. *Tunnelling & Underground Space Technology* 20 (2005), No. 2, pp. 175–182.
- [5] Amantini, E., Cabon, F., Moretto, A.: Groundwater management during the construction of underground hydrocarbon storage in rock cavern. In *Proceedings of the 9th International Mine Water Association Congress, Spain, 2005*, pp. 311–315.
- [6] ÖNORM B 2203-1: Underground works – Works contract – Part 1: Cyclic tunnel excavation (conventional tunnelling). Austrian Standard, Edition 2001-12-01.
- [7] Ganesh, J. B.: Application of the Grouting Intensity Number (GIN) method for Grouting of Rock Caverns. *Tunnelling and Underground Construction Society, Singapore; Hulme Prize Paper Competition, 2009*.
- [8] Kudtarkar, D. M., Patil, A., Mohanty, S. K., Nawani, P. C.: Site investigations and rock mass characterizations for crude oil strategic storage cavern project, Visakhapatnam – A case study. In *Proceedings of the International Conference on*

- Underground Space Technology, Bangalore, India, 2011, paper no. SC-03, pp. 1–11.
- [9] *Mohanty, S. K., Sigl, O., Krenn, F., Höfer-Öllinger, G.*: Underground crude oil storage projects in India/Unterirdische Rohölkavernen in Indien. *Geomechanics and Tunnelling* 6 (2013), No. 5, pp. 509–518.
- [10] *Naithani, A. K.*: Underground rock caverns for strategic crude oil storage in India – nature of studies, design and construction. *Current Science* 103 (2012), No. 5, pp. 490–496.
- [11] Austrian Society for Geomechanics: Guideline for the Geotechnical Design of Underground Structures with Conventional Excavation. Salzburg, 2010.
- [12] SWECO: Strategic Storage of Crude Oil at Visakhapatnam – tender phase, Basic Engineering Design and Geotechnical Factual Reports including drawings. Unpublished, 2007.
- [13] TunnelTalk: India builds its first oil storage caverns. *TunnelTalk Annual Review* 2011, p. 54.
- [14] *Sigl, O., Millen B., Höfer-Öllinger, G.*: The underground crude oil storage caverns of Visakhapatnam, India, *Geomechanics and Tunnelling* 6 (2014), No. 5, pp. 155–162.

Distinct Element Modelling on the Effect of Wellbore Arrangement on Fracture Propagation during Multi-Stage Hydraulic Fracturing

Distinkte Elemente Modellierung zum Effekt der Bohrlochanordnung auf die Rissausbreitung beim Multifrac-System

P.L.P. Wasantha, H. Konietzky, T. Xu

College of Engineering and Science, Victoria University, Melbourne, Australia
Geotechnical Institute, TU Bergakademie Freiberg, Freiberg, Germany
Center for Rock Instability and Seismicity Research, Northeastern University,
Shenyang, PR China

Abstract

Multi-stage hydraulic fracturing was simulated using Universal Distinct Element Code (UDEEC). Five sequential stimulation stages were simulated considering two different wellbore arrangements – horizontal (i. e. parallel to the minor principal stress direction) and diagonal – and the horizontal spacing between stimulations was varied to 50 m and 100 m. The fluid was injected to each wellbore at a constant rate for 100 seconds. Both wellbore arrangements displayed a marked asymmetry of fracture propagation about the wellbore that could lead to reservoir underutilization. A directional bias of fracture propagation was observed where the major fracture component of each stimulation stage was propagated in alternating directions except for the case of the lowest stimulation spacing of diagonal wellbore arrangement. A greater stress shadow effect was observed when the stimulations were closely-spaced regardless of the type of wellbore arrangement. The fractures were also observed to extend even after the actual stimulation period due to the stress shadow of subsequent stimulations and this effect was found to be more pronounced for closely-spaced stimulation stages. The overall fracture lengths were greater for horizontal wellbore arrangement for any stimulation spacing considered compared to those of diagonal wellbore arrangement. Overall, the results indicate that the stress shadow effect considerably affects the hydraulic fracture propagation in multi-stage fracturing and wellbore arrangement and spacing have to be optimized to maximize the stimulated reservoir volume.

Zusammenfassung

Mittels des Universal Distinct Element Codes (UDEEC) wurde Multi-fracturing simuliert. Fünf aufeinanderfolgende Stimulationen für zwei verschiedene Bohrlochkonstellationen wurden betrachtet – horizontal (d. h. parallel zur Richtung der kleineren Hauptnormalspannung) und diagonal. Der horizontale Abstand zwischen den Stimulationen variiert zwischen 50 m und 100 m. Das Fluid wird in jedes Bohrloch mit einer jeweils konstanten Rate für 100 s injiziert. Beide Bohrlochkonstellationen zeigen eine markante Asymmetrie ums Bohrloch, was zu einer ungenügenden Ausnutzung des Reservoirs führen kann. Eine Neigung der Rissausbreitung wird in der Form beobachtet, dass sich die Risse bei jeder Stimulation in jeweils alternierende Richtungen ausbrei-

ten, mit Ausnahme des Falls mit dem geringsten Stimulationsabstand bei der diagonalen Bohrlochkonstellation. Ein starker Druckschatteneffekt wird für eng beieinander liegende Stimulationen unabhängig von der Bohrlochkonstellation beobachtet. Die Risse wachsen auch nach der aktuellen Stimulationsperiode weiter wegen des Druckschatteneffekts der danach folgenden Stimulationen. Dieser Effekt ist stärker ausgeprägt, wenn die Stimulationen räumlich eng beieinander liegen. Die generelle Risslänge ist größer bei horizontaler Bohrlochkonstellation für jeden Stimulationsabstand verglichen mit der diagonalen Bohrlochkonstellation. Zusammenfassend lässt sich sagen, dass der Druckschatteneffekt signifikante Auswirkungen auf die hydraulische Rissausbreitung beim Multi-stage fracturing hat und sowohl Bohrlochkonstellation als auch Stimulationsabstand optimiert werden müssen, um die Reservoirstimulation zu maximieren.

1 Introduction

The horizontal drilling techniques have enabled multi-stage hydraulic fracturing from a single wellbore which has resulted in a marked increase in productivity of natural gas production from Shale and tight resources. Multi-stage fracturing is also used in engineered geothermal systems (EGS) to create pathways for efficient fluid flow and heat exchange (Kumar and Ghassemi 2019). In any of the application, multi-stage fracturing results in a greater stimulated reservoir volume and improved reservoir permeability compared to single-stage fracturing.

Spacing between different stimulation stages is a key parameter in fracturing designs of multi-stage fracturing. Conventional wisdom suggests that closer spacing between different stages increases the stimulated reservoir volume and hence the production from unconventional hydrocarbon reservoirs. However, instead of getting higher production per stage, closer spacing can lead to incrementally less hydrocarbon production per stage (Dohmen et al. 2015). The stress redistribution induced during one fracturing stage affects the growth of hydraulic fractures in the subsequent stage, which is known as stress shadowing, is the main driver that creates the anomalies in stimulated fracture geometries between different stages of multi-stage fracturing. Stress shadow is a well-known effect observed in the field (Vermylen and Zoback 2011) and numerical simulations (e.g. Nagel and Sanchez-Nagel 2011; Kresse et al. 2013; Taghichian et al. 2014; Zangeneh et al. 2015; Wasantha et al. 2019). Therefore, the spacing between stages needs to be optimized to maximise the efficiency of fracturing treatments by taking stress shadow effect into account.

Hydraulic fracturing is generally carried out following one of two schemes – (1) simultaneous fracturing, where multiple cluster zones are created at the same time, and (2) sequential fracturing, where clusters are created sequentially. Zipper fracturing where two or more horizontal wells are simultaneously or sequentially fractured has been studied in the literature as a technique to maximise the stimulated rock volume (e.g. Sesetty and Ghassemi 2015a; Kumar and Ghassemi 2016). A modified zipper fracturing where an initial offset between the clusters of two or more horizontal wells is maintained has been studied in the literature although no noteworthy increase in stimulated rock volume is reported (Sesetty and Ghassemi 2015a; Sesetty and Ghassemi 2015b). Clearly, the wellbore arrangement has an important implication on the stimulated reservoir volume during multi-stage fracturing. This paper investigates the fracture propagation characteristics during multi-stage hydraulic fracturing with horizontal and diagonal wellbore arrangements using a distinct element method (DEM)-based numerical simulation program.

2 Methodology

Fully coupled hydro-mechanical analyses were performed using Universal Distinct Element Code (UDEC). It has been successfully used in several studies in the literature for hydraulic fracturing simulations (e.g. Wasantha et al. 2019; Preisig et al. 2015; Zangeneh et al. 2015). As the fluid flow is only permitted along existing open contacts in UDEC fractures were pre-embedded for hydraulic fracture propagation. The fracturing fluid (i. e. water) is injected to a domain at a pre-determined location of each embedded fracture and the fracture contacts are broken upon receiving sufficient hydro-

lic pressure enabling the fluid flow. These embedded fractures were oriented perpendicular to the minor principal stress direction since the hydraulic fractures generally propagate perpendicular to the minor principal stress direction at higher major to minor principal stress ratios, as suggested by many studies in the literature (e.g. Hubbert and Willis 1957; Wang 2016; Wasantha et al. 2019). It is assumed that the fluid flow into blocks is negligible which is reasonable for less permeable reservoir rocks. First, single-stage fracturing was simulated and the variations of fracture length, width and wellbore pressure were recorded against fluid injection time and compared with the corresponding variations estimated based on the KGD analytical fracture model (Khristianovic and Zheltov 1955; Geertsma and de Klerk 1969) to validate the numerical models. The model validation procedure and the outcomes can be found in Wasantha et al. (2019).

Multi-stage fracturing was simulated using 1000 m x 2000 m models and five sequential fracturing stages were considered. Two scenarios of wellbore placement were modelled; (1) wellbores are located horizontally (i. e. parallel to the minor principal stress direction), (2) wellbores are located diagonally. The minor and major principal stresses applied to the models were 80 MPa and 160 MPa, respectively. The fluid was injected at a constant rate of 0.0833 m³/sec for 100 seconds for each stimulation stage and the horizontal spacing between wells was varied to 50 m and 100 m. The properties assigned for the blocks, embedded fractures for hydraulic fracture propagation, and fracturing fluid are shown in Table 1.

Table 1: Properties assigned to block material, fractures and fracturing fluid of UDEC models

Block (intact material) properties	
Density (kg/m ³)	2600
Elastic modulus (GPa)	50
Poisson's ratio	0.25
Cohesion (MPa)	25
Friction angle (°)	53
Fracture properties	
Cohesion (MPa)	25
Residual cohesion (MPa)	0
Friction angle (°)	53
Residual friction angle (°)	0
Dilation angle (°)	20
Fracture toughness (MPa·m ^{1/2})	1.5
Fracturing fluid properties (incompressible)	
Density (kg/m ³)	1000
Viscosity (Pa·sec)	0.001
Injection rate (m ³ /sec)	0.0833

3 Results and Discussion

Hydraulic fracture geometries observed after five sequential fracturing stages for both cases of wellbore arrangements – i. e. horizontal and diagonal – are shown in Figure 1. A strong interaction between the fractures created at various stages can be

observed for the case of 50 m spacing for both horizontal and diagonal wellbore arrangements. This was a product of the stress shadow effect and as the spacing between stimulations increases the stress shadow effect becomes less profound. In addition, a significant asymmetry of fracture propagation about the wellbores can be observed in Figure 1 for both types of wellbore arrangements, which eventually leads to a reduced stimulated reservoir volume. After the first stimulation, nearly all fractures show a directional bias in fracture propagation. While the cases (a), (b) and (d) show the directional bias of the major fracture segment in alternating directions, case (c) shows that the major fracture components of all four stages after the first stage are unidirectionally oriented. This was attributed to the differences in stress redistribution patterns after each stimulation stage and during fracture propagation.

The overall created fracture lengths observed after the total five stages of stimulations for each considered case are shown in Table 2. It can be seen that the horizontal wellbore arrangement has produced the greatest fracture lengths for both cases of spacing. In addition, Table 2 shows that closer spacing of stimulations has created longer fracture lengths for both cases of wellbore arrangement considered. Figure 2 shows the lengths of all fractures after each stage of stimulations. It is clear from Figure 2 that nearly all fractures have extended even after their actual stimulation period of 100 seconds. This was due to the stress shadow effect where the stimulation of later stages creates a stress shadow that drove the created fractures further in previous stages. This effect is more pronounced when the stimulations are closely spaced.

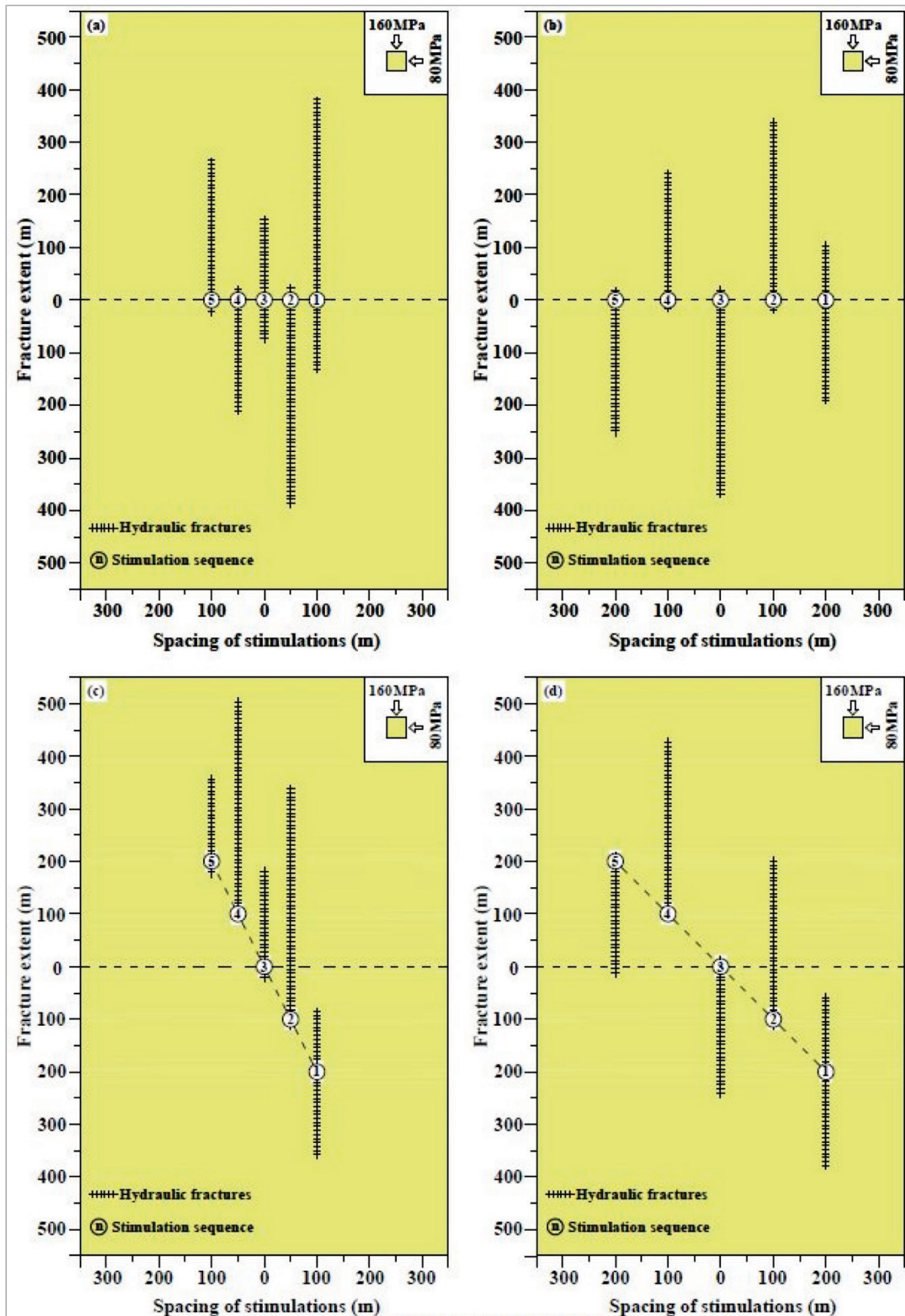


Fig.1: Fracture geometries after 100 seconds fluid injection for each stage (a) horizontal wellbore arrangement 50 m spacing, (b) horizontal wellbore arrangement 100 m spacing, (c) diagonal wellbore arrangement 50 m spacing, and (d) diagonal wellbore arrangement 100 m spacing.

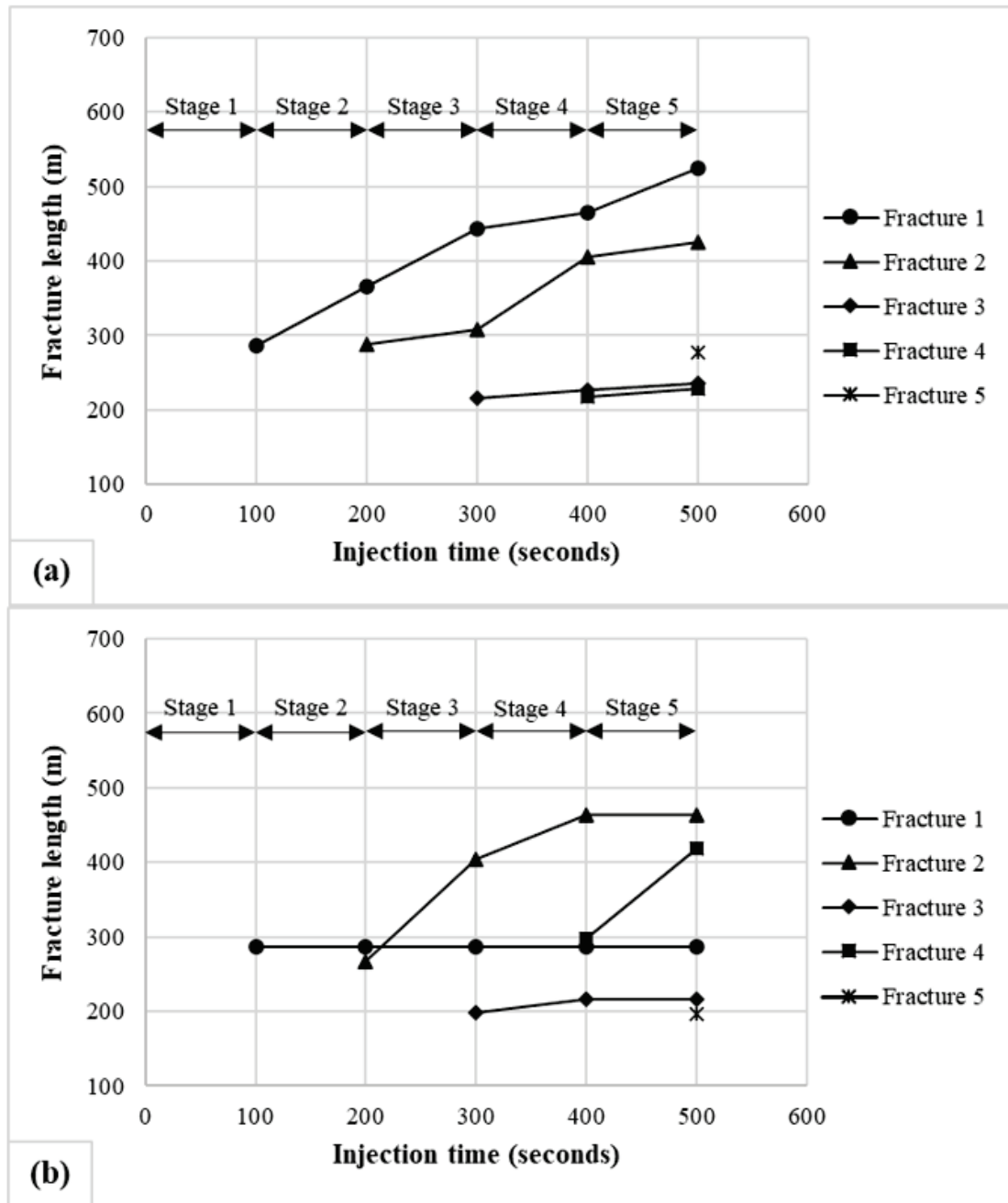


Fig.2: Fracture geometries after each fracturing stage for (a) horizontal wellbore arrangement 50 m spacing, and (b) diagonal wellbore arrangement 50 m spacing.

Table 2: Total fracture length observed for each case of stimulation

Wellbore arrangement	Total fracture length (m)	
	50 m spacing	100 m spacing
Horizontal arrangement	1,692	1,630
Diagonal arrangement	1,582	1,515

4 Conclusions

Universal Distinct Element Code (UDEEC) was used to simulate the multi-stage hydraulic fracturing under two types of wellbore arrangements – horizontal (i. e. parallel to the minor principal stress direction) and diagonal. Five sequential stages were considered for each wellbore arrangement. The horizontal spacing between stimulations was varied and fluid was injected at a constant rate for 100 seconds for each stimulation stage. Fracture propagation was observed to be highly asymmetric about the wellbore for both cases of wellbore arrangement which was attributed to the stress shadow effect. Fractures continued to extend even after the actual stimulation period due to the stress shadow of subsequent stimulations which was found to be more pronounced for closer stimulations. The overall fracture length for any stimulation spacing was observed to be greater for horizontal wellbore arrangement than the corresponding lengths of diagonal wellbore arrangement. Finally, the results of the numerical simulations indicate that the stress shadow effect can significantly affect the resulting stimulated reservoir volume after the fracturing treatment and the wellbore arrangement and spacing have to be optimized to achieve the desired outcomes.

5 Acknowledgements

The work was partially supported by the National Science Foundation of China (51811530312)

6 References

- Dohmen T, Zhang JJ, Blangy JP (2015) ‘Stress Shadowing’ effect key to optimizing spacing of multistage fracturing. *The American Oil & Gas Reporter*, September.
- Geertsma J, de Klerk F.(1969) A rapid method of predicting width and extent of hydraulically induced fractures. *Journal of Petroleum Technology*, 21: 1571-1581 (SPE 2458).
- Khrstianovic SA, Zheltov YP (1955) Formation of vertical fractures by means of highly viscous liquid. In: *Proceedings of the 4th World Petroleum Congress*, Rome, pp. 579-586.
- Kresse O, Weng X, Gu H, Wu R (2013) Numerical modeling of hydraulic fractures interaction in complex naturally fractured formations. *Rock Mechanics and Rock Engineering*, 46: 555-568.
- Kumar D, Ghassemi A (2016) A three-dimensional analysis of simultaneous and sequential fracturing of horizontal wells. *Journal of Petroleum Science and Engineering*, 146: 1006-1025.
- Kumar D, Ghassemi A (2019) Multistage hydraulic fracturing of EGS wells with application to FORGE, In: *Proceedings of the 44th Workshop on Geothermal Reservoir Engineering*, Stanford University, Stanford, California, pp. 11-13.
- Nagel NB, Sanchez-Nagel M (2011) Stress shadowing and microseismic events: a numerical evaluation. *Society of Petroleum Engineers*, SPE 147363.
- Preisig G, Eberhardt E, Hosseinian A, Bustin M (2015) Coupled hydromechanical modeling of rock mass response to hydraulic fracturing: outcomes related to the enhancement of fracture permeability. In: *Proceedings of the 13th International Congress of Rock Mechanics (ISRM 2015)*, 10-13 May, Montréal, Canada.

- Sesetty V, Ghassemi A (2015a) A numerical study of sequential and simultaneous hydraulic fracturing in single and multi-lateral horizontal wells. *Journal of Petroleum Science and Engineering*, 132: 65–76.
- Sesetty V, Ghassemi A (2015b) Simulation of simultaneous and zipper fractures in shale formations. In: *Proceedings of the 49th US Rock Mechanics/Geomechanics Symposium*. San Francisco, CA, USA, pp. 1–9.
- Taghichian A, Zaman M, Devegowda D (2014) Stress shadow size and aperture of hydraulic fractures in unconventional shales. *Journal of Petroleum Science and Engineering*, 124: 209-221.
- Vermilyen JP, Zoback MD (2011) Hydraulic fracturing, microseismic magnitudes, and stress evolution in the Barnett shale, Texas, USA. *Society of Petroleum Engineers, SPE 140507*.
- Wang H (2016) Numerical investigation of fracture spacing and sequencing effects on multiple hydraulic fracture interference and coalescence in brittle and ductile reservoir rocks. *Engineering Fracture Mechanics*, 157: 107-124.
- Wasantha PLP, Konietzky H, Xu C (2019) Effect of in-situ stress contrast on fracture containment during single-and multi-stage hydraulic fracturing. *Engineering Fracture Mechanics*, 205: 175-189.
- Zangeneh N, Eberhardt E, Bustin RM (2015) Investigation of the influence of stress shadows on horizontal hydraulic fractures from adjacent lateral wells. *Journal of Unconventional Oil and Gas Resources*, 9: 54-64.

The influence of stylolite on mechanical behavior of limestone: digital-image based discrete element analysis

**Der Einfluss von Stylolit auf das mechanische Verhalten von Kalkstein:
Digitalbildbasierte Analyse diskreter Elemente**

Tao Xu, Zhen Heng, Bo Zhao, Jingke Lu, Jiantao Lu

Center for Rock Instability and Seismicity Research, Northeastern University,
Shenyang 110819, China

Abstract

Stylolites are common and pervasive in the sedimentary formations. In the present manuscript, the influence of stylolite in limestone on the strength of limestone and the crack evolution in the limestone were numerically and experimentally studied based on digital image based discrete element method. The digital image based stylolite was constructed by box dimension method to study the fractal dimension of the horizontal and vertical stylolite in limestone. The results show that the stylolite in limestone is a self-affine fractal structure in nature. The stylolite weakens the uniaxial compressive strength of limestone by about 20 % on average, but it has negligible effect on elastic modulus of limestone. The initiation and propagation of crack is closely related to the stylolite in limestone during the failure of stressed limestone. Moreover, numerical simulations show that the thickness, position, and number of the stylolite in limestone have significant effects on the uniaxial compressive strength of the limestone.

Zusammenfassung

Stylolites sind in den Sedimentformationen häufig und weit verbreitet. In dem vorliegenden Artikel wurden der Einfluss von Stylolit in Kalkstein auf die Festigkeit von Kalkstein und die Rissentwicklung im Kalkstein numerisch und experimentell untersucht, basierend auf der auf digitalen Bildern basierenden diskreten Elementmethode. Der auf digitalen Bildern basierende Stylolit wurde nach der Box-Dimension-Methode konstruiert, um die fraktale Dimension des horizontalen und vertikalen Stylolithen in Kalkstein zu untersuchen. Die Ergebnisse zeigen, dass der Stylolith in Kalkstein eine selbstaffine fraktale Struktur in der Natur ist. Der Stylolith schwächt die einachsige Druckfestigkeit von Kalkstein um durchschnittlich etwa 20 %, hat jedoch einen vernachlässigbaren Einfluss auf den Elastizitätsmodul von Kalkstein. Die Entstehung und Ausbreitung von Rissen hängt eng mit dem Stylolithen in Kalkstein während des Versagens von belastetem Kalkstein zusammen. Darüber hinaus zeigen numerische Simulationen, dass Dicke, Position und Anzahl des Stylolithen in Kalkstein signifikante Auswirkungen auf die einachsige Druckfestigkeit des Kalksteins haben.

1 Introduction

Stylolite deposition process is a common special geological structure [1, 2] by the inter-particle pressure solution formation, and it can be widely founded in carbonate rocks, sandstone and shale [3, 4]. Gratier, Muquet, Hassani and Renard [5], Katsman [6] and Ebner, Koehn, Toussaint and Renard [7] reproduced the pressure solution process under natural conditions by experimental and numerical simulation method. Koehn et al. [8] pointed out that pressure solution process is non-uniform particles of random process of dissolution. Microscopic particles dissolved in rock under the tectonic stress differences, the stylolite exhibits an extremely complex geometrical morphology and surface roughness [4, 9], and the internal stylolite contains a lot of insoluble residue, such as calcite, quartz, iron oxide and dolomite [10]. Fractal geometry was used to describe the complex geometrical morphology by the power spectrum method $P \propto k^{-1-2H}$, it is found that the stylolite is a self-affine fractal structure with surface roughness H [11] and fractal dimension D [12-14], and it has a scale-invariant characteristic [15]. Geometrical morphology of stylolite can be used to analyze and predict the paleo-stress and displacement of strata [16, 17]. Due to the characteristics of the gap formed by partial pressure solution, stylolite affects fluid flow process in rock [18, 19]. Though great progress has been made to study the formation mechanism of stylolites in stone, little attention has been paid to the effect of stylolites on the mechanical properties of rocks [20]. For mining and geotechnical engineering, the impact of stylolites on the mechanical properties of rock (strength and elastic modulus, etc.) is usually involved in the stability of rock mass. Therefore, it is of great theoretical and practical significance to study the effect of stylolites on the mechanical properties of limestone. Digital image processing technology makes a great contribution to study the inhomogeneous rock structures [21]. In view of the complex microscopic and macroscopic characteristics of the stylolite, numerical simulation based on digital image has been a popular method to solve the deformation and failure of rock with complex microstructures. Wu, Zuo, Wang, Yi, Chen, Yu, Li, Sunwen, Xu, Wang and Li [22] studied the effect of joint on the failure of rock mass combined the digital image technique with finite element (FEM). Shi, Li, Xu and Wang [23] introduced the complex modeling approach and carried out a lot of research about digital image processing technology in DEM. In the present paper, based on the digital image processing technology, the fractal characteristics of the stylolite and its effect on uniaxial compressive strength of limestone are experimentally and numerically studied.

2 Digital image based discrete element method

Digital image processing (DIP) is a computerized technique by which a scene is captured electronically and transformed into a two-dimensional pixel image and then processed so that significant information can be extracted by mathematical algorithms. DIP has been used in geotechnical engineering for quantitative investigations of the orientations, distributions and shapes of aggregates in asphalt concrete [24], observation of crack networks in cement-based materials [25] and constructing discontinuity trace maps [26]. Yue et al. [27] studied mechanical responses of rock and other geomaterials by taking into account their internal structures and inhomogeneities with DIP technique and found that the inhomogeneity of material has significant effect on the stress distribution in rock mass.

2.1 Digital representation of stylolites

Generally, a colorful image is composed of three original colors, simplified by R, G and B. According to the pixel chromatic aberration of each color, the threshold of different segmentation is determined, so as to separate different micro-particles in rock mass to represent the heterogeneous characteristics of rock particles. For the gray image of limestone, the RGB color difference is not pronounced in the RGB model and the effect of image segmentation is not very clear, so this method is not often used. For the grayscale image, the method using gray value of pixel can solve this problem. First, the image of rock should be transformed into a grayscale image. The grayscale value of the picture is made up by each pixel, which could be obtained by using the weighted average method. And the gray scale ranges from 0 to 255. Secondly, the appropriate gray value should be selected as a threshold which is used to distinguish the stylolite and the rock matrix. Finally, the processed gray-scale image is transformed into a two-dimensional pixel image, in which the gray-scale value of the pixel is set to 0 or 1. It means the whole image only contain black and white. Because some portions of the limestone images are not very clear, the method of partial color burn is used to improve the effect of image segmentation. Using the image of limestone with the horizontal stylolite as an example, the rock image is transformed into grayscale image and the A-A' gray value in the image is scanned to determine the grayscale segmentation threshold between stylolites and rock matrix. The location of scan line is shown in Figure 1 and the result of pixel scan is shown in Figure 2. Figure 2 illustrates the scan line covers the stylolite and rock at the same time, and the gray value of stylolites is less than that of the rock. As a result, the gray value of 126 is selected as the segmentation threshold of these two materials. Figure 3 depicts the rock two-dimensional pixel image after gray value segmentation, and the stylolite area and the rock matrix area could be clearly distinguished in the image after the processing of digital image.

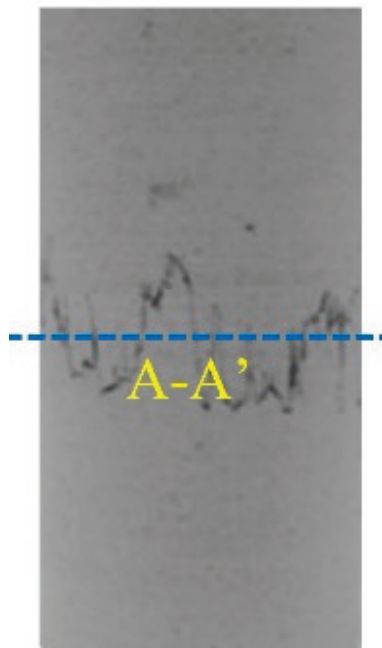


Fig.1: Location of scan line

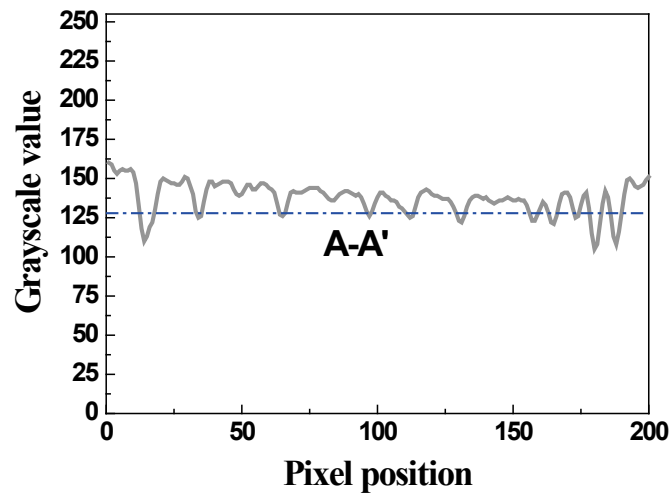


Fig.2: Grayscale curve

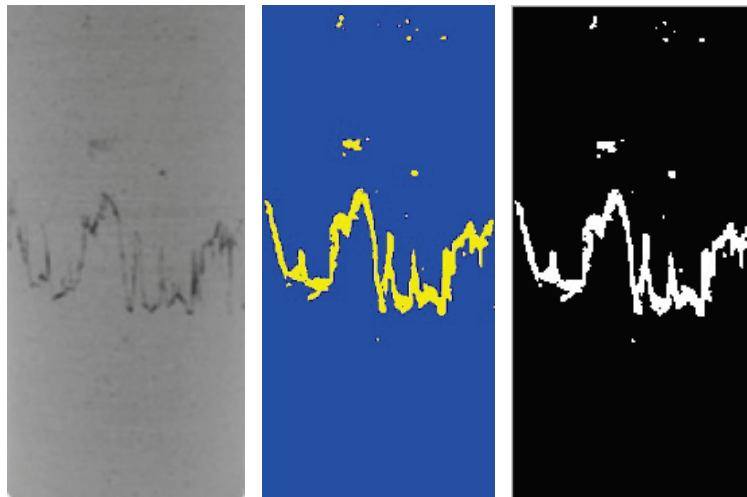


Fig.3: Digital representation of stylolites

2.2 Numerical model of stylolite in limestone

In bonded particle model in PFC, rock material is represented as an assembly of circular disks bonded together at their contact points and confined by planar walls. The particles are bonded together at their contact to simulate a competent rock. There are two basic bonding models supported in PFC: a contact-bonded model and a parallel-bonded model. A contact bond approximates the physical behavior of a vanishingly small cement-like substance lying between and joining the two bonded particles. The contact bond behaves as a parallel bond of radius zero. Thus, a contact bond does not have a radius or shear and normal stiffness as does a parallel bond, and cannot resist a bending moment, on the contrary, it can only resist force acting at the contact point. The contacts bonds are assigned with specified tensile and shear strength which allows resistance to tension and shear to exist at the contact until the force at the contact exceeds the strength of the bond. In order to generate a contact bonded particle model in PFC2D, the following microscopic parameters, Ball-to-ball Contact Modulus, stiffness ratio K_N over K_S , ball friction coefficient, contact Normal Bond Strength, contact Shear Bond Strength, Ratio of Standard Deviation to mean of bond strength both in

normal and shear direction, and minimum Ball radius, are defined using the routines provided (Cundall and Strack, 1979). Defining a parallel-bonded particle model requires additional three micro-parameters, parallel-bond radius multiplier, parallel-bond modulus, and parallel-bond stiffness ratio. In this paper, bonded particle models are created by assuming that particles are bonded together using the parallel bonded model. The thickness of model is equal to the size of a particle and the plane strain condition was established in the PFC2D model.

The heterogeneity and discontinuity of rock mass can be represented in PFC2D, but it is difficult and infeasible to generate complex model in PFC2D. However, it is feasible to build complex model in CAD, so complex physical model with model boundary and stylolite thickness is firstly constructed in CAD according to the electronic image of the rock, meanwhile a numerical model with the same dimension is also established in the PFC. Then the information parameters of the particles and the walls are imported into the CAD model. It is feasible to judge and determine whether the particles fall into the stylolite area according to the position of particles center, and the particles fallen into the stylolite area are numbered and grouped in CAD, and the renumbered and regrouped particles are imported back into the PFC model to generate a digital image based rock model with stylolites. The limestone samples with stylolite and the corresponding generated digital image based PFC2D models are presented in Fig. 4.

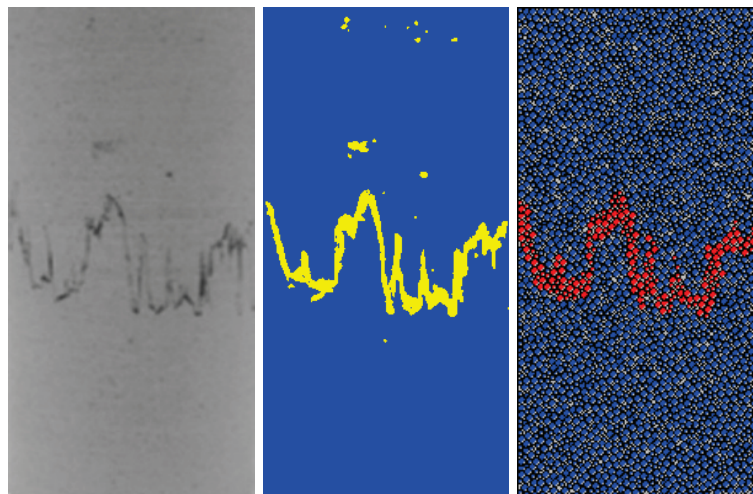


Fig.4: Model construction process by digital image based PFC2D model

3 Comparisons between experimental results and numerical simulations

3.1 Model setup and input parameters

The Oxfordian limestone samples were taken from the 174 m deep Oxford limestone of the Bill coal mine near the underground research laboratory in the south of France [28]. The intact rock samples nominally 40 mm long and 20 mm in diameter without and with stylolite of different inclination angles (0° , 63° , and 90°) were prepared from the 100 mm diameter limestone cores (Figure 5). A parallel bond model in PFC was used to simulate the contact characteristics between stylolite particles and rock particles in limestone (Figure 5). The density of granular media is consistent with the density of limestone. The meso-scale input parameters of numerical model are verified against experimental results (Table 2).

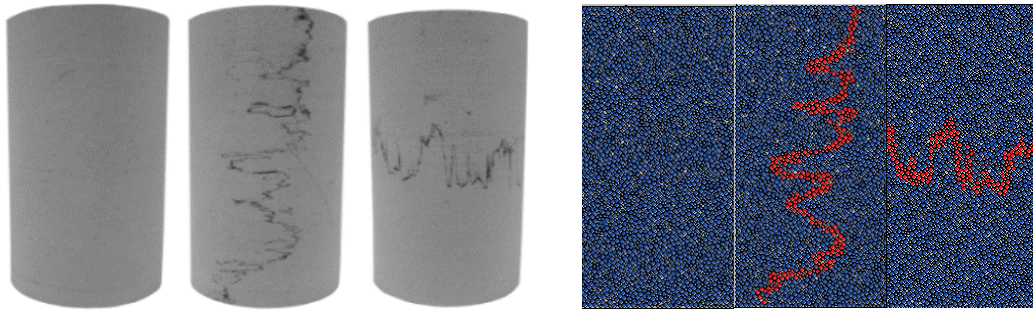


Fig.5: Limestone samples and the corresponding digital image based numerical models

Table 1 Mesoscopic input parameters of numerical model

Compo- sition	Mesoscopic parameters	Value
Rock	ball size ratio	1.66
	ball density (kg·m ⁻³)	2660
	ball-ball contact modulus (Pa)	12e9
	ball stiffness ratio (kn/ks)	1.0
	ball friction coefficient	0.5
	parallel-bond normal strength (mean and variance/ Pa)	30e6(15e6)
	parallel-bond shear strength (mean and variance /Pa)	75e6(20e6)
	parallel-bond modulus (Pa)	12e9
	minimum ball radius	0.02
	parallel-bond radius multiplier	1.0
	parallel-bond modulus (Pa)	12e9
	parallel-bond stiffness ratio(kn/ks)	1.0
Stylo- lite	ball-ball contact modulus	9.6e9
	ball stiffness ratio (kn/ks)	1.0
	ball friction coefficient	0.5
	parallel-bond normal strength (Pa)	24e6
	parallel-bond shear strength (Pa)	60e6

3.2 Modeling results

Figure 6 shows the experimental and numerical curves of free-styrolite limestone and limestone with styrolites. It can clearly seen that the numerical simulation could well reflect the progressive failure process of the limestone in the laboratory.

Figure 7 shows the evolution of acoustic emission (AE) events in limestone. The acoustic emission distributions in limestone at 0.05 %, 0.15 % and 0.25 % axial strain rates were investigated. When the strain rate reaches 0.15 %, the AE events containing large magnitude energy occur and are localized in the limestone. Compared with the whole limestone sample, the AE events containing large magnitude energy in the sample, which has the styrolite, mainly concentrate in the area of the styrolite and around the area. The vertical AE and inclined styrolite have more pronounced effect on the evolution of internal crack of limestone, and AE events mainly located in the region of the styrolite. When the peak stress is close to the ultimate compressive strength (axial strain rate reaches to 0.25 %), AE events cluster as faults, indicating that the macroscopic failure appears in the limestone.

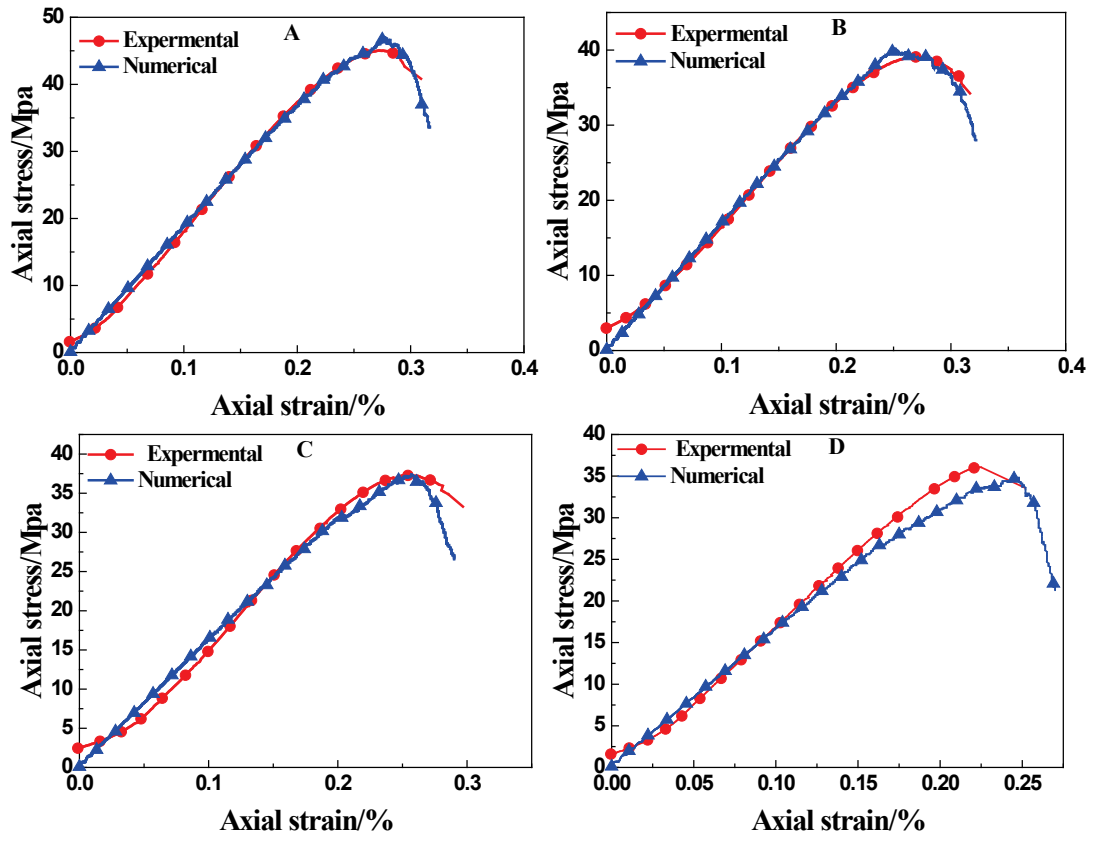


Fig.6: Comparisons between experimental and numerical stress-strain curves(A: intact rock; B: limestone with horizontal stylolites; C: limestone with vertical stylolites; D: limestone with incline stylolites)

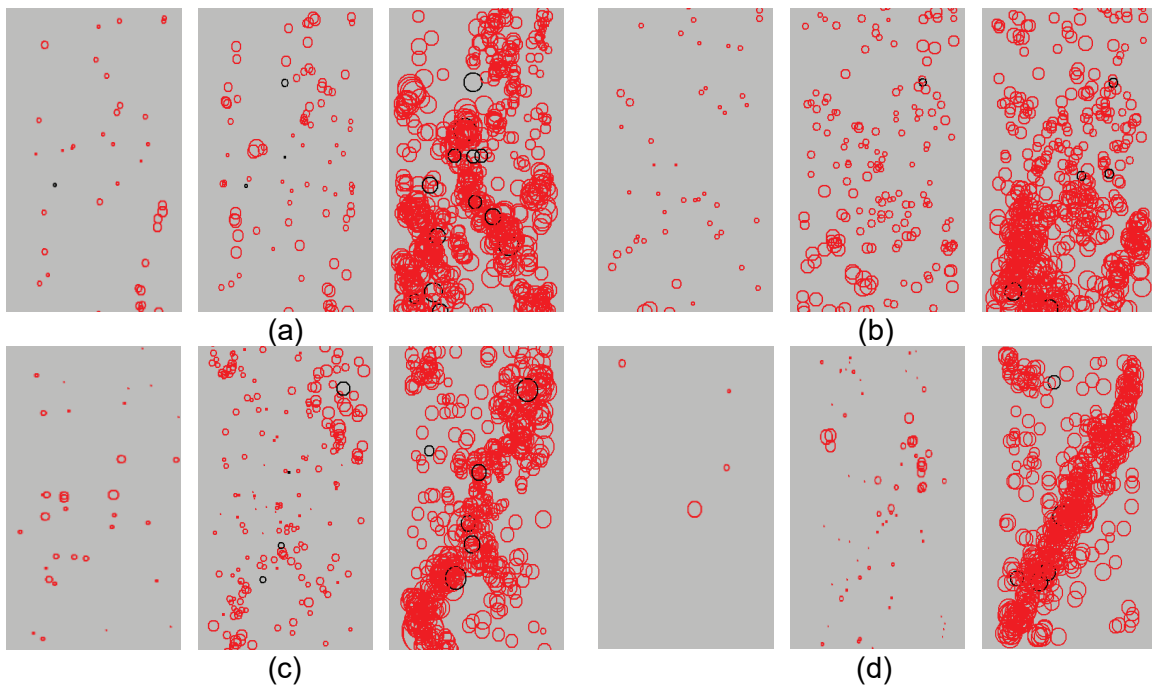


Fig.7: AE evolution in limestone with different angles of stylolites

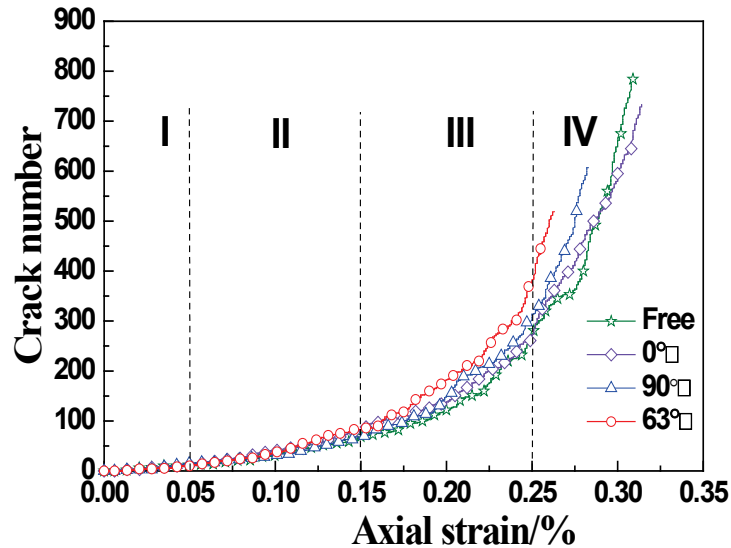


Fig.8: Crack number-axial strain curve

Figure 8 shows the evolution of the number of cracks in model sample with axial strains. It can be seen that the number of the crack could be divided into four stages, stage I and stage II are the stable development stage of cracks, and stage III is the instable development stage, stage IV is the post-peak stage. In the stage I, the number of cracks in the limestone sample is almost the same, and the curves in Fig. 8 are almost identical. In the stage II, the number of cracks increases linearly, but the number of cracks in the limestone specimen with inclined stylolite is the highest. For the stage III, the slope of the crack curve increases, the growth rate of cracks increases exponentially with the slope, indicating that the crack development is unstable. The crack develops rapidly at this stage. The slope of stage IV rapidly increase, which demonstrates that the limestone has failed. The number of cracks in inclined limestone is the highest under the same axial strain rate, and the number of cracks in intact limestone is the least. The stylolite accelerates the evolution process of internal damage of limestone, and the dip of inclined stylolite has great influence on the internal crack growth in limestone.

3.3 Influence of stylolite inclination on UCS and elastic modulus

Figure 9 shows the comparisons between experimental and numerical uniaxial compression strength of limestones with different stylolite inclinations. It can be clearly seen from Figure 9 that, stylolites with different dip angles reduce the peak strength of limestone. The peak strength of the limestone with horizontal stylolite is the highest, and the peak strength of the limestone with the inclination of 63° is is the lowest. And the peak strength of limestone decreases by about 20 %. The elastic modulus of limestone in different inclinations of stylolites fluctuates around 16 GPa, and the effect of stylolites on the elastic modulus of limestone is inremarkable.

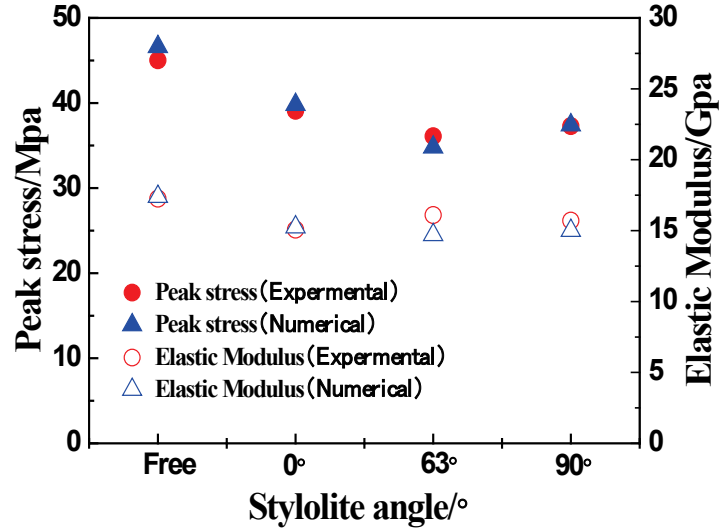


Fig.9: Experimental and numerical results on the effect of stylolite angle

4 Impact of stylolites on limestone strength

4.1 Weierstrass-Mandelbrot function representation

The structure of stylolites is influenced by formation composition, temperature, ground stress and other natural conditions, and the developmental characteristics are remarkable [29]. The influence of thickness, position, number, spacing and geometric shape of the stylolite on the mechanical properties of limestone was studied by considering the self-affine fractal characteristics of the stylolite geometry and the Weierstrass-Mandelbrot (W-M) function [30] self-affine fractal curve to simulate the geometry of the stylolite. The W-M function can be expressed as

$$W_0(t) = (1 - W^2)^{-0.5} \sum_{n=0}^{\infty} W^n e^{2\pi i b^n t} \quad (6)$$

where t represents time for an analysis performed in frequency space, or the homogeneous direction of the flow for an analysis performed in wavenumber space.

The W-M function is defined on the interval $[0, 1]$. It is everywhere continuous, yet nowhere differentiable. Hence, while its graph is connected, it looks “jagged” when viewed on arbitrarily small scales. And it is a fractal function with the fractal dimension D . The sinusoidal form of the W-M function (Figure 10) discussed by Karl Weierstrass is used in present paper. The expression is as following:

$$F(t) = \sum_{n=0}^{\infty} \left(\frac{3}{2}\right)^{(D-2)n} \sin\left(\frac{3}{2}\right)^n t \quad (7)$$

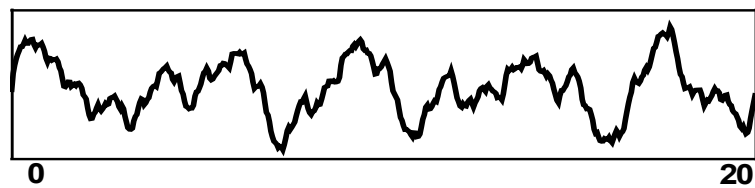


Fig.10: W-M fractal curve with $D=1.1$

4.2 Modeling results

Due to the difficulty in the preparation of rock specimen, it is of practical significance to numerically investigate the effect of stylolites on the strength of limestone. The n -range (1, 10), t -range (0, 20), $D = 1.1$, and 20 mm in length of the fractal curves are used in the numerical model. The numerical models with different fractal dimensions were obtained after the process of digital image according to the rock images [28]. The fractal dimension was obtained by the power spectral density method. Numerical models are set as 40 mm x 20 mm, the input parameters for the particles in the model shown in Figure 11 are the same as those in Table 2. The differences of the stylolite among the models mainly lie in thickness, position, number, spacing and geometrical morphology. The thickness of stylolites are 1, 1.5, 2, 2.5 and 3 mm, respectively, the positions from the top of the model specimen are 5, 10, 20, 30, and 35 mm, respectively, the spacings between stylolites are 8, 12, 16, 20 and 24 mm, respectively, and the fractal dimensions of the stylolite are 1.299, 1.480, 1.560 and 1.614, respectively.

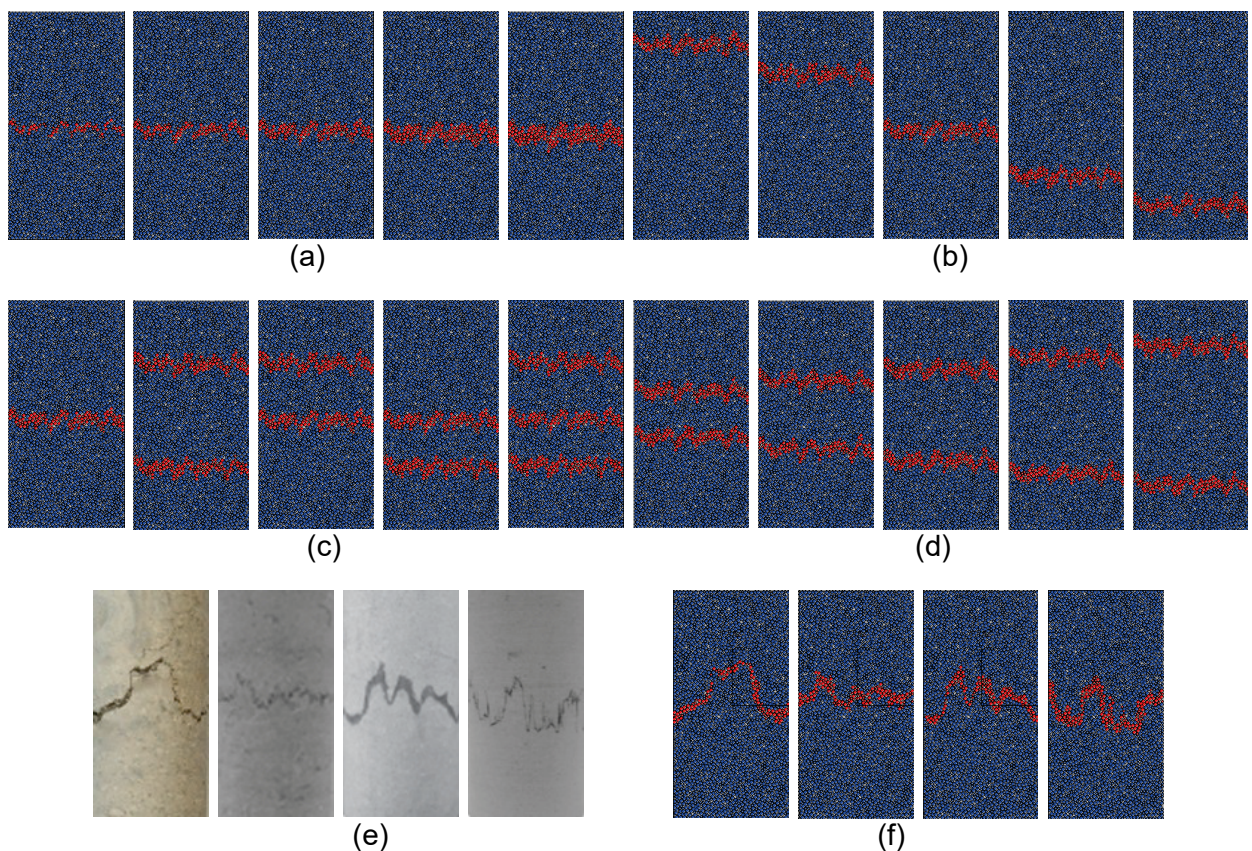


Fig.11: Numerical models of limestone with different developmental factors of stylolites (a: thickness, b: location, c: number, d: spacing, f: fractal dimension; e: limestone samples)

Figure 12 is the effect of different layouts of stylolite on the peak strength of limestone. The numerical simulations show that the peak strength decreases with the thickness of the stylolite. The position of stylolite in limestone also affects the peak strength of limestone. When the stylolite is in the middle of the specimen, the peak strength is the highest. With the increase of the number of stylolites, the peak strength of limestone decreases. The limestone has a higher strength when the number of stylolites is two and the stylolites locate in the middle-upper of the specimen, which reveals that when the number of stylolites is constant, the main influencing factor of the peak strength is

the location of stylolites. The peak strength slightly varies with the increase of the spacings between stylolites, and the corresponding peak strength of specimens ranges from 36 to 38 MPa. For the limestone with two stylolites, the peak strength ranges from 36 to 40 MPa in various spacings between stylolites. Compared with the peak strengths in different numbers of stylolites, the influence of the spacings on the peak strength could be effected by the number of stylolites. As the fractal dimension of the stylolite increases, the peak strength of the limestone decreases. However, in contrast to the peak strength at the fractal dimension of 1.560, the peak strength at the fractal dimension of 1.614 is higher. It may be due to the effect of the spacings and the location of the stylolite.

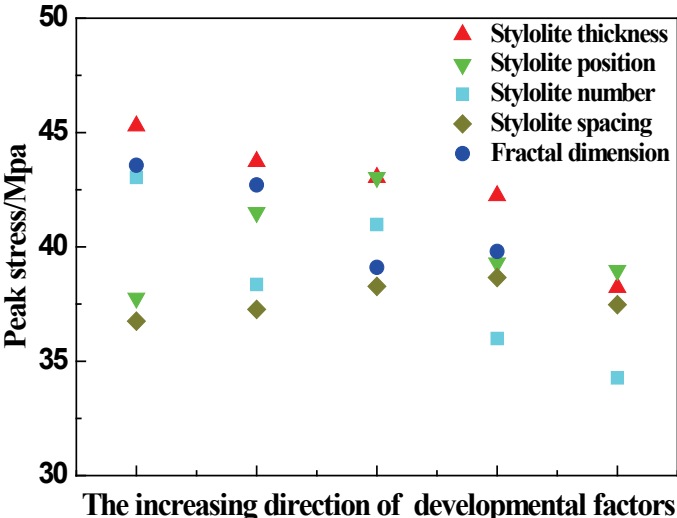


Fig.12: Influence of different factors of stylolites on limestone strength

Table 3 Simulated results of stylolites with different factors

Thickness/mm	1	1.5	2	2.5	3
Peak stress/MPa	45.3	43.7	43.0	42.241	38.2
Position/mm	5	10	20	30	35
Peak stress/MPa	37.8	41.5	43.0	39.3	38.9
number	1	2(top-under)	2(middle-top)	2(middle-under)	3
Peak stress/MPa	43.0	38.4	40.9	36.0	34.3
Spacing/mm	8	12	16	20	24
Peak stress/MPa	36.8	37.3	38.3	38.7	37.5
D/mm	1.3	1.5	1.6	1.6	
Peak stress/MPa	43.6	42.7	39.1	39.8	

5 Conclusions

In the present paper, the fractal characteristics of stylolite and the influence of stylolite in limestone on the uniaxial compressive strength of limestone are experimentally and numerically studied. The fractal dimension of horizontal stylolite and vertical stylolite was analyzed based on digital image processing technology. The influence of the stylolite on the uniaxial compressive strength of limestone and the crack evolution process of the limestone were studied through experimental tests and numerical simulations. The results show that the stylolite is a self-affine fractal structure in nature, and the

vertical stylolite has a large roughness. The stylolite weakens the strength of limestone by about 20 % on average, the stylolite has negligible effect on the elastic modulus of limestone. In the failure process of limestone, crack initiation and propagation in limestone is closely related to the stylolite, and the stylolite accelerates the damage and failure of the limestone. Numerical simulations show that the thickness, position, and the number of the stylolite have significant effect on the uniaxial compressive strength of the limestone.

6 Acknowledgements

The work was jointly supported by NSFC (51974062, 41672301, 51950410595, 51761135102) and Fundamental Research Funds for the Central Universities of China (N180101028).

7 References

- [1] R. Tada, R. Siever, Pressure solution during diagenesis, *Annual Review of Earth and Planetary Sciences*, 17 (1989) 89.
- [2] E. Tondi, M. Antonellini, A. Aydin, L. Marchegiani, G. Cello, The role of deformation bands, stylolites and sheared stylolites in fault development in carbonate grainstones of Majella Mountain, Italy, *Journal of Structural Geology*, 28 (2006) 376-391.
- [3] W. C. Park, E. H. Schot, Stylolites: Their nature and origin, *Journal of Sedimentary Petrology*, 38 (1968) 175-191.
- [4] E. H. Rutter, Pressure solution in nature, theory and experiment, *Journal of the Geological Society*, 140 (1983) 725-740.
- [5] J. P. Gratier, L. Muquet, R. Hassani, F. Renard, Experimental microstylolites in quartz and modeled application to natural stylolitic structures, *Journal of Structural Geology*, 27 (2005) 89-100.
- [6] R. Katsman, Extensional veins induced by self-similar dissolution at stylolites: Analytical modeling, *Earth & Planetary Science Letters*, 299 (2010) 33-41.
- [7] M. Ebner, D. Koehn, R. Toussaint, F. Renard, The influence of rock heterogeneity on the scaling properties of simulated and natural stylolites, *Canadian Journal of Zoology*, 81 (2011) 763-770.
- [8] D. Koehn, F. Renard, R. Toussaint, C. Passchier, Growth of stylolite teeth patterns depending on normal stress and finite compaction, *Earth and Planetary Science Letters*, 257 (2007) 582-595.
- [9] H. V. Dunnington, Stylolite Development Post-Dates Rock Induration, *Journal of Sedimentary Research*, 24 (1954) 27-49.
- [10] D. C. P. Peacock, I. N. Azzam, Development and scaling relationships of a stylolite population, *Journal of Structural Geology*, 28 (2006) 1883-1889.
- [11] A. Hansen, J. Schmittbuhl, G. G. Batrouni, F. A. de Oliveira, Normal stress distribution of rough surfaces in contact, *Geophysical Research Letters*, 27 (2000) 3639-3642.
- [12] C. N. Drummond, D. N. Sexton, Fractal structure of stylolites, *Journal of Sedimentary Research*, 68 (1998).
- [13] J. Schmittbuhl, F. Renard, J.P. Gratier, R. Toussaint, Roughness of stylolites: implications of 3D high resolution topography measurements, *Physical Review Letters*, 93 (2005).

- [14] A. Brouste, F. Renard, J. P. Gratier, J. Schmittbuhl, Variety of stylolites' morphologies and statistical characterization of the amount of heterogeneities in the rock, *Journal of Structural Geology*, 29 (2007) 422-434.
- [15] M. Ebner, D. Koehn, R. Toussaint, F. Renard, J. Schmittbuhl, Stress sensitivity of stylolite morphology, *Earth & Planetary Science Letters*, 277 (2009) 394-398.
- [16] J. P. Petit, M. Mattauer, Palaeostress superimposition deduced from mesoscale structures in limestone: the Matelles exposure, Languedoc, France, *Journal of Structural Geology*, 17 (1995) 245–247, 249–256.
- [17] R. T. A. Rolland, P. Baud, N. Conil, P. Landrein Morphological analysis of stylolites for paleostress, *International Journal of Rock Mechanics & Mining Sciences*, 67 (2014) 212-225.
- [18] M. J. Heap, P. Baud, T. Reuschle, P. G. Meredith, Stylolites in limestones: Barriers to fluid flow?, *Geology*, 42 (2013) 51-54.
- [19] H. K. H. T. Olierook, Nicholas E. Hamilton, P. Joseph, Mechanisms for permeability modification in the damage zone of a normal fault, northern Perth Basin, Western Australia, *Marine & Petroleum Geology*, 50 (2014) 130-147.
- [20] E. Padmanabhan, B. Sivapriya, K. H. Huang, A. K. Askury, W. S. Chow, The impact of stylolites and fractures in defining critical petrophysical and geomechanical properties of some carbonate rocks, *Geomechanics and Geophysics for Geo-Energy and Geo-Resources*, 1 (2015) 55-67.
- [21] Z. Q. Yue, S. Chen, L. G. Tham, Finite element modeling of geomaterials using digital image processing, *Computers and Geotechnics*, 30 (2003) 375-397.
- [22] Z. Wu, Y. Zuo, S. Wang, T. Yi, S. Chen, Q. Yu, W. Li, J. Sunwen, Y. Xu, R. Wang, B. Li, Numerical simulation and fractal analysis of mesoscopic scale failure in shale using digital images, *Journal of Petroleum Science and Engineering*, 145 (2016) 592-599.
- [23] C. Shi, D. J. Li, W. Y. Xu, R. Wang, Discrete element cluster modeling of complex mesoscopic particles for use with the particle flow code method, *Granular Matter*, 17 (2015) 377-387.
- [24] Z. Q. Yue, I. Morin, Digital image processing for aggregate orientation in asphalt concrete mixtures, *Canadian Journal of Civil Engineering*, 23 (1996) 480-489.
- [25] A. Ammouche, D. Breysse, H. Hornain, O. Didry, J. Marchand, A new image analysis technique for the quantitative assessment of microcracks in cement-based materials, *Cement and Concrete Research*, 30 (2000) 25-35.
- [26] F. Lemy, J. Hadjigeorgiou, Discontinuity trace map construction using photographs of rock exposures, *International Journal of Rock Mechanics and Mining Sciences*, 40 (2003) 903-917.
- [27] S. Chen, Z. Q. Yue, L. G. Tham, Digital image-based numerical modeling method for prediction of inhomogeneous rock failure, *International Journal of Rock Mechanics and Mining Sciences*, 41 (2004) 939-957.
- [28] P. Baud, A. Rolland, M. Heap, T. Xu, M. Nicole, T. Ferrand, T. Reuschle, R. Toussaint, N. Conil, Impact of stylolites on the mechanical strength of limestone, *Tectonophysics*, 690 (2016) 4-20.
- [29] L. L. Ben-Itzhak, E. Aharonov, Z. Karcz, M. Kaduri, R. Toussaint, Sedimentary stylolite networks and connectivity in limestone: Large-scale field observations and implications for structure evolution, *Journal of Structural Geology*, 63 (2014) 106-123.
- [30] M. Berry, Z. Lewis, On the Weierstrass-Mandelbrot Fractal Function, *Proceedings of The Royal Society A: Mathematical, Physical and Engineering Sciences*, 370 (1980) 459-484.